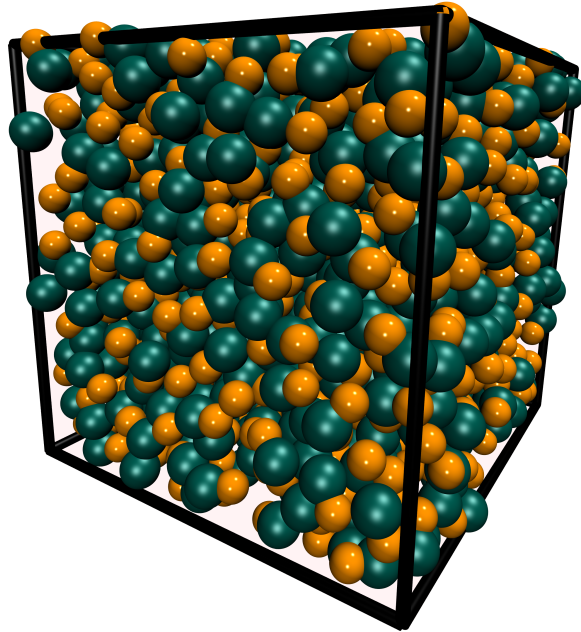


Doctor of Philosophy  
Doctoral Thesis in Condensed Matter Physics



**Expanding the Class of R-simple Systems:  
The Weeks-Chandler-Andersen Liquid and the Asymmetrical  
Dumbbell Plastic Crystals**

Author: Eman Attia



**Supervisor:** Assoc. Prof. Ulf R. Pedersen  
**Co-supervisor:** Prof. Jeppe C. Dyre

**Glass & Time**  
**Department of Science and Environment**  
**Roskilde University**  
Universitetsvej 1  
Building 27  
4000 Roskilde, Denmark

# Abstract

---

In 2008, Bailey *et al.* [1] classified a class of liquids that show hidden scale invariance in some regions of the phase diagram. These liquids are referred to as R-simple systems. They present interesting consequences and simple properties. Their simplicity lies in the fact that curves can be traced out in their phase diagram called isomorphs, along which many properties are invariant to a high degree. To explore this simplicity, a framework was formulated, the isomorph theory. This thesis is an investigation of two systems, the Weeks-Chandler-Andersen (WCA) system and the asymmetrical dumbbell model (ASD) system in the light of isomorph theory. The work proves the WCA system as an R-simple system, showing hidden scale invariance and obeying the isomorph theory with some interesting observations. The WCA system is demonstrated to exhibit "extreme density scaling" unlike any other R-simple system in the low temperature/-density region of the phase diagram, with an unprecedented variation of the density scaling exponent. The WCA system shows to be very far from an inverse power law system while exhibiting the hidden scale invariance. The second system, the ASD system, shows hidden scale invariance in both the liquid and the plastic-crystalline phases of the phase diagram and obeys the isomorph theory where its predictions follow in the liquid and plastic crystalline phases. The ASD plastic crystals are the first plastic crystals to be investigated for the hidden scale invariance. In summary, the work presented expands the R-

simple systems family to include the WCA liquid and the ASD liquid along with the ASD plastic-crystals.

# Dansk Resumé

---

I 2008 klassificerede Bailey *m.fl.* [1] en gruppe af væsker, der viser skjulte skaleringsinvarianter i nogle områder af faseagrammet. Disse væsker refereres til som R-simple systemer. De giver anledning til interessante konsekvenser og simple egenskaber. Deres enkelthed ligger i, at kurver kan følges i deres faseagram, benævnt isomorfier, hvor mange egenskaber i meget høj grad er invariante. For at udforske denne forenkling yderligere er der formuleret et metodeapparat, nemlig isomorfitheorien. I denne afhandling undersøges to systemer, Weeks-Chandler-Andersen (WCA)-systemet, og det asymmetriske dumbbell-model (ASD)-system, begge i relation til isomorfitheorien. Arbejdet i denne afhandling efterviser WCA som et R-simpelt system med en skjult skaleringsinvariant, der er en hovedidentifikation inden for isomorfitheorien, langs isomorfierne i faseagrammet, og det eftervises at efterfølge isomorfitheorien med nogle interessante observationer. WCA-systemet eftervises at udvise såkaldt "ekstrem densitetsskalering" med en hidtil uset variation af densitetsskaleringsekspONENTEN, i modsætning til andre isomorfivæsker i lavtemperatur- og -densitetsregionen af faseagrammet. Ydermere, så viser WCA-systemet sig at være langt fra et inverst potenslovssystem, medens det udviser skjult skaleringsinvariant. Det andet system, ASD-systemet, indikerer skjult skaleringsinvariant i både den flydende og plastiske krystalfase i faseagrammet, og systemet efterlever isomorfitheorien, hvor forudsigelserne i den flydende og plastiske krystalfase følges. ASD-plastikkrytallerne

er de første plastikkrystaller, der undersøges for skjult skaleringsinvariant. Det præsenterede arbejde udvider den R-simple systemfamilie til også at omfatte WCA- og ASD-væsken samt ASD-plastikkrystallerne.

# Guide to the Reader

---

This doctoral thesis describes the work done of the Roskilde University PhD program between July 2019 till September 2022. The work has been supervised by Ulf R. Pedersen and Jeppe C. Dyre and conducted during the COVID-19 time within the *Glass and Time* group. This work resulted in three research papers reprinted in section "Reprints of Articles and Posters." Only two of the research papers are discussed in the thesis below as the third had a minor contribution by me. Due to COVID-19, most of the conferences and scientific gatherings were canceled. Most talks and presentations were conducted online. My oral presentations (not included) and posters (included in "Reprints of Articles and Posters") have been presented in the PhD days conducted by Roskilde University, *Glass and Time* workshops and the annual Molecular Dynamics meetings.

Chapter 1 is an introduction to the theory of liquids and the aim of the work presented, which is hidden scale invariance investigation in both the WCA and ASD systems. Chapter 2 explains the theory behind the main motive of this thesis, which is the isomorph theory. Chapter 3 discusses the method used to generate the research data, which is computer simulations and molecular dynamics in particular. Chapter 4 covers in detail the investigation of the Weeks-Chandler-Andersen system. We follow each finding in the Chapter by a brief summary and discussion. Chapter 5 covers in detail the investigation of the asymmetrical dumbbell model. We follow each finding in the Chapter by a brief summary and discussion. Chapter 6 is the overall

conclusion of the work done in Chapter 4 and 5. We here summarize our findings and the achieved goals of this research work presented.

# Acknowledgements

---

I would like to thank everyone in the Glass and Time group for their great help and understanding that kept me going throughout my thesis time in Denmark. Special thanks to Ulf Pedersen, my main supervisor, for his patience and knowledge he has given me throughout my PhD time. Special thanks also to Jeppe Dyre for his mentorship and encouragement. Truly showed me how a leader, a boss or whoever in charge of supervising other people should act. I would like to thank Heine for fixing code errors, Joachim Niemann-Larsen for his time and for translating the abstract, and Nada Attia for simply existing.



# List of Publications

---

Paper I: E. Attia, J. C. Dyre and U. R. Pedersen. *Phys. Rev. E*, 103, 062140 (2021).

Paper II: E. Attia, J. C. Dyre, and U. R. Pedersen. [arXiv:2209.11498](https://arxiv.org/abs/2209.11498).

Paper III: E. Attia, J. C. Dyre, and U. R. Pedersen. *J. Chem. Phys.* 157, 034502 (2022).



# Contents

---

<b>Abstract</b>	<b>i</b>
<b>Dansk Resumé</b>	<b>iii</b>
<b>Guide to the Reader</b>	<b>v</b>
<b>Acknowledgements</b>	<b>vii</b>
<b>List of Publications</b>	<b>ix</b>
<b>Contents</b>	<b>xi</b>
<b>1 Introduction</b>	<b>1</b>
1.1 Liquid State of Matter . . . . .	1
1.2 Liquids in Computer Simulations . . . . .	4
1.2.1 Simple Liquids . . . . .	5
1.2.2 Roskilde Simple Liquids . . . . .	11
1.3 Motive and Aims: Expanding the Hidden Scale Invariance Systems . . . . .	13
1.3.1 The Weeks-Chandler-Andersen System . . . . .	13
1.3.2 The Asymmetric Dumbbell Model System . . . . .	17
<b>2 Empirical Motivations for the Isomorph Theory</b>	<b>21</b>

---

2.1	Connecting Entropy Scaling and Density Scaling . . . . .	21
2.2	Hidden Scale Invariance . . . . .	29
2.3	Consequences of Isomorph Theory . . . . .	31
2.3.1	Strong Correlations between Potential Energy and the Virial . . . . .	32
2.3.2	Generating Isomorphs: Density Scaling Exponent	36
2.3.3	Isomorphs: Lines of Invariant Structure and Dy- namics . . . . .	38
<b>3</b>	<b>Methods: Computer Simulations</b>	<b>43</b>
3.1	Molecular Dynamics . . . . .	43
3.2	Simulated Systems . . . . .	46
<b>4</b>	<b>Hidden Scale Invariance of the Weeks-Chandler-Andersen System</b>	<b>49</b>
4.1	The Weeks-Chandler-Andersen System: Definition and Setup . . . . .	49
4.2	Density Scaling in the High Temperature Region . . . . .	54
4.2.1	Structure and Dynamics Invariance . . . . .	54
4.3	Extreme Density Scaling in the Low Temperature Region	61
4.3.1	Mean-field Theory for the Density Scaling Ex- ponent Extreme Variation at Low Temperatures	72
<b>5</b>	<b>Hidden Scale Invariance in the Asymmetrical Dumb- bell System</b>	<b>77</b>
5.1	The Asymmetrical Dumbbell System: Definition and Setup . . . . .	77
5.2	Validating Against Literature Viscous Data . . . . .	78
5.3	Systematic Numerical Investigation in the Asymmetri- cal Dumbbell System . . . . .	84
5.3.1	Isomorphs in the Liquid Phase . . . . .	84
5.3.1.1	Structure and Dynamics Invariance . . . . .	95

---

5.3.2	Isomorphs in the Plastic-Crystalline Phase . . .	108
5.3.2.1	Structure and Dynamics Invariance . .	111
5.3.2.2	Transition: From Plastic-Crystalline State to Glassy State . . . . .	130
<b>6</b>	<b>Conclusion</b>	<b>135</b>
	<b>Bibliography</b>	<b>138</b>
	<b>Appendices</b>	<b>149</b>
	<b>Appendix A Fourth-Order Runge Kutta Method: Trac- ing Better Isomorphs</b>	<b>151</b>
	<b>Appendix B Data Analysis Tools for LAMMPS: Useful Home-made Scripts</b>	<b>161</b>
B.1	Calculations of the Mean Square Displacement (MSD)	163
B.2	Calculation of the Radial Distribution Function (RDF)	165
B.3	Calculations of the Velocity Auto-correlation (VAC) Func- tion . . . . .	167
B.4	Calculations of the Rotational Auto-correlation (RAC) Function . . . . .	169
	<b>Reprints of Articles and Posters</b>	<b>173</b>
	<b>Declaration of Co-authorship</b>	<b>217</b>



# CHAPTER 1

## Introduction

---

### 1.1 Liquid State of Matter

In every day experience, we encounter the three well-known states of matter: the solid, the gas or the liquid. This can be seen in the apple we eat, the perfume we smell or the water we drink etc. Each state can be differentiated from the other by the strength of the interactions between its constituents [2]. In a liquid, the interaction between the particles is not as weak as it is in the gases or as strong as it is in the solids. Compared to solids, liquids have less ordered arrangement of atoms or molecules and no long-range order. This can be seen in the lab in diffraction experiments. In such experiments, crystalline solids give sharp Bragg reflections demonstrating an ordered arrangement of atoms or molecules, unlike liquids [3]. A liquid can flow and change its shape.

When it comes to differentiating liquids from gasses, the flow, which is the main characteristic we use to define liquids, doesn't hold for liquids only. Liquids so as gases, can flow under constant shear stress, no matter how small. Both are considered "fluid." Thus, this leads us to a fundamental question: can the liquid be distinguished from the gas then?

In order to answer the question, we shift to a thermodynamic interpretation. The liquid phase can be interpreted as an equilibrium state of matter in a limited zone of the thermodynamic space in coexistence

with the gas phase on the higher volume side and the solid phase in the lower volume region. These three regions can be represented as a

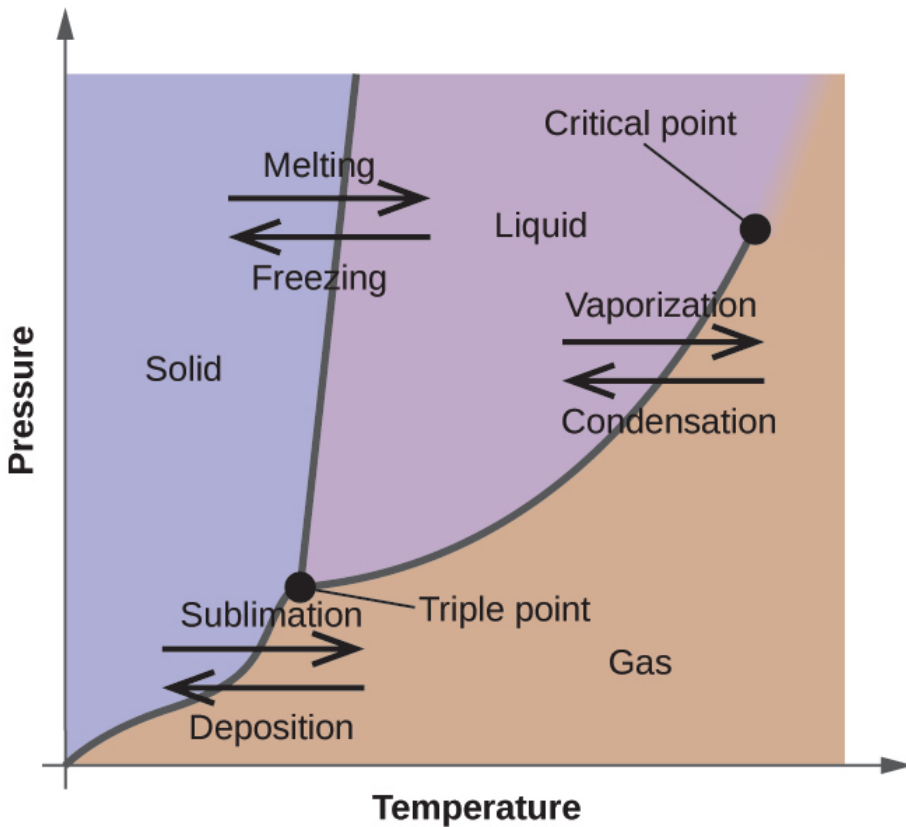


**Figure 1.1.** Phase diagram of a single-component system as a function of Pressure (P) and temperature (T). The two curves starting from the triple point are the melting line (from the blue region to the purple region) and the vaporization line (from the purple region to the brown region). Figure from Ref. [4].

dimensional plot of pressure and temperature called "phase diagram."

In this phase diagram, the triple point (TP) is a point where solid, liquid and gas have the same pressure and temperature with different volumes (Fig. 1.1). The coexistence curves of a liquid with solid and gas start from the TP. The liquid phase is the area between these coexistence curves till the critical point. Another important point in the phase diagram is the critical point which is defined by a critical pressure  $P_c$  and critical temperature  $T_c$ . This point marks the end of the gas-liquid coexistence curve, super-critical fluid is formed and there is no phase boundary (The top point in Fig. 1.1). At temperatures below the critical temperature, two fluid phases can coexist in equilibrium, the liquid is interpreted as the denser phase while the less dense phase is the gas.

Therefore, a distinction definition of a liquid state may not be present as one sole definition. Gas and liquid phases can coexist at the same pressure and temperature with different densities [3]. Moreover, the phase diagram in Fig 1.1 is of a single-component system, which is the simplest case. For different liquids or multi-component liquids (atomic or molecular), arise other challenges. It becomes more complicated to define the liquid state.

Apart from the challenging definition, liquids exhibit other interesting phenomena. Some liquids can go into other metastable states rather than the conventional phase transitions [3, 5] i.e, they don't crystallize upon cooling down below the freezing point. For a liquid to crystallize, it needs to be slow-cooled so that the system is allowed to reach equilibrium crystalline phase [3]. If a liquid is cooled fast instead, it becomes "supercooled." The movement of the liquid atoms or molecules slows down, but won't reach the slow crystalline phase. If the movement slows down to nearly a stop, the liquid enters another state. This state is called the "glass state." It is not a state of equilibrium since the crystal is thermodynamically stable by having a lower free energy. In the glassy state, the dynamics of crystalline growth is frozen and crystallization is avoided. Figure 1.2 illustrates

this transition state as a function of volume ( $V$ ) and temperature ( $T$ ).

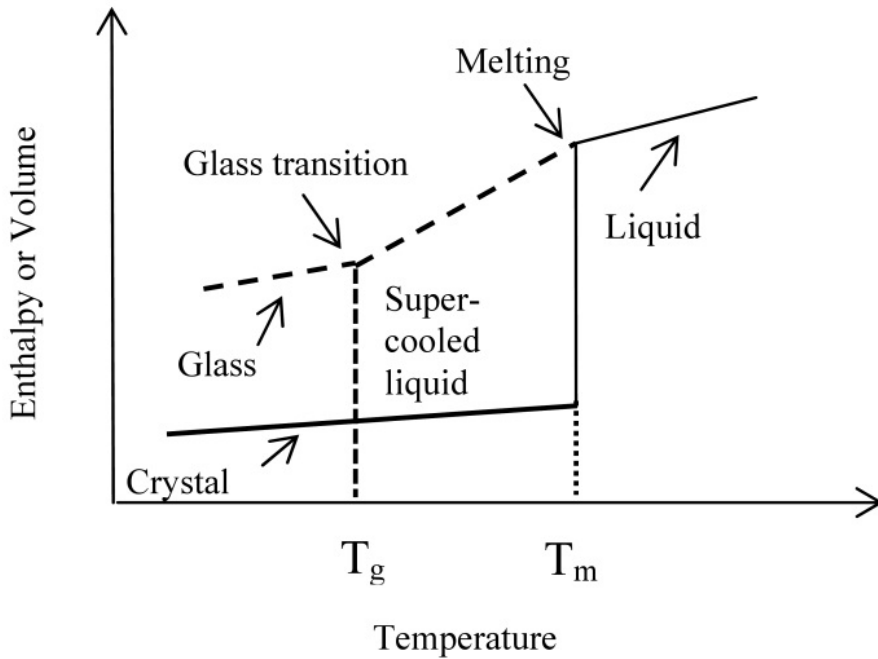


**Figure 1.2.** The liquid, glassy and crystalline states as a function of volume and temperature.  $T_g$  is glass transition temperature and  $T_m$  is melting temperature. Figure from Ref. [6].

## 1.2 Liquids in Computer Simulations

Liquids can have many phenomena that are interesting to study. They can avoid crystallization and be super-cooled. They can also reach the

glassy state and become glass. Thus, understanding the behavior of liquids becomes a wide research topic in condensed matter.

With the rise of computing power, computer simulations come to take part in the liquid-state studies as well. More complex calculations can be executed making it possible to further understand the physics of liquids and test any theoretical predictions.

Liquids can be represented in computer simulations with various models. They can be represented as model systems of particles (whether atoms or molecules) interacting through "simple" pair potentials or also through more "complicated" inter-atomic potentials. Other methods such as *ab initio* molecular dynamics can be used. It avoids the pair potentials and considers the ground state electron calculations using the density functional (DFT) theory [7]. Simulated systems can become more complex. Here, we focus only on the simple approach.

## 1.2.1 Simple Liquids

To simulate a liquid, we need to represent its microscopic state as an input for a computer simulation program. For any system, atomic or molecular, the positions and momenta define the current state of the system. We can describe a system of  $N$  particles as a sum of the kinetic and potential energy functions of the set of coordinates  $\mathbf{r}_i$  and momenta  $\mathbf{p}_i$  of each particle  $i$  such that

$$\mathbf{R} = (\mathbf{r}_1, \mathbf{r}_2, \dots, \mathbf{r}_N) \quad (1.1)$$

$$\mathbf{P} = (\mathbf{p}_1, \mathbf{p}_2, \dots, \mathbf{p}_N) \quad (1.2)$$

$$H(\mathbf{R}, \mathbf{P}) = U(\mathbf{R}) + K(\mathbf{P}) \quad (1.3)$$

Here,  $K$  is the kinetic energy,  $U$  is the potential energy and  $H$  is the Hamiltonian of the system. From the potential energy  $U$ , an equation of motion can be obtained in Newtonian form [8]. The forces  $\mathbf{f}_i$  acting

on the particles then can be calculated through the gradient of the potential energy  $U$ . If  $m_i$  is the mass of the particle  $i$ , the force acting on the particle  $i$  can be calculated as

$$\mathbf{f}_i = -\nabla_{\mathbf{r}_i} U(\mathbf{R}) \quad (1.4)$$

In computer simulations, the potential energy is separated into terms involving pairs of molecules, triplets, etc. Since we are adapting the simple approach, the potential energy is represented as a pair-potential  $v(r_{ij})$

$$U(\mathbf{R}) = \sum_{i>j}^N v(r_{ij}) \quad (1.5)$$

in which  $r_{ij}$  is the distance between particle  $i$  and  $j$  such that  $r_{ij} = |\mathbf{r}_i - \mathbf{r}_j|$ .

With the simple approach in mind, we introduce four models that are widely used to simulate simple liquids. The theory of simple liquids is based on the assumption that the liquid state is governed by the repulsive part of the interaction potential between its constitutions. When it comes to simple pair-potential representation, the hard-sphere (HS) model is perhaps the most simple [2]. It is a simple model that is still used in simulations and in comparing to liquid state theory [8]. The interaction between the particles which are represented as hard spheres is the pair potential  $v(r)$ . The separation distance between two particles is  $r$  such that pair potential approximation gives a good description of the liquid properties

$$v(r) = \begin{cases} \infty, & r < d \\ 0, & r > d \end{cases} \quad (1.6)$$

where  $d$  is the hard sphere diameter. This model has relevance to real, physical systems. The state-point dependent properties of the system

depend only on the packing fraction

$$\eta = (\pi/6)\rho d^3 \quad (1.7)$$

where  $\rho$  is the density [2] and doesn't depend on temperature as in real systems (only as a trivial scaling of velocities). So, to relate the properties of a real system to those of the HS system, a sort of "matching" is needed. This can be achieved by varying the hard sphere diameter  $d$  that depends on the density and temperature of the real system in question. The HS system can have many advantages, yet, it can't describe a liquid close to the critical point or to the liquid-gas transition [2].

Based on the same assumption proposed by the theory of simple liquids that only the repulsive forces determine the behavior of the liquid phase, another simple potential arises, the inverse power law potential (IPL). It is defined as

$$v_{IPL}(r) = \epsilon(\sigma/r)^n \quad (1.8)$$

where  $\sigma$  is the separation the particles reach when  $v(r) = 0$  or the collision parameter and  $\epsilon$  is the depth of the potential at the minimum of  $v(r)$ . Systems that interact via the IPL are called soft spheres systems. The HS can be thought of as a special or a limit case of the IPL when the exponent  $n \rightarrow \infty$ . Similar to HS, Hoover *et al.* [9] show that the thermodynamics properties of soft sphere systems can be scaled by the factor

$$\rho^{n/3}/T \quad (1.9)$$

where  $n$  is the IPL exponent. Alternatively, this factor can be written as

$$TV^{n/3} \quad (1.10)$$

With one parameter to control the thermodynamics properties, the phase diagram of IPL and HS systems become a one-dimensional phase diagram.

The third system we discuss is one of the most frequently used pair-potentials. It is simple enough, yet can describe the real interactions of a system such as Argon. It is the Lennard-Jones (LJ) potential. Unlike the IPL, it consists of an attractive part and a repulsive part. This potential was suggested by Sir John Lennard-Jones who gave the

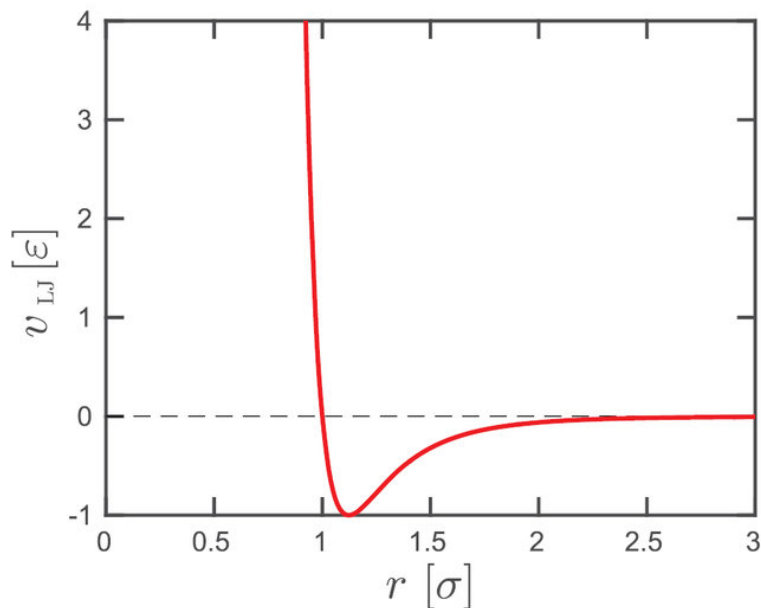


**Figure 1.3.** The Lennard-Jones potential  $v(r)$  represented as a function of the pair distance between the particles,  $r$ . The minimum of the potential is at  $r = 2^{1/6}\sigma$ . Figure from Ref. [10].

description of the potential energy as a function of the separation of the particles (Fig. 1.3).

$$v(r) = 4\epsilon[(\sigma/r)^{12} - (\sigma/r)^6] \quad (1.11)$$

Based on van der Waal's ideas [11], many properties of liquids are dependent on the fact that inter-molecular forces consist of short ranged harsh repulsions and long ranged weak attractions. This is typically what we see here. This potential consists of a steep repulsive part at short distances till distance  $r_c = 1.122\sigma$  that rise up to an attractive tail at longer distances as shown in Fig. 1.3. LJ potential can present the properties of liquid argon with good approximation in computer simulations with the parameters  $\sigma = 3.4 \text{ \AA}$  and  $\epsilon/k_B = 120 \text{ K}$ ,  $k_B$  is the Boltzmann constant.

With time and more attempts to present pair potentials that can describe wide variety of systems, the fourth system we discuss here came to life, the "Weeks-Chandler Andersen" potential. The Weeks-Chandler-Andersen (WCA) potential was first proposed by Weeks *et al.* in 1971 [12]. The WCA potential is similar to the well-known standard LJ pair potential. Yet, the main difference is that the WCA potential is cut at the LJ potential minimum and subsequently shifted by adding a constant, such that the minimum is lifted to zero (Fig. 1.4). That results in a purely repulsive pair potential given by:

$$v(r) = \begin{cases} 4\epsilon [(r/\sigma)^{-12} - (r/\sigma)^{-6}] + \epsilon & (r < 2^{1/6}\sigma) \\ 0 & (r > 2^{1/6}\sigma) \end{cases} \quad (1.12)$$

where  $\sigma$  is the particle radius and  $\epsilon$  is the energy depth of the LJ potential well at its minimum at  $r = 2^{1/6}\sigma$ . Although the total potential is repulsive, it is composed of repulsive  $r^{-12}$  and attractive  $r^{-6}$  components. The WCA system was originally devised as a reference fluid in perturbation treatment for the LJ fluid, where the repulsion is to be responsible for the liquid structure and the attraction is treated as a minor perturbation. It is of a significant importance as it is used widely for larger systems such a bio-molecules and polymers [14].

When it comes to molecular systems, we can still use the atomic approach. The chemical bonds can be thought of as an inter-atomic

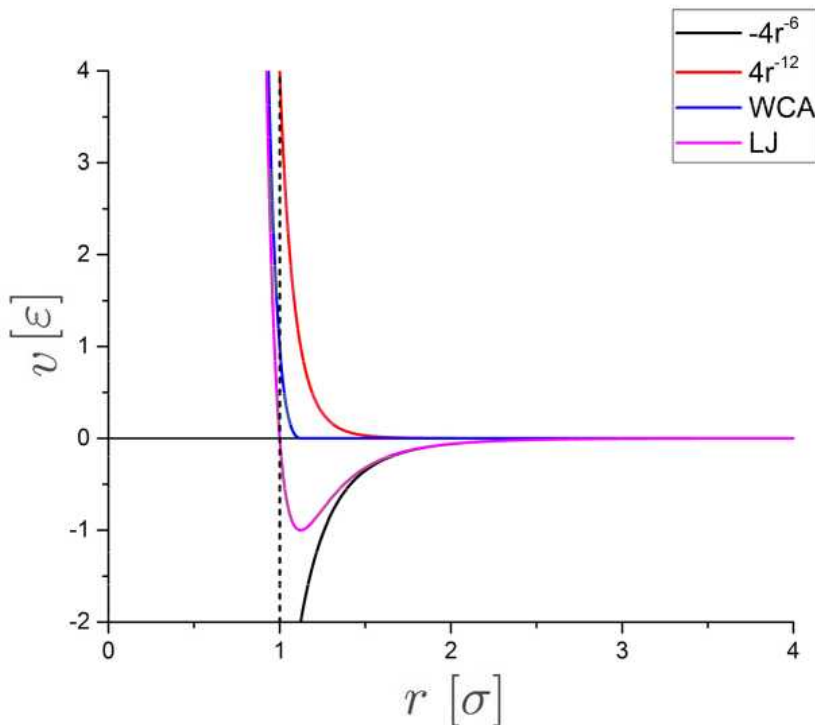


**Figure 1.4.** Comparison of attractive and repulsive Lennard-Jones (LJ) potential and short-range repulsive Weeks-Chandler-Andersen (WCA) potential. We can see how the WCA is truncated and shifted up. Figure from Ref. [13].

potential energy term added. The bonds can be either treated as classic harmonic springs (flexible bonds) or as rigid constraints. The molecule can be treated as a rigid unit with fixed bond lengths and fixed angles as well [8]. Later, we study molecules of connected LJ spheres. The method we use for such calculations is molecular dynamics. It is discussed in Chapter 3.

## 1.2.2 Roskilde Simple Liquids

Simulations using simple models show that different systems often have very similar structure and dynamics [8]. For instance, it is shown that the structure of the hard-sphere fluid doesn't differ in any significant way from that corresponding to more complicated inter-atomic potentials, at least under conditions close to crystallization [2]. Simple liquids models then are not just simple, but useful as well. In the simple HS and IPL, the physical properties, as mentioned earlier, depend only on one thermodynamic parameter, the density. This leads to a trivial scaling in which the phase diagram is one-dimensional. In 2008, the Glass and Time group in Roskilde university started to develop their own definition of simple liquids. According to the Roskilde group, simple liquids are liquids that exhibits hidden scale invariance in the symmetry of the potential energy function  $U(\mathbf{R})$  in which the configuration  $\mathbf{R}$  of a system of  $N$  particles in terms of the particle coordinates is defined by  $\mathbf{R} \equiv (\mathbf{r}_1, \dots, \mathbf{r}_N)$ . This class of liquids has simpler properties than other liquids. Hence, with the Roskilde approach, these liquids are defined as "Roskilde-simple liquids" or "R-simple liquids."

Unlike the HS or IPL systems, in which the thermodynamic properties exhibit an expected density "scaling", this class of liquids exhibits non-trivial "hidden" scaling. The thermodynamic properties of Roskilde simple liquids depend on the density and the temperature combined, not just one of them. R-simple liquids include many atomic and molecular model systems such as the single-component and multi-components LJ models [15,16], the rigid-bond flexible LJ chain model (polymer model) [17], the Yukawa model [1, 18], asymmetric dumbbell models [19], the Lewis-Wahnström OTP model [19], and many metallic systems as well [20].

Figure 1.5 [1] shows that an IPL with the effective inverse power law exponent  $n = n_{eff} = 18$  can match the LJ potential for distances of

length-scales of typical interactions at a given state point. It deviates only in the attractive part. Roskilde-simple liquids then take a step further towards liquid simplicity. Their phase diagram is not a trivial one-dimensional phase diagram, but an "effective" one-dimensional phase diagram.

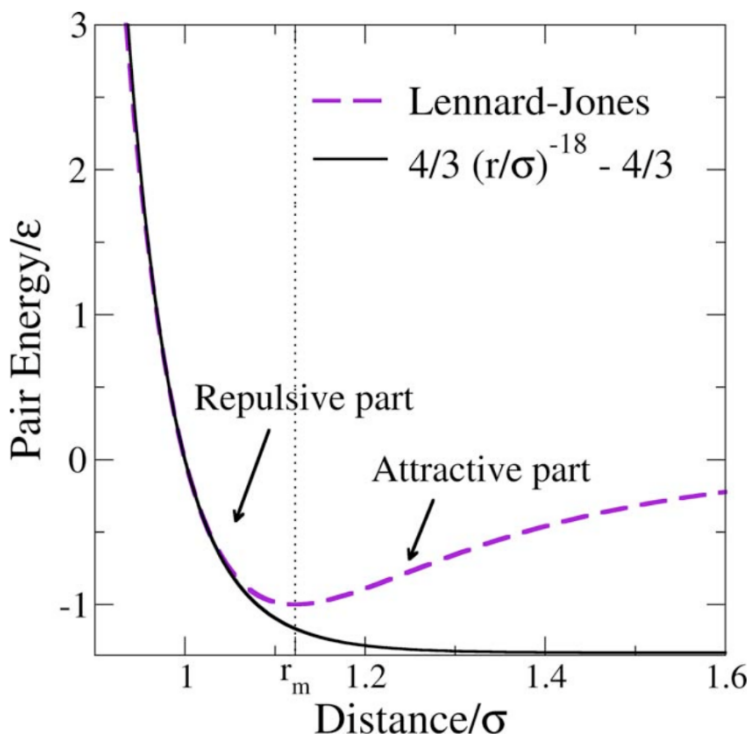


**Figure 1.5.** An inverse power law potential with an exponent of  $n = 18$  leading to an “effective inverse power law” potential that matches the Lennard-Jones potential and its first two derivatives at the point  $r = \sigma$ . At  $r_m$ , we can see the separation between the repulsive and attractive parts of the Lennard-Jones potential. Figure from Ref. [1].

## 1.3 Motive and Aims: Expanding the Hidden Scale Invariance Systems

This work aims at expanding the class of R-simple liquids or precisely, the systems that exhibit hidden scale invariance. We check for the hidden scale invariance in two systems with two different potentials. We then proceed to investigate the consequences of the hidden scale invariance in the phase diagram of both systems. The isomorph theory and the consequences of hidden scale invariance are discussed in Chapter 2.

### 1.3.1 The Weeks-Chandler-Andersen System

In 2009, Berthier and Tarjus [21] tried to reproduce the structure and the viscous dynamics of Kob-Andersen LJ (KABLJ) liquid with the Kob-Andersen Weeks-Chandler-Andersen (KABWCA) liquid. Since the structure of dense fluids is to a good approximation determined by their repulsive forces based on the liquid-state theory [2, 22], the KABWCA liquid is expected to give the same structure and dynamics of the KABLJ liquid. The KABLJ is a binary 80:20 mixture of particles A and B. Both types of particles have the same mass  $m$ . All particles interact via Lennard-Jones potential. In the KABWCA liquid, they interact via the standard WCA potential instead. The parameters of the various interaction potentials are as follows:  $\epsilon_{AA} = 1.0$ ,  $\sigma_{AA} = 1.0$ ,  $\epsilon_{AB} = 1.5$ ,  $\sigma_{AB} = 0.8$ ,  $\epsilon_{BB} = 0.5$  and  $\sigma_{BB} = 0.88$  [23].

They concluded that, the structure of the two liquids can be the same. But, the dynamics are different especially at low temperatures.

In 2010, Pedersen *et al.* [24] reproduced the same results as Berthier and Tarjus with an additional binary liquid, the Kob-Andersen repulsive inverse power (KABIP) liquid where the interaction potential is IPL. For the IPL liquid, the exponent  $n$  is chosen to be  $= 15.48$  to fit the slope  $\gamma = 5.16$  of the constant-volume equilibrium fluctuations of virial  $W$  versus potential energy  $U$  of the KABLJ liquid at three state points with same density in the super-cooled regime such that  $n = \gamma \times 3 = 15.48$ . The motivation for this is given later in Chapter 2. Figure 1.6 shows that the three systems almost gives the same

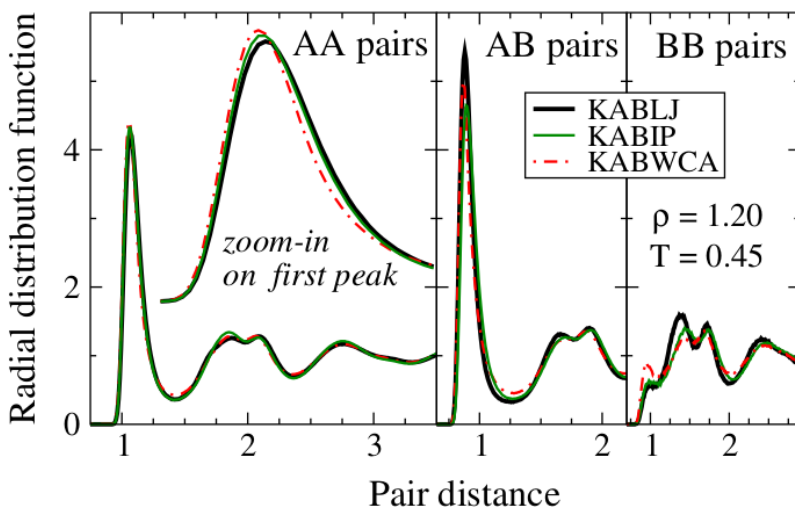


**Figure 1.6.** The radial distribution functions of the AA, AB, and BB particle pairs of the KABLJ, KABIP, and KABWCA liquids at  $\rho = 1.20, T = 0.45$ . The structure of the three systems is almost the same (the curves are almost collapsing). Figure from Ref. [24].

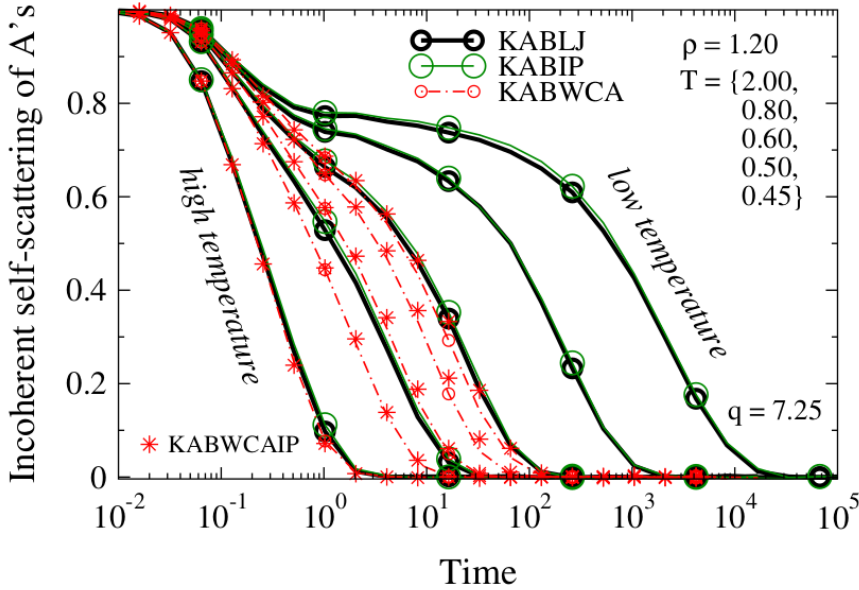


**Figure 1.7.** Incoherent intermediate self-scattering function for the A particles of the KABLJ, KABIP, KABWCA and KABWCAIP liquids along the same density ( $\rho = 1.20$ ) isochoire for five temperatures,  $T = 0.45, 0.5, 0.6, 0.8, 2.0$  in LJ units. The dynamics of the KABWCA liquid (connected red open circles) doesn't match with KABLJ's at low temperatures (connected black open circles), but can be reproduced with the KABWCAIP liquid (connected red stars). Figure from Ref. [24].

structure. The structure is probed by the AA, AB and BB particles radial distribution functions (RDF) [24]. It is defined as the probability of finding a particle at a distance  $r$  from another particle. When it comes to dynamics, Pedersen *et al.* shows that the KABWCA liquid dynamics can be reproduced instead when the IPL is used to represent the repulsive forces. Figure 1.7 shows that the KABWCA give

the same dynamics as the KABWCAIP liquid at high and low temperatures unlike the KABLJ one. The dynamics are probed via the A particles incoherent intermediate self-scattering function. The intermediate scattering function is defined as the Fourier transform of the Van Hove function where  $k$  is the wave vector or the probability density of finding particle  $i$  in the vicinity of  $r$  after time  $t$ ,

$$F(\mathbf{k}, t) = \int d\mathbf{r} G(\mathbf{r}, t) e^{-i\mathbf{k} \cdot \mathbf{r}} \quad (1.13)$$

It is a measure of how the structure of a system relaxes. It can be defined as a self part  $F_s(\mathbf{k}, t)$  and distinct part  $F_d(\mathbf{k}, t)$ . The self-intermediate function  $F_s(\mathbf{k}, t)$  is directly measured in experiments i.e, Neutron Spin Echo [25]. In simulations, it can be computed from the particle trajectories as

$$F_s(\mathbf{k}, t) = \frac{1}{N} \sum_{j=1}^N \langle \exp[i\mathbf{k} \cdot (\mathbf{r}_i(t) - \mathbf{r}_i(0))] \rangle \quad (1.14)$$

where  $N$  is the number of particles and  $(\mathbf{r}_i(t) - \mathbf{r}_i(0))$  is the displacement of particle  $i$  after time  $t$ . The brackets denote an ensemble average.

As a widely used potential in the field of condensed matter simulations i.e, in polymers or protein-polymer conjugations [14,26,27], these findings from Pedersen *et al.* motivated the investigation of the single-component Weeks-Chandler-Andersen (SCWCA) system. In Chapter 4, we study the SCWCA system to understand its dynamics and see whether it is a Roskilde simple liquid. We present the hidden-scale investigation in the liquid region of the SCWCA phase diagram. In particular, we show that its density-scaling exponent  $\gamma$  throughout the phase diagram varies much more than that of most other systems.

## 1.3.2 The Asymmetric Dumbbell Model System

The asymmetric dumbbell system is a simple molecular system that can be easily super-cooled, i.e., avoid crystallization [19]. This makes the ASD model suitable for numerical studies as a simple, single-component glass-forming model of non-spherically symmetric constituents [16, 28–30]. Each molecule consists of two different Lennard-Jones (LJ) spheres, one big A and one smaller B connected by a rigid bond. If the rigid bond between the two spheres is of length = 0.584 in A particle LJ units, the model mimics toluene [31]. The values of the parameters used are as follow; for particle A, the distance and energy units are  $\sigma_{AA} = \epsilon_{AA} = 1$  and the particle mass is  $m_A = 1$ . While for particle B,  $\sigma_{BB} = 0.788$ ,  $\epsilon_{BB} = 0.117$  and  $m_B = 0.195$  (in A particle units). For  $AB$  interaction,  $\sigma_{AB} = 0.894$  and  $\epsilon_{AB} = 0.342$  [19]. This system has been shown to have strong virial potential energy  $WU$  correlations in the thermal-equilibrium constant-volume fluctuations in the viscous liquid region [19]. Thus, it exhibits the hidden scale invariance and so-called isomorphs (Chapter 2) can be traced out in that region of the phase diagram. Ingebrigtsen *et al.* [19] in Fig. 1.8 show structure and dynamics invariance along a traced isomorph in the viscous region of the ASD phase diagram. The structure is probed via AA particle reduced radial distribution function. The dynamics is probed via the reduced A particle incoherent intermediate scattering function. In the same reference, the variation of the Pearson correlation coefficient  $R$  which is a measure of how strongly  $UW$  are correlated is investigated at the state point  $\rho = 0.932, T = 0.465$  along different bond lengths (Fig. 1.9). Yet, no further data regarding structure or dynamics at such different bond lengths is included. Therefore, in this work, we extend the investigation to the less viscous liquid and plastic crystalline phases and study the effects of bond-length variation. In

Chapter 5, we reproduce the same data from literature and present the hidden scale and the bond-length variation investigation in the less viscous liquid and plastic-crystalline phases. This work is the first investigation of the hidden scale invariance in plastic crystals.

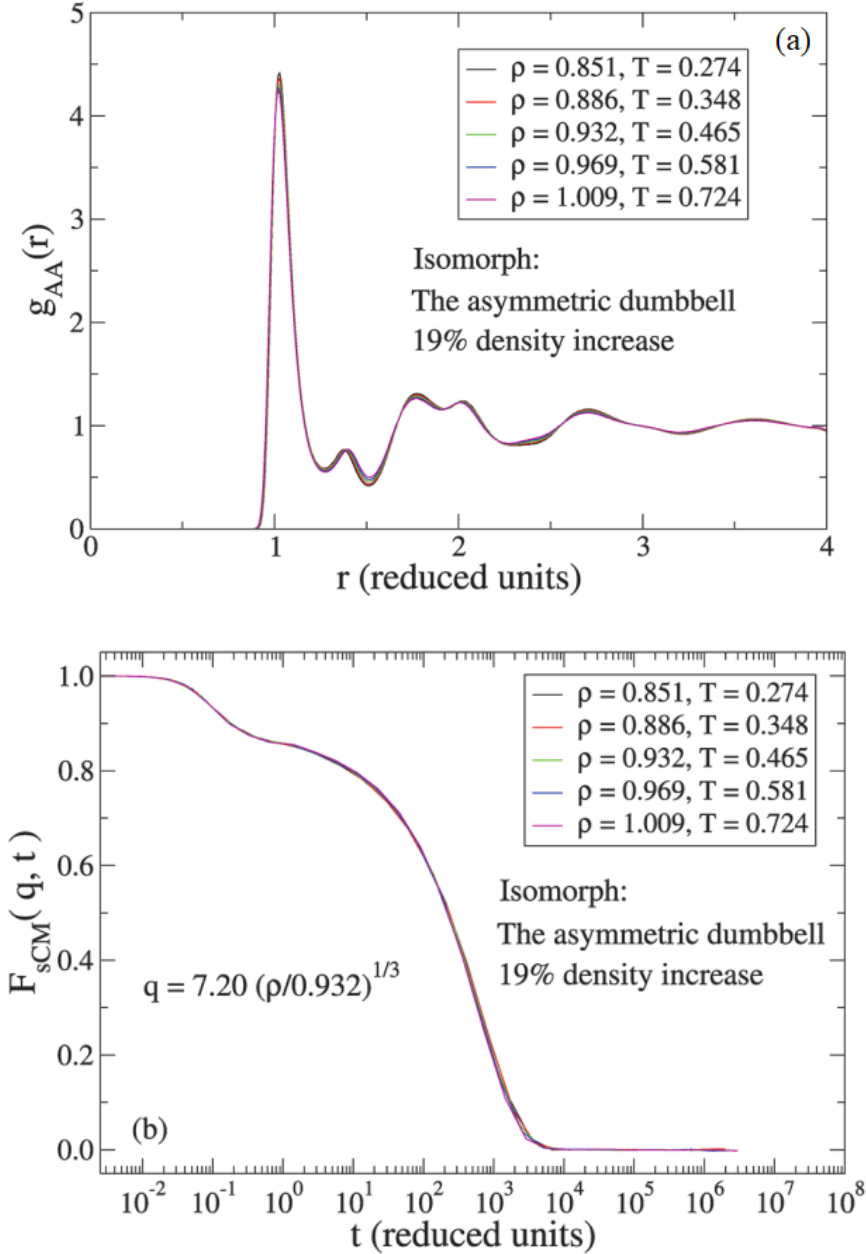


**Figure 1.8.** (a) The reduced radial AA distribution function of the listed five state-points along an isomorph (b) the A-particle incoherent intermediate scattering function of the same state points. The data for all the state points collapse, showing approximately good invariance in (a) structure and (b) dynamics. Figure from Ref. [19].

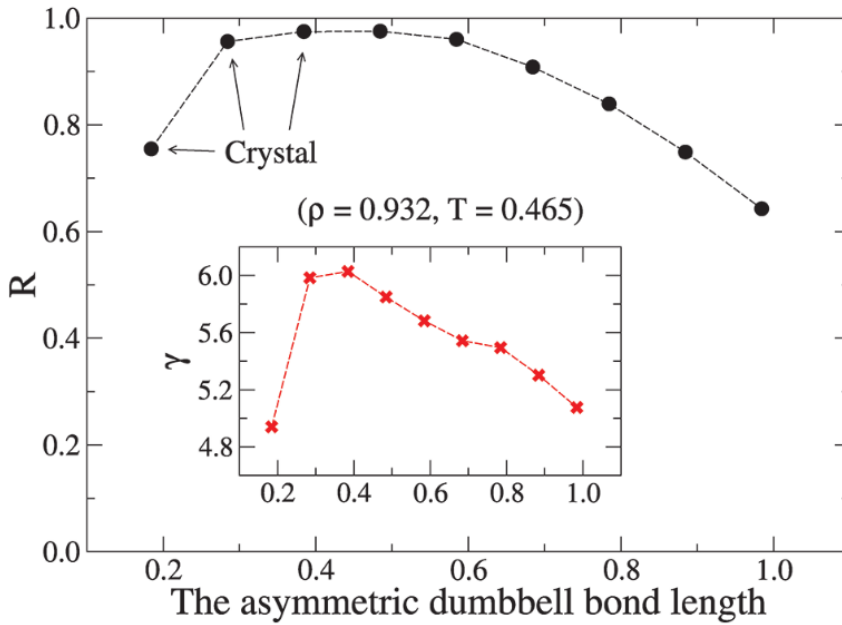


**Figure 1.9.** The variation of the Pearson correlation coefficient  $R$  as a function of the ASD bond length at  $\rho = 0.932, T = 0.465$  in LJ units. The inside figure is the variation of the density scaling exponent  $\gamma$  as a function of the ASD bond length. Figure from Ref. [19].

# CHAPTER 2

## Empirical Motivations for the Isomorph Theory

---

### 2.1 Connecting Entropy Scaling and Density Scaling

When liquids are super-cooled, they enter a metastable thermodynamic state as discussed in the previous chapter. The structure and dynamics of this state is of a great interest as it helps to understand the inter-atomic behavior of the super-cooled liquids. In various super-cooled systems, the time to reach the super-cooled phase or for the structure of the system to "relax" upon cooling is defined as the structural relaxation time  $\tau_\alpha$  (recall Fig. 1.7). The relaxation time  $\tau_\alpha$  is monitored and linked to the structure and dynamics. It is shown that, for the structure, there is no much of a change [32], while for the dynamics, there is a huge change or dependence per say. To further understand the dynamics link to  $\tau_\alpha$  and how it changes with temperature when approaching  $T_g$ , many experiments are conducted to

tackle this question and to figure the control parameters. It is seen in various systems that, when the temperature decreases, the dynamics slows down. Temperature shows to have the higher impact on the dynamics more than other variable quantities i.e, density. The reason can be is that, when the temperature decreases, the energy decreases and the movement of molecules is hindered. Moreover, while the temperature decreases, the volume decreases as well. This can cause steric constraints or jamming of the motions as well. [33–35]. On the other hand, for van der Waals molecular liquids, temperature doesn't seem to be the dominant quantity. It shows that the density has the stronger effect on the dynamics. For a larger systems like polymers, the near-neighbor interactions among directly-bonded segments don't get affected that much by changes in volume or density. On the other hand, for the molecular systems, with smaller volume, the density is more affecting as the intermolecular interactions are the ones dominating the scene [32].

Based on these views, the structural relaxation time  $\tau_\alpha$  dependence on thermodynamic properties such as pressure, density or volume become a research target. Experimental data has shown that  $\tau_\alpha$  doesn't depends on temperature only, but depends on other variables as well such as  $P$  and  $V$ . The relaxation time dependence on density or volume is empirically shown to follow

$$\tau_\alpha \propto f(TV^\gamma) \quad (2.1)$$

where  $V$  is the volume,  $T$  is the temperature and  $\gamma$  is a material specific constant [32,36]. This relation is expected in the IPL systems as seen previously in chapter one. The exponent here is  $\gamma = n/3$ . This  $\gamma$  is regarded in experiments as a material constant that differs from one material to another [5]. This  $\gamma$  conveys dynamic data about the system. Since the main aim is to understand what happens to the dynamics,  $\gamma$  becomes an important quantity to study. The relation between  $\gamma$  and  $\tau_\alpha$  is observed and plotted for various materials. Fig. 2.1 shows the

$(TV)^\gamma$  versus  $\log \tau_\alpha$  scaling for various polymers. Figure 2.2 shows the  $(TV)^\gamma$  versus  $\log \tau_\alpha$  data for super-cooled molecular liquids [5,37].

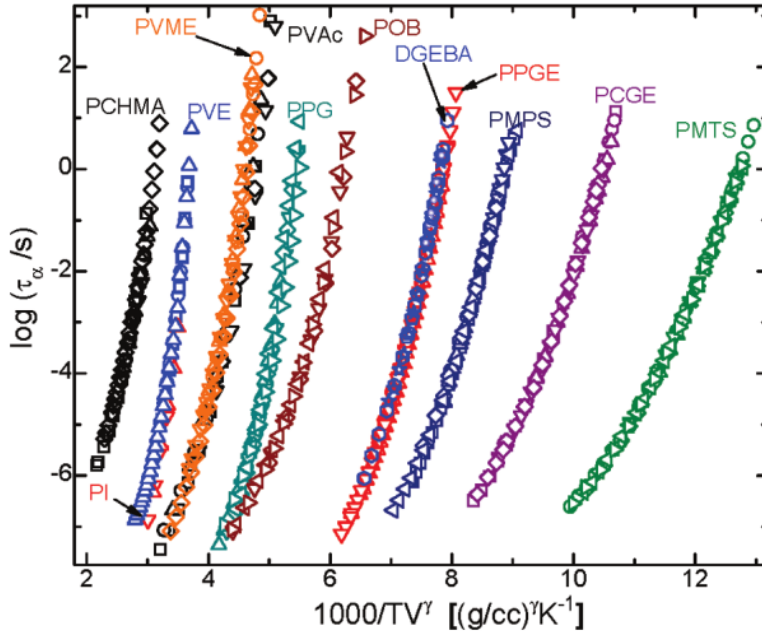


**Figure 2.1.** The relaxation times of different polymers as a function of temperature times the specific volume raised to power of  $\gamma$  of each polymer.  $\gamma$  varies between  $2.9 \leq \gamma \leq 5.0$ . Figure from Ref. [32].

Driven from the scientific curiosity of whether  $\gamma$  is actually a constant or not, many experiments and computer simulations have been devoted to study that matter. The Glass and Time group started to study the density-relaxation time dependence to find the answer. In 2009, Schröder *et al.* [38] have shown that  $\gamma$  depends on both density and temperature. They then defined it as a density-scaling exponent. Afterwards, Böhling *et al.* [39] show with experimental and simulation

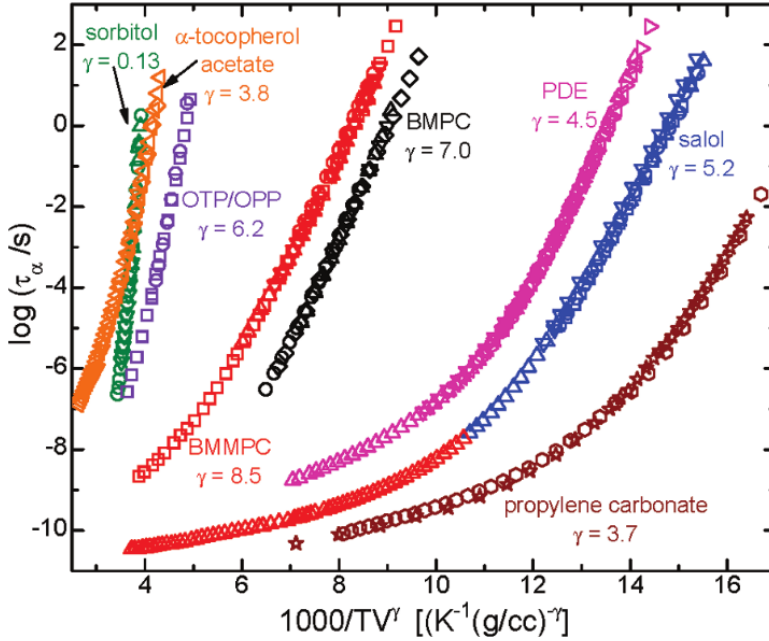


**Figure 2.2.** The relaxation times of different super-cooled liquids as a function of temperature times the specific volume raised to power of  $\gamma$  values listed on the figure. Figure from Ref. [32].

data that the relaxation time is a function of  $h(\rho)$  over temperature, where  $\rho$  is the density and the function  $h(\rho)$  depends on the system. When  $T$  and  $\rho$  data for two van der Waals liquids, dibutylphthalate (DBP) and decahydroisoquinoline (DHIQ) are plotted in logarithmic plots (Fig. 2.3), the slope is deviating from the expected power-law scaling (shown as dashed straight line in Fig. 2.3 (c) and (f)). This is proposing that  $\gamma$  is not a material constant, but in fact a state-point dependent exponent. Following on the same line of work, Sanz *et al.* [40] confirm these finding. They see that  $\gamma$  may vary with density

and temperature (Fig. 2.4). The density scaling exponent  $\gamma$  is then defined as

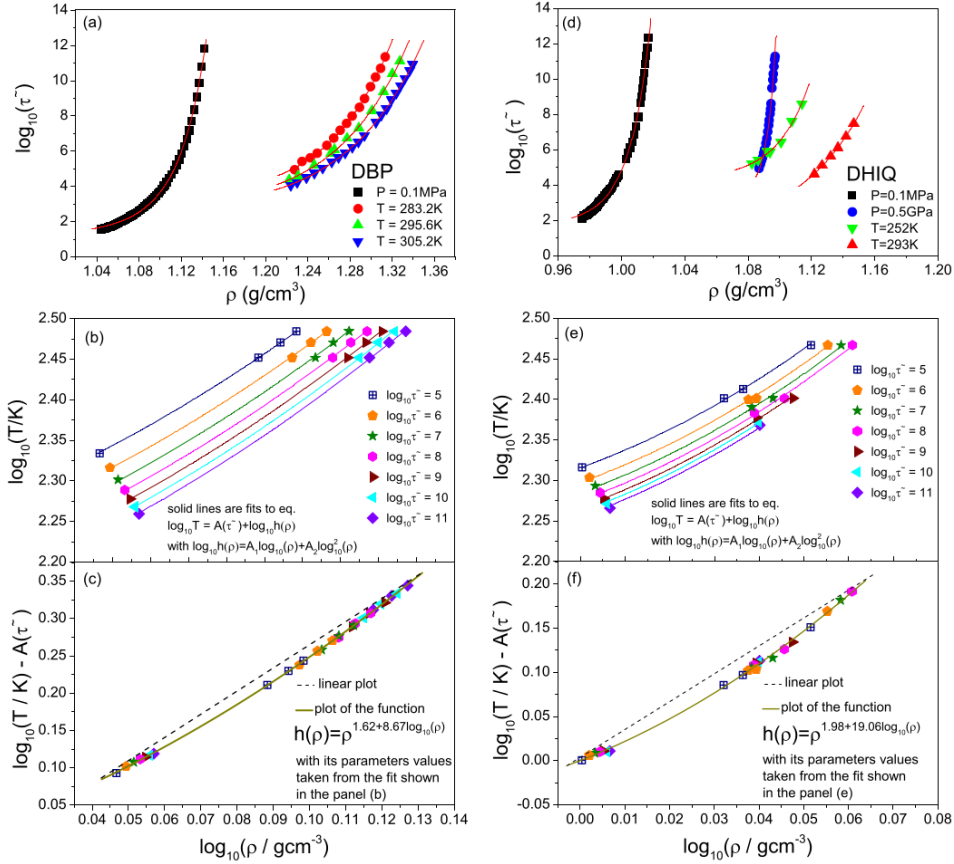


**Figure 2.3.** The density dependence of isobaric and isothermal structural relaxation times  $\tau_\alpha$  in reduced units of (a) DBP and (d) DHIQ. The isochronal dependence of  $\log_{10} T$  versus  $\log_{10} \rho$  determined at a given  $\tau_\alpha$  for (b) DBP and (e) DHIQ. The isochrones vertically shifted by the fitted values  $A\tau_\alpha$  for (c) DBP and (f) DHIQ. Figure from Ref. [39].

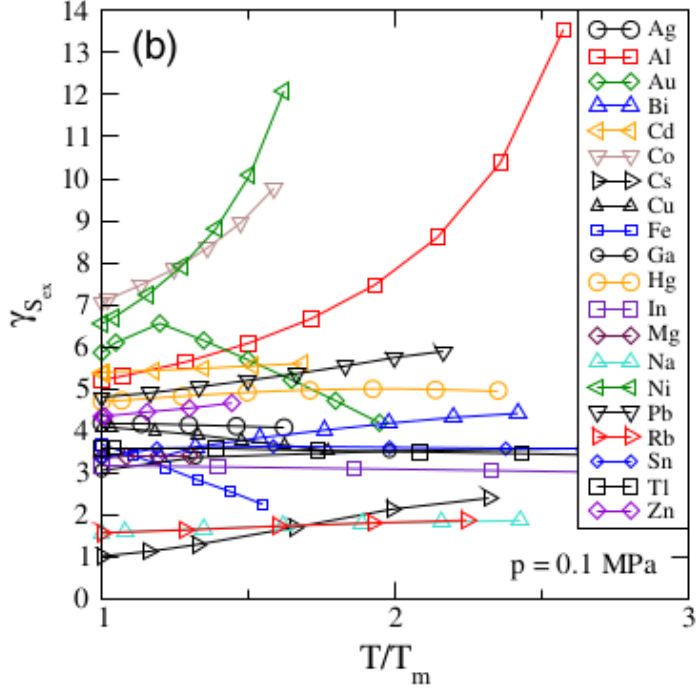


**Figure 2.4.** The density-scaling exponents of the configurational adiabat for liquid metals. We can see that  $\gamma$  is varying with each metallic system. Figure from Ref. [40] and based on experimental work from Ref. [37].

$$\gamma_{\tau_\alpha}(\rho, T) \equiv \left( \frac{\partial \log T}{\partial \log \rho} \right)_{\tau_\alpha} \quad (2.2)$$

Afterwards, the  $\gamma$  is related to configurational adiabats or lines that can be traced in the phase diagram along which the excess entropy is constant  $\gamma_{S_{ex}}$ . Here the excess entropy is defined as the entropy in excess of the ideal gas contribution,  $S_{ex} \equiv S - S_{id}$ .  $\gamma$  is then defined as

$$\gamma_{S_{ex}}(\rho, T) \equiv \left( \frac{\partial \log T}{\partial \log \rho} \right)_{S_{ex}} \quad (2.3)$$

Where  $\gamma_{S_{ex}}(\rho, T)$  is a state-point dependent variable along constant excess entropy lines rather than a constant value of a material.

With further work, the group links the excess entropy scaling law proposed by Rosenfeld in 1977 [41–43] to Equation 2.3 [44]. According to Rosenfeld’s scaling law, the reduced relaxation time and diffusion constant of a liquid are functions of the excess entropy. The idea of the scaling came when the reduced-unit properties of the hard sphere (HS) system are determined by only the packing fraction. One single parameter or a number here governs the thermodynamic picture (Fig. 2.4). This supported the idea of excess-entropy scaling [45]. The scaling has seen to withhold in some systems such as nitrogen and methane [46, 47]. Exceptions also have been seen, such as the water models and the Gaussian core model [48–53].

Using Rosenfeld’s law with the new formulated density-scaling exponent led to the discovery of a hidden scale invariance in the potential energy functions of various systems. These systems are defined now as Roskilde simple systems as mentioned in Chapter 1 [45]. With such propositions, the team developed the isomorph theory [45, 54]. The isomorph theory provides a simpler look at the phase diagram of liquids. The phase diagram can be seen as a one-dimensional with regard to several properties. In the coming section, we introduce the isomorph theory in detail.

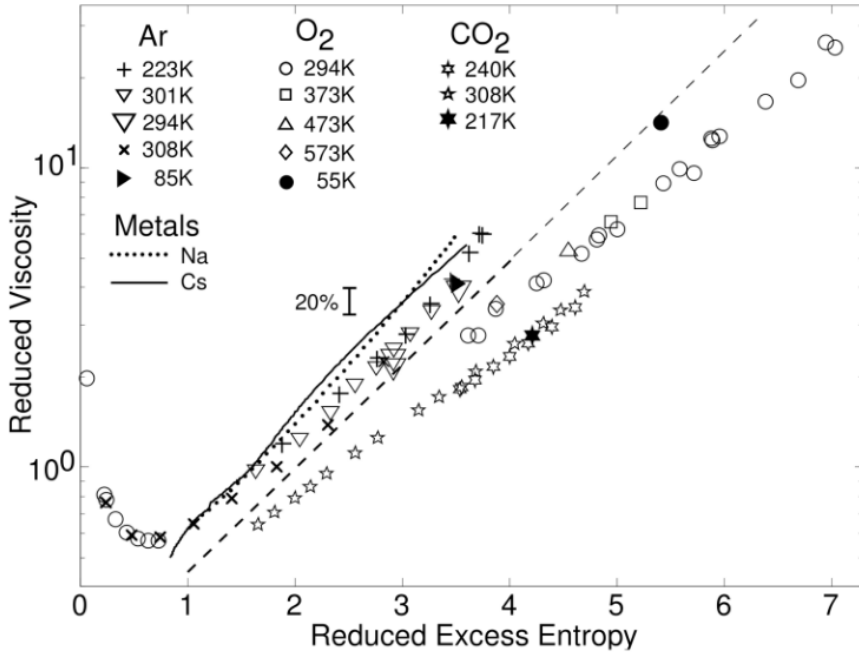


**Figure 2.5.** Experimental data for the reduced viscosity at different temperatures and pressures plotted against excess entropy for five non-associated systems. The metal data are taken along the liquid-vapor equilibrium line. The dashed line is the exponential entropy dependence Rosenfeld deduced from his 1977 computer simulations. The figure and caption from Ref. [45] and [46], respectively.

## 2.2 Hidden Scale Invariance

Isomorph Theory is a framework that explores the consequences of the hidden scale invariance that is shown in Roskilde simple systems. It is approximate theory, only exact for systems with Euler homogeneous potential energy function i.e., systems interacting via inverse power law (IPL) potentials [1, 18, 55]. In the newest 2014 formulation of isomorph theory, a Roskilde simple system is defined by the property that whenever two configurations  $\mathbf{R}_a$  and  $\mathbf{R}_b$  refer to the same density, one has

$$U(\mathbf{R}_a) < U(\mathbf{R}_b) \Rightarrow U(\lambda\mathbf{R}_a) < U(\lambda\mathbf{R}_b) \quad (2.4)$$

This implies that if two configurations have the same potential energy, their scaled versions also have the same potential-energy. Thus, a rigorous definition of R-simple systems is the property

$$U(\mathbf{R}_a) = U(\mathbf{R}_b) \Leftrightarrow U(\lambda\mathbf{R}_a) = U(\lambda\mathbf{R}_b) \quad (2.5)$$

This is only rigorously obeyed if  $U(R)$  is an Euler-homogeneous function plus a constant, but it applies to a good approximation for many other systems, e.g., single- and multi component LJ systems, the Yukawa pair potential, and the Morse pair potential [45, 54]. This reflects that the isomorph theory is inherently approximate for all realistic models. Equation 2.5 may also apply for molecular models like the ASD model, in which case the centers of masses are scaled uniformly whereas intra-molecular bond lengths and molecular orientations are kept unchanged.

Consider a system in equilibrium at the density  $\rho$  and  $V$  is the volume. The entropy  $S$  may be written as a sum of the ideal-gas entropy  $S_{\text{id}}$  (at the same density and temperature) and the so-called excess entropy  $S = S_{\text{id}} + S_{\text{ex}}$ . For the ideal gas,  $S_{\text{ex}} = 0$ , but for any

system with interactions  $S_{\text{ex}} < 0$ . The intuitive explanation is that no matter what the nature of the interactions is, such a system must be less disordered than an ideal gas. The microscopic excess entropy function  $S_{\text{ex}}(\mathbf{R})$  is defined as the thermodynamics excess entropy of a system with average potential energy equal to  $U(\mathbf{R})$  at the density  $\rho$  of the configuration  $\mathbf{R}$ , i.e.,

$$S_{\text{ex}}(\mathbf{R}) \equiv S_{\text{ex}}(\rho, U(\mathbf{R})) \quad (2.6)$$

It follows from statistical mechanics that  $S_{\text{ex}}(\mathbf{R})$  is proportional to the logarithm of the number of configurations with the same density and potential energy as  $\mathbf{R}$ . Inverting Eq. 2.6 leads to

$$U(\mathbf{R}) = U(\rho, S_{\text{ex}}(\mathbf{R})) \quad (2.7)$$

in which the right hand side is the thermodynamic equilibrium potential energy as a function of density  $\rho$  and thermodynamic excess entropy  $S_{\text{ex}}$ , evaluated by substituting  $S_{\text{ex}} = S_{\text{ex}}(\mathbf{R})$ .

Let  $\mathbf{R}_1$  and  $\mathbf{R}_2$  be two configurations at densities  $\rho_1$  and  $\rho_2$  respectively. Now, suppose we have configuration  $\mathbf{R}_1$  at  $\rho_1$  with the same reduced coordinate vector as  $\mathbf{R}_2$ , a configuration at density  $\rho_2$  (which is invariant upon a uniform scaling).

$$\rho_1^{\frac{1}{3}} \mathbf{R}_1 = \rho_2^{\frac{1}{3}} \mathbf{R}_2 = \tilde{\mathbf{R}} \quad (2.8)$$

It follows from  $S_{\text{ex}}(\mathbf{R}) \equiv S_{\text{ex}}(\rho, U(\mathbf{R}))$  and the micro-canonical expression for the excess entropy [54]

$$S_{\text{ex}}(\rho, U)/k_B = -N \ln N + \ln \left( \text{Vol} \{ \tilde{\mathbf{R}} | U(\rho^{-1/3} \tilde{\mathbf{R}}) < U \} \right) \quad (2.9)$$

(where "Vol" refers to the volume of the set in question, which is the  $\tilde{\mathbf{R}}$  integral of the unity function over all configurations  $\mathbf{R} = \rho^{-1/3} \tilde{\mathbf{R}}$

with potential energy below  $U$ , i.e., obeying  $U(\mathbf{R}) < U$ . If "Vol" is reduced coordinate configuration-space volume, one has

$$S_{\text{ex}}(\mathbf{R}_1)/k_B = -N \ln N + \ln(\text{Vol}\{\tilde{\mathbf{R}}|U(\rho_1^{-1/3}\tilde{\mathbf{R}}) < U(\mathbf{R}_1)\}) \quad (2.10)$$

$$S_{\text{ex}}(\mathbf{R}_2)/k_B = -N \ln N + \ln(\text{Vol}\{\tilde{\mathbf{R}}|U(\rho_2^{-1/3}\tilde{\mathbf{R}}) < U(\mathbf{R}_2)\}) \quad (2.11)$$

Because  $\mathbf{R}_2 = \rho_2^{-1/3} \rho_1^{1/3} \mathbf{R}_1$ , using  $\lambda = \rho_2^{-1/3} \rho_1^{1/3}$  in Eq. (2.3) to the inequality of the first set in Eq. 2.10, the two sets become identical. Thus,  $S_{\text{ex}}(\mathbf{R}_1) = S_{\text{ex}}(\mathbf{R}_2)$ . Which means, for Roskilde simple systems,  $S_{\text{ex}}(\mathbf{R})$  depends only on the configuration's reduced coordinate

$$S_{\text{ex}}(\mathbf{R}) = S_{\text{ex}}(\tilde{\mathbf{R}}) \quad (2.12)$$

Thus, Eq.  $U(\mathbf{R}) = U(\rho, S_{\text{ex}}(\mathbf{R}))$  becomes

$$U(\mathbf{R}) = U(\rho, S_{\text{ex}}(\tilde{\mathbf{R}})) \quad (2.13)$$

Equation 2.13 is a key identity in isomorph theory. All predictions of the isomorph theory may be derived from it.

## 2.3 Consequences of Isomorph Theory

To identify a Roskilde simple liquid, the potential energy landscape has to be mapped for the hidden scale invariance as we mentioned above. As a consequence of the hidden scale invariance, Roskilde

simple liquids exhibit strong correlations between potential energy  $U$  and virial fluctuations  $W$  in the  $NVT$  ensemble (see below). The effect of such correlations on the physical properties of the system have been studied in many of their publications [15, 16, 18, 38]. It also led to the discovery of curves in the thermodynamic phase diagram of such liquids along which the structure and the dynamics are invariant. These curves can also be found in the crystalline phases of Roskilde simple liquid as well [56]. These curves are called isomorphs. Based on Eq. 2.13, the dynamics at two isomorph state points are identical in the following “same movie” sense. Filming the motion of the molecules at one state point results in the same movie at a different, isomorph state point, except for a uniform scaling of space and time. This implies several dynamic isomorph invariants and that the reduced-unit structure is isomorph invariant. We discuss all of the consequences in the coming sub-sections.

### 2.3.1 Strong Correlations between Potential Energy and the Virial

If a system exhibits hidden scale invariance or belong to the Roskilde simple liquid systems, strong correlations between potential energy  $U$  and virial fluctuations  $W$  in the  $NVT$  ensemble are expected. In particular, Eq. 2.13 implies strong correlations between the constant-volume fluctuations of the virial  $W$  and the potential energy  $U$ . From the general equation of state  $PV = Nk_B T + W$ , at any state point the average of  $W(\mathbf{R})$  gives the contribution to the pressure from interactions. The potential energy determines the virial and then which implies these quantities are strongly correlated. The virial  $W$  is then

defined by

$$W(\mathbf{R}) \equiv -\frac{1}{3}\mathbf{R} \cdot \nabla U(\mathbf{R}) \quad (2.14)$$

If we have two configurations,  $\mathbf{R}_a$  and  $\mathbf{R}_b$  with same density and same potential energy,  $U(\mathbf{R}_a) = U(\mathbf{R}_b)$ . Since,  $U(\lambda\mathbf{R}_a) = U(\lambda\mathbf{R}_b)$ , taking the derivative of this with respect to  $\lambda$  results in  $\mathbf{R}_a \cdot \nabla U(\lambda\mathbf{R}_a) = \mathbf{R}_b \cdot \nabla U(\lambda\mathbf{R}_b)$ , which for  $\lambda = 1$  implies

$$W(\mathbf{R}_a) = W(\mathbf{R}_b)$$

This implies 100%  $UW$  correlations. Hidden scale invariance is usually only approximate, however the degree of correlation is quantified by the Pearson correlation coefficient  $R$ .  $R$  is measured through the averages of both virial  $\langle\Delta W\rangle$  and potential energy fluctuations  $\langle\Delta U\rangle$  from computer simulations. The virial  $W$  is obtained from the general equation of state  $PV = Nk_B T + W$ . At any state point, the average of  $W$  is the contribution to the pressure from interactions and  $U$  is the potential energy of the system. The Pearson correlation coefficient  $R$  is

$$R(\rho, T) = \frac{\langle\Delta W \Delta U\rangle}{\sqrt{\langle(\Delta W)^2\rangle\langle(\Delta U)^2\rangle}} \quad (2.15)$$

where  $\Delta$  denotes the instantaneous deviations from the equilibrium mean value and the  $\langle\rangle$  denote the  $NVT$  ensemble. Figure 2.6(b) shows the equilibrium fluctuations of potential energy  $U$  and virial  $W$  for simulation in the  $NVT$  ensemble of the asymmetrical dumbbell system. The reference state point is  $\rho = 0.932$ ,  $T = 0.465$  in LJ units. Liquids are considered strongly correlated when the correlation coefficient  $R > 0.9$ . This is usually the case in liquids dominated by van der Waals or weakly ionic interactions. In the case for the asymmetrical dumbbell

system, the viscous-region is highly  $UW$  correlated since  $R = 0.96$  at the reference state point (Fig. 2.6(a)).

Unlike systems with strong Coulomb forces such as hydrogen or covalent bond, the correlations are weaker resulting in  $R < 0.9$ . Also, the degree of correlation or the value of  $R$  depends on where you are in the phase diagram of the system. It depends on the density  $\rho$  and temperature  $T$  of the given state point as well. In isomorph theory, whenever invariance is mentioned for a quantity, it is defined by using macroscopic thermodynamics quantities as reference units. The length unit is defined by the number density ( $\rho \equiv N/V$ ) which is the total number of particles  $N$  confined in a system volume  $V$ . The energy unit is defined by the temperature of the system such  $e_0 \equiv k_B T$  where  $k_B$  is the Boltzmann constant. The time unit is defined by the density and the thermal velocity such that  $t_0 \equiv \rho^{-1/3} \sqrt{m/k_B T}$  where  $m$  is the particle mass. These units have been used by Rosenfeld in 1977 and referred to as "reduced units" [41].

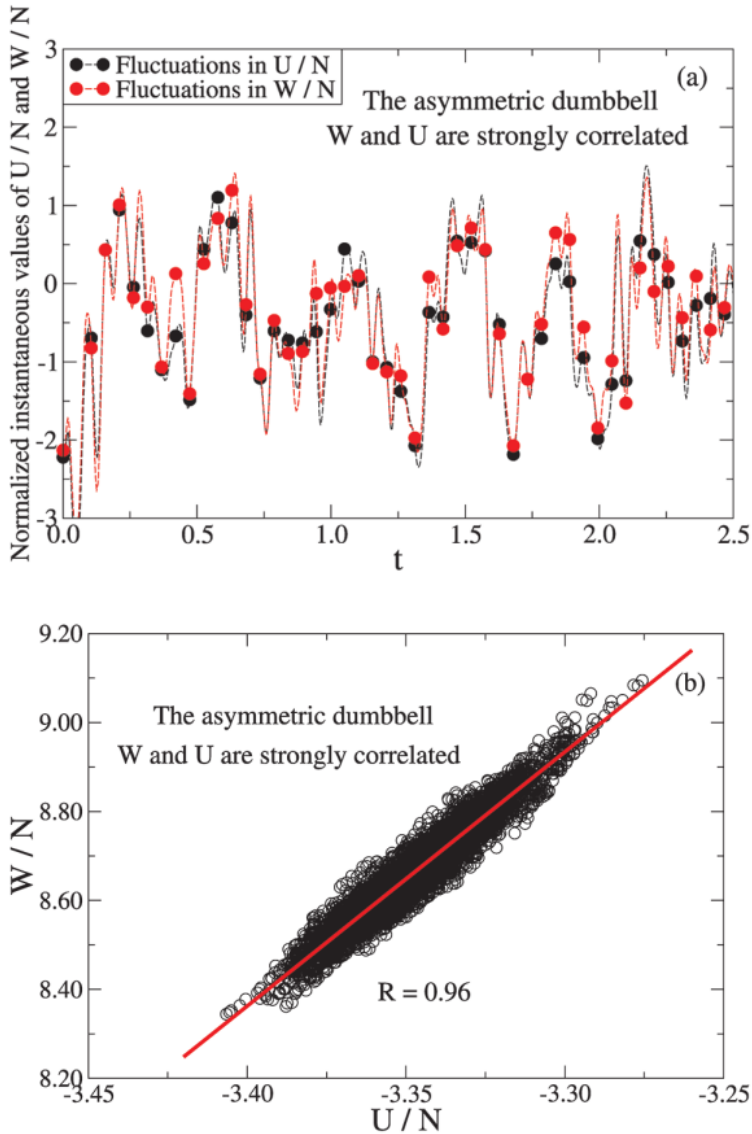


**Figure 2.6.** (a) The equilibrium fluctuations of potential energy  $U$  and virial  $W$  for the simulation in the  $NVT$  ensemble of an asymmetrical dumbbell system (b) a scatter plot of the instantaneous values of  $U$  and  $W$  from the same simulation. The correlation coefficient is seen to be higher than 0.90 indicating an R-simple liquid in the viscous region. Figure from Ref. [19].

## 2.3.2 Generating Isomorphs: Density Scaling Exponent

If we look at systems interacting through inverse power law (IPL) potential where  $v(r) \propto r^{-n}$ , the potential energy  $U$  and the virial  $W$  are perfectly correlated with a correlation coefficient  $R = 1$  and a constant density exponent  $\gamma = n/3$ . But, for other systems, such as the Lennard-Jones system for example,  $U$  and  $W$  are strongly correlated but not as perfectly as in IPL systems and  $R < 1$ . This makes it crucial to calculate the proportionality constant between the instantaneous fluctuations of  $U$  and  $W$  which can help predict the virial of different configuration.

The constant of proportionality between the equilibrium virial and potential-energy fluctuations at a given state point denoted by  $\gamma$  and referred to as the density scaling exponent is characterized by

$$\Delta W(t) \cong \gamma \Delta U(t) \quad (2.16)$$

and calculated directly in simulations from the general fluctuation expression

$$\frac{\langle \Delta W \Delta U \rangle}{\langle (\Delta U)^2 \rangle} = \gamma(\rho, S_{\text{ex}}) \quad (2.17)$$

Here the angular brackets denote canonical  $NVT$  averages [57].

The density scaling exponent  $\gamma$  was thought to be constant from experimental data. Isomorph theory showed that  $\gamma$  may vary with temperature. To derive  $\gamma$  as a state-point dependent variable, we start with the known relation of the excess entropy  $S_{\text{ex}}$  as a function of volume  $V$  and temperature  $T$ . Along an isomorph that is characterized by  $dS_{\text{ex}} = 0$ , one has

$$\left( \frac{\partial S_{\text{ex}}}{\partial V} \right)_T dV + \left( \frac{\partial S_{\text{ex}}}{\partial T} \right)_V dT = 0 \quad (2.18)$$

From the Maxwell relation for configurational degrees of freedom and the virial  $W$  which is the configurational contribution to pressure ( $p = Nk_B T + W$ )

$$\left(\frac{\partial S_{\text{ex}}}{\partial V}\right)_T = \frac{1}{V} \left(\frac{\partial W}{\partial T}\right)_V \quad (2.19)$$

By substituting Eq. (2.19) into Eq. (2.18) then

$$\frac{1}{V} \left(\frac{\partial W}{\partial T}\right)_V dV + \left(\frac{\partial S_{\text{ex}}}{\partial T}\right)_V dT = 0 \quad (2.20)$$

and

$$\frac{1}{V} \left(\frac{\partial W}{\partial T}\right)_V dV + \left(\frac{\partial S_{\text{ex}}}{\partial T}\right)_V T d \ln T = 0 \quad (2.21)$$

Since  $\left(\frac{\partial U}{\partial T}\right)_V = T \left(\frac{\partial S}{\partial T}\right)_V$  and  $(1/V)dV = d \ln V = -d \ln \rho$ , equation. (2.21) can be rewritten as:

$$-\left(\frac{\partial W}{\partial T}\right)_V d \ln \rho + \left(\frac{\partial U}{\partial T}\right)_V d \ln T = 0 \quad (2.22)$$

The slope  $\gamma$  or the density scaling exponent can be calculated as

$$\gamma(\rho, S_{\text{ex}}) \equiv \left(\frac{\partial \ln T}{\partial \ln \rho}\right)_{S_{\text{ex}}} = \frac{\langle \Delta W \Delta U \rangle}{\langle (\Delta U)^2 \rangle} \quad (2.23)$$

Configurational adiabats or curves of constant excess entropy  $S_{\text{ex}}$ , can be traced out numerically. Specifically, the last term of Eq. 2.23 specifies how the density-scaling exponent  $\gamma$  may be calculated numerically from an  $NVT$  simulation at the state point in question. In this

way, one avoids the tedious thermodynamic integrations necessary to determine excess entropy throughout the thermodynamic phase diagram. Integrating the first-order differential equation defined by the second equality sign in Eq. 2.23, in order to determine how temperature varies with density along an isomorph, is in principle straightforward. The highly accurate fourth-order Runge-Kutta (RK4) integration method is recently implemented for this [58]. In this thesis work, we only use the RK4 as the main integration method to trace configurational adiabats or isomorphs in any system to investigate. RK4 method is discussed in detail in Appendix A. After tracing the configurational adiabats, the dynamics and structure can be checked for invariance. Invariance is expected in Roskilde simple liquids.

### 2.3.3 Isomorphs: Lines of Invariant Structure and Dynamics

Isomorph theory depends on the reduced coordinate  $\tilde{\mathbf{R}}$  such that  $\tilde{\mathbf{R}} = \rho^{1/3}\mathbf{R}$ . Configurational adiabats traced with Eq. 2.13 in mind along the same excess entropy can result in invariant structure and dynamics curves in the phase diagram of any Roskilde simple liquid system. These invariant curves are one of the most profound consequences of isomorph theory and named isomorphs. In reduced coordinates, Newton's second law for a system of identical masses is

$$d^2\tilde{\mathbf{R}}/d\tilde{t}^2 = \tilde{\mathbf{F}} \quad (2.24)$$

in which the reduced force vector is defined from the full force vector  $\tilde{\mathbf{F}}$  (all particle forces joined into a single vector) by  $\tilde{\mathbf{F}} \equiv \mathbf{F}\rho^{-1/3}/k_B T^{27}$ . For Roskilde simple system, the reduced force is a function of the reduced configuration vector,

$$\tilde{\mathbf{F}} = \tilde{\mathbf{F}}(\mathbf{R}) \quad (2.25)$$

Since  $\nabla = \rho^{-1/3} \tilde{\nabla}$ ,

$$\tilde{\mathbf{F}} = -\nabla U = -(\partial U / \partial S_{\text{ex}})_\rho \rho^{1/3} \tilde{\nabla} S_{\text{ex}}(\tilde{\mathbf{R}}) \quad (2.26)$$

Since  $(\partial U / \partial S_{\text{ex}})_\rho = T$ , this means that

$$\tilde{\mathbf{F}} = -\tilde{\nabla} S_{\text{ex}}(\tilde{\mathbf{R}}) / k_B \quad (2.27)$$

Thus, the reduced force is a unique function of the reduced coordinates and as two state points on a given isomorph correspond to the same reduced coordinate vectors  $\tilde{\mathbf{R}}$ . This shows that the reduced-unit dynamics and structure are invariant along the isomorphs. Figures 2.7 and 2.8 show the invariance in the structure and the dynamics of isomorphs traced in the Face-centered-cubic (FCC) crystal Lennard-Jones system in comparison with isotherms, curves with the same temperature and isochores, which are curves with the same density. Figure 2.7 shows the radial distribution (RDF) functions Figure 2.8 shows the mean square displacement (MSD) which is a quantity to investigate the dynamics of a system. It is the square of distance a particle has moved in the system  $\langle |\tilde{\mathbf{r}}(\tilde{t}) - \tilde{\mathbf{r}}(\tilde{0})|^2 \rangle$ . Here, reduced units are used and hence referred to with a tilde e.g.  $\tilde{\mathbf{r}} = \rho^{1/3} \mathbf{r}$  and  $\tilde{t} = \rho^{1/3} \sqrt{m/T} t$ . For the figures, the word "reduced" is stated instead on both axes.

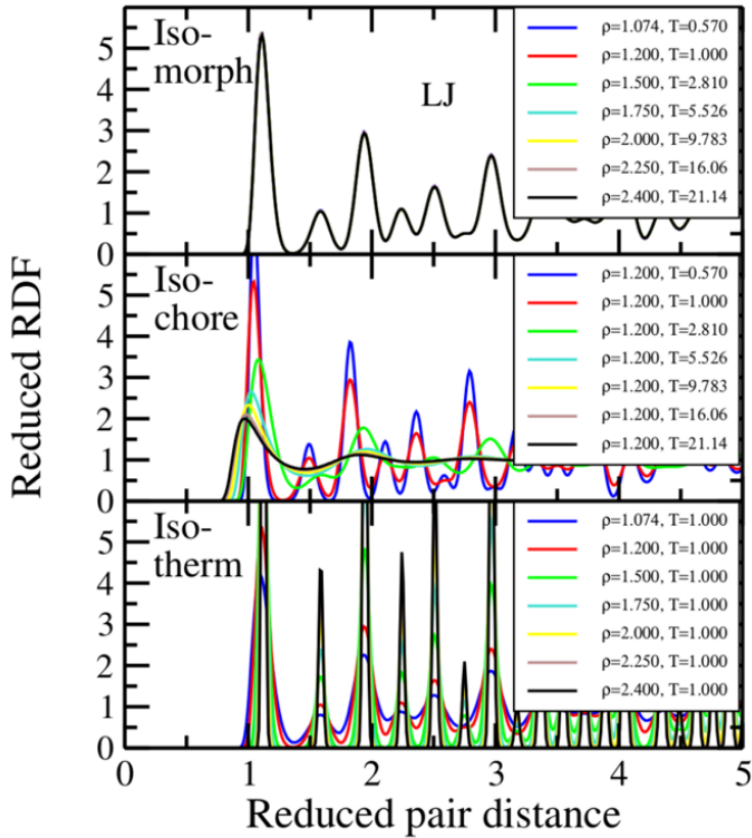


**Figure 2.7.** The reduced radial distribution functions of crystalline isomorphs in the FCC-crystal LJ crystal system. The state points along the isomorph in the top panel shows invariance in comparison to the isochore and the isotherm. Figure from Ref. [56].

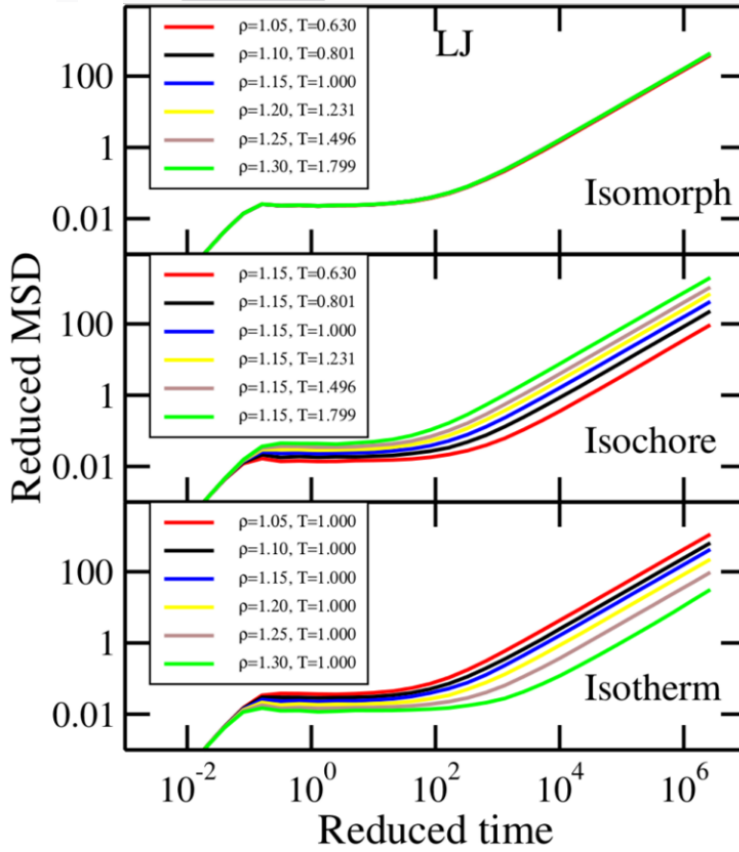


**Figure 2.8.** The mean square displacement of crystalline isomorphs in the FCC LJ crystal system with vacancies (defected crystal). The state points along the isomorph in the top panel shows invariance in comparison to the isochore and the isotherm. Figure from Ref. [56].



# CHAPTER 3

## Methods: Computer Simulations

---

### 3.1 Molecular Dynamics

With the help of computers, tedious analytical calculations that can take long hours to be done can be carried out faster. The field of condensed matter has benefited a lot from such numerical computational method. The study of the physics of liquids has achieved many successes with computer simulations. There are two main techniques in simulation, the Monte Carlo method and the molecular dynamics (MD) method [59]. Molecular dynamics is the main method used to produce the work in this thesis. From its name, the dynamics of the system, whether atomic or molecular are described using classical Newtonian mechanics. To explain this, let us consider a system of  $N$  particles confined in a simulation box. This box is surrounded by other boxes that are virtual copy of the same box or what we call "periodic boundaries" to avoid the problems of interacting with other surfaces (Fig. 3.1). The surfaces can induce a problem as we are trying to simulate a finite system and take in consideration the interactions only within the finite system. With periodic boundaries, we are able to simulate an finite system and use it to approximate an infinite system. If a particle leaves the simulation box at one side, an identical parti-

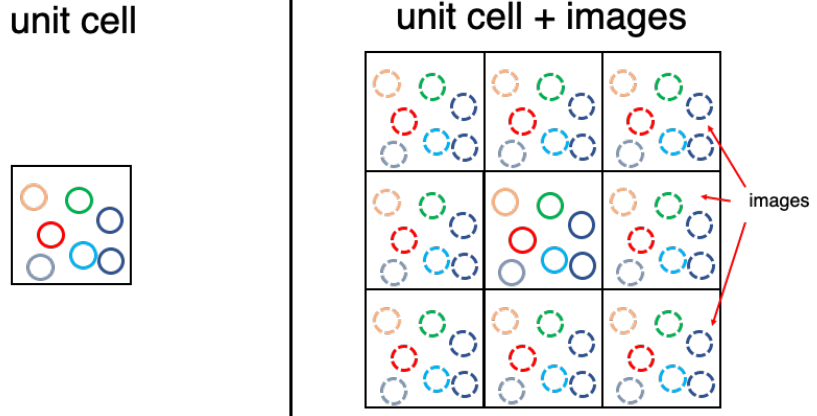


**Figure 3.1.** Illustration of the simulation box or unit cell and its virtual copies around it. The circles inside represent the particles within one box.

cle enters the box at the other. In practice, the interactions between each particle and the closest periodic image of its neighbors or the minimum image convention is only considered. With minimum image convention, if we have particle  $i$  and  $j$ , above the cutoff  $r_c > L/2$ , where  $L$  is the box length, the potential between  $i$  and the nearest image of  $j$  will be considered instead. This is important as this keeps the conservation of the system, and allow the calculations of average macroscopic properties. Now, as we have described the environment, what about the interaction between the particles. The interaction will be a pair potential like the Lennard-Jones potential that we have discussed before or it can also any different potential such as the WCA. In molecular dynamics, we set an initial configuration of our particles with initial positions and velocities. From these, we can integrate the classical equations of motion numerically to update the system. The integration in this sense will depend greatly on the size of the numerical time step  $dt$  used to solve the equations. The time-step is governed

by the parameters of the studied point in system (i.e., density) and the potential used. Then, an algorithm is developed to integrate the equations of motions. Algorithms vary, but we mention the one we use, the "Leap-Frog" algorithm. In simulations, the potential energy is expressed in terms of the pair potential such that for a system of  $N$  particles

$$U(\mathbf{R}) = \sum_{i>j}^N v(r) \quad (3.1)$$

in which  $r$  is the distance between particle  $i$  and  $j$  such that  $r = |\mathbf{r}_i - \mathbf{r}_j|$ . Let us choose a pair potential to express the potential energy of the system, i.e., the Lennard Jones potential (recall Chapter 1)

$$v^{LJ}(r) = 4\epsilon \left( (\sigma/r)^{12} - (\sigma/r)^6 \right) \quad (3.2)$$

As seen in chapter 1, the force acting on particle  $i$   $\mathbf{f}_i$  in a system can be obtained as the gradient of the potential energy which is now expressed as a pair potential

$$\mathbf{f}_i = -\nabla_{r_i} U^{LJ}(\mathbf{R}) \quad (3.3)$$

where  $\nabla_{r_i} = \frac{\partial}{\partial x_i} \hat{i} + \frac{\partial}{\partial y_i} \hat{j} + \frac{\partial}{\partial z_i} \hat{z}$ . Then, through Newton's equation of motion, the velocities and positions and velocities can be obtained numerically

$$\frac{d\mathbf{v}_i}{dt} = \frac{\mathbf{f}_i(t)}{m_i} \quad (3.4)$$

and

$$\frac{d\mathbf{r}_i}{dt} = \mathbf{v}_i(t) \quad (3.5)$$

To solve the last two equations numerically by MD simulations, time must be discretized in small steps  $h$ . With the Leap-Frog algorithm, the system is updated by determining the velocities at half-integer time step  $h/2$  and then using the velocities to compute the new positions. The velocity at the half time step of particle  $i$  is

$$\mathbf{v}_i\left(t + \frac{h}{2}\right) = \mathbf{v}_i\left(t - \frac{h}{2}\right) + h \frac{\mathbf{f}_i}{m_i} \quad (3.6)$$

The new position based on the old position for particle  $i$  is calculated as

$$\mathbf{r}_i\left(t + \frac{h}{2}\right) = \mathbf{r}_i(t) + h \mathbf{v}_i\left(t + \frac{h}{2}\right) \quad (3.7)$$

The Leap-frog algorithm, which is the modified version of the Verlet algorithm avoids the squaring of the time step to update the system. Thus it is favored in simulations [60].

In simulations, we know how the equations of motions are integrated and we ensure energy conservation. We have a fixed number of particles, volume and conserved total energy, therefore such simulation is an  $NVE$  ensemble. With the idea of having easier parameters to control in mind, other algorithms have been developed to keep the pressure or/and the temperature constant, giving rise to  $NVT$  or  $NPT$  simulations. This is usually done by applying a thermostat or a barostat respectively such as the Nosé-Hoover we use in our  $NVT$  simulations [61–63].

## 3.2 Simulated Systems

This section, we provide information about the systems we simulated. Simulations are done with the RUMD and LAMMPS software packages. LAMMPS [64] is a molecular dynamics code with a focus on

materials modeling from Sandia National Laboratories, Temple University. It stands for Large-scale Atomic/Molecular Massively Parallel Simulator and includes potentials for solid-state materials (metals, semiconductors) and soft matter (biomolecules, polymers) and coarse-grained or mesoscopic systems. It can be used to model atoms or, more generically, as a parallel particle simulator at the atomic, meso, or continuum scale. It runs on single processors or in parallel using message-passing techniques and a spatial-decomposition of the simulation domain. Many of its models have versions that provide accelerated performance on central processing units (CPUs) and graphics processing units (GPUs). RUMD [65,66] is another molecular dynamics code developed at Roskilde university in Denmark (2008-present). It stands for Roskilde University Molecular Dynamics. RUMD uses CUDA programming library for C++ developed by NVIDIA on many-core Graphical Processor Units (GPUs) to solve complex computational problems.

**The single-component Lennard Jones (SCLJ) liquid:** A liquid system with 4000 particles LJ particles in cubic box interacting with the LJ potential. The LJ system is used to compare RK4 method results of tracing configurational adiabats with the Weeks-Chandler-Andersen (WCA) system. Results are in appendix A.

**The single-component Weeks-Chandler-Andersen (SCWCA) liquid:** A liquid system with 4000 LJ particles in cubic box interacting via the WCA potential. The WCA potential is the same as the standard LJ pair potential, but cut at its minimum and subsequently shifts the potential by adding a constant such that the minimum is lifted to zero [12]. The result is the purely repulsive pair potential. The WCA system is used in all the simulations in chapter 4.

**Asymmetric dumbbells liquid and plastic crystal:** A systems of 4000 asymmetric dumbbells (for the literature comparison, 1000 dumbbells were simulated instead). The ASD system is a toy model of toluene where a phenyl-group  $C_6H_5-$  and the methyl group  $-CH_3$

are represented as as Lennard-Jones spheres, one big  $A$  and one smaller  $B$ , connected with a rigid bond (Fig. 3.2 (right)). The ASD system is used in all the simulations in chapter 5.

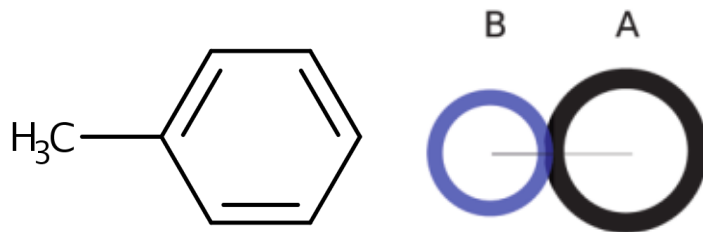


**Figure 3.2.** Chemical structure of toluene (left) and the asymmetric dumbbell model (right). It consists of two LJ sites with a bond length of  $0.58\sigma$  in  $A$  particle units.

# CHAPTER 4

## Hidden Scale Invariance of the Weeks-Chandler- Andersen System

---

### 4.1 The Weeks-Chandler-Andersen System: Definition and Setup

In Chapter 1, we introduce the WCA potential as purely repulsive potential such that [12].

$$v(r) = \begin{cases} 4\varepsilon [(r/\sigma)^{-12} - (r/\sigma)^{-6}] + \varepsilon & (r < 2^{1/6}\sigma) \\ 0 & (r > 2^{1/6}\sigma) \end{cases} \quad (4.1)$$

The potential is truncated at the LJ potential minimum and shifted up by adding a constant, such that the minimum is lifted to zero (Fig. 1.4, P. 10). The phase diagram of WCA system exhibits a solid-liquid phase diagram with no vapor-liquid co-existence region as far the LJ

system [12]. In fact, like any system of purely repulsive particles, the WCA system doesn't have a critical nor triple points (Fig. 4.1). The WCA co-existence data has been calculated by the Monte Carlo simulations [67] and molecular dynamics as well [68]. The co-existence lines also has been predicted by using an equation of state of the repulsive LJ system with the calculated free energy of the fluid and solid phases [69]. Recently, Attia *et al.* in paper III [70] have re-determined the WCA co-existence lines as the old data from de Kuijper *et al.* [67], Ahmed and Sadus [68] and Mizaeinia *et al.* [69] are inaccurate especially at low temperatures. Therefore, we use our recent data of the co-existence lines from paper III [70] in Fig 4.2. The purely repulsive potential WCA potential is commonly used for larger systems. It is computationally cheap due to the short truncation distance. As mentioned in the introduction, many publications simulating molecular fluids such as polymers or protein-polymer conjugation have been using the WCA potential [14, 26, 27]. For instance, Christopher *et al.* modeled the protein-polymer interactions using the WCA potential to compare with experimental data [71]. Their coarse-grained model is used for various systems with varying protein-polymer interactions.

In this Chapter, we study the single component Weeks-Chandler-Andersen (SCWCA) system by molecular dynamics (MD) simulations in the canonical  $NVT$  ensemble using the Nosé-Hoover thermostat [8, 61, 62]. The simulated system consists of 4000 particles in a cubic box with periodic boundaries. The simulations are performed RUMD [65, 66]. The Leapfrog algorithm is used with the time step size  $dt = 0.0025$ . Such small step size is used to carefully update the atomic system. The simulation runs for  $50 \times 10^6$  time steps for equilibration and  $25 \times 10^6$  time steps for runtime for each state point obtained. For the conducted post analysis of the structure and dynamics, the units used are the isomorph reduced units (Chapter 2). The reduced quantities are marked by a tilde i.e,  $\tilde{r}$ ,  $\tilde{t}$  and  $\tilde{D}$ .

The first step in our investigation is to check whether the SCWCA system is a Roskilde simple system. Therefore, we aim to identify state points in the phase diagram where the Pearson correlation coefficient is high such that  $R > 0.9$

$$R = \frac{\langle \Delta U \Delta W \rangle}{\sqrt{\langle (\Delta U)^2 \rangle \langle (\Delta W)^2 \rangle}}$$

From these state points, we can then trace out configurational adiabats in the phase diagram. The integration method used is the fourth-order Runge Kutta (RK4) integration method. It is implemented to give higher accuracy than other integration methods, i.e., Euler's method (Appendix A discusses the RK4 method).

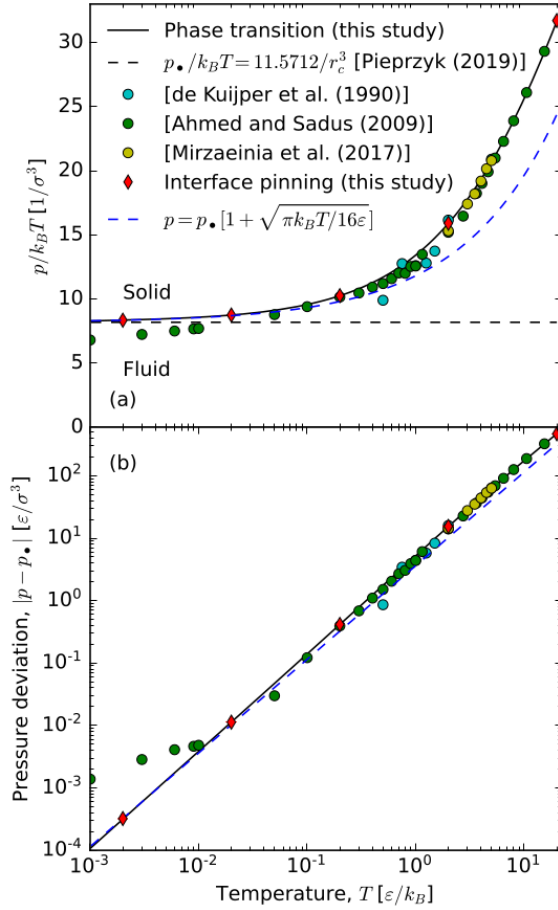


**Figure 4.1.** Comparison between the coexistence pressure as a function of the temperature from literature and from paper III [70]. The solid black line shows the reduced coexistence pressure  $p/k_B T$  as a function of the temperature and the black dashed line is the  $T \rightarrow 0$  HS limit. The blue dashed line shows that at low temperatures, the pressure scales as  $T^{3/2}$  as expected from HS theories. It is clear that there is deviation at low temperatures especially for Ahmed and Sadus's data [68], while the recent data (red diamonds) from paper III [70] has the correct low temperature limit. Figure from paper III [70].

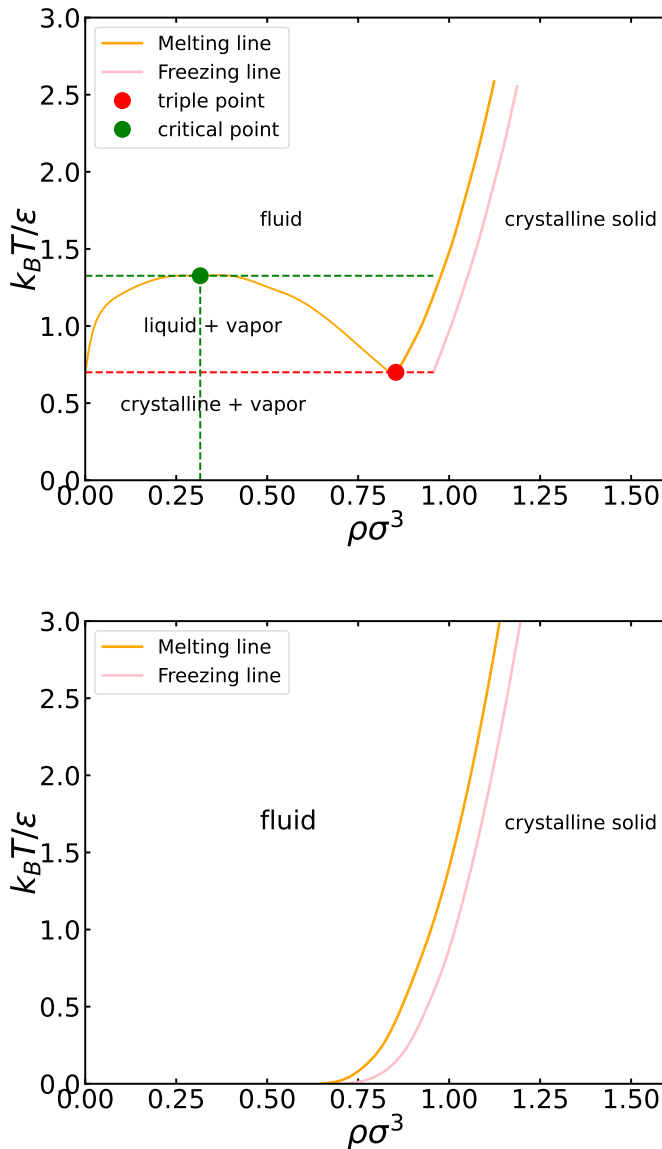


**Figure 4.2.** A comparison between the the phase diagram of the standard LJ system showing the liquid-vapor co-existence region (upper figure) and the phase diagram of the WCA system (lower figure). The co-existence lines are from paper III [70]. The temperature and density are in LJ units.

## 4.2 Density Scaling in the High Temperature Region

A configurational adiabat is an isomorph only for the state points with strong virial potential-energy  $UW$  correlations, i.e., when  $R \geq 0.9$ . We start with the state point  $\rho = 0.84$ ,  $T = 0.694$  (the triple point for the LJ system) to trace out an isomorph and check for strong  $UW$  correlations. Along with the isomorph, we trace an isotherm (a line with state points of the same temperature and varying densities) and an isochore (a line with state points of the same density and varying temperatures) starting from the same reference state point for structure and dynamics comparison. It is a significant consequence of the isomorph theory to have the invariance that can be visibly noticeable in the figures in comparison with the isotherms and isochores respectively. Figure 4.3 shows a snapshot of how the simulated system looks like in the liquid phase. Figure 4.4 shows the traced isomorph in the SCWCA phase diagram along with the isotherm and isochore. Figure 4.5 shows the variation of the correlation coefficient  $R$  as a function of density. It is observed that, for all the state points,  $R$  is relatively high such that  $R > 0.9$ . This is evident that the SCWCA exhibits strong  $UW$  correlation in the liquid region of the phase diagram.

### 4.2.1 Structure and Dynamics Invariance

Next, the structure and the dynamics of the state points along the isomorph to check for invariance are investigated. The structure is probed via the radial distribution functions (RDF) of the reduced pair-distance. The dynamics is probed via the reduced mean squared displacement (MSD) as a function of the reduced time. So, for further

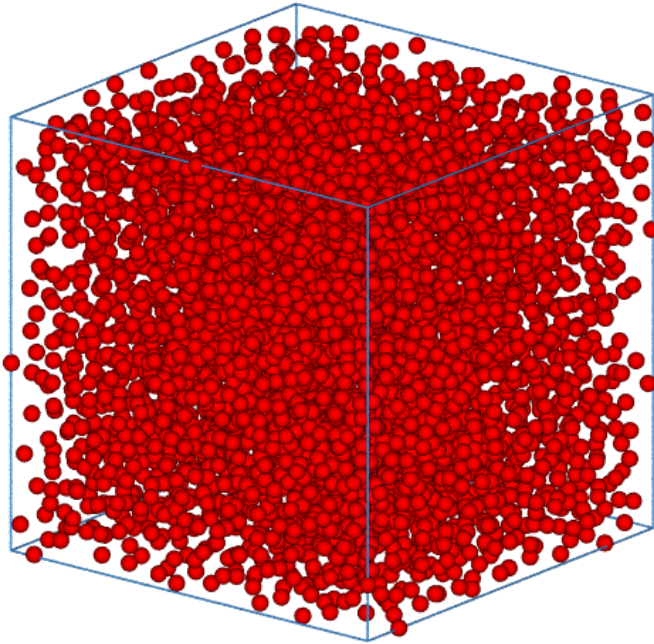


**Figure 4.3.** Snapshot of the WCA configuration consisting of 4000 particles at  $\rho = 0.84$  and  $T = 0.695$  in LJ units. Each particle is represented as a red sphere.

investigation, the low density region is explored. The goal is to reach the lowest density possible through integration along the density to see what happens to the density scaling exponent  $\gamma$ , which is also the isomorph slope. In Fig. 4.6 we see that there is good invariance in the structure along the isomorph compared to the isochore and the isotherm. It is observed that the height of the first peak increases as the temperature decreases. This is explained later in the chapter. Looking at the dynamics, the reduced mean square displacement of the state points along the isomorph show good invariance compared

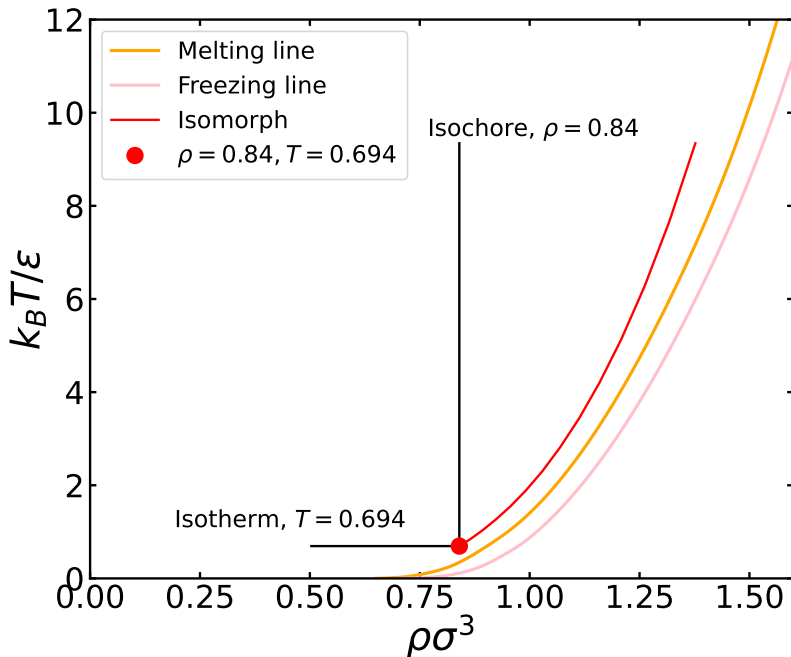


**Figure 4.4.** The phase diagram of the SCWCA system. The red line is the traced isomorph from the state point  $\rho = 0.84$  and  $T = 0.694$ . The black lines are the isochore and the isotherm traced out from the same start point. The co-existence lines are from Ref. [69].

to the isotherm and isochore (Fig. 4.7). Thus, the WCA can be considered as a Roskilde simple liquid. We check the variation of the density scaling exponent  $\gamma$  along the isomorph as a function of density is shown in Fig. 4.8. The range of the density-scaling exponent  $\gamma$  variation is found not to be significantly different from the LJ system.

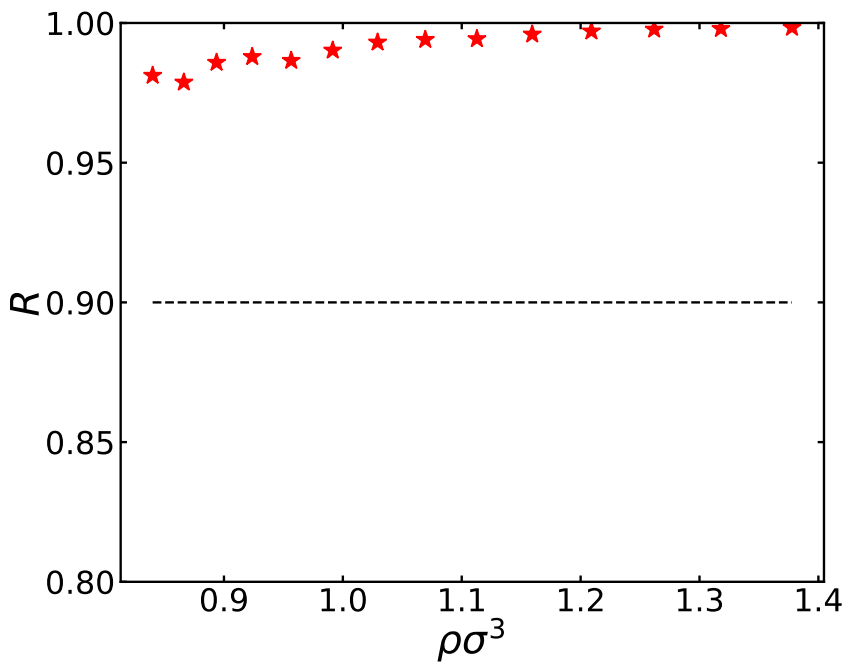


**Figure 4.5.** The correlation coefficients for all state points as a function of density. All the state points have high correlation  $R$  along the isomorph in Fig. 4.4.

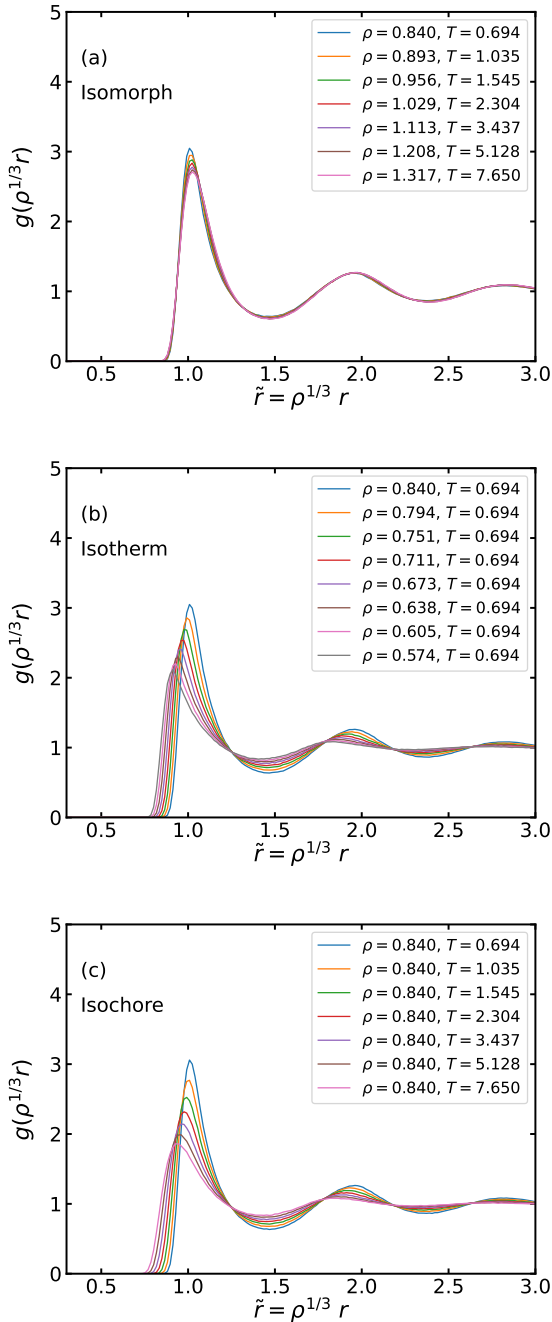


**Figure 4.6.** The radial distribution functions along the state points of the traced isomorph, isotherm and the isochore respectively in the WCA system in the density region  $0.8 < \rho < 1.35$  in Fig. 4.4. We can see invariance in (a) isomorph unlike (b) the isochore or (c) the isotherm.

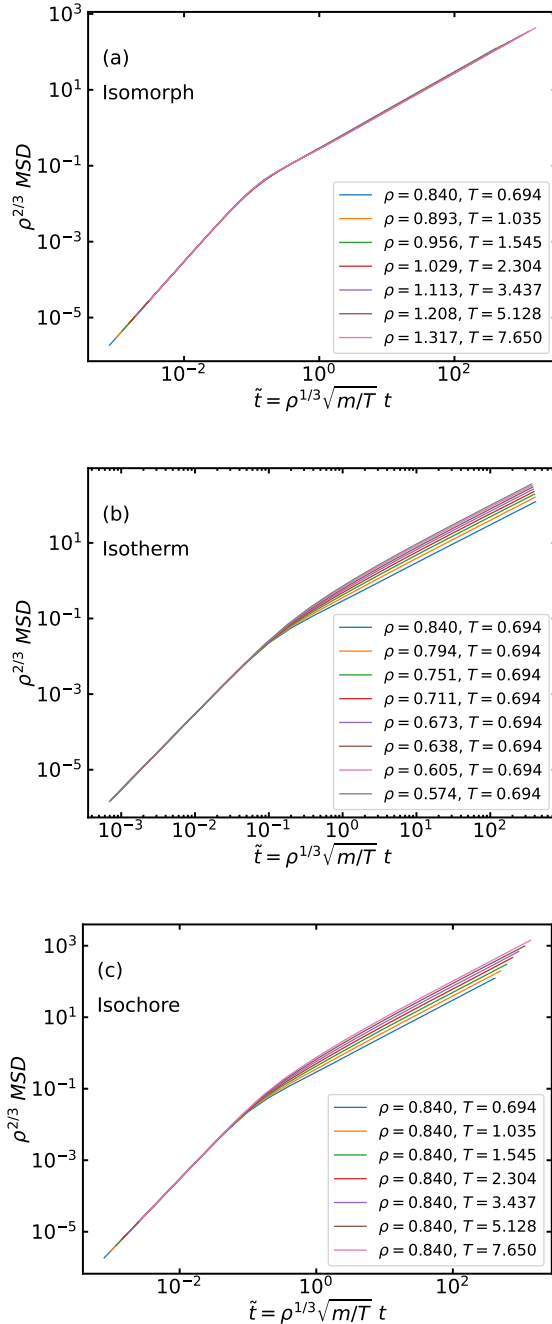


**Figure 4.7.** The mean square displacement along the state points of the traced isomorph, isotherm and the isochore respectively in the WCA system in the density region  $0.8 < \rho < 1.35$  in Fig. 4.4. We can see invariance in (a) isomorph unlike (b) the isochore or (c) the isotherm.

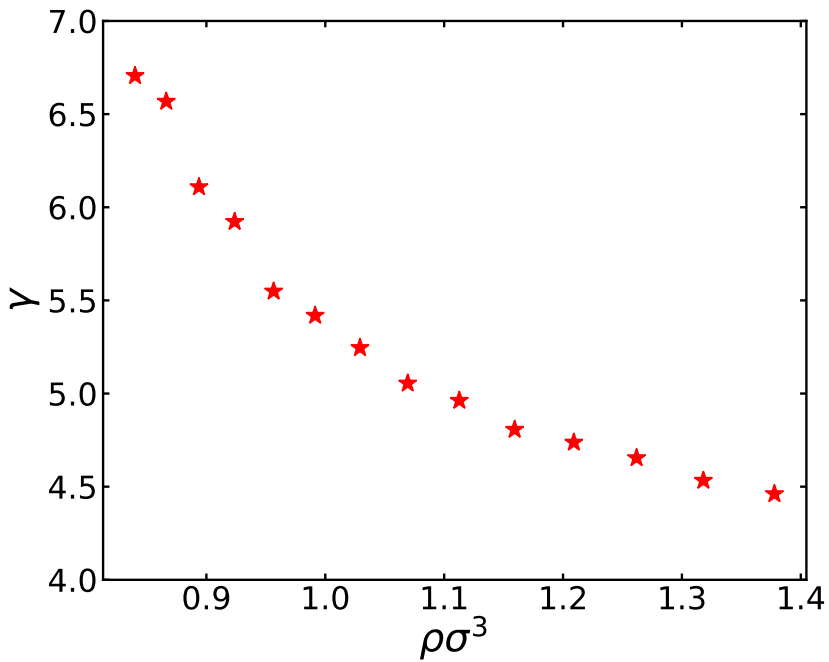


**Figure 4.8.** The density scaling exponent  $\gamma$  for all state points are plotted as a function of density along the isomorph plotted in Fig. 4.4.  $\gamma$  increases as the density decreases.

## 4.3 Extreme Density Scaling in the Low Temperature Region

In the previous section, the density scaling exponent is shown to be increasing when going lower in density in the high temperature region. This is similar to what is seen for the LJ system [1]. As a result of this finding, the low density region is of the main focus. Isomorphs are integrated along the temperature instead to reach the lowest temperature-density state points possible. This is not possible for the LJ system due to the gas-liquid co-existence line. Accordingly, four isomorphs are traced out from different state points by RK4 method (Appendix A). The state points have the same density  $\rho = 0.84$  and different temperatures  $T = 0.3, 0.6, 1.0, 2.0$ . The integration goes up to temperature  $T \approx 15$ . Then, from the highest state point reached of each isomorph, the integration goes down to reach the lowest densities/temperatures possible before the simulations become unstable. Three isotherms and three isochores are traced out as well for structure and dynamics comparison. The three isochores start from the densities  $\rho = 0.84, 1.0, 1.2$  respectively with a temperature range  $0.2 \leq T < 15$ . The three isotherms start from temperatures  $T = 0.6, 2.7, 12.1$  respectively with a density range  $0.56 \leq \rho < 1.5$ .

Figure 4.9 shows the isomorphs traced in the thermodynamic phase diagram of the WCA system in the low temperature region. The yellow and orange lines represent the freezing and melting lines [67, 68]. The blue, green, and purple lines marked 1, 2, and 3, respectively, are the isomorphs of main focus. The red dashed line is a fourth isomorph (marked 0) is in the liquid-solid coexistence region/the supercooled liquid phase which is not of our interest. The horizontal lines are three isotherms and the vertical lines are three isochores. After tracing the isomorphs, the correlation coefficients are plotted as a function of

density and temperature to check for strong virial potential-energy  $UV$  correlations. Fig. 4.10 shows high correlation coefficient values  $R \geq 0.9$  for all state points simulated.

Surprisingly, a collapse is seen when  $R$  is plotted as a function of temperature. That may indicate that  $R$  is merely controlled by the temperature. Moreover,  $R$  is noticed to increase with increasing density and temperature, approaching unity. This reflects the fact that the  $(r/\sigma)^{-12}$  term of the pair potential dominates the interactions in these limits as an inverse-power-law pair potential has  $R = 1$ . This dominance is explained by a mean-field theory in which we assume that the interactions at low densities are dominated by single-pair interactions, see Sub-section 4.3.1.

Figure 4.11 shows the variation of the density scaling exponent  $\gamma$  along the density, temperature and pressure respectively. It is observed that  $\gamma$  increases monotonically as either density, pressure, or temperature is lowered. The  $\gamma$  varies by more than two decades in the low-density of the phase diagram. In comparison, the LJ system has a density-scaling exponent that varies less than 50% throughout the phase diagram. Previously, Casalini and Ransom have suggested that the pressure is the controlling parameter for  $\gamma$  [72]. But, by looking at the Fig. 4.11(a) and (f), we can conclude that  $\gamma$  is primarily controlled by the temperature, not the pressure nor density.

After investigating the variations of the correlation coefficients and the density scaling exponents, the structure and the dynamics along the isomorphs are the next to check as a part of the hidden scale invariance investigation. Figure 4.12 shows the reduced RDFs data along the three isotherms, isochores, and isomorphs. The isotherms and the isomorphs are almost in the same density range. The isochores, on the other hand, are almost in the same temperature range as the corresponding isomorphs, i.e, not in the super-cooled regime. Along the isomorphs, the RDFs show some variation at the first peak maximum (lowest row), but in comparison to the isotherms and iso-

chores, there is excellent overall invariance of the RDF. For all of the three isomorphs, we find that the peak height increases as the temperature decreases. This is an effect of larger  $\gamma$  resulting in a higher first peak. To understand this difference, we can use the IPL system as a reference. In IPL system, we can trace perfect isomorphs as  $\gamma = n/3$ . When  $n$  increases, the forces become more repulsive. Therefore, taking Boltzmann probability in mind, the probability of finding two particles at the distance  $r$ , proportional to  $\exp(-Ar^{-n}/k_B T)$ , decreases as  $n \rightarrow \infty$ . This limits the RDF at distances below the first peak. Let us consider the particles in the first coordination shell. If they exhibit isomorph invariance, some of the RDF are limited to locate particles at small  $r$  i.e, distances below the first peak. Thus, the RDF locates the particles at larger  $r$  instead, resulting in a higher first peak.

For the dynamics, Fig. 4.13 shows data for the reduced MSD as a function of the reduced time along the three isotherms, isochores, and isomorphs. It can be seen that, the isomorphs exhibit invariance in comparison to the isotherms and isochores shown in the first two rows. Figure 4.14 shows how both the diffusion coefficients  $D$  and the reduced diffusion coefficients  $\tilde{D}$  vary along the three isomorphs. The upper figures demonstrate a large variation in  $D$  along each isomorph. The lower figures show  $\tilde{D}$  getting more constant as temperature approaches zero for each isomorph. In fact, it is not constant as the WCA system is not a perfect IPL system and the temperatures of the isomorphs change by more than four order of magnitude. Thus, the reduced diffusion coefficient is considered almost isomorph invariant.

Now, since the reduced diffusion coefficients  $\tilde{D}$  are approaching  $T \rightarrow 0$ , then the reduced diffusion coefficient when  $T = 0$  should be of a value that will corresponds to a jammed system, as  $\tilde{D} \rightarrow 0$  when the system jams. For the SCWCA system, when the temperatures decreases,  $\gamma$  increases and the system starts to behave as a hard-sphere system (HS). The HS system has a maximum density that corresponds to the random closed-packed (rcp) structure at nearly 64% packing

fraction. In Fig. 4.15, we see a black star that represents  $\tilde{D} = 0$  density which is following the same expected empirical fitted curve plotted (dashed line).

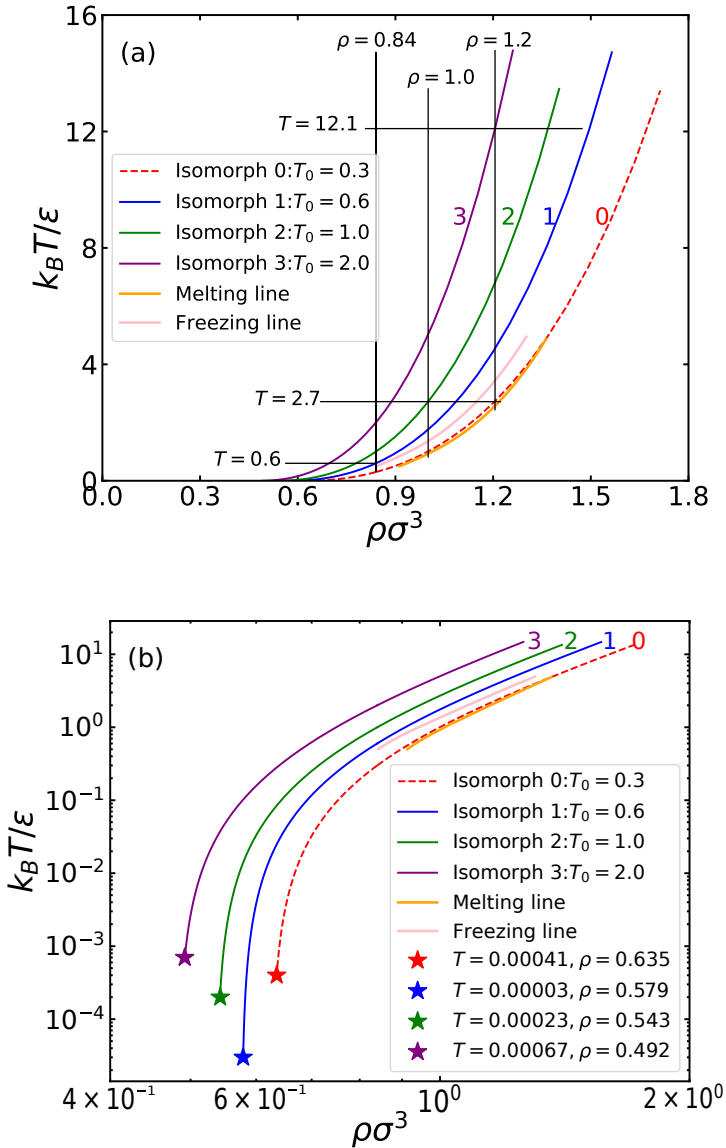


**Figure 4.9.** (a) The phase diagram of the WCA with the isomorphs traced. The horizontal lines are three isotherms and the vertical lines are three isochores that will be used for comparison of structure and dynamics variations to those along the isomorphs. The freezing and melting lines are shown as yellow and orange lines. (b) The four isomorphs shown in a logarithmic temperature-density phase diagram.

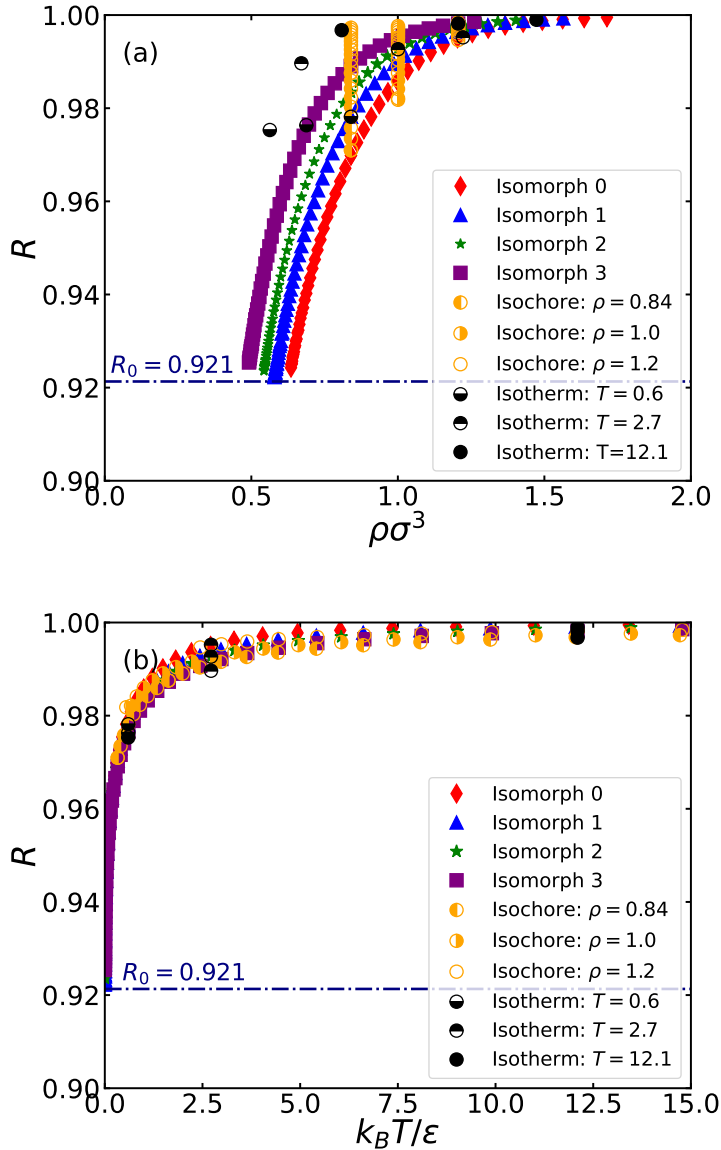


**Figure 4.10.** The correlation coefficients plotted (a) against density (b) against temperature. The  $R_0$  is the  $R$  limit at low temperature region  $T \rightarrow 0$ . This is discussed in Sub-section (4.3.1).

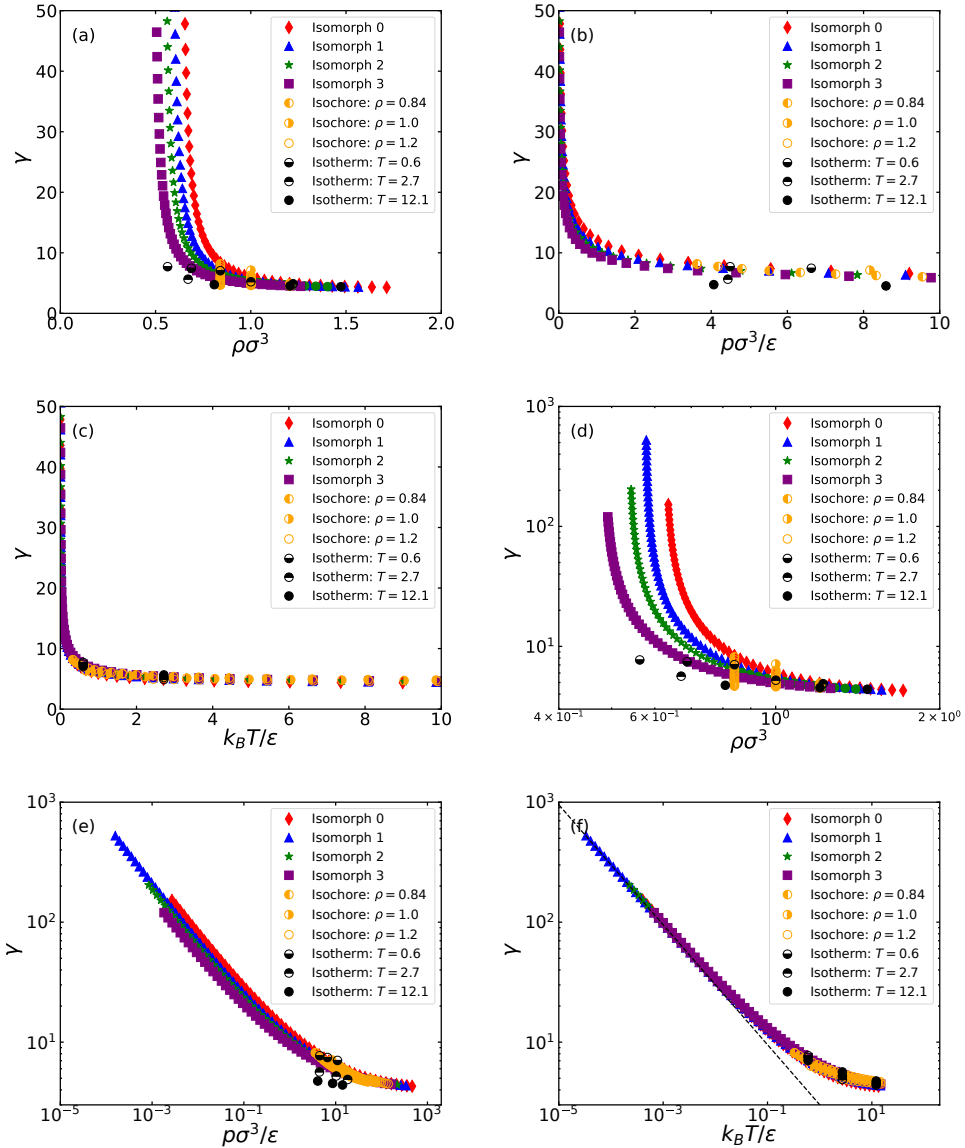


**Figure 4.11.** The density scaling exponent  $\gamma$  plotted for the state points studied as (a) linear plot as a function of density (b) logarithmic plot as a function of density (c) linear plot as a function of pressure (d) logarithmic plot as a function of pressure (e) linear plot as a function of temperature (f) logarithmic plot as a function of temperature. Full symbols are isomorph state-point data, half open circles are isochore and isotherm data. The dashed line is the low-temperature limit of the mean-field theory in Subsection 4.3.1.

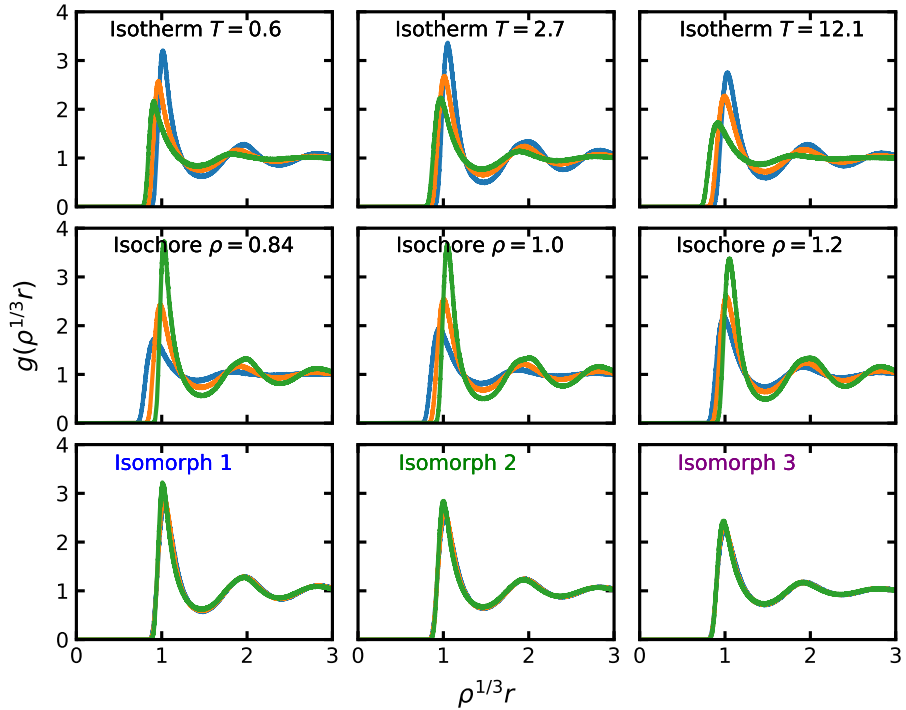


**Figure 4.12.** The radial distribution functions (RDF) for the three isotherms, isochores, and isomorphs. The green curves give the lowest temperature/density, the orange curves give the mid temperature/density, and the blue curves give the highest temperature/density. We can see visible invariance along the isomorphs in comparison to the isotherms and isochores.

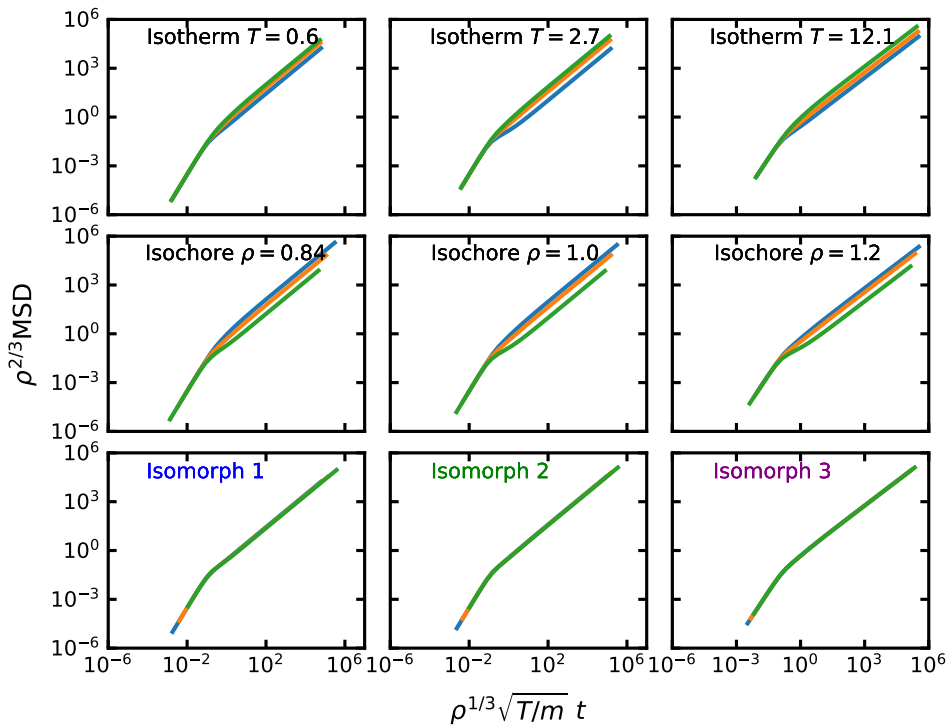


**Figure 4.13.** The mean-squared displacement (MSD) plotted against time for the three isotherms, isochores, and isomorphs. The state points and colors are the same as in Fig. 4.12. We can see visible invariance along the isomorphs in comparison to the isotherms and isochores.

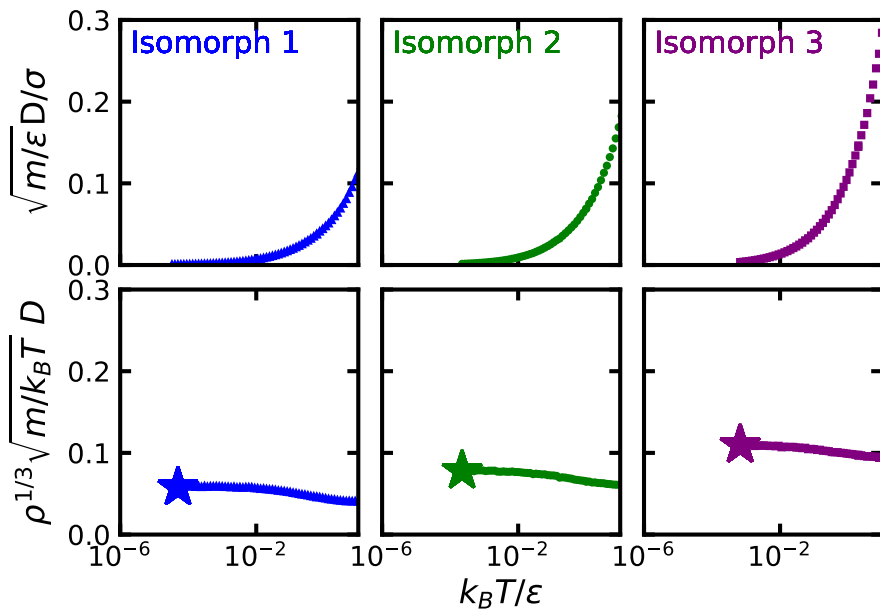


**Figure 4.14.** Diffusion coefficients along isomorphs (1-3) in MD units (upper row) and in reduced units (lower row), plotted as functions of the logarithm of the temperature

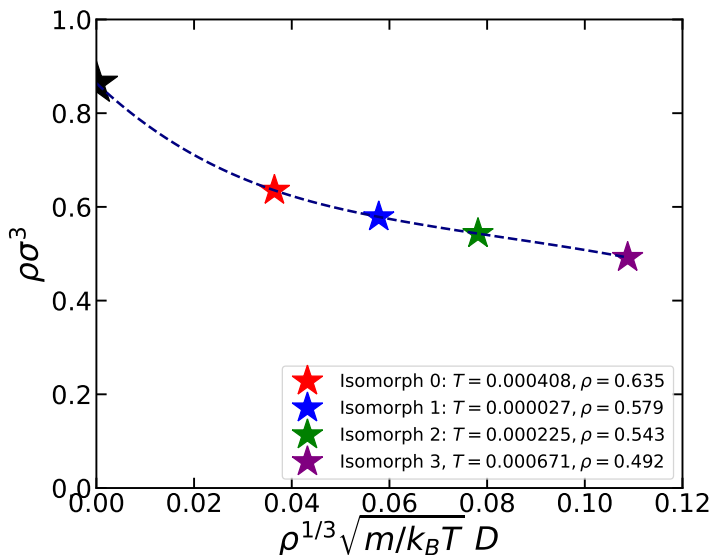


**Figure 4.15.** The reduced diffusion coefficients at the lowest temperature and density for isomorphs 1-3 in Fig 4.9. The points are fitted by a cubic spline function (dashed curve). The black star is the calculated random close-packing (rcp) density ( $\rho = 0.864$ ).

### 4.3.1 Mean-field Theory for the Density Scaling Exponent Extreme Variation at Low Temperatures

This section briefly presents a mean-field theory for estimating the virial potential-energy correlation coefficient  $R$  and the density-scaling exponent  $\gamma$ . Details are given in paper I [58].

Based on Refs [73–76], we assume that the individual pair interactions are statistically independent. This is expected to be a good approximation at relatively low densities. At low densities it is reasonable to regard the pair distances as uncorrelated, i.e., to treat the interactions in a mean-field way. In the low-density limit, almost none of the frozen particles overlap. Thus, free volume in the low-density limit approaches the entire volume  $V$ . Based on that view, we calculate the single-particle partition function and make the following predictions. At the low-density limit, the  $\gamma$  and  $R$  at low densities depend only of  $T$ , which explains the observation in Fig. 4.11. The  $\gamma$  and  $R$  in the low-density limit are from these assumptions given by

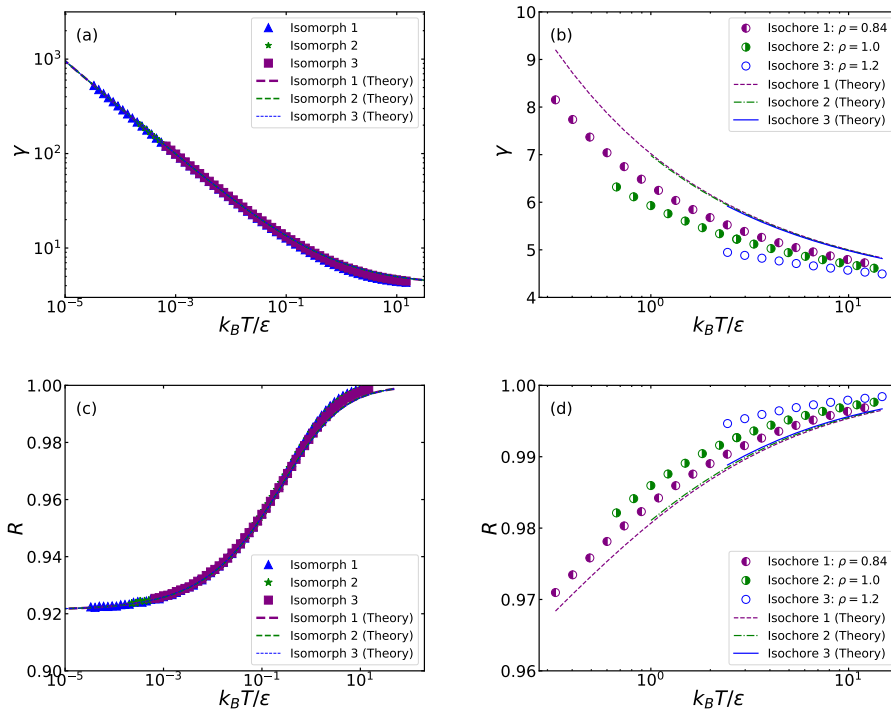
$$\gamma_0 = \frac{4r_c\sqrt{2k_2}}{9\sqrt{\pi T}} = \frac{16}{3\sqrt{\pi T}} \quad (T \rightarrow 0) \quad (4.2)$$

and

$$R_0 = \sqrt{\frac{8}{3\pi}} = 0.921 \dots \quad (T \rightarrow 0). \quad (4.3)$$

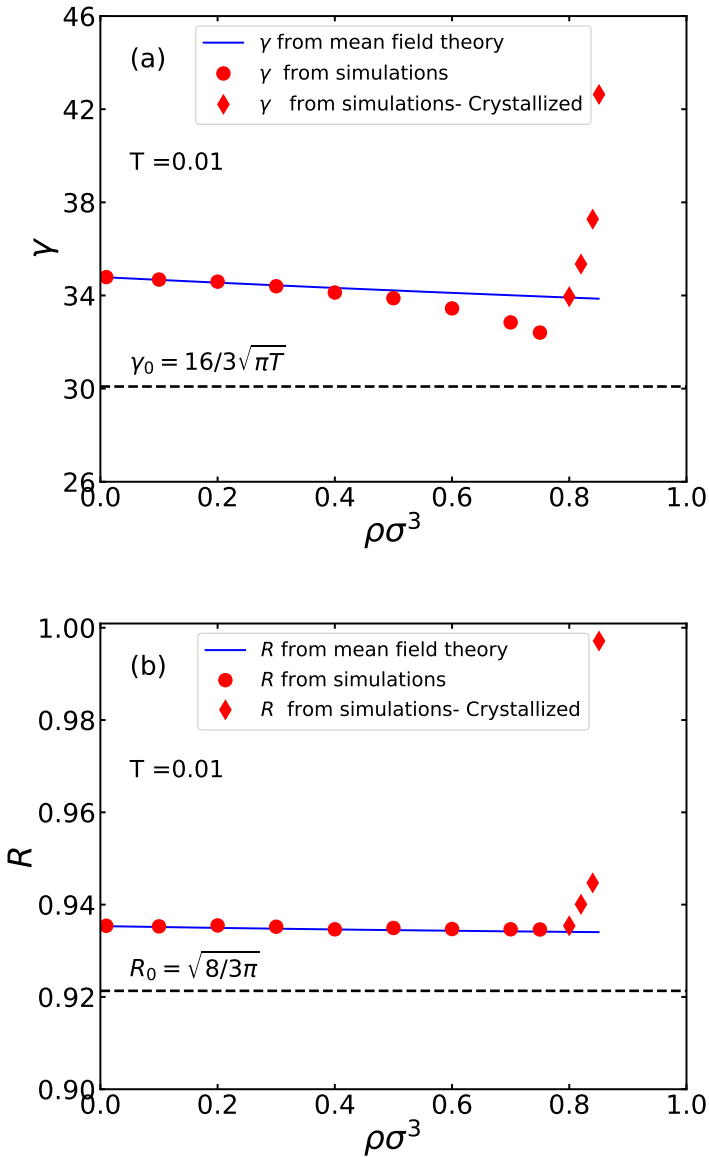
$k_2$  is obtained from the second term of tailor-expanding the WCA pair potential with the assumption that the probability distribution  $p(r)$  concentrates around  $r_c$  at low temperature such that  $k_1 = 0$  and  $k_2 = 36\sqrt[3]{4}$ .

Figure 4.16 compares the predictions of the mean-field theory to data along isomorphs and isochores. There is good overall agreement. Systematic deviations are visible in (b) and (d), however, which focus on densities that are now low enough to avoid frozen-particle overlap. Along with Fig. 4.16, Fig. 4.17 shows the mean-field predictions for  $\gamma$



**Figure 4.16.** Comparing the predictions of the mean-field theory for  $\gamma$  and  $R$  as functions of the temperature (dashed lines) to simulation results. (a) and (c) show results along the three isomorphs in the low-temperature region (b) and (d) show results along the three isochores in the high-temperature region where the mean-field theory is not expected to be accurate.

and  $R$  at  $T = 0.01$  plotted as a function of the density. As expected, the theory works well at low densities, even though one is here still not quite at the  $T \rightarrow 0$  limit marked by the horizontal lines.



**Figure 4.17.** The density dependence of (a)  $\gamma$  and (b)  $R$  at  $T = 0.01$ . Results are also shown for high-density samples that crystallized during the simulations.



# CHAPTER 5

## Hidden Scale Invariance in the Asymmetrical Dumbbell System

---

### 5.1 The Asymmetrical Dumbbell System: Definition and Setup

The asymmetrical dumbbell (ASD) is designed to be a constrained simple molecular model. Because of the asymmetry, the model is easily super-cooled, i.e., avoids crystallization [19]. In Chapter 1, the ASD system is detailed (P.17). This system is studied by molecular dynamics (MD) simulations in the canonical  $NVT$  ensemble using the Nosé-Hoover thermostat [8]. The simulated system consists of 8000 particles (4000 molecules) in a cubic box with periodic boundaries. The simulations are performed using the open-source RUMD [65, 66]. The Leapfrog algorithm is used with the time step size  $dt = 0.001$ .

Such small step size is used to carefully update the constraint system. The simulation runs for  $10^6$  time steps for equilibration and  $10^6$  time steps for runtime for each state point obtained. For the conducted post analysis of the structure and dynamics, the units used are the isomorph reduced units. These units are defined as such, the energy unit  $e_0 \equiv k_B T$ , the length unit  $l_0 \equiv \rho^{-1/3}$ , and the time unit  $t_0 \equiv \rho^{-1/3} \sqrt{m_A/k_B T}$  in which  $T$  is the temperature,  $\rho$  is the density defined as the total number of atoms confined in the simulation box ( $N/V$ ),  $m_A$  is the particle A mass and  $k_B$  is the Boltzmann constant. These units vary with each state point. Exceptions to the use of isomorphic reduced units apply for density and temperature that are by definition both unity in reduced units. The density and temperature are reported in LJ units. After setting up the system, the hidden scale invariance is investigated in both the liquid and plastic crystalline phases of the ASD phase diagram. A systematic numerical investigation is run by tracing out configurational adiabats or isomorphs in both of the two regions. The first section covers the liquid region of the phase diagram as the first part of the investigation. The second section covers the investigation in the crystalline region.

## 5.2 Validating Against Literature Viscous Data

The first step of the investigation in the liquid phase is to trace out an isomorph starting from the reference state point  $\rho = 0.932$ ,  $T = 0.465$  and bond length of 0.58 in A particle units from literature [19]. Figure 5.1 shows a snapshot of how the ASD simulated system looks like in the liquid phase. Afterwards, four different isomorphs are traced out with different bond lengths between A and B particles of the ASD

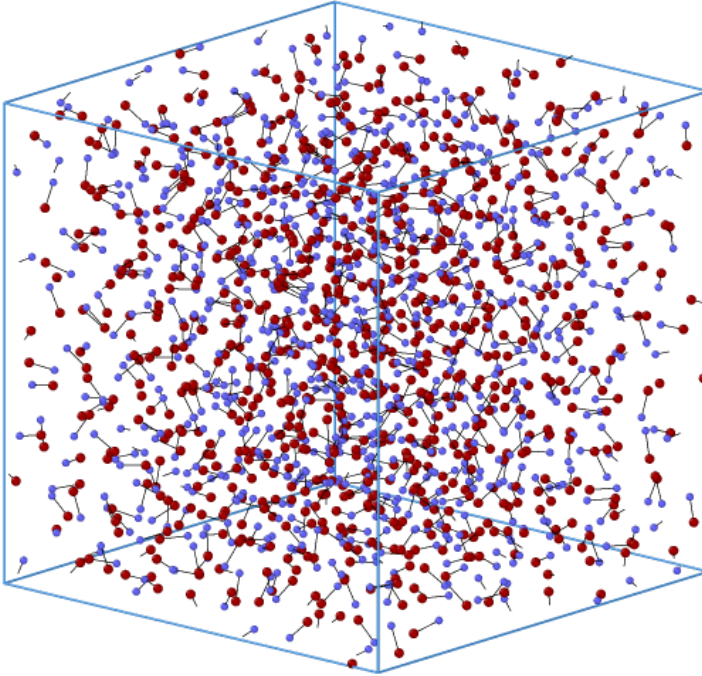


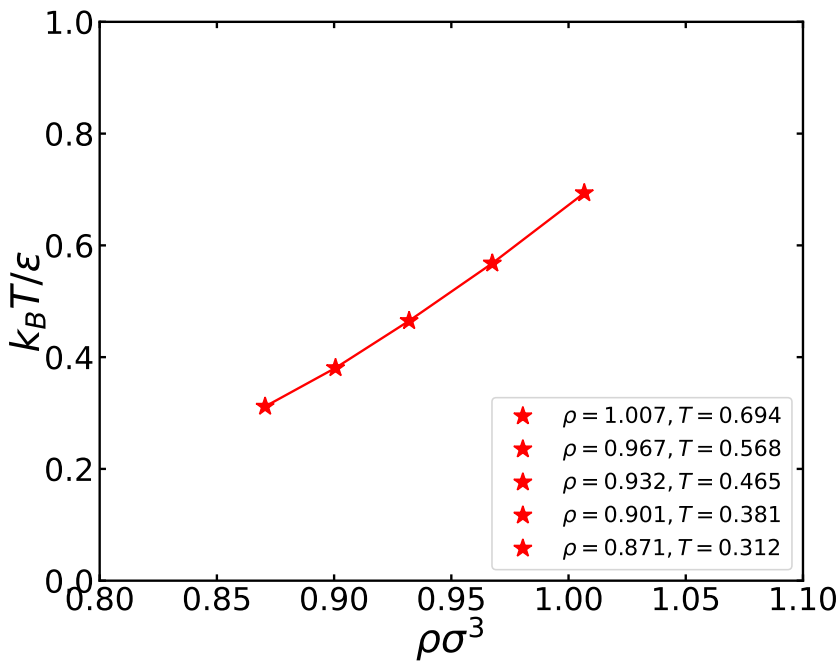
**Figure 5.1.** Snapshot from the liquid configuration at st the liquid state point  $\rho = 0.8, T = 0.8$ . Particles A are the red, particles B are the blue. The bond length between particle A and B in this configuration is 0.58 in A particle units.

molecule. In terms of the largest A particle radius, data for the bond lengths 0.05, 0.1, 0.2 and 0.5 is reported. All isomorphs start from the same density and temperature  $\rho = 1.5, T = 1.5$ . Each isomorph is traced out with an isotherm starting from the same reference state point for structure and dynamics comparison. Then, the structure and the dynamics of the state points along each isomorph and isotherm of the same bond length respectively are investigated. The structure, is probed by the radial distribution functions (RDF) of the reduced

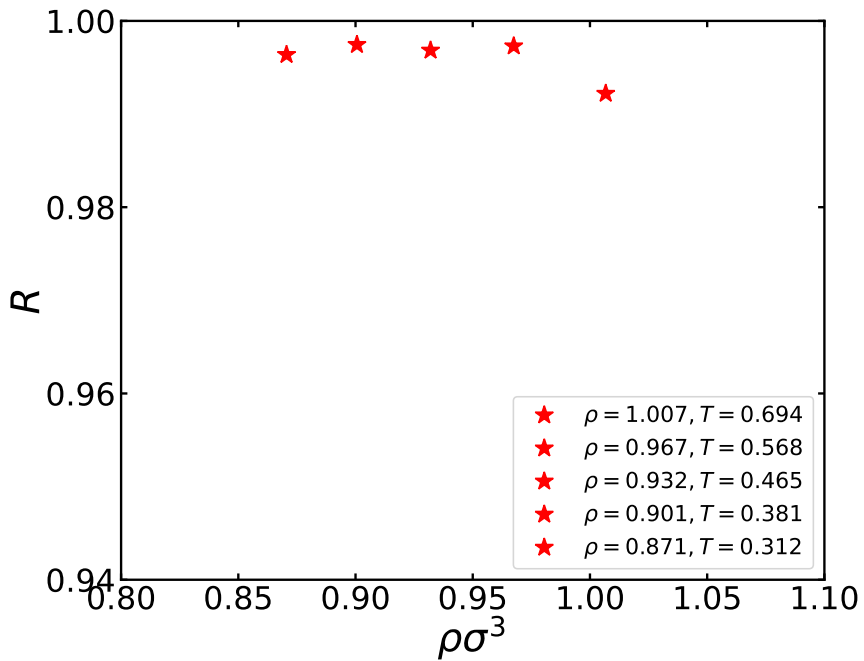
pair-distance. The dynamics are probed by the reduced mean square displacements (MSD) as functions of reduced time and the rotational auto-correlation (RAC) functions.

Figure 5.2 shows the traced isomorph from the reference state point  $\rho = 0.932, T = 0.465$  [19] in the ASD phase diagram. It is traced up to  $\rho = 1.007$  using the fourth-order Runge Kutta (RK4) method with density step size  $h = 0.2$ . Then, it is traced down with the same method and step size  $h = 0.2$  to  $\rho = 0.871$ . This isomorph is referred to in Figs. as RK4 traced isomorph. Unlike the literature isomorphs, all isomorphs in this thesis are traced out by the RK4 method for accuracy (check Appendix A for more details). Isomorph from Ref. [19] is traced by Euler's integration method. Isomorph from Ref. [77] is traced by the atomic force method. In Fig. 5.3, the correlation coefficients of the state points along the RK4 traced isomorph are plotted. The correlation coefficient  $R$  is higher than 0.99 for all of the state points.

The structure and dynamics along the RK4 traced isomorph are shown in Fig. 5.4 and compared to literature [19, 77]. For structure, the reduced AA radial distribution functions are compared. For the dynamics, the A particle intermediate -scattering functions with the  $q$  vector calculated based on the position of the first peak are compared. The end-to-end vector  $\langle \vec{n}(0) \cdot \vec{n}(\tilde{t}) \rangle$  rotational auto-correlation of the unit vector  $\vec{n}$  from A to B plotted as a function of the reduced time  $\tilde{t}$  are also compared. Because of the normalization this quantity always starts in unity at time zero. In Fig. 5.4, invariance along the structure and dynamics of the RK4 traced isomorph is seen as in literature. Both of the rotational auto-correlation functions show the behavior expected in the viscous regime, with a small damp then a complete long decay around  $\tilde{t} \approx 10^3$ .



**Figure 5.2.** A liquid isomorph traced out using fourth-order Runge Kutta (RK4) method with density step size 0.2 in the ASD thermodynamic phase diagram. The reference state point is  $\rho = 0.932, T = 0.465$ . The isomorph is traced up to  $\rho = 1.007$ , then down to  $\rho = 0.871$ . The bond length between the A and B particle of the molecule is 0.58 in A particle units.



**Figure 5.3.** The correlation coefficient  $R$  of each state point as a function of density along the traced liquid isomorph of Fig. 5.2. All the points have high correlation such,  $R \geq 0.99$  which is proposed by isomorph theory to define an isomorph state point.

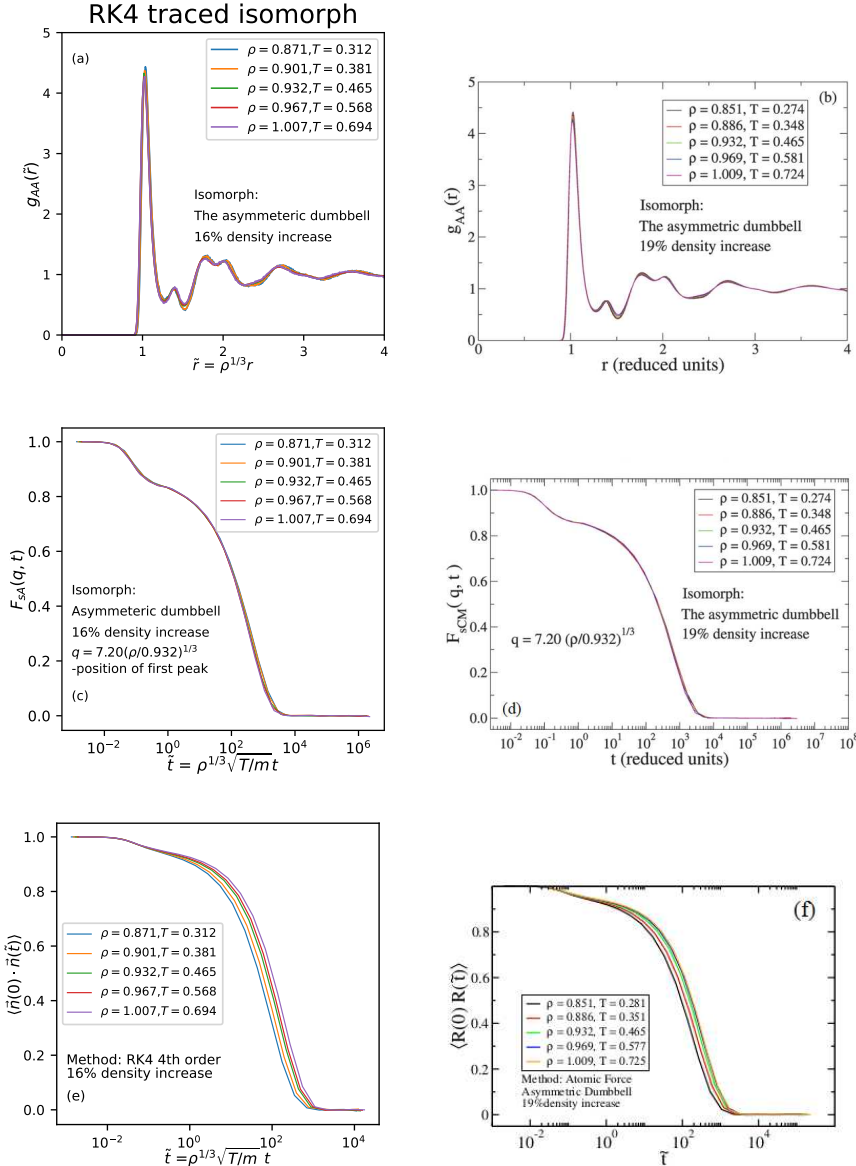


**Figure 5.4.** The AA radial distribution functions for the state points along (a) the RK4 traced isomorph (b) the isomorph from ref [19]. The density increase along the two isomorphs is comparable (16% and 19%). The A-particle intermediate scattering functions for the state points along (c) the RK4 traced isomorph (d) the isomorph from Ref. [19]. The end-to-end vector rotational auto-correlation function of (e) the RK4 traced isomorph (f) the isomorph from Ref. [77] in which  $\mathbf{R}$  is the unit vector.

## 5.3 Systematic Numerical Investigation in the Asymmetrical Dumbbell System

### 5.3.1 Isomorphs in the Liquid Phase

After comparing to literature, we proceed with tracing the other isomorphs for our systematic investigation. Fig. 5.5 shows the four isomorphs traced out in the ASD liquid phase diagram. They all start at the same reference start point,  $\rho = 1.5, T = 1.5$ . The thermodynamic values of the reference state point of each isomorph is listed in Table 5.1. A systematic increase is seen in the temperature of the last

**Table 5.1.** Thermodynamic values of the reference state point of each liquid isomorph along with the bond length in LJ units.

Bond length [ $1/\sigma$ ]	$T$ [ $\varepsilon/k$ ]	$\rho$ [ $1/\sigma^3$ ]	$p$ [ $\sigma^3\varepsilon$ ]	$\gamma$	$R$
0.050	1.500	1.500	1.089	5.474	0.850
0.100	1.500	1.000	1.049	5.548	0.850
0.200	1.500	1.500	1.606	5.941	0.894
0.500	1.500	1.500	7.496	6.116	0.961

traced state point with increasing the bond length. Looking at the correlation coefficients  $R$  of the state points along the isomorphs and isotherms (Fig. 5.6), the correlation coefficient  $R$  is noted to be below 0.9 at the reference state point. Since some Roskilde simple systems can have high correlations in only some of regions or higher than other regions in phase diagram, the criteria of  $R > 0.9$  is arbitrary. Thus,

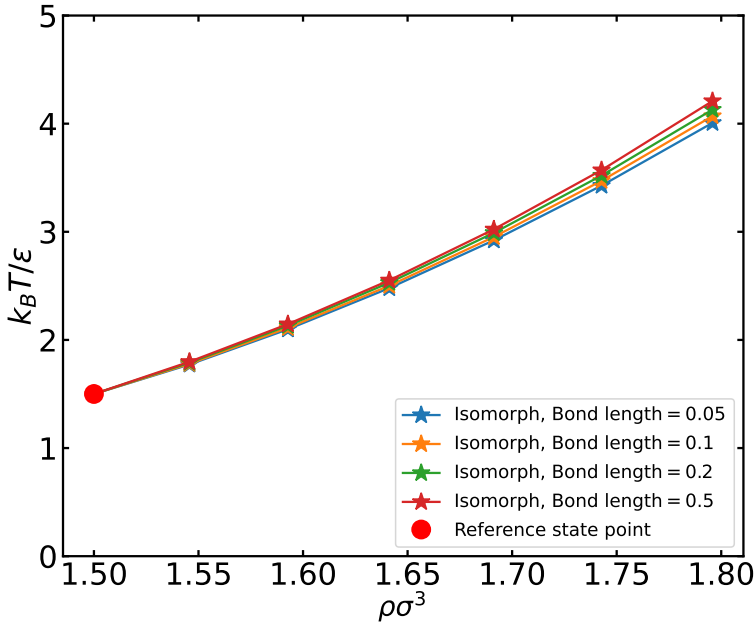


**Figure 5.5.** Four isomorphs traced out in the liquid regime of ASD thermodynamic phase diagram using the RK4 method with density step size 0.01. Each isomorph is traced with a different bond length between particle A and B, starting from 0.05 till 0.5 in LJ units.

this is still defined as high correlation. Moreover, the “good-isomorph” property depends on the quantity in question because in practice some reduced unit quantities are more isomorph invariant than others. How invariant a given property appears to depend on how large a density range is being explored. For the bond length 0.5, the correlation coefficient is relatively high for all the state points. For the density scaling exponent  $\gamma$ , the values are comparable and in range  $5.0 \leq \gamma \leq 6$ , which is typical for LJ liquid (Fig. 5.7).

Looking at the reference state point only, the correlation coefficient  $R$  and the density scaling exponent  $\gamma$  are plotted in Figs. 5.8(a) and

5.8(b) as functions of the bond length. Some extra values of  $R$  and  $\gamma$  of bond lengths (0.15, 0.25, 0.3, 0.4, 0.6, 0.7) are added at the same reference state point  $\rho = 1.5, T = 1.5$  in order to have a better view of the  $\gamma$  variation. Looking at the correlation coefficient  $R$  (Fig. 5.8(a)),  $R$  tends to increase with increasing bond length then starts to drop slightly, but still above 0.9. Looking at  $\gamma$  (Fig. 5.8(b)), the values range between  $5.0 \leq \gamma \leq 6.0$ . A small decrease is seen though after bond length 0.4, but still within the range stated above for typical LJ liquid. For the  $\gamma$  at the final state point of each isomorph at  $\rho = 1.796$ , a slight increase from the smallest bond length 0.05 till the highest 0.5 is observed (Fig. 5.9 (a)). As the temperature increases (Fig. 5.9(b)), the repulsive part of the potential is dominating and resulting in  $\gamma$  increasing.

Continuing with the investigation at the reference state point, the structure and the dynamics are checked. Fig. 5.10 shows the AA, AB and BB reduced radial distribution functions of the state point  $\rho = 1.5, T = 1.5$  of each isomorph with different bond lengths 0.05, 0.1, 0.2, 0.5. Similar behavior along the AA reduced radial distribution function for the four isomorphs is observed. For the AB and BB reduced radial distribution functions, the first peak changes significantly. At bond length 0.5, the BB RDF is almost constant. The observed variation of the AB and BB RDFs can be interpreted as a consequence of the near invariance of the AA particle RDF as the bond length is increased. The structure of the ASD liquid may be thought of as primarily determined by the large A particles, which behave like standard LJ particles that are not bothered much by existence of the B particles. This is because the B particles are smaller and have significantly lower interaction energy parameters. The B particles are to a significant degree “slaves” of the A particles and constrained to be close to the A particle of the same molecule. When the bond length increases, the B particles place themselves in many possible positions around the A particles, which for all bond lengths have almost the RDF of a single-component LJ

liquid. The “B slaving A” picture is confirmed by the AB RDF, which (except for the vertical line coming from the intra-molecular AB bond correlation) gives data for the AB correlations between different ASD molecules. The AB RDF is diminishing as the bond length increases, but less than the BB RDF because the relative order of the A particles is partly inherited by the AB RDF.

For the dynamics, Fig. 5.11 shows data for the reduced-time dependence of the reduced-unit mean-square displacement of the A and B particles for the four isomorphs. The A particle motion shows to be pretty similar at all bond lengths, which is consistent with the A particles to a significant extent behaving as if the B particles were not present, as i.e. as a single-component LJ liquid. At short times, the longer the bond, the longer the ballistic regime. The B particles move faster than the A particles as they have lower mass. At long times for both A and B particle, the longer the bond, the slower the movement as the particles enter the diffusion regime. This results in lower diffusion coefficient as the bond length increases (Fig. 5.12).

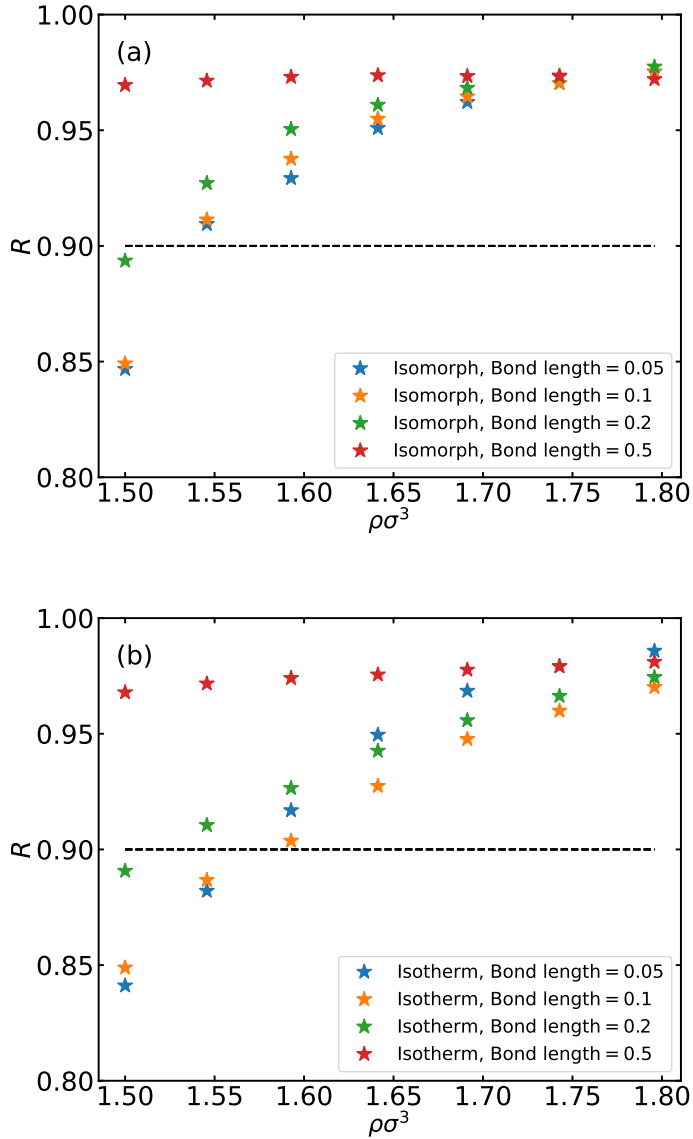


**Figure 5.6.** (a) The variation of correlation coefficient  $R$  along the state points of each isomorph of different bond lengths (b) The variation of correlation coefficient  $R$  along the state points of each isotherm of different bond lengths.

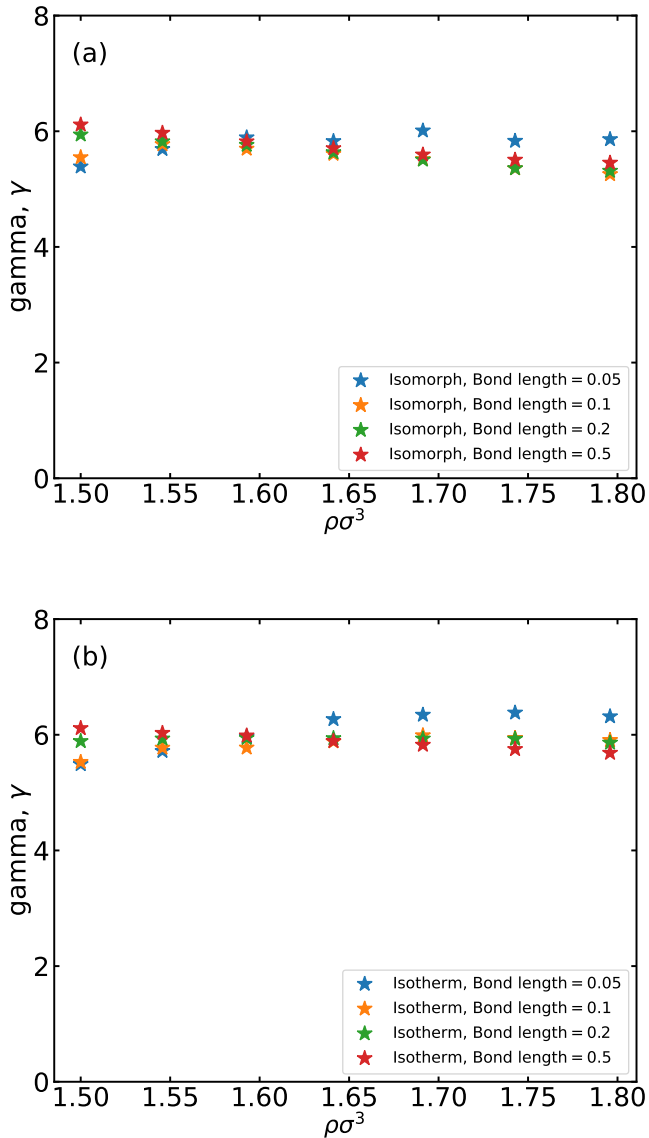


**Figure 5.7.** (a) The variation of the density scaling exponent coefficient  $\gamma$  along the state points of each isomorph of different bond lengths (b) The variation of the density scaling exponent coefficient  $\gamma$  along the state points of each isotherm of different bond lengths.

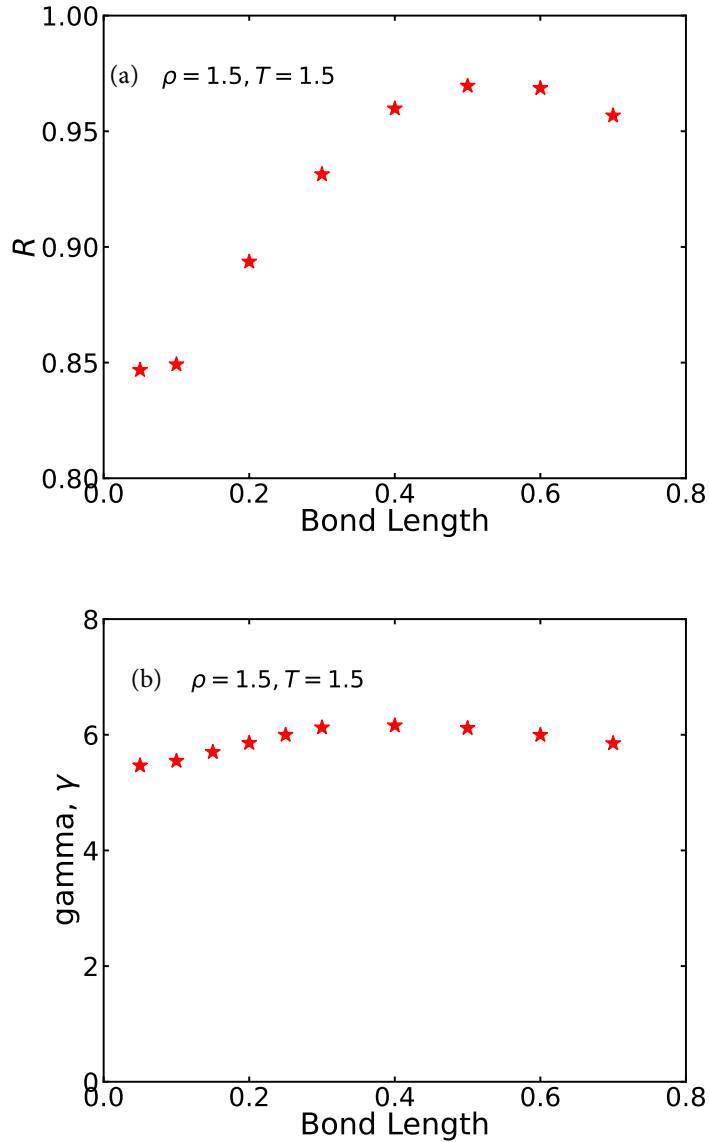


**Figure 5.8.** (a) The variation of  $R$  at the initial start point  $\rho = 1.5, T = 1.5$  of each isomorph with different bond lengths. (b) The variation of  $\gamma$  at the initial start point  $\rho = 1.5, T = 1.5$  of each isomorph with different bond lengths.

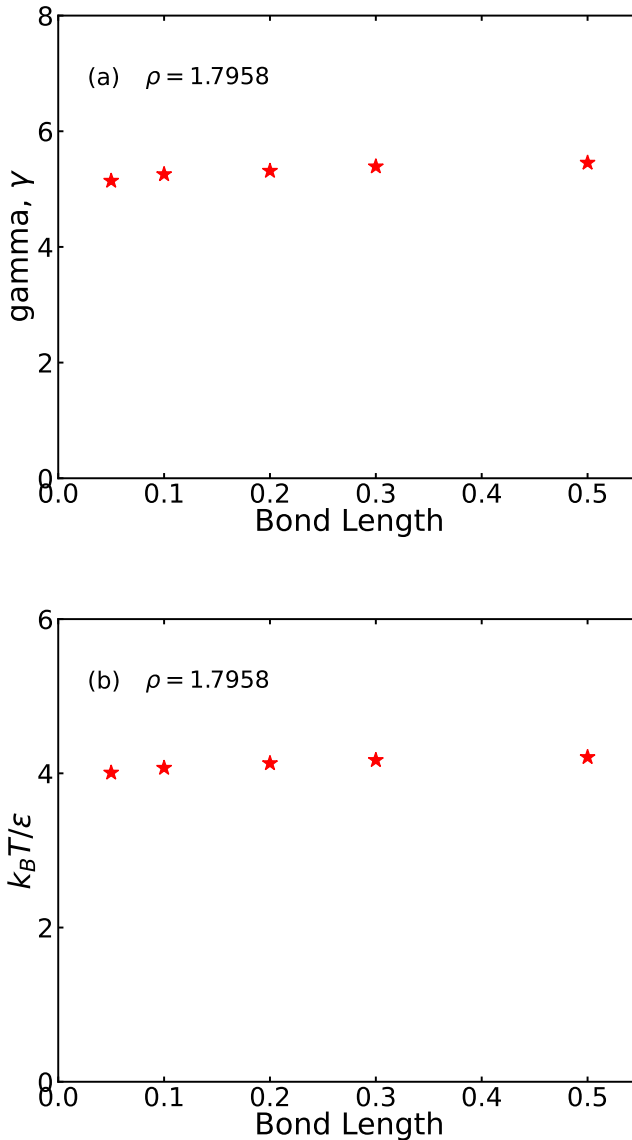


**Figure 5.9.** (a)  $\gamma$  at the final state point  $\rho = 1.796$  of each isomorph plotted as a function of the bond length. (b) The temperature,  $T$  at the final state point  $\rho = 1.796$  of each isomorph plotted as a function of the bond length. An increase can be seen as with each state point, the temperature increases with increasing the bond length, thus bigger  $\gamma$ . While at the reference start point the temperature is fixed at  $T = 1.5$  for each bond length.

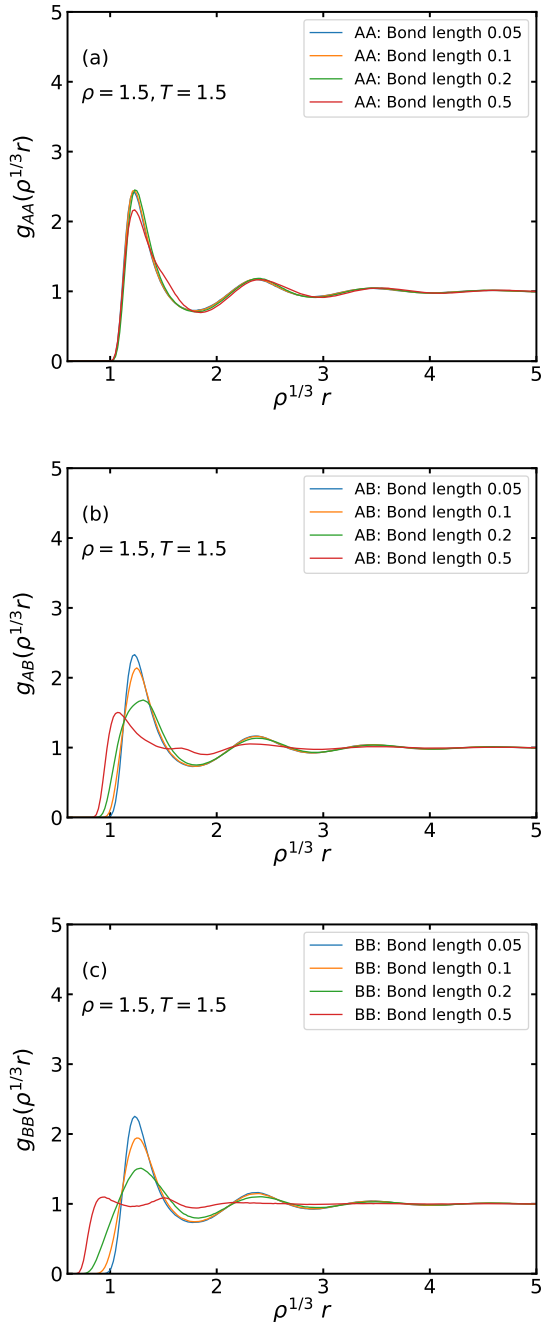


**Figure 5.10.** (a) The reduced AA radial distribution functions of the state point  $\rho = 1.5, T = 1.5$  of each isomorph in the bond lengths range of 0.05, 0.1, 0.2, 0.5. (b) The reduced AB radial distribution functions (c) The reduced BB radial distribution functions.

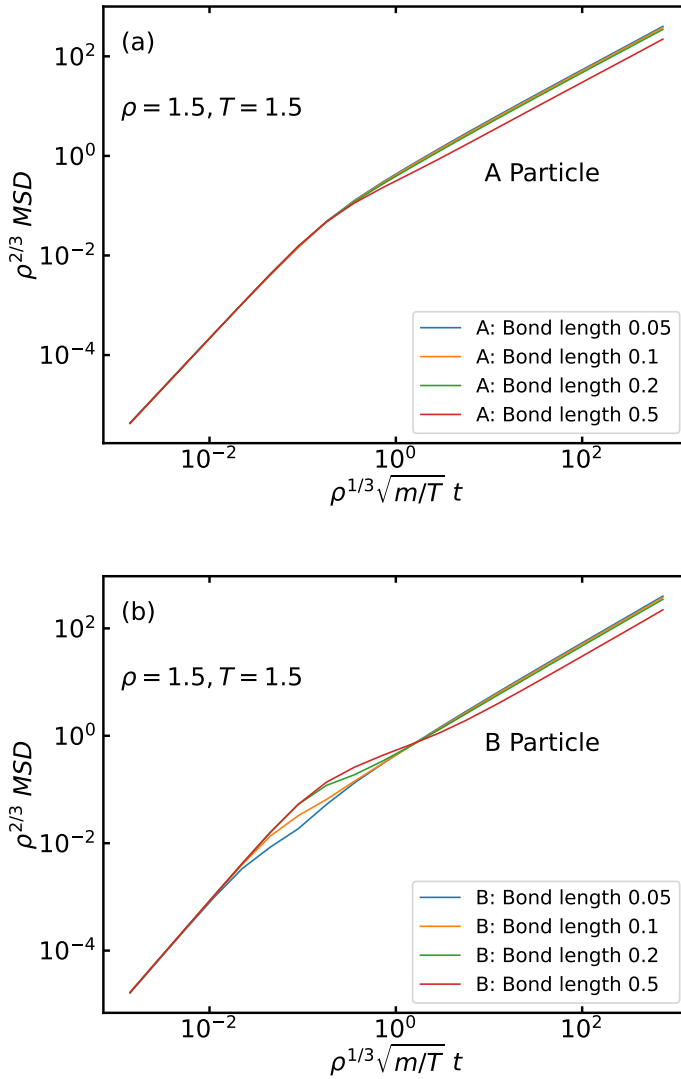


**Figure 5.11.** (a) The mean square displacement of particle A of the state point  $\rho = 1.5, T = 1.5$  of each isomorph with different bond lengths of 0.05, 0.1, 0.2, 0.5. (b) The mean square displacement of particle B of the state point  $\rho = 1.5, T = 1.5$ .

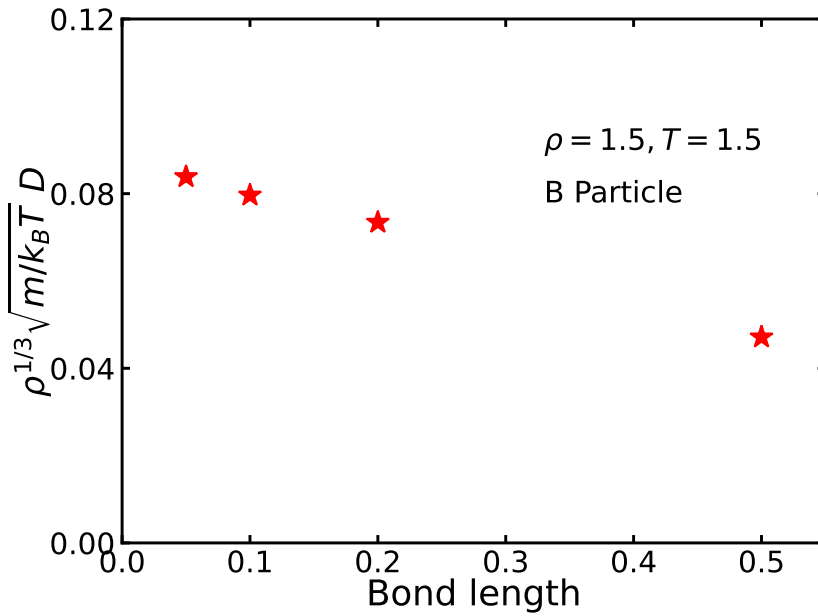


**Figure 5.12.** The diffusion coefficient calculated at the state point  $\rho = 1.5, T = 1.5$  of each isomorph with different bond lengths of 0.05, 0.1, 0.2, 0.5. It is clearly seen that with plotting the diffusion constants against the bond length that the longer the bond, the smaller the diffusion constant due to slow movements of the particles. The behavior is similar for the A particle by comparison from Fig. 5.11

### 5.3.1.1 Structure and Dynamics Invariance

In this sub-section, we continue with the investigation of the other state points along the isomorphs. The structure and dynamics are checked for the isomorphs starting from the lowest bond length 0.05 till the longest 0.5. Figures 5.13, 5.14, 5.15 and 5.16 show that along the reduced AA, AB, BB radial distribution functions, better invariance is observed in all of the isomorphs compared to the isotherms plotted next to them, especially in the first peak. The thick vertical line in the AB RDF comes from the fixed bond length, which in reduced units varies with density. When the bond length is relatively small i.e., 0.05, there is no much change in the AA, AB and BB radial distribution functions. As the bond length increases, variations start to appear in the width of the first peak. It gets broader. For the longest bond length in the range 0.5, the first peak almost diminishes and splits into two peaks (Fig. 5.16). This follows as a consequence of the small B particles acting as "slaves" to the large A particles. At small bond length i.e., 0.05, the structure of the ASD particles is similar to LJ particles governed by the A particles and not bothered much by the existence of the B particles. When the bond gets longer, the peak gets broader as the B particles place themselves in many possible positions around the A particles. The same behavior is seen Fig. 5.10 at the reference state point.

For the dynamics, Figs. 5.17, 5.18, 5.19 and 5.20 show data for the reduced mean square displacement of the A and B particles of each isomorph and isotherm of the same bond length respectively. The data are isomorph-invariant to a good approximation, but not isotherm-invariant. The A particle motion is pretty similar for all bond lengths i.e., as in a single-component LJ liquid. The same behavior is seen in Fig. 5.11 at the reference state point. At long times, the A and B particles follow each other resulting in the same long-time MSD for all bond lengths. This also applies along the isotherms. An interesting

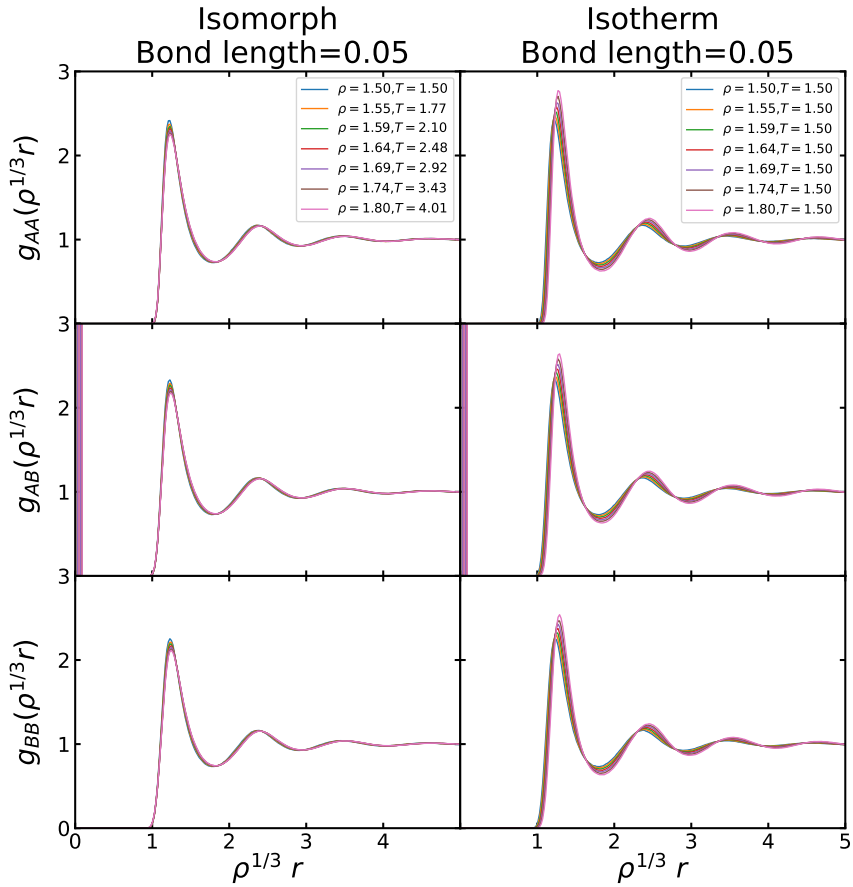


**Figure 5.13.** The AA, AB and BB radial distribution functions of isomorph of bond length 0.05 along with the isotherm of the same bond length 0.05 respectively.

feature appears at intermediate times for the B particle MSD in short

bond lengths i.e., 0.05. At such short bond length, there is a slight kink that at longer bond lengths develops into an indication of a plateau. We interpret this as an effect of the fact that the fast ballistic motion of the B particles in their motion around the A particles eventually “saturates”. This is confirmed in Fig. 5.21 (discussed next), showing that the rotational auto-correlation function for bond length 0.05 has a (negative) minimum in this range around  $\tilde{t} \approx 0.1$ .

Next for dynamics, the normalized end-to-end vector  $\langle \vec{n}(0) \cdot \vec{n}(\tilde{t}) \rangle$  rotational auto-correlation (RACs) functions are investigated. We don’t expect the state points reduced rotational auto-correlation functions to have perfect collapse as in reduced radial distribution functions or the mean square displacement. This is because the moment of inertia is not isomorph invariant because the bond length along each isomorph is fixed and not scaled with the density. The reduced rotational auto-correlation functions give an indication of the system phase, the orientation of the molecules and the effect of each bond length on the rotation of the molecules. Figures 5.21 and 5.22 show the RACs of each isomorph and isotherm of the same bond length. Comparing the RACs of the isomorphs and isotherms, we see much smaller variance along the RACs of the isomorphs showing more invariant rotation along the isomorphs, especially in bond length 0.5. We can see how the reduced rotational auto-correlation functions change from fast decay to slower smooth decay. The damping or the negative minimum mirrors the fast rotation of the molecules at the small bond lengths. It signals a more than 90 degree rotation of the molecule, while in the longer bond length, the molecules rotate slower with longer decay and no negative minimum. In Fig. 5.21(a), at bond length 0.05, the two particles moves as one. The rotation of the molecule happens vigorously and it rests at short time around  $\tilde{t} < 0.1$ . When bond length is 0.5 (Fig. 5.22), the molecules rotate slower and relaxes at  $\tilde{t} \geq 1.0$ . As a consequence of the short bond length 0.05, the B particle mean square displacement of the same isomorph shows the small kink mentioned

earlier. Comparing the reduced time  $\tilde{t}$  at which this kink happens with the time of the negative minimum of the rotational auto-correlation (RAC) function of the same isomorph, we can see it occurs at almost the same time  $\tau_{roc} \approx 0.1$ . Finally, in Fig. 5.22(h), along the isotherm of bond length 0.5, larger variation along the isotherm is seen compared to the isomorph (5.22(g)). This is because the density decoupling is higher in bond length 0.5 as the density increases while the temperature is still the same  $T = 1.5$ .

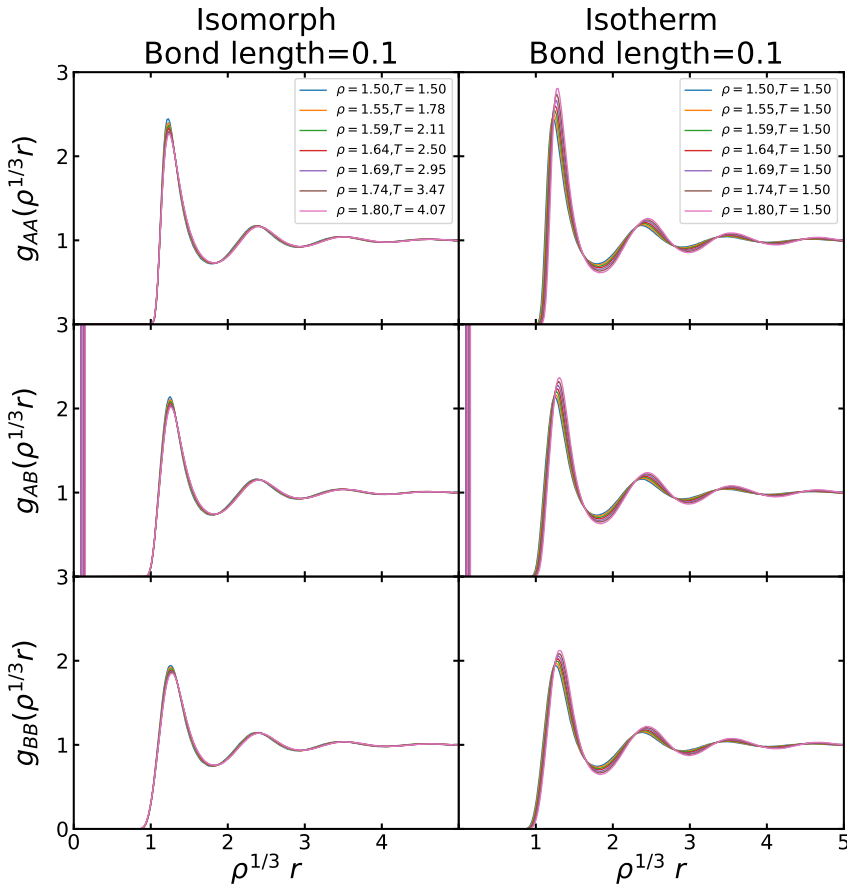


**Figure 5.14.** The AA, AB and BB radial distribution functions of isomorph of bond length 0.1 along with the isotherm of the same bond length 0.1 respectively. The first peak in the BB radial distribution function starts to get broader as the bond increases and B particle start to move away from A. Invariance is seen along the isomorph compared to the the isotherm.

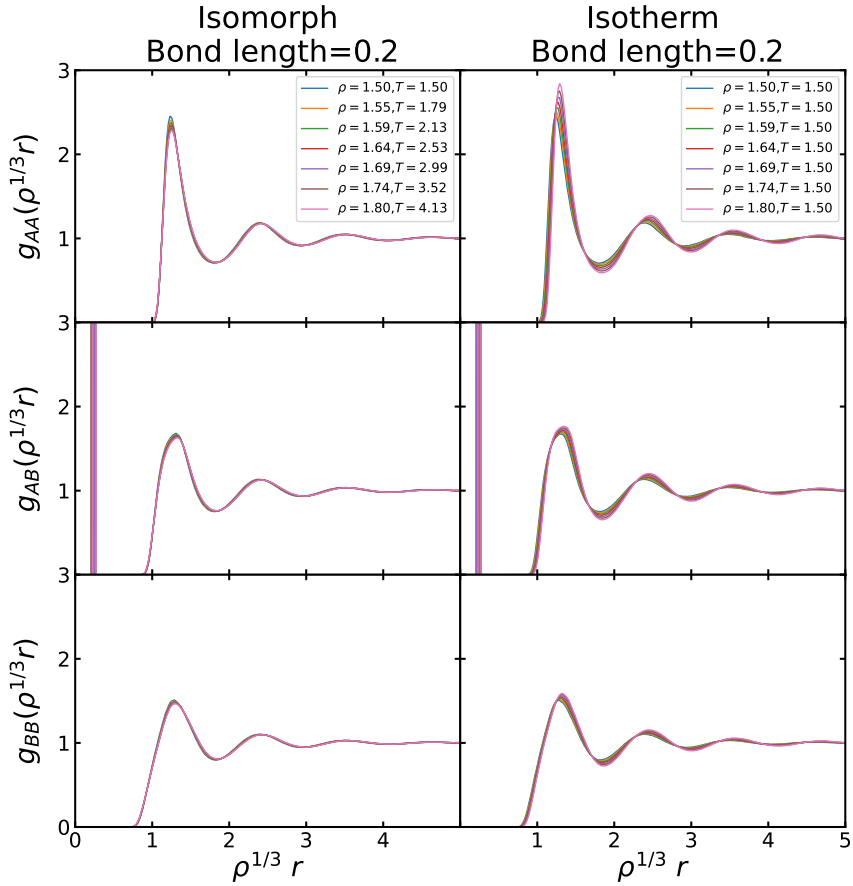


**Figure 5.15.** The AA, AB and BB radial distribution functions of isomorph of bond length 0.2 along with the isotherm of the same bond length 0.2 respectively. The first peak of the BB radial distribution function is getting even lower while the invariance withhold along the isomorph.

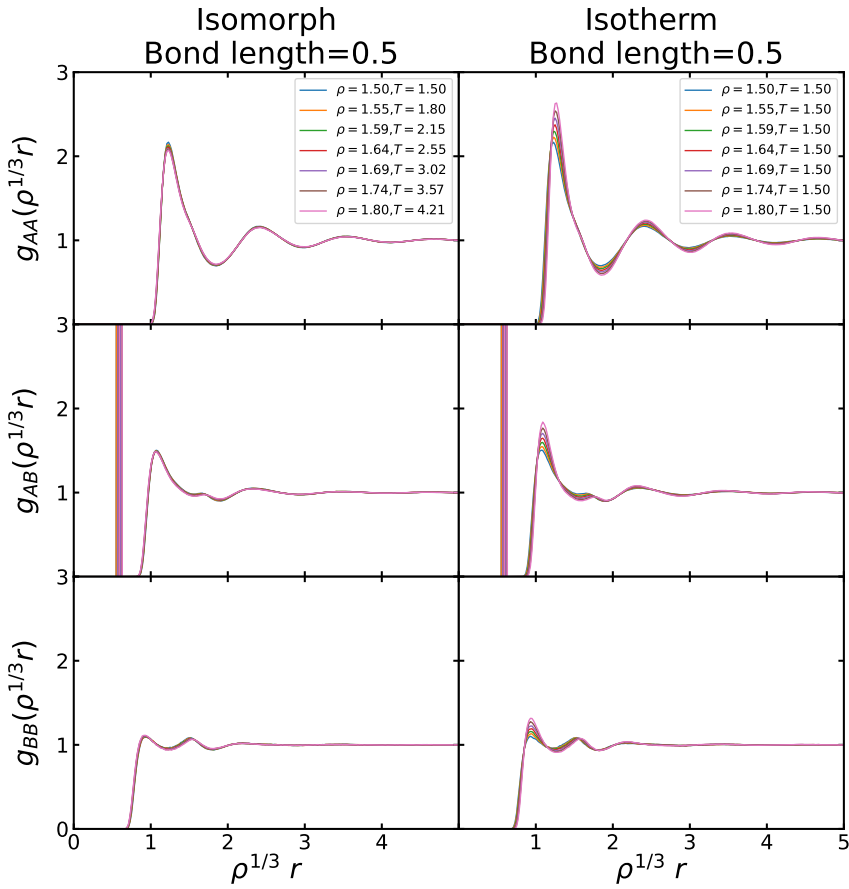


**Figure 5.16.** The AA, AB and BB radial distribution functions of isomorph of bond length 0.5 along with the isotherm of the same bond length 0.5 respectively. Here the first peak of the AB radial distribution function is broader than the above and almost no second peak. There is still also invariance along the isomorph.

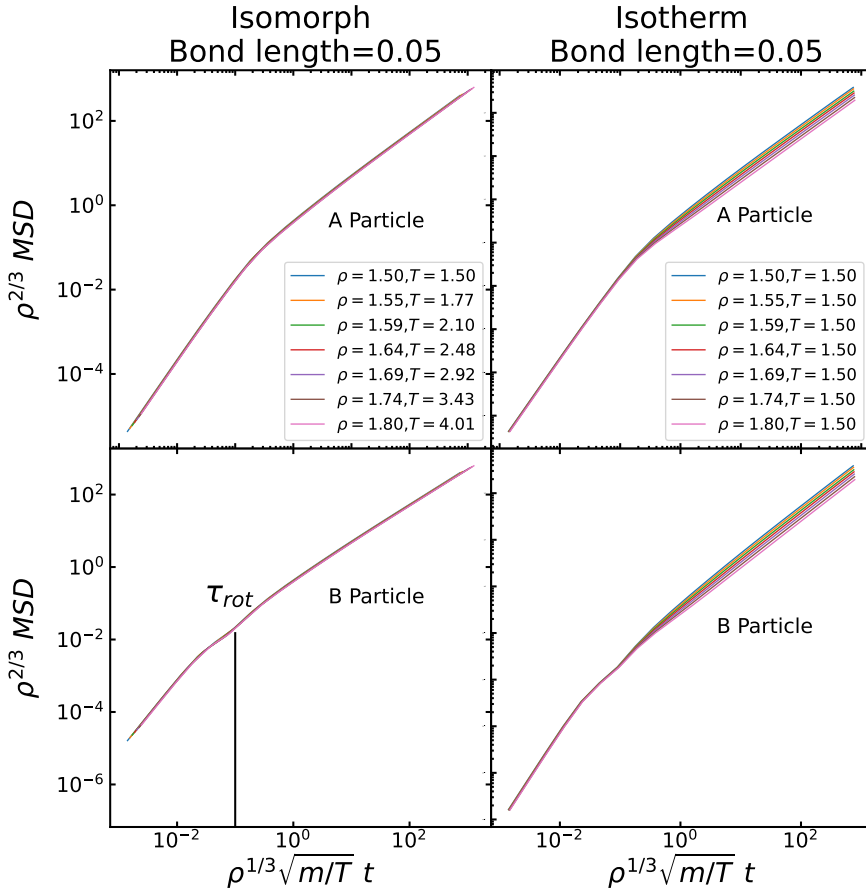


**Figure 5.17.** The A and B reduced mean square displacement along isomorph of bond length 0.05 and the isotherm of the same bond length 0.05 respectively. There is invariance along the isomorph in both A and B reduced mean square displacement.

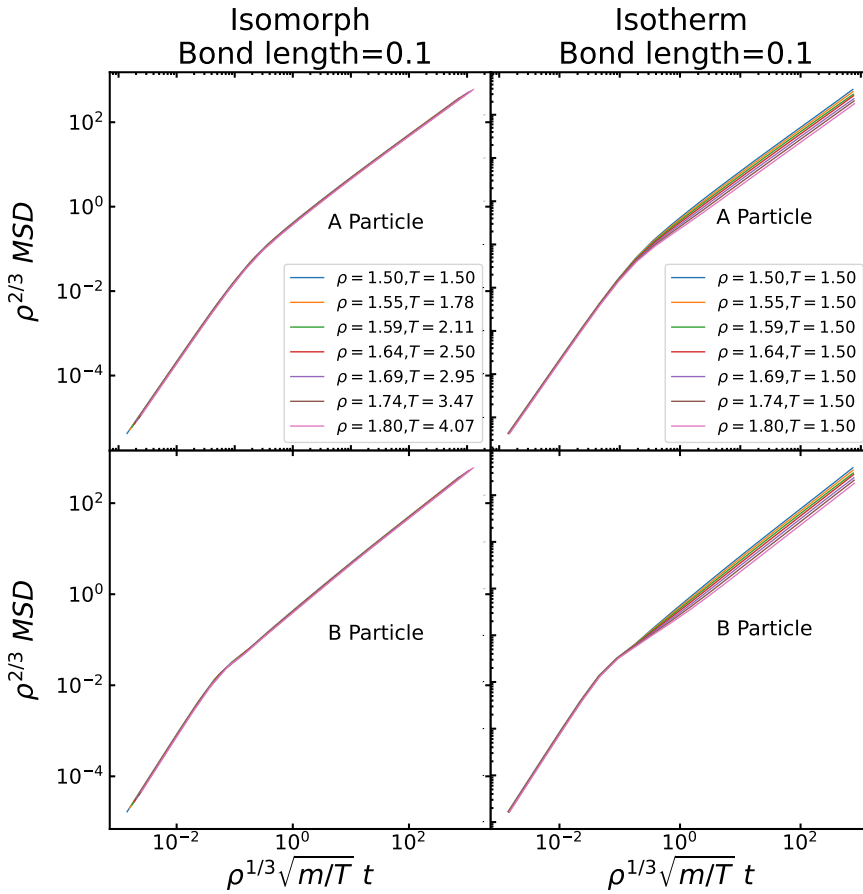


**Figure 5.18.** The A and B reduced mean square displacement along isomorph of bond length 0.1 and the isotherm of the same bond length 0.1 respectively. There is invariance along the isomorph in both A and B reduced mean square displacement.

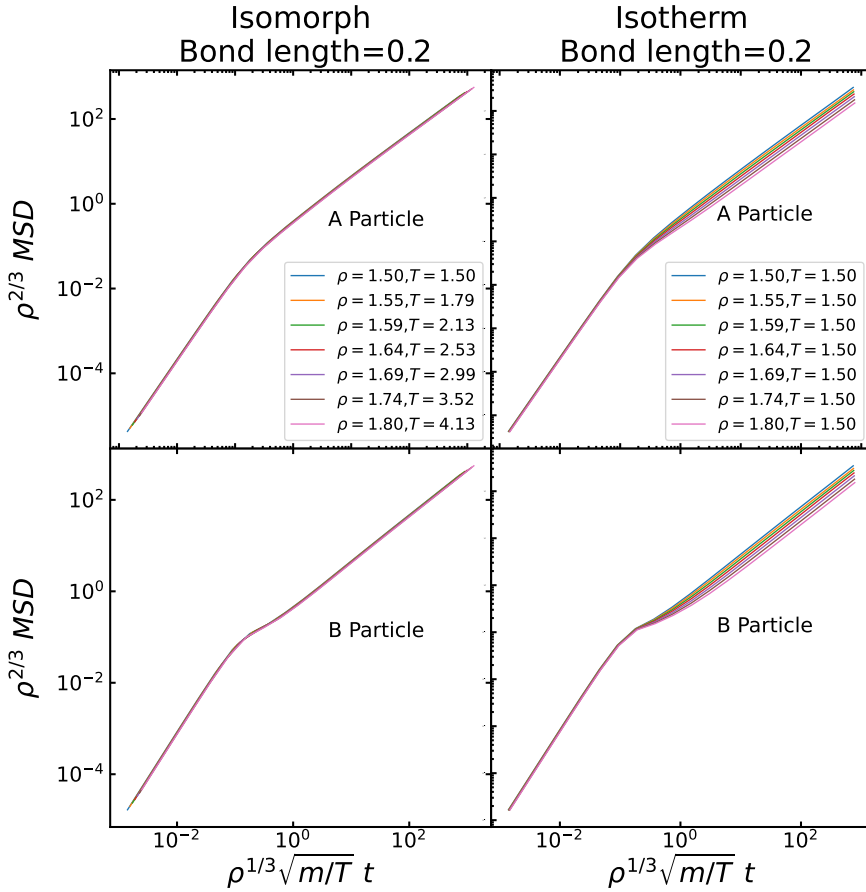


**Figure 5.19.** The A and B reduced mean square displacement along isomorph of bond length 0.5 and the isotherm of the same bond length 0.5 respectively. There is invariance along the isomorph in both A and B reduced mean square displacement.

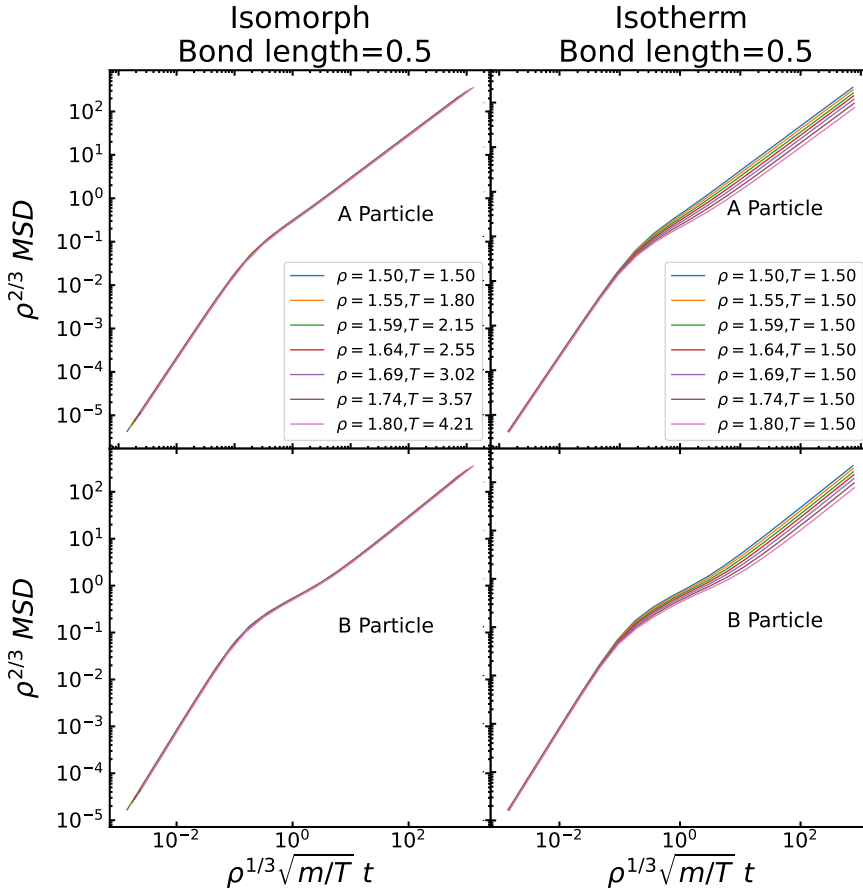


**Figure 5.20.** The A and B reduced mean square displacement along isomorph of bond length 0.5 and the isotherm of the same bond length 0.5 respectively. There is invariance along the isomorph in both A and B reduced mean square displacement.

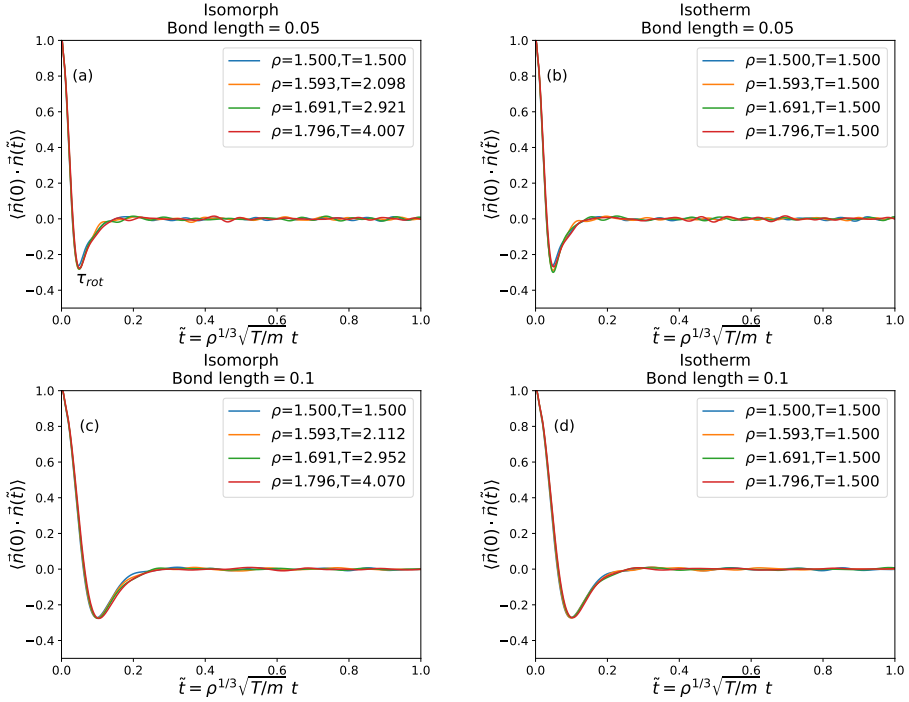


**Figure 5.21.** (a) The rotational auto-correlation of isomorph of bond length 0.05 and (b) of isotherm of bond length 0.05. We can see a fast decay to zero at time  $\tilde{t} > 0.1$ . (c) The rotational auto-correlation of isomorph of bond length 0.1 and (d) of isotherm of bond length 0.1. The decay starts to be a bit slower, at time  $\tilde{t} \geq 0.2$

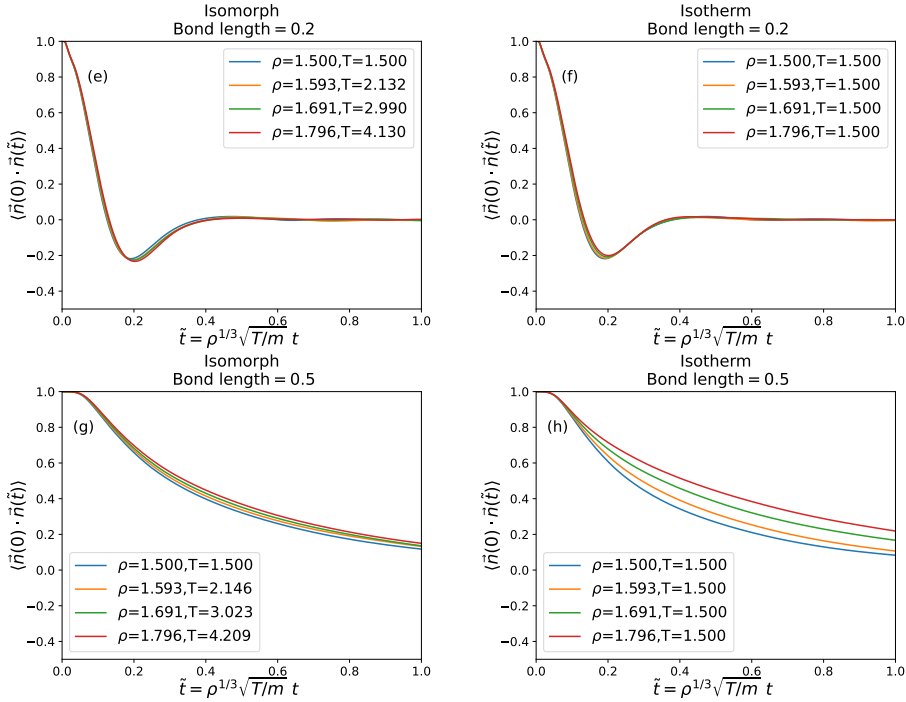


**Figure 5.22.** (e) The rotational auto-correlation of isomorph of bond length 0.2 and (f) of isotherm of bond length 0.2. We can see a fast decay to zero at time  $\tilde{t} > 0.3$ , but not as fast as in bond length 0.05 and 0.1 (g) The rotational auto-correlation of isomorph of bond length 0.5 and (h) of isotherm of bond length 0.5. The decay is much slower  $\tilde{t} \geq 1.0$  and it is smoother, doesn't go below zero as we see in all other bond lengths.

### 5.3.2 Isomorphs in the Plastic-Crystalline Phase

Moving to the crystalline phase, we trace out four isomorphs starting from the same reference state point  $\rho = 2.2, T = 0.5$ . The simulation runs with the same parameters including the same system size and time step as in the liquid phase. Results for the plastic crystalline phase for the bond lengths 0.05, 0.1, 0.2, and 0.3. are reported For bond lengths larger than 0.3, the systems were liquid at the reference state point. A typical crystal configuration is shown in Fig. 5.23. We clearly see that the system is ordered comparing to Fig. 5.1. The order is not perfect, however, because the bond directions are disordered. This is the signal of a plastic crystal in which the center of masses order on a crystalline lattice (in this case a face-centered cubic lattice) while the molecular orientations vary more or less randomly because the molecules are free to rotate. At a higher densities with relatively low temperature, there is a transition to the less ordered glassy phase in which the bond orientations are restricted as seen in Sub-section 5.3.2.2.

In Fig. 5.24, the four isomorphs traced out are shown in the crystalline region of the ASD phase diagram. The thermodynamic values of the reference state point of each isomorph is listed in Table 5.2. The temperature of the final state point is decreasing till bond length 0.2, then afterwards increases for bond length 0.3. The correlation coefficients  $R$  along the four isomorphs and isotherms are shown in Fig. 5.25(a) and (b) respectively. For all of the state points along the isomorphs and the isotherms, unlike the liquid phase, the correlation coefficient  $R$  is high such that  $R > 0.95$ . That is evident for strong  $UW$  correlation in the plastic crystalline region of ASD phase diagram. It decreases slightly though when the bond increases, but still above 0.95. Shifting to the density scaling exponent  $\gamma$ , the values

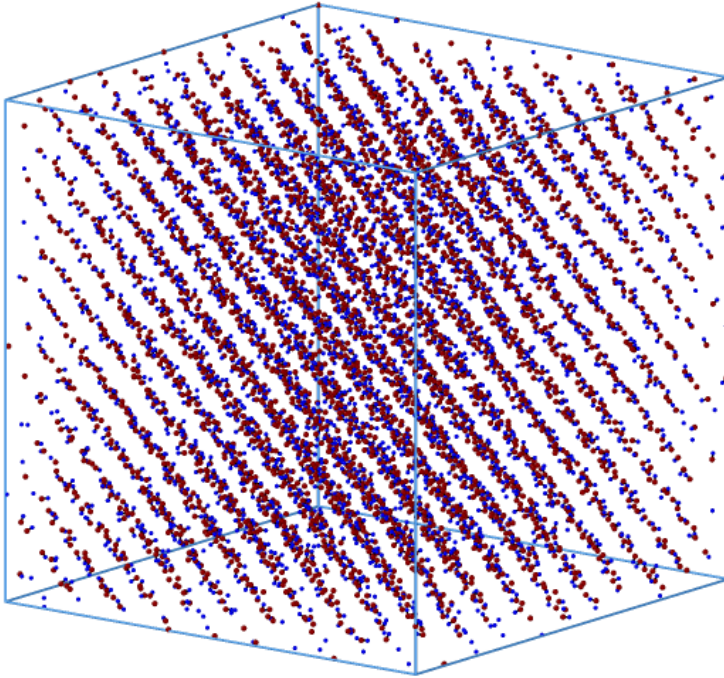


**Figure 5.23.** Snapshot from the plastic crystal configuration at the state point  $\rho = 2.2, T = 0.5$  and bond length = 0.2 in LJ units. Particles A are the red, the B particles are the blue.

are comparable and around  $5 \leq \gamma < 6$  (Fig. 5.26). Figure 5.27 shows the correlation coefficient  $R$  and the density scaling exponent  $\gamma$  at the reference state point only of each isomorph. The  $R$  is high all the bond lengths such that  $R > 0.99$  and the  $\gamma$  is  $5.0 \leq \gamma \leq 6.0$ . At the final state point  $\rho = 2.634$ , the same variation of  $\gamma$  is seen as in the reference state point, but when the bond length is 0.3,  $\gamma$  value is much higher (Fig. 5.28).

Figure 5.29 shows the AA, AB and BB radial distribution functions at the reference state point. In Fig. 5.29(a), the AA reduced RDFs

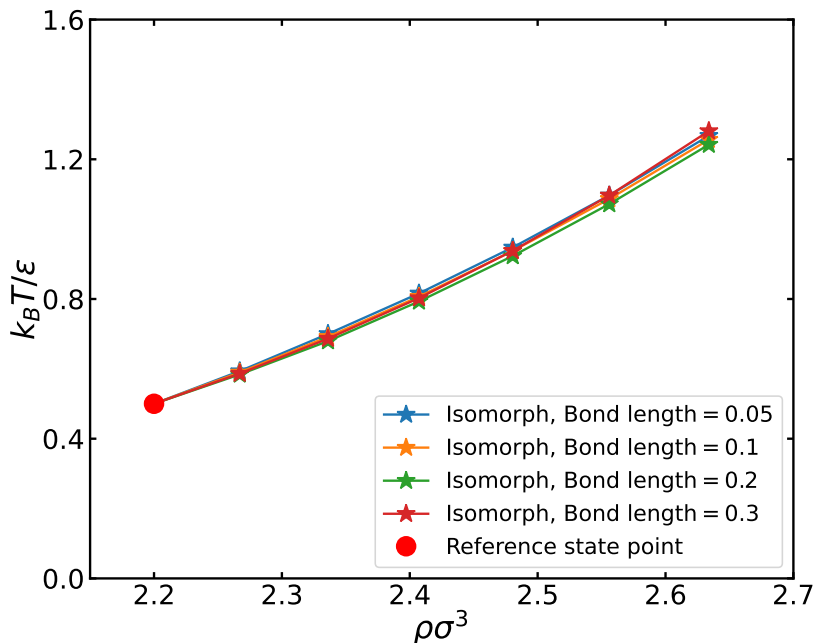


**Figure 5.24.** Four isomorphs traced out in the crystalline regime of ASD thermodynamic phase diagram using the RK4 method with density step size 0.01. Each isomorph is traced with a different bond length between particle A and B, starting from 0.05 till 0.3 in LJ units.

show well-defined order due to the almost crystalline ordering of the A particles for all bond lengths. In contrast, the AB and BB RDFs vary significantly because of the rotation of the B particles around the A particles. In these cases, the most ordered RDFs are those of the shortest bonds, which reflects the slaving of the B particles to the A particles that are well ordered. Looking at the mean square displacement (MSD) on the other hand, the A particle mean square displace-

**Table 5.2.** Thermodynamic values of the reference state points of each isomorph along with the bond length in LJ units.

Bond length [ $1/\sigma$ ]	$T$ [ $\varepsilon/k$ ]	$\rho$ [ $1/\sigma^3$ ]	$p$ [ $\sigma^3\varepsilon$ ]	$\gamma$	$R$
0.050	0.500	2.200	0.497	5.497	0.997
0.100	0.500	2.200	1.173	5.503	0.996
0.200	0.500	2.200	5.191	5.191	0.992
0.300	0.500	2.200	15.279	5.579	0.990

ment shows the same time for the ballistic regime of all isomorphs. For the A particles, the results are very similar for the different bond lengths, although bond length 0.3 deviates from the three smaller ones by having a somewhat larger long-time plateau. We have no good explanation for this, but deviations for the longest bond length from the three others are also noted in some of the later figures. For the B particles, long-time plateaus vary considerably. When the bond is larger, the plateau gets larger. This is because the B particles rotate around the A particles and a larger bond length gives them more freedom to do so, resulting in a larger long-time plateau. Moreover, the B particles move faster compared to A particles. When the bond get longer, the long-time plateau showing the elastic constant of the crystal gets higher, in a more systematic way (Fig. 5.30(b)). As the bond gets longer, the crystal can be seen as "less hard" or ordered, especially through B particles displacement. That indicates the important role the B particles in the dynamics of the plastic crystals obtained.

### 5.3.2.1 Structure and Dynamics Invariance

Moving from the reference state point to other state points along the isomorphs, we investigate the structure and the dynamics starting

from the lowest bond length 0.05 till the longest 0.5. Figures 5.31, 5.32, 5.33 and 5.34 show the reduced AA, AB, BB radial distribution functions for all isomorphs and isotherms, respectively. Better invariance in all of the isomorphs is observed compared to the isotherms plotted next to them, especially in the first peak. For the relatively small bond length of 0.05, there is no much change in the AA, AB and BB radial distribution functions. This is a consequence of the fact that all B particles are constrained to be very close to an A particle. As the bond length increases, very good isomorph collapse is seen in all cases, but variations in the height of the first AB and BB peak compared to the AA particle RDF start to be seen. As seen in the liquid phase, this is interpreted as deriving from rotations of the molecules. To investigate the dynamics of the plastic-crystal systems, the A and B particle mean square displacements are checked. Figs. 5.35, 5.36, 5.37 and 5.38 show visible invariance along all of the isomorphs compared to the isotherms. In contrast, there is a notable variation along the corresponding isotherms for both A and B particles. Only at short times (in the ballistic regime), invariance along the isotherms is observed, but this is as mentioned a consequence of the definition of the reduced units.

Moving to the normalized end-to-end vector  $\langle \vec{n}(0) \cdot \vec{n}(\tilde{t}) \rangle$  rotational auto-correlation (RACs) functions, we can have an indication about the system phase and how the molecules rotate in the plastic crystals of different bond lengths. Figures 5.39 and 5.40 show the rotational auto-correlation function of each isomorph and isotherm of the same bond length. Comparing the RACs of the isomorphs and isotherms, we see much smaller variance along the RACs of the isomorphs showing more invariant rotation along the isomorphs, especially in bond length 0.3. We can see how the reduced rotational auto-correlation functions change from fast decay to slower smooth decay. The damping or the negative minimum mirrors the fast rotation of the molecules at the small bond lengths. It signals a more than 90 degree rotation of the

molecule. In the longer bond length, the molecules rotate slower with longer decay and no negative minimum in the RAC. In Fig. 5.39(a), at bond length 0.05, the two particles moves as one and the rotation of the molecule happens vigorously and it rests at short time around  $\tilde{t} < 0.1$ . With bond length 0.5 (Fig. 5.40), the molecules rotate slower and relaxes at  $\tilde{t} \geq 1.0$ . In Fig. 5.40(g) and (h), along the isomorph of bond length 0.3, we can see much larger variation along the isotherm compared to the isomorph. This is because the density decoupling is higher along bond length 0.5 as the density increases while the temperature is relatively low  $T = 0.5$ . The rotation gets slower and slower as the system starts to exit the plastic crystalline phase.

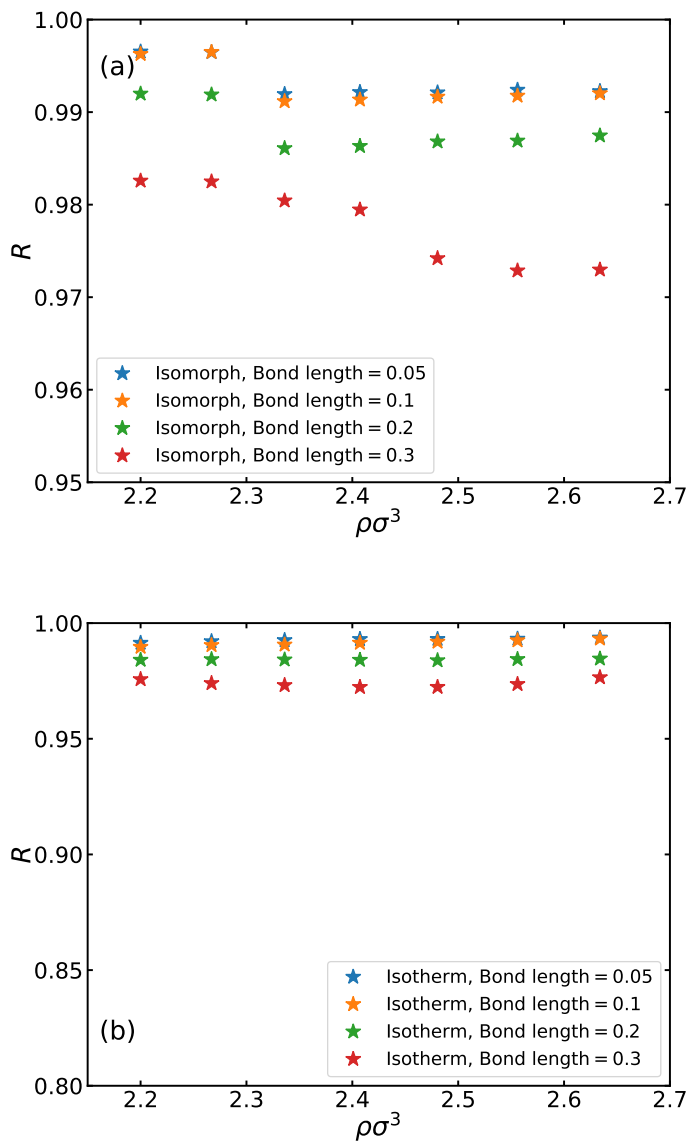


**Figure 5.25.** (a) The variation of correlation coefficient  $R$  along the state points of each isomorph of different bond lengths (b) The variation of correlation coefficient  $R$  along the state points of each isotherm of different bond lengths.

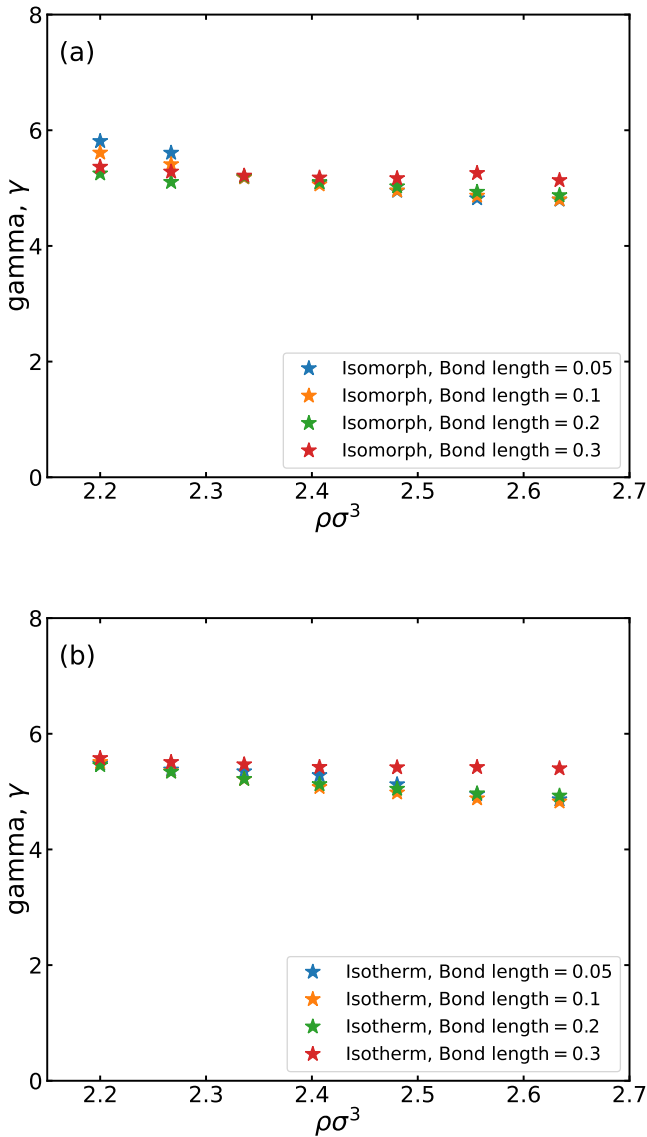


**Figure 5.26.** (a) The variation of the density scaling exponent  $\gamma$  along the state points of each isomorph of different bond lengths (b) The variation of the density scaling exponent  $\gamma$  along the state points of each isotherm of different bond lengths.

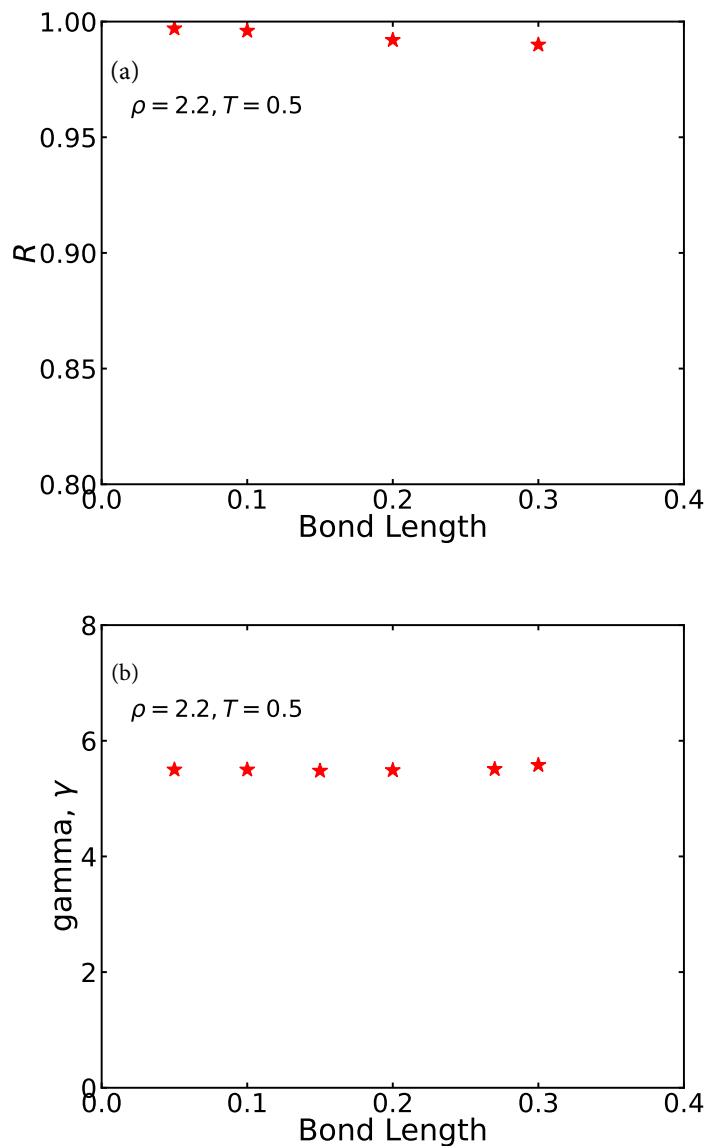


**Figure 5.27.** (a) The variation of the correlation coefficient  $R$  at the reference state point  $\rho = 2.20, T = 0.5$  of each isomorph plotted as a function of the bond length. (b) The variation of the density scaling exponent  $\gamma$  at the reference state point  $\rho = 2.20, T = 0.5$  of each isomorph plotted as a function of the bond length.

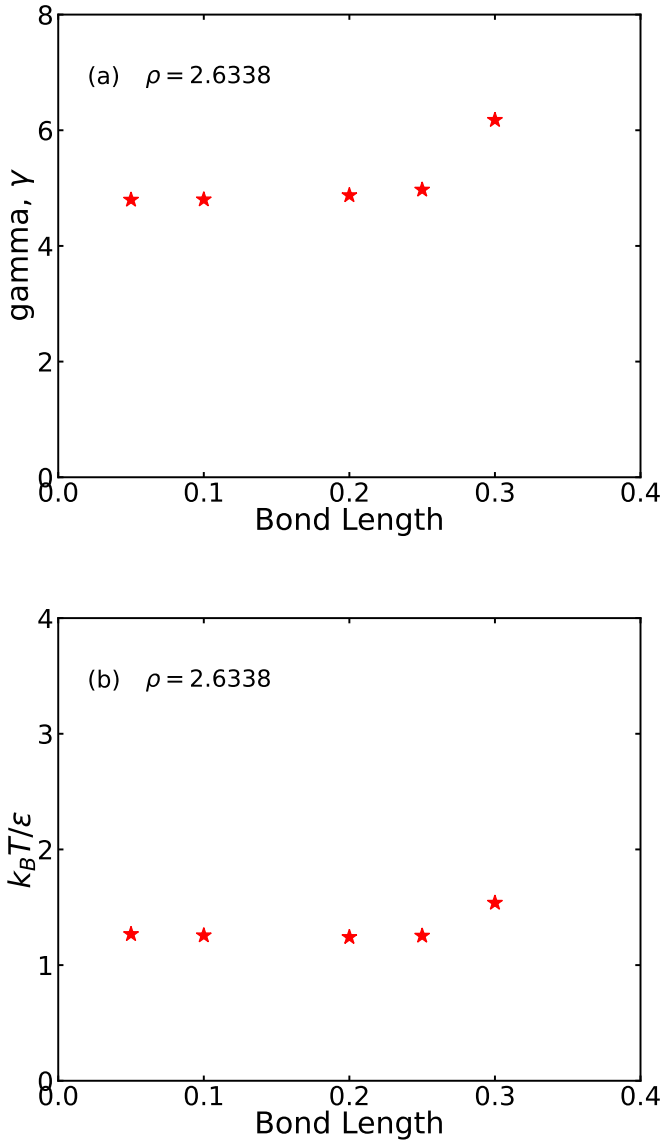


**Figure 5.28.** (a) The variation of the density scaling exponent  $\gamma$  at the final state point  $\rho = 2.634$  of each isomorph plotted as a function of the bond length (b) the temperature,  $T$  at the final state point  $\rho = 2.634$  of each isomorph plotted as a function of the bond length.

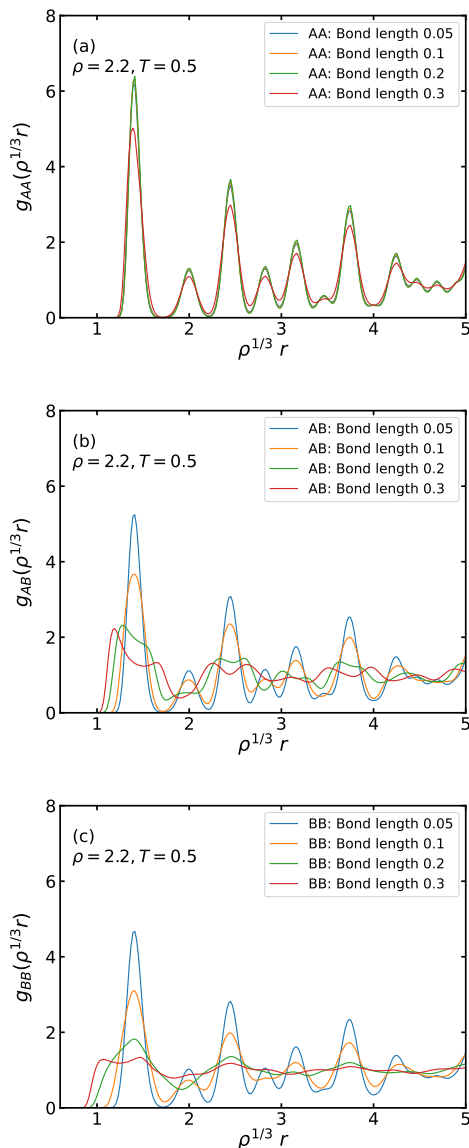


**Figure 5.29.** (a) The radial distribution functions  $g(r)_{AA}$  of the state point  $\rho = 2.2, T = 0.5$  of each isomorph with different bond lengths of 0.05, 0.1, 0.2, 0.3. (b) The radial distribution functions  $g(r)_{AB}$  of the state point  $\rho = 2.2, T = 0.5$  (c) The radial distribution functions  $g(r)_{BB}$  of the state point  $\rho = 2.2, T = 0.5$ .

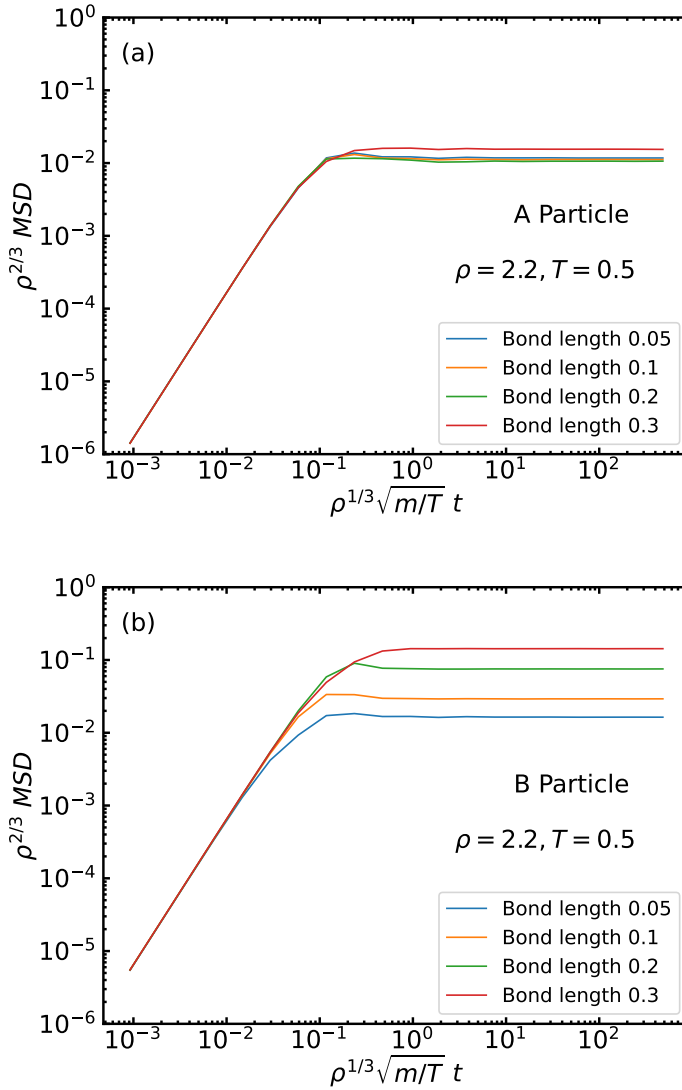


**Figure 5.30.** (a) The mean square displacement of particle A of the state point  $\rho = 2.2, T = 0.5$  of each isomorph with different bond lengths of 0.05, 0.1, 0.2, 0.3. (b) The mean square displacement of particle B of the state point  $\rho = 2.2, T = 0.5$ .

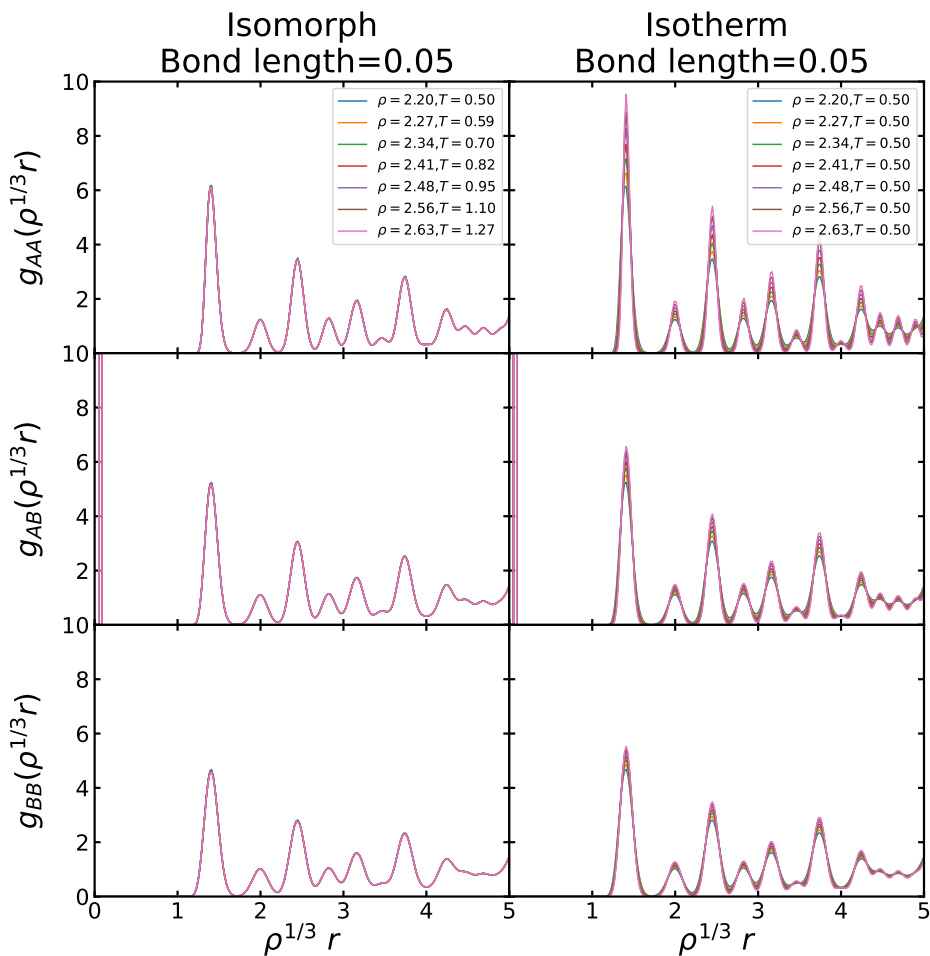


**Figure 5.31.** The AA, AB and BB radial distribution functions of isomorph of bond length 0.05 along with the isotherm of the same bond length 0.05 respectively. Invariance is seen along the isomorph.

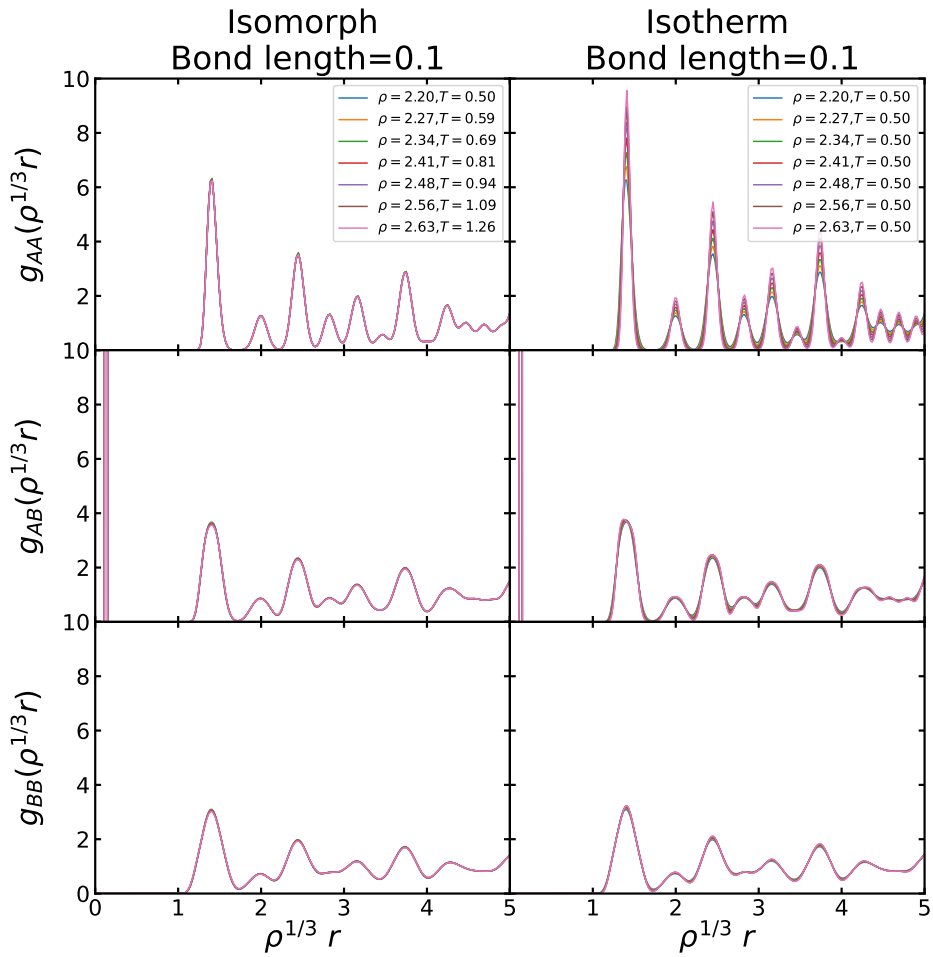


**Figure 5.32.** The AA, AB and BB radial distribution functions of isomorph of bond length 0.1 along with the isotherm of the same bond length 0.1 respectively. Invariance is seen along the isomorph.

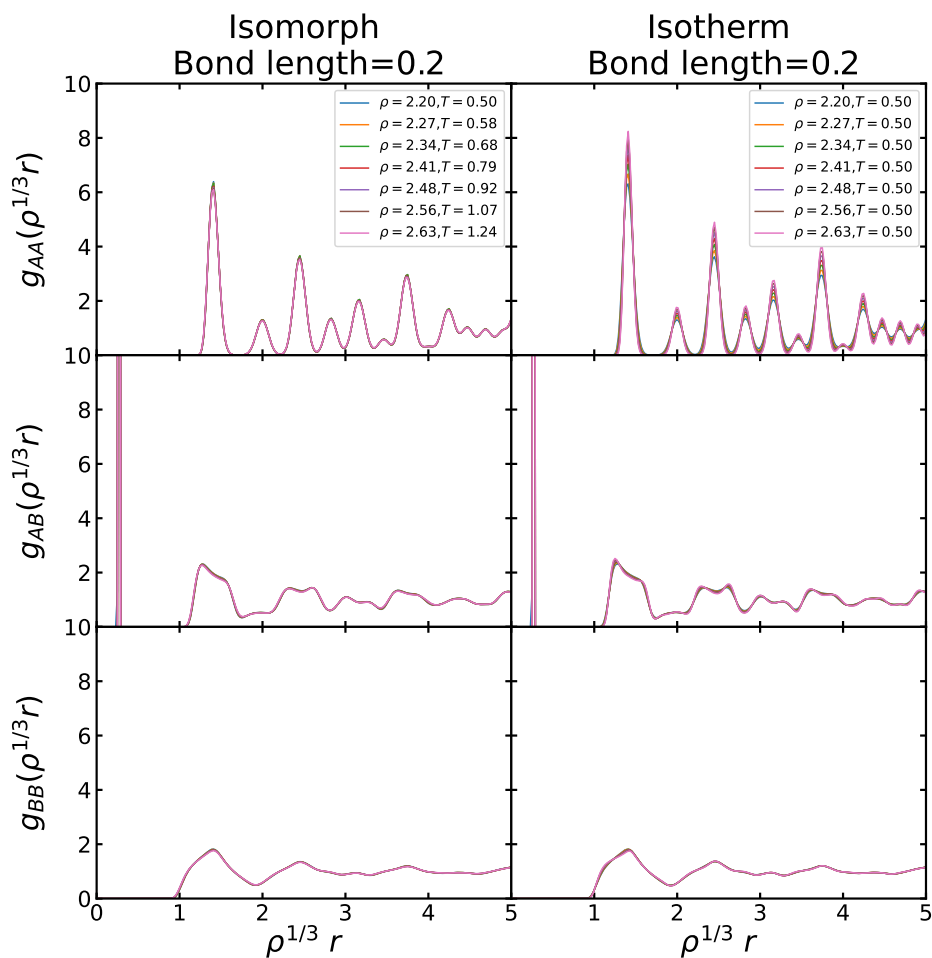


**Figure 5.33.** The AA, AB and BB radial distribution functions of isomorph of bond length 0.2 along with the isotherm of the same bond length 0.2 respectively. Invariance is seen along the isomorph.

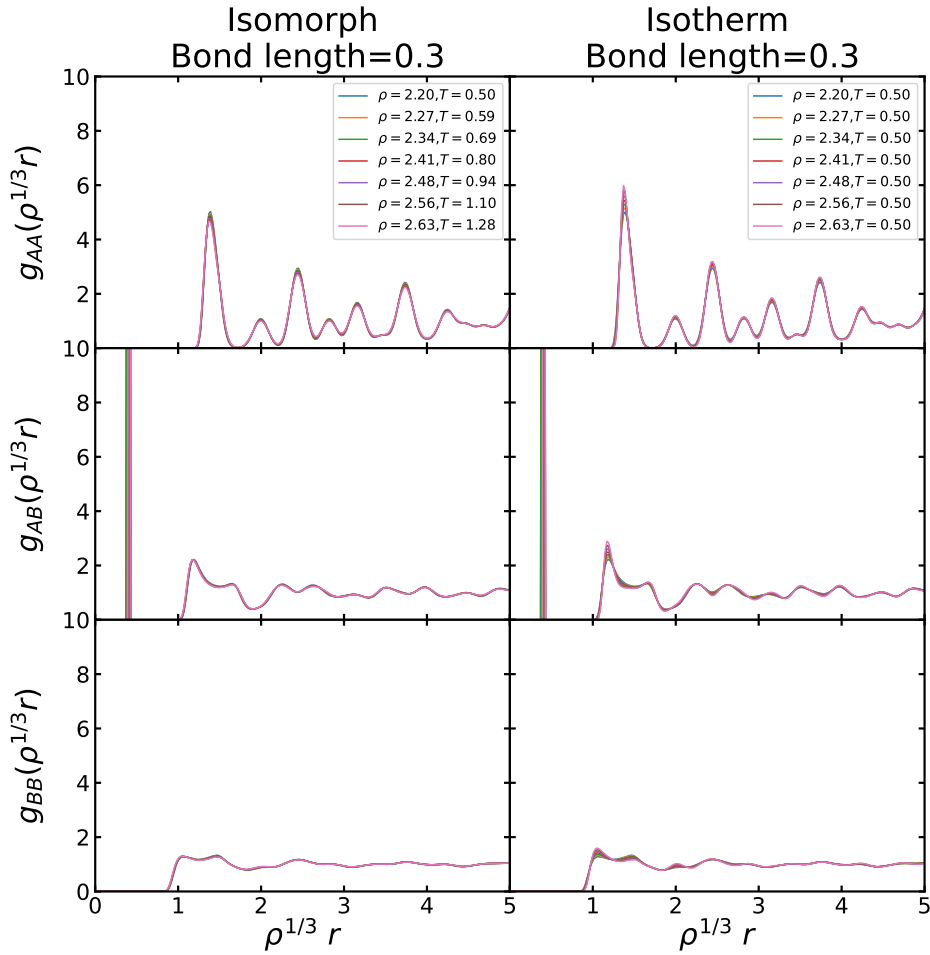


**Figure 5.34.** The AA, AB and BB radial distribution functions of isomorph of bond length 0.3 along with the isotherm of the same bond length 0.3 respectively. We can see the flattening of the first peak. Invariance is seen along the isomorph.

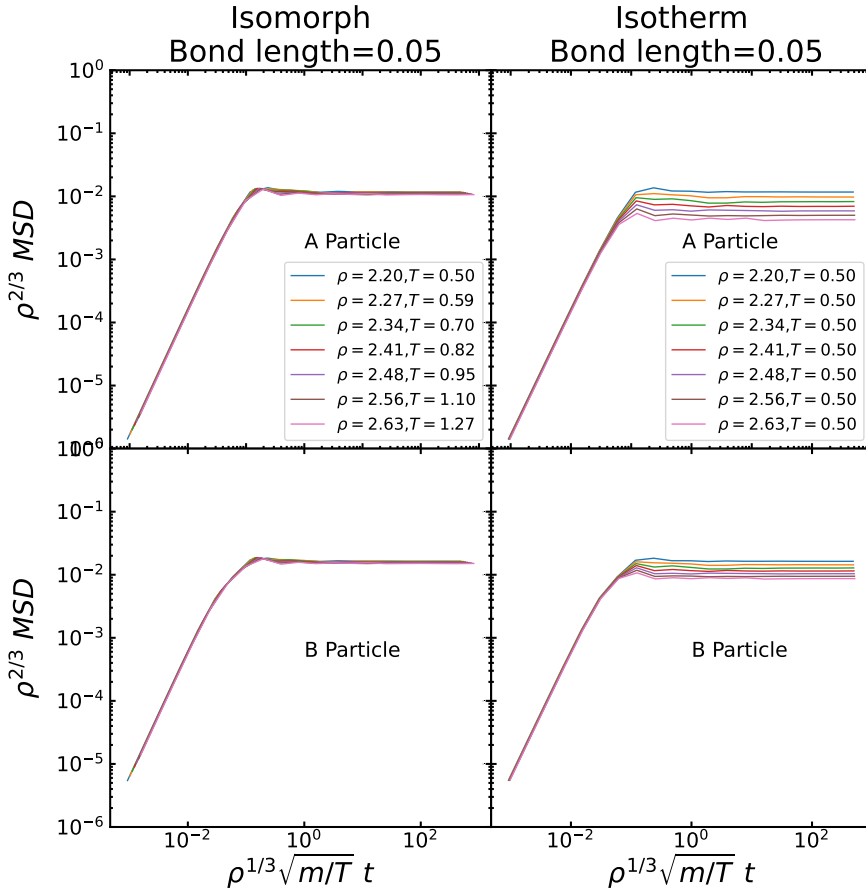


**Figure 5.35.** The A and B reduced mean square displacement along isomorph of bond length 0.05 and the isotherm of the same bond length 0.05 respectively. There is invariance along the isomorph in both A and B reduced mean square displacement unlike along the isotherm.

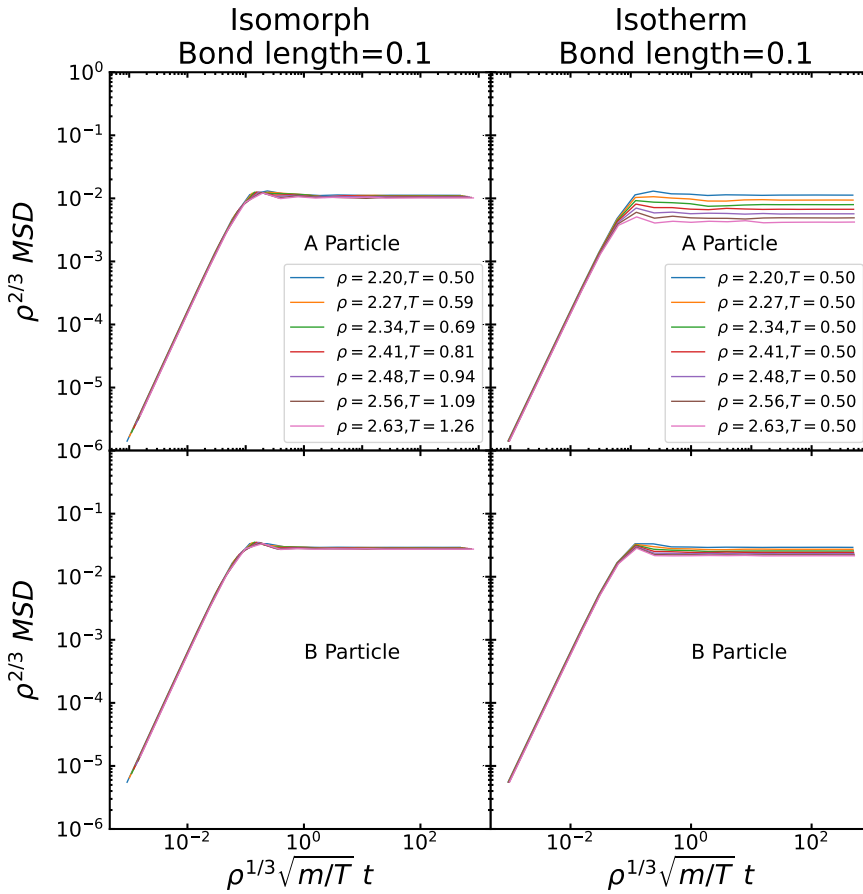


**Figure 5.36.** The A and B reduced mean square displacement along isomorph of bond length 0.1 and the isotherm of the same bond length 0.1 respectively. There is invariance along the isomorph in both A and B reduced mean square displacement unlike along the isotherm.

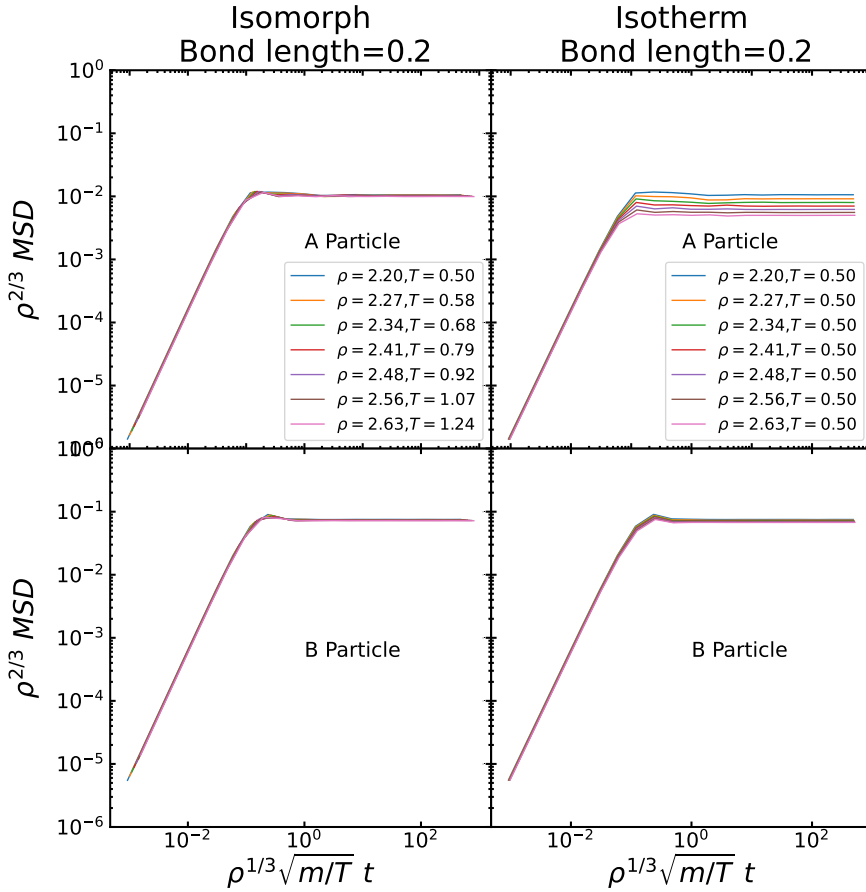


**Figure 5.37.** The A and B reduced mean square displacement along isomorph of bond length 0.2 and the isotherm of the same bond length 0.2 respectively. There is invariance along the isomorph in both A and B reduced mean square displacement better than along the isotherm.

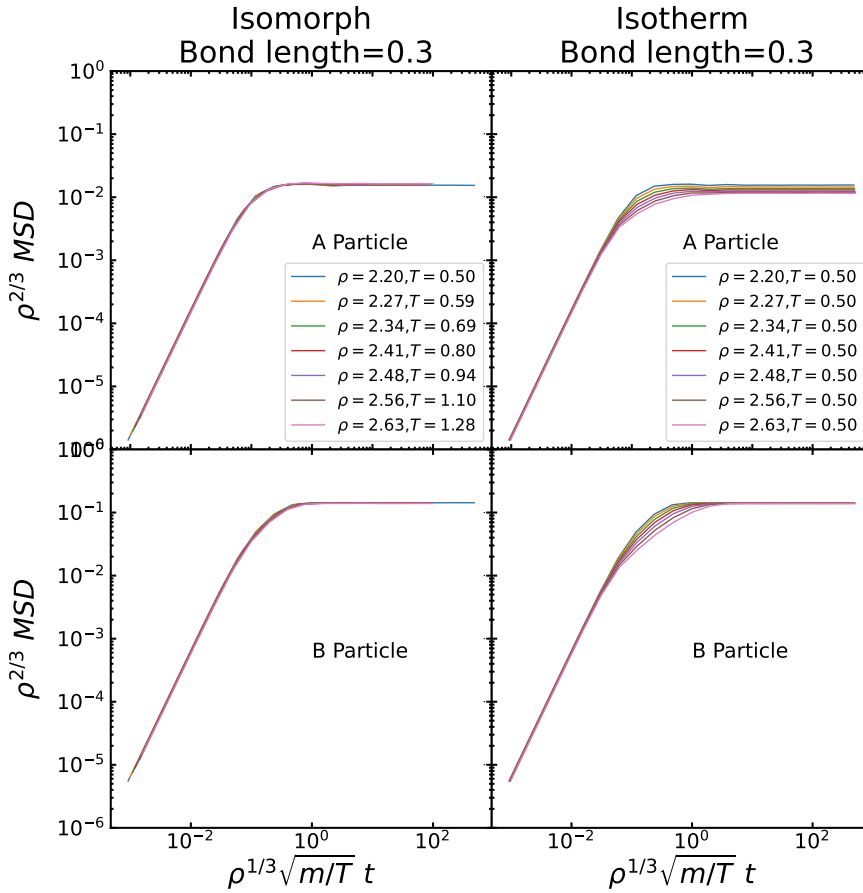


**Figure 5.38.** The A and B reduced mean square displacement along isomorph of bond length 0.3 and the isotherm of the same bond length 0.3 respectively. There is invariance along the isomorph in both A and B reduced mean square displacement unlike along the isotherm. For B particle MSD of the isotherm, the variation is mainly in the time of entering the long-time MSD plateau.

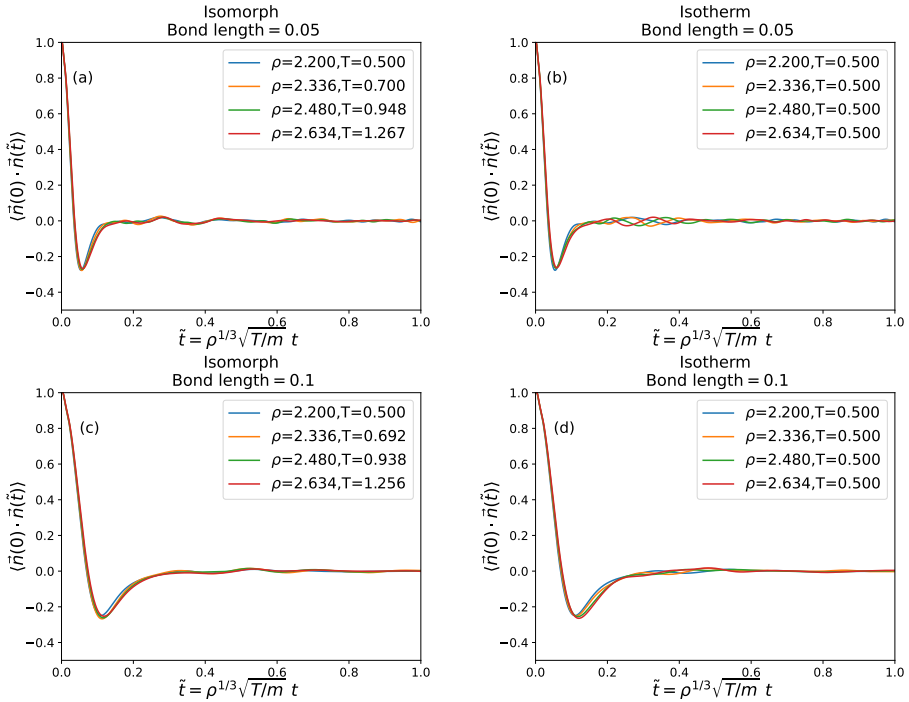


**Figure 5.39.** (a) The rotational auto-correlation of isomorph of bond length 0.05 and (b) of isotherm of bond length 0.05. A fast decay to zero is seen at time  $\tilde{t} \geq 0.1$ . (c) The rotational auto-correlation of isomorph of bond length 0.1 and (d) of isotherm of bond length 0.1. The decay starts to be a bit slower, at time  $\tilde{t} \geq 0.2$ .

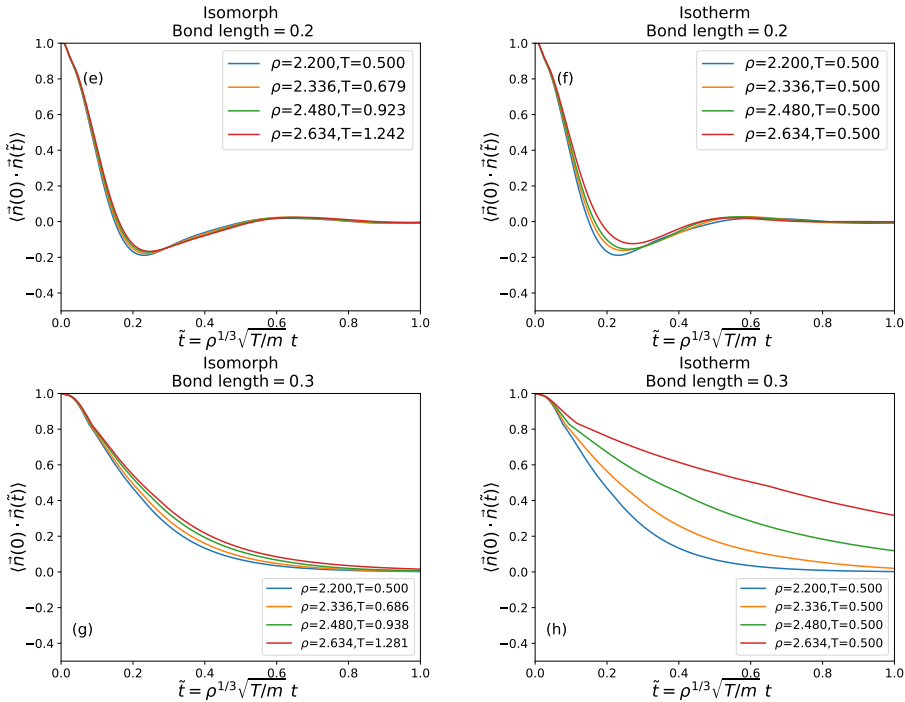


**Figure 5.40.** (e) The rotational auto-correlation of isomorph of bond length 0.2 and (f) of isotherm of bond length of 0.2. We can see decay around  $\tilde{t} \geq 0.4$  to zero. We still see damping below zero that indicates fast rotation. (g) The reduced rotational auto-correlation of isomorph of bond length 0.3 and (h) of isotherm of bond length 0.3. Here, the decay is slower. As the bond length is getting longer, the B particles rotate slower. In the isotherm, we see higher decoupling as the density increases with the fixed low temperature  $T = 0.5$  and the rotation starts to be hindered.

### 5.3.2.2 Transition: From Plastic-Crystalline State to Glassy State

As more density decoupling is seen along the isotherm of the longest bond 0.3, the state points at higher density along the same isotherm are investigated. Figure 5.41 shows the AA, AB, BB reduced radial distribution functions of the state points of density  $2.634 \geq \rho \geq 3.485$ . Temperature is fixed at  $T = 0.5$ . The A particles seem not have the same crystalline-behaviour, while the AB and BB RDFs show visible variations. As the density increases, it is clear from the BB reduced radial distribution function that, the structure gets towards a more restricted mobility state. The B particles have random arrangements at low-densities, but starts to have more preferred arrangements at high densities. This shift can be a glassy state transition. The mean square displacement of both particles A and B show the same finding. In Fig. 5.42, we can see that the long-time MSD gets lower and lower as the density increases. The rotation auto-correlation function also shows that in Fig. 5.43. Above  $\rho = 2.970$ , there is no decay or rotation, showing more restricted mobility or glassy state.

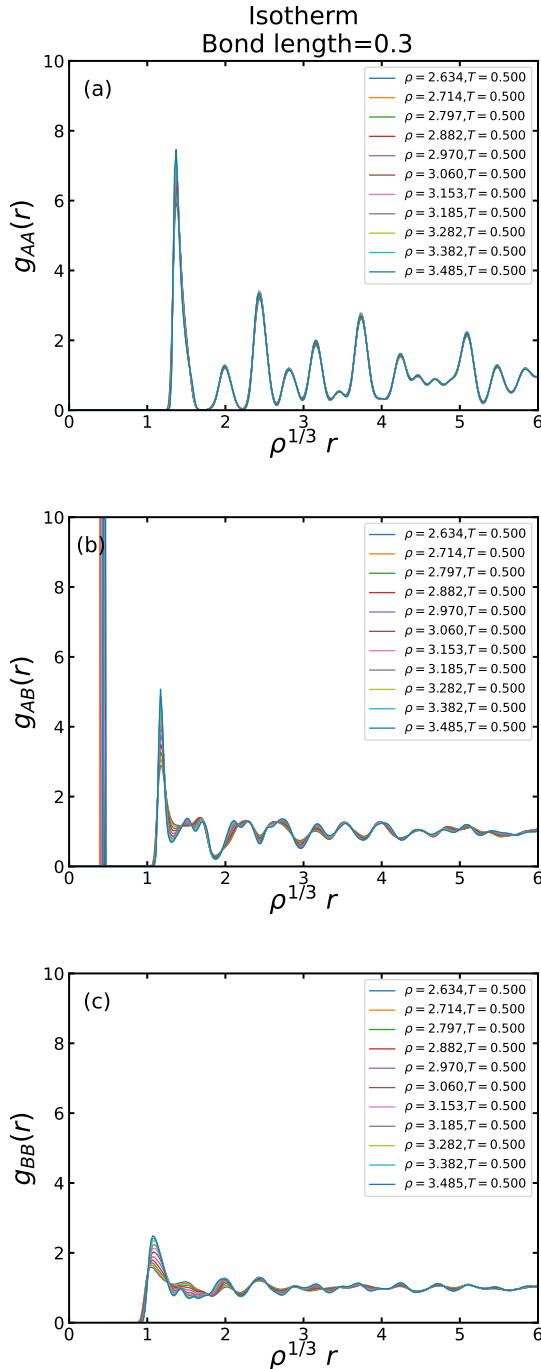


**Figure 5.41.** The AA, AB and BB radial distribution functions along higher density state points of the isotherm of bond length 0.3. The AB and BB RDFs show that B particles start to have more preferred arrangements at high densities. This shift can be seen as a glassy state transition.

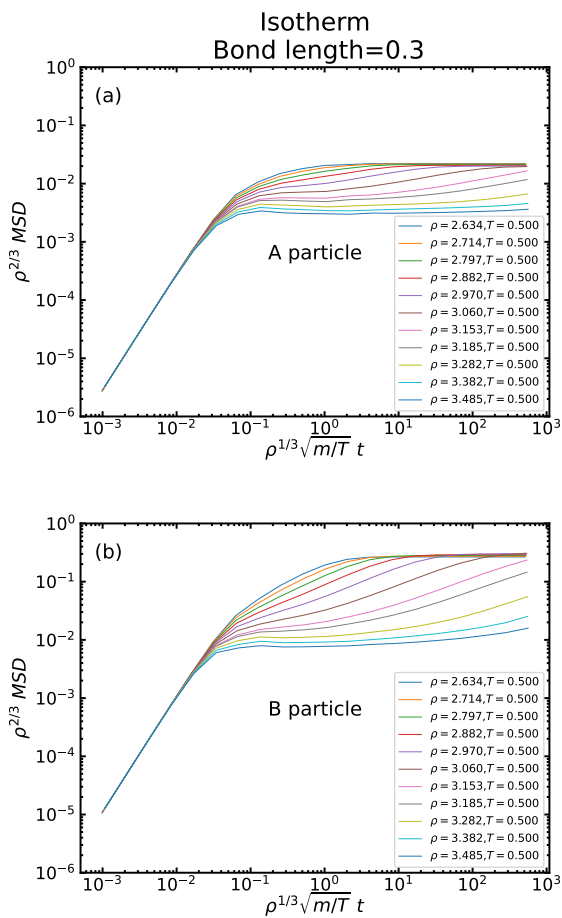


**Figure 5.42.** The A and B reduced mean square displacement along isotherm of bond length 0.3 at higher densities. We can observe the change to much lower movement which can indicate the transition to the glassy state.

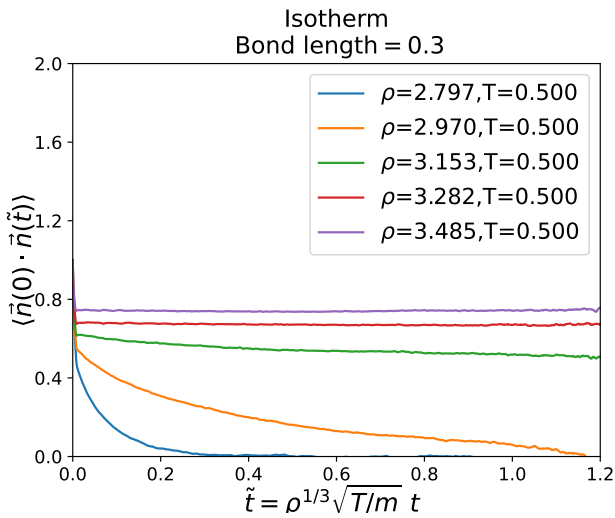


**Figure 5.43.** The rotational auto-correlation of higher density state points along the isotherm of bond length 0.3. At  $\rho = 2.797$ , We can see a slow decay  $\tilde{t} \approx 0.3$  in the function to zero. As the density is increasing with the same temperature  $T = 0.5$ , the movement of B particle is restricted and it can't rotate easier. We can see then a plateau and no decay of the rotational auto-correlation functions at  $\rho \geq 3.153$  which can indicate the transition to the glassy state.



# CHAPTER 6

## Conclusion

---

Coming to the end of this work, we conclude the following based on the data presented in Chapter 4 and 5. The investigation of the single-component Weeks-Chandler-Andersen (SCWCA) system and the symmetrical dumbbell (ASD) system shows that both systems exhibit hidden scale invariance. As a consequence, the isomorph theory applies in both systems. The SCWCA system is shown to be deviant from the IPL system. In fact, it is an R-simple liquid. For a single bond length, the ASD system has been shown previously by Ingebrigtsen *et al.* [19] to be an R-simple system in the viscous region. We show for a range of bond lengths that the liquid and the plastic-crystalline phases join as well. The ASD plastic crystals are the first application of Isomorph theory in plastic crystals.

The Weeks-Chandler-Andersen system is unlike any other Roskilde simple liquid. While R-simple systems follow density scaling in isomorph theory with density scaling exponents that range from 1-8 and often with relatively small variations throughout the phase diagram, something else interesting is observed in the WCA system. The density scaling exponent is shown to rapidly increase way above 8 in the low temperature/density region of the phase diagram. Along an isomorph, we have found a variation of more than a factor of hundred of the density-scaling exponent. We refer to this huge variation as "extreme density scaling." Moreover, the WCA shows high  $UW$  correlations with  $R > 0.9$  throughout the whole phase diagram. This makes it stand out from the rest of the Roskilde simple liquids in

which correlations are high only in some of the regions in the phase diagram. Invariance is observed in the structure and dynamics along the isomorphs in comparison to isotherms or isochores. The WCA system therefore obeys density scaling and shows an extreme density scaling in the low density/temperature region.

The asymmetrical dumbbell system is an R-simple liquid that exhibits hidden scale invariance in the viscous liquid region. We show that it exhibits hidden scale invariance as well in the less viscous-region for a range of bond lengths with relatively high  $UW$  correlations  $R > 0.85$ . It also exhibits the hidden scale invariance in the plastic-crystalline phase for a range of bond lengths with higher  $UW$  correlations  $R > 0.95$ . Since the criteria  $R > 0.90$  is arbitrary, we consider both regions to have strong correlations. Isomorphs are traced out in both of the regions in the phase diagram. Invariance is observed in the structure and dynamics along the isomorphs in comparison to the isotherms. We also investigated the limit of the bond-length variation in the liquid and the plastic-crystalline phase. At relatively small bonds i.e., 0.5, we have seen the A particles dominating the structure scene. As the bond length increases and the B particles place themselves in many possible positions around the A particles, A particles still dominate the scene. We introduce the "B slaving A" picture that is confirmed by the AA, AB and BB radial distribution functions along with the A and B particles mean square displacements of the ASD molecules.

We started the thesis with the liquid state and how it can be defined in terms of thermodynamics. As complex as the liquid state can be, a simple approach is always sought to understand its physics. The isomorph theory explores a class of systems with simple properties that can help navigate through this complexity. Expanding the class of R-simple systems is a step closer toward simplicity. We have achieved the research goal that we set for the thesis presented. The further research that can be conducted to build on this work is: to investigate

---

the hidden scale invariance in other plastic-crystal forming systems to expand the R-simple systems. Also, other techniques such as the *ab initio* calculations can be introduced to include more realistic view of the organic molecular systems i.e., ASD, OTP etc. to have a broader picture of the R-simplicity in such systems.



# Bibliography

---

- [1] N. P. Bailey, U. R. Pedersen, N. Gnan, T. B. Schröder, and J. C. Dyre, “Pressure-energy correlations in liquids. I. Results from computer simulations,” *J. Chem. Phys.*, vol. 129, p. 184507, 2008.
- [2] J. P. Hansen and I. R. McDonald, *Theory of Simple Liquids*. London: Academic Press, 1990.
- [3] P. Gallo and M. Rovere, *Physics of Liquid Matter*. Springer, 2021.
- [4] P. Flowers, K. Theopold, L. R. Richard, S. F. Austin, and W. R. Robinson, *Chemistry 2e*. OpenSTAX, 2019.
- [5] C. M. Roland, S. Hensel-Bielowka, M. Paluch, and R. Casalini, “Supercooled dynamics of glass-forming liquids and polymers under hydrostatic pressure,” *Rep. Prog. Phys.*, vol. 68, p. 1405–1478, 2005.
- [6] A. R. Kelly, D. A. Susan, and S. Cenkowski, *Polymer Science: Approach to Physico-Chemical Characterization and Processing of Pulse Seeds*. InTech, 2013.
- [7] R. Car and M. Parrinello, “Unified approach for molecular dynamics and density-functional theory,” *Phys. Rev. L*, vol. 55, no. 22, p. 2471, 1985.

- 
- [8] M. P. Allen and D. J. Tildesley, *Computer Simulation of Liquids*. Oxford University Press, USA, 1989.
- [9] W. G. Hoover, M. Ross, and K. W. Johnson, “Soft-sphere equation of state,” *J. Chem. Phys.*, vol. 52, no. 10, p. 4931, 1970.
- [10] J. C. Dyre, “Simple liquids’ quasiuniversality and the hard-sphere paradigm,” *J. Phys.: Condens. Matter*, vol. 28, p. 323001, 2016.
- [11] J. D. van der Waals, *Lehrbuch der Thermodynamik*. Salzwasser-Verlag GmbH, 2012.
- [12] J. D. Weeks, D. Chandler, and H. C. Andersen, “Role of repulsive forces in determining the equilibrium structure of simple liquids,” *J. Chem. Phys.*, vol. 54, no. 12, pp. 5237–5247, 1971.
- [13] L. Teich and C. Schröder, “Hybrid molecular and spin dynamics simulations for ensembles of magnetic nanoparticles for magnetoresistive systems,” *Sensors*, vol. 15, pp. 28826–28841, 2015.
- [14] M. Kröger, *Models for Polymeric and Anisotropic Liquids*. Springer, Berlin, 2005.
- [15] T. B. Schröder, N. Gnan, U. R. Pedersen, N. P. Bailey, and J. C. Dyre, “Pressure-energy correlations in liquids. V. Isomorphs in generalized Lennard-Jones systems,” *J. Chem. Phys.*, vol. 134, no. 16, p. 164505, 2011.
- [16] N. Gnan, T. B. Schröder, U. R. Pedersen, N. P. Bailey, and J. C. Dyre, “Pressure-energy correlations in liquids. IV. “Isomorphs” in liquid phase diagrams,” *J. Chem. Phys.*, vol. 131, no. 23, p. 234504, 2009.
- [17] A. A. Veldhorst, J. C. Dyre, and T. B. Schröder, “Isomorph scaling of flexible Lennard-Jones chain,” *J. Chem. Phys.*, vol. 141, p. 054904, 2013.

- [18] N. P. Bailey, U. R. Pedersen, N. Gnan, T. B. Schrøder, and J. C. Dyre, “Pressure-energy correlations in liquids. II. Analysis and consequences,” *J. Chem. Phys.*, vol. 129, no. 18, p. 184508, 2008.
- [19] T. S. Ingebrigtsen, T. B. Schrøder, and J. C. Dyre, “Isomorphs in model molecular liquids,” *J. Phys. Chem.*, vol. 116, pp. 1018–1034, 2021.
- [20] L. Friedehiem, J. C. Dyre, and N. P. Bailey, “Hidden scale invariance at high pressure in gold and five other face-centered-cubic metal crystals,” *Phys. Rev. E*, vol. 99, p. 022142, Feb 2019.
- [21] L. Berthier and G. Tarjus, “Nonperturbative effect of attractive forces in viscous liquids,” *Phys. Rev. Lett.*, vol. 103, p. 170601, 2009.
- [22] D. Henderson, J. A. Barker, and S. Kim, “Theory of liquid state,” *J. Quan. Chem.*, vol. 3, pp. 265–292, 1969.
- [23] W. Kob and H. C. Andersen, “Scaling behavior in the  $\beta$ -relaxation regime of a supercooled Lennard-Jones mixture,” *Phys. Rev. Lett.*, vol. 73, no. 10, pp. 1376–1379, 1994.
- [24] U. R. Pedersen, T. B. Schrøder, and J. C. Dyre, “Repulsive reference potential reproducing the dynamics of a liquid with attractions,” *Phys. Rev. L.*, vol. 105, p. 157801, 2010.
- [25] J. Copley, *The Fundamentals of Neutron Powder Diffraction*. US Government Printing Office, 2001.
- [26] J. T. Bosko, B. D. Todd, and R. J. Sadus, “Internal structure of dendrimers in the melt under shear: A molecular dynamics study,” *J. Chem. Phys.*, vol. 121, no. 1091, p. 1091, 2004.

- 
- [27] M. Kröger, “Simple models for complex non-equilibrium fluids,” *Phys. Rep.*, vol. 390, p. 453, 2004.
- [28] S. Kämmerer, W. Kob, and R. Schilling, “Dynamics of the rotational degrees of freedom in a supercooled liquid of diatomic molecules,” *Phys. Rev. E*, vol. 56, p. 5450, 1997.
- [29] R. Chopra, T. M. Truskett, and J. R. Errington, “Excess entropy scaling of dynamic quantities for fluids of dumbbell-shaped particles,” *J. Chem. Phys.*, vol. 133, p. 104506, 2010.
- [30] D. Fragiadakis and C. M. Roland, “Characteristics of the Johari-Goldstein process in rigid asymmetric molecules,” *Phys. Rev. E*, vol. 88, p. 042307, 2013.
- [31] U. R. Pedersen, T. Christensen, T. B. Schrøder, and J. C. Dyre, “Feasibility of a single-parameter description of equilibrium viscous liquid dynamics,” *Phys. Rev. E*, vol. 77, p. 011201, Jan 2008.
- [32] C. M. Roland, “Relaxation phenomena in vitrifying polymers and molecular liquids,” *Macromolecules*, vol. 43, p. 7875, 2010.
- [33] J. D. Ferry, *Viscoelastic Properties of Polymers*. Wiley, New York., 3rd ed., 1980.
- [34] G. S. Grest and M. H. Cohen, “Liquids, Glasses, and The Glass Transition: A Free-volume Approach,” *Adv. Chem. Phys.*, vol. 48, p. 455, 1981.
- [35] T. Miyamoto and K. J. Shibayama, “Free-volume model for ionic conductivity in polymers,” *J. Appl. Phys.*, vol. 44, p. 5372, 1973.
- [36] C. M. Roland, K. L. Ngai, P. G. Santangelo, X. H. Qiu, M. D. Ediger, and D. J. Plazek, “Macromolecules,” vol. 34, p. 6159, 2001.

- [37] R. N. Singh, S. Arafin, , p. George, A. K. Temperature-dependent thermo-elastic properties of s, and d-block liquid metal, “Temperature-dependent thermo-elastic properties of s-, p- and d-block liquid metals,” *Physica (Amsterdam)*, vol. 387B, p. 344, 2007.
- [38] T. B. Schrøder, N. P. Bailey, U. R. Pedersen, N. Gnan, and J. C. Dyre, “Pressure-energy correlations in liquids. III. Statistical mechanics and thermodynamics of liquids with hidden scale invariance,” *J. Chem. Phys.*, vol. 131, no. 23, p. 234503, 2009.
- [39] T. S. I. L. Bøhling, A. Grzybowski, M. Paluch, J. C. Dyre, and T. B. Schrøder, “Scaling of viscous dynamics in simple liquids: theory, simulation and experiment,” *New J. of Physics*, vol. am, p. 113035, 2012.
- [40] A. Sanz, T. Hecksher, H. Wase, J. C. Dyre, K. Niss, and U. R. Pedersen, “Experimental evidence for a state-point-dependent density-scaling exponent of liquid dynamics,” *Phys. Rev. L.*, vol. 122, p. 055501, 2019.
- [41] Y. Rosenfeld, “Relation between the transport coefficients and the internal entropy of simple systems,” *Phys. Rev. A*, vol. 15, pp. 2545–2549, Jun 1977.
- [42] Y. Rosenfeld, “A quasi-universal scaling law for atomic transport in simple fluids,” *J. Phys. Condens. Matter*, vol. 11, p. 5415, 1999.
- [43] N. Jakse and A. A. Pasturel, “Excess entropy scaling law for diffusivity in liquid metals,” *Sci. Rep.*, vol. 6, p. 20689, 2016.
- [44] J. C. Dyre, “Perspective: Excess-entropy scaling,” *J. Chem. Phys.*, vol. 149, no. 21, p. 210901, 2018.

- 
- [45] J. C. Dyre, “Hidden scale invariance in condensed matter,” *J. Phys. Chem. B*, vol. 118, p. 10007, 2014.
- [46] E. H. Abramson and H. West-Foyle, “Viscosity of Nitrogen Measured to Pressures of 7 GPa and Temperatures of 573 K,” *Phys. Rev. E*, vol. 77, p. 041202, 2008.
- [47] E. H. Abramson, “Viscosity of Methane to 6 GPa and 673 K,” *Phys. Rev. E*, vol. 84, p. 062201, 2011.
- [48] S. Prasad and C. Chakravarty, “Onset of simple liquid behaviour in modified water models,” *J. Chem. Phys.*, vol. 140, p. 164501, 2014.
- [49] M. Agarwal, M. Singh, R. Sharma, M. P. Alam, and C. Chakravarty, “Relationship between structure, entropy, and diffusivity in water and water-like liquids,” *J. Phys. Chem. B*, vol. 114, p. 6995–7001, 2010.
- [50] Y. D. Fomin, V. N. Ryzhov, and N. V. Gribova, “Breakdown of excess entropy scaling for systems with thermodynamic anomalies,” *Phys. Rev. E*, vol. 81, p. 061201, 2010.
- [51] R. Chopra, T. M. Truskett, and J. R. Errington, “On the use of excess entropy scaling to describe single-molecule and collective dynamic properties of hydrocarbon isomer fluids,” *J. Phys. Chem. B*, vol. 114, pp. 16487–16493, 2010.
- [52] M. J. Pond, J. R. Errington, and T. M. Truskett, “Generalizing Rosenfeld’s excess-entropy scaling to predict long-time diffusivity in dense fluids of brownian particles: From hard to ultrasoft interactions,” *J. Chem. Phys.*, vol. 134, p. 081101, 2011.
- [53] M. J. Pond, W. P. Krekelberg, V. K. Shen, J. R. Errington, and T. M. Truskett, “Composition and concentration anomalies

- for structure and dynamics of gaussian-core mixtures,” *J. Chem. Phys.*, vol. 131, p. 161101, 2009.
- [54] T. B. Schröder and J. C. Dyre, “Simplicity of condensed matter at its core: Generic definition of a Roskilde-simple system,” *J. Chem. Phys.*, vol. 141, no. 20, p. 204502, 2014.
- [55] U. R. Pedersen, N. P. Bailey, T. B. Schröder, and J. C. Dyre, “Strong pressure-energy correlations in van der waals liquids,” *Phys. Rev. E*, vol. 100, p. 015701, 2008.
- [56] D. E. Albrechtsen, A. E. Oslen, U. R. Pedersen, T. B. Schröder, and D. J. C., “Isomorph invariance of the structure and dynamics of classical crystals,” *Phys. Rev. B*, vol. 90, p. 094106, 2014.
- [57] N. P. Bailey, L. Bøhling, A. A. Veldhorst, T. B. Schröder, and J. C. Dyre, “Statistical mechanics of Roskilde liquids: Configurational adiabats, specific heat contours, and density dependence of the scaling exponent,” *J. Chem. Phys.*, vol. 139, no. 18, p. 184506, 2013.
- [58] E. Attia, J. C. Dyre, and U. R. Pedersen, “Extreme case of density scaling: The Weeks-Chandler-Andersen system at low temperatures,” *Phys. Rev.*, vol. 00, p. 002100, 2021.
- [59] D. Frenkel and B. Smit, *Understanding Molecular Simulations: from Algorithms to Applications*. Academic Press, second ed., 2001.
- [60] L. Verlet, “Computer experiments on classical fluids. i. thermodynamical properties of lennard-jones molecules,” *Phys. Rev.*, vol. 98, pp. 98–103, 1967.

- [61] S. Nosé, “A unified formulation of the constant temperature molecular dynamics methods,” *J. Chem. Phys.*, vol. 81, pp. 511–519, 1984.
- [62] S. Nosé, “A molecular dynamics method for simulations in the canonical ensemble,” *Mol. Phys.*, vol. 52, pp. 255–268, 1984.
- [63] W. G. Hoover, “Canonical dynamics: Equilibrium phase space distributions,” *Phys. Rev. A*, vol. 31, p. 1695, 1985.
- [64] A. P. Thompson, H. M. Aktulga, R. Berger, D. S. Bolintineanu, W. M. Brown, P. S. Crozier, P. J. in 't Veld, A. Kohlmeyer, S. G. Moore, T. D. Nguyen, R. Shan, M. J. Stevens, J. Tranchida, C. Trott, and S. J. Plimpton, “LAMMPS - a flexible simulation tool for particle-based materials modeling at the atomic, meso, and continuum scales,” *Comp. Phys. Comm.*, vol. 271, p. 10817., 2022.
- [65] N. Bailey, T. Ingebrigtsen, J. H., A. Veldhorst, L. Bøhling, C. Lemarchand, A. Olsen, A. Bacher, L. Costigliola, U. Pedersen, H. Larsen, J. Dyre, and T. Schrøder, “Rumd: A general purpose molecular dynamics package optimized to utilize GPU hardware down to a few thousand particles,” *SciPost Phys.*, vol. 3, 12 2017.
- [66] CUDA, “Website, <http://www.nvidia.com/object/cuda>,” *URL Link*.
- [67] A. D. de Kuijper, J. A. Scouten, and J. P. J. Michels, “The melting line of the Weeks–Chandler–Anderson Lennard-Jones reference system,” *J. Chem. Phys.*, vol. 93, pp. 3515–3519, 1990.
- [68] A. Ahmed and R. Sadus, “Phase diagram of the Weeks-Chandler-Andersen potential from very low to high temperatures and pressures,” *Phys. Rev. E, Statistical, nonlinear, and soft matter physics*, vol. 80, p. 061101, 12 2009.

- [69] A. Mirzaeinia, F. Feyzi, and S. M. Hashemianzadeh, “Equation of state and Helmholtz free energy for the atomic system of the repulsive Lennard-Jones particles,” *J. Chem. Phys.*, vol. 147, p. 214503, 2017.
- [70] E. Attia, J. C. Dyre, and U. R. Pedersen, “Comparing four hard-sphere approximations for the low-temperature wca melting line,” *J. Chem. Phys.*, vol. 157, p. 034502, 2022.
- [71] C. N. Lam, C. D., M. Wang, W. R. Chen, and B. D. Olsne, “The shape of protein–polymer conjugates in dilute solution,” *J. Poly. Chem.*, vol. 54, pp. 292–302, November 2015.
- [72] R. Casalini and T. C. Ransom, “On the pressure dependence of the thermodynamical scaling exponent  $\gamma$ ,” *Soft Matter*, vol. 16, p. 4625, 2020.
- [73] A. K. Bacher, T. B. Schrøder, and J. C. Dyre, “The EXP pair-potential system. I. Fluid phase isotherms, isochores, and quasiuniversality,” *J. Chem. Phys.*, vol. 149, p. 114501, 2019.
- [74] A. K. Bacher, T. B. Schrøder, and J. C. Dyre, “The EXP pair-potential system. II. Fluid phase isomorphs,” *J. Chem. Phys.*, vol. 149, p. 114502, 2018.
- [75] M. T. and J. Kurchan, “Approximate scale invariance in particle systems: A large-dimensional justification,” *EPL*, vol. 114, p. 60002, 2016.
- [76] T. Maimbourg, J. C. Dyre, and L. Costigliola, “Density scaling of generalized Lennard-Jones fluids in different dimensions,” *SciPost Phys.*, vol. 9, p. 90, 2020.
- [77] Z. Sheydaafar, *Predicting scaling properties of fluids from individual configurations: Pseudoisomorphs*. PhD thesis, May 2021.

- 
- [78] T. L. Castello and P. Toliás, “Small step method (general),” *Personal Communication*.
- [79] H. P. William, S. A. Teukolsky, W. T. Vetterling, and B. P. Flannery, *Numerical Recipes 3rd Edition: The Art of Scientific Computing*. Cambridge University Press, 3 ed., 2007.
- [80] J. K. Johnson, J. A. Zollweg, and K. E. Gubbins, “The Lennard-Jones equation of state revisited,” *Mol. Phys.*, vol. 78, no. 3, pp. 591–618, 1993.
- [81] I. Kolafa, J. Nezbeda, “The Lennard-Jones fluid: an accurate analytic and theoretically-based equation of state,” *Fluid Phase Equilib*, vol. 100, no. 1, pp. 1–36, 1994.
- [82] M. Mecke, A. Müller, J. Winkelmann, J. Vrabec, J. Fischer, R. Span, and W. Wagner, “An accurate Van der Waals-type equation of state for the Lennard-jones Fluid,” vol. 17, pp. 391–404, 01 1996.
- [83] M. Gottschalk, “An EOS for the Lennard-Jones fluid: A virial expansion approach,” *AIP Advances*, vol. 9, no. 12, p. 125206, 2019.
- [84] M. Thol, G. Rutkai, A. Köster, R. Lustig, R. Span, and J. Vrabec, “Equation of state for the Lennard-Jones fluid,” *J. Phys. and Chem. Ref. Data*, vol. 45, no. 2, p. 023101, 2016.

# Appendices



# APPENDIX A

## Fourth-Order Runge Kutta Method: Tracing Better Isomorphs

---

The density scaling exponent  $\gamma$  is the slope of the lines of constant  $S_{ex}$  in the  $(\ln T, \ln \rho)$  plane which are isomorphs for any Roskilde simple system. The density scaling exponent  $\gamma$  as we have shown before in chapter two is required for the integration can be calculated from the thermal equilibrium virial potential-energy fluctuations in an  $NVT$  simulation

$$\gamma(\rho, S_{ex}) = \frac{\langle \Delta W \Delta U \rangle}{\langle (\Delta U)^2 \rangle} = \left( \frac{\partial \ln T}{\partial \ln \rho} \right)_{S_{ex}} \quad (\text{A.1})$$

In the following, we denote the *theoretical slope* by  $f$ , i.e., the slope without the unavoidable statistical noise of any MD simulation. Let  $(x, y)$  be  $(\ln \rho, \ln T)$  (occasionally it is better to choose instead  $(x, y) = (\ln T, \ln \rho)$ ). Then, accordingly let

$$\frac{dy}{dx} = f(x, y) \quad (\text{A.2})$$

be the slopes  $\gamma$  and  $\frac{T}{\rho}\gamma$ .  $h$  is the change in  $x$ , where  $x$  and  $y$  are either  $\ln \rho$  and  $\ln T$  or  $\rho$  and  $T$ . Using the general formula for Euler method, the next point from  $(x_i, y_i)$  as

$$x_{i+1} = x_i + h \quad (\text{A.3})$$

$$y_{i+1} = y_i + hf(x_i, y_i) + O(h^2) \quad (\text{A.4})$$

The RK4 method requires four evaluations per integration step. Let

$$k_1 = hf(x_i, y_i) \quad (\text{A.5})$$

$$k_2 = hf(x_i + \frac{1}{2}h, y_i + \frac{1}{2}k_1) \quad (\text{A.6})$$

$$k_3 = hf(x_i + \frac{1}{2}h, y_i + \frac{1}{2}k_2) \quad (\text{A.7})$$

$$k_4 = hf(x_i + h, y_i + k_3) \quad (\text{A.8})$$

Then,  $(x_{i+1}, y_{i+1})$  is computed as

$$x_{i+1} = x_i + h \quad (\text{A.9})$$

$$y_{i+1} = y_i + k_1/6 + k_2/3 + k_3/3 + k_4/6 + O(h^5) \quad (\text{A.10})$$

In case of configurational adiabats such that, slope =  $\gamma$ ,  $x = \ln \rho$  and,  $y = \ln T$ , the RK4 step can also be written as

$$y_{i+1} = y_i a^{(\gamma_1 + 2\gamma_2 + 2\gamma_3 + \gamma_4)/6} \quad (\text{A.11})$$

with  $\gamma_1 = \gamma(x_i, y_i)$ ,  $\gamma_2 = \gamma(x_i\sqrt{a}, y_ia^{\gamma_1/2})$ ,  $\gamma_3 = \gamma(x_i\sqrt{a}, y_ia^{\gamma_2/2})$  and  $\gamma_4 = \gamma(x_ia, y_ia^{\gamma_3})$  where  $a$  is a fixed ratio  $a = x_{i+1}/x_i$  [78]. In Euler, the error term is  $O(h^2)$ , while RK4 method reduces the error to  $O(h^5)$  [79]. In addition to this truncation error, the quality of the integration also depend on the statistical error on the estimated slopes. The interpolation between the state points is done with a cubic Hermite spline as follows. We define  $x_\phi$  as a point between the two adjacent points  $x_i, x_{i+1}$  such that  $x_i \leq x_\phi < x_{i+1}$  and  $0 \leq \phi \leq 1$  is between 0 and 1. We interpolate by fitting a third degree polynomial  $y = Ax_\phi^3 + Bx_\phi^2 + Cx_\phi + D$ . By introducing reduced coordinates,  $\tilde{y} = [y - y_i]/[y_{i+1} - y_i]$ , the polynomial of the reduced coordinates is  $\tilde{y}_\phi = a\phi^3 + b\phi^2 + c\phi$ . Then the  $y_\phi$  equals

$$y_\phi = y_i + [y_{i+1} - y_i][a\phi^3 + b\phi^2 + c\phi] \quad (\text{A.12})$$

The reduced slopes are  $\tilde{f}_i = f_i \frac{x_{i+1} - x_i}{y_{i+1} - y_i}$  and  $\tilde{f}_{i+1} = f_{i+1} \frac{x_{i+1} - x_i}{y_{i+1} - y_i}$ ,  $\tilde{f}_i, \tilde{f}_{i+1}$  are the slopes at  $x_i, x_{i+1}$  respectively. The coefficients are then  $a = \tilde{f}_i + \tilde{f}_{i+1} - 2$ ,  $b = 3 - 2\tilde{f}_i - \tilde{f}_{i+1}$  and  $c = \tilde{f}_i$ . While the simple Euler method has a truncation error scaling as  $O(h^2)$ , the truncation error of RK4 scales as  $O(h^5)$ . This allows for significantly larger steps along  $x$  and thus smaller number of steps.

To compare the Euler and RK4 methods, we use each method to integrate a configurational adiabat from the same state point  $\rho = 0.84$  and  $T = 0.694$ , up to density  $\rho = 1.30$ . The final temperature at the highest density reached is recorded. Then, we integrate backward till  $\rho = 0.84$  as seen in Fig. A.1 The difference in temperature from the two integration at the initial state point is calculated and denoted, temperature error,  $\Delta T$ . This quantity provides a convenient accuracy test of the two methods because if the method is 100% accurate,  $\Delta T = 0$ . Comparing the logarithmic attempts individually, it is clearly shown that the RK4 method gives smaller temperature error,  $\Delta T$ , compared to Euler (Fig. A.2). The change in density or the step size  $h$  is 0.1 for

Euler and 0.4 for RK4 which counts for the same simulation time. As a further investigation of the error on the RK4 method, we take the full step  $h$  as two half steps  $h/2$ . The truncation error is then raised to the sixth order, one order higher than RK4. Figure A.3 shows the difference between the total error as a function of the logarithmic difference in the temperature from using full step  $h = 0.4$  and the two half steps  $h = 0.2$  ( $\log T_{0.2} - \log T_{0.4}$ ) at different simulation time steps. Comparing the total error of the two methods indicates the accuracy of RK4 as the two methods converges to an error of  $10^{-2}$  due to the truncation of higher order terms. At smaller simulation time steps, the statistical error dominates and the data are scattered. When the simulation time increases, the truncation error is dominating and the statistical error decreases. The truncation error can be reduced by making  $h$  smaller. When the user chooses the simulation time that is long enough to minimize the statistical error, the RK4 has comparable truncation error to double step RK at each step size. Expensive longer simulations and extra calculations of higher order methods can be avoided by choosing the small  $h$  and long simulation time. To confirm that the state points are on adiabats or configurational adiabat, the equation of state (EOS) of the LJ fluid is used as a reference. Several functional forms of the EOS for the Lennard Jones fluid system can be found in literature [80–83]. Here we use the one formulated by Thol *et al.* [84]. Helmholtz energy  $\alpha$  consists of 6 polynomial, 6 exponential, and, 11 Gaussian bell-shaped terms. Thermodynamic properties can be calculated and its derivatives. The excess entropy of each state point then is calculated and plotted against the state point's density (Fig. A.4). The state points of the configurational adiabat are produced by RK4,  $h = 0.04$  which yields sufficient number of state points to demonstrate the consistency of the excess entropy values obtained. As shown in Fig. A.4, the excess entropy values are almost constant, indicating that the two approaches of computing configurational adiabats are consistent. The average was then calculated of all the excess

entropy values,  $(S_{ex})_{avg} = -3.610$  and the deviation from the average is shown in Fig. A.4. The agreement with the configurational adiabat of this EOS is excellent.

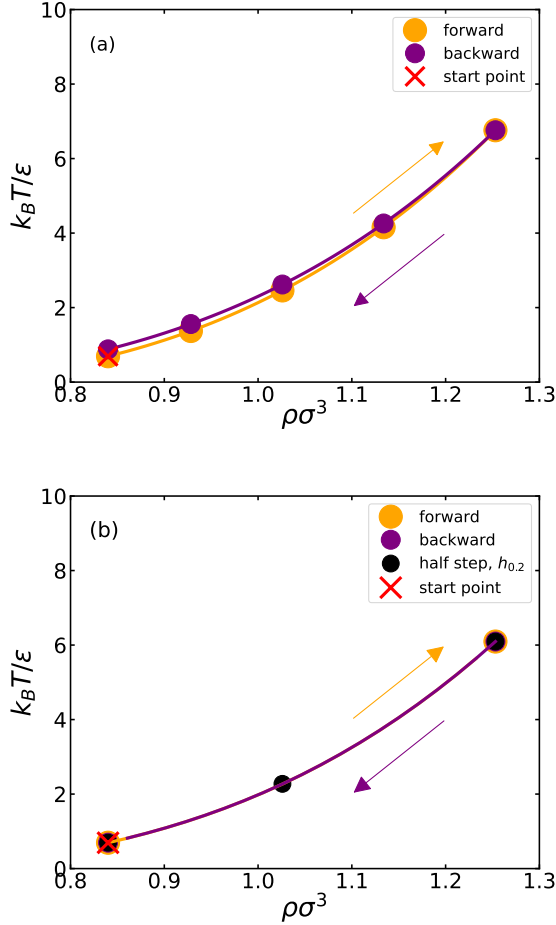


**Figure A.1.** Configurational adiabat of the WCA system traced out in the thermodynamic phase diagram. (a) The Euler method; (b) the RK4 method. The Euler integration uses a log-density step of size  $h = 0.1$  (steps in density of  $e^{0.1} - 1 \simeq 10\%$ ), while the RK4 uses  $h = 0.4$ , corresponding to density variation of  $e^{0.4} - 1 \simeq 50\%$ . The temperature difference of the here presented combined forward-backwards integration  $\Delta T$  provides a convenient measure of the maximum error of the predicted temperature. We find  $\Delta T \simeq 0.186$  for the Euler algorithm and  $\Delta T \simeq 0.002$  for the RK4 algorithm. The solid lines are interpolations using a cubic Hermite spline.

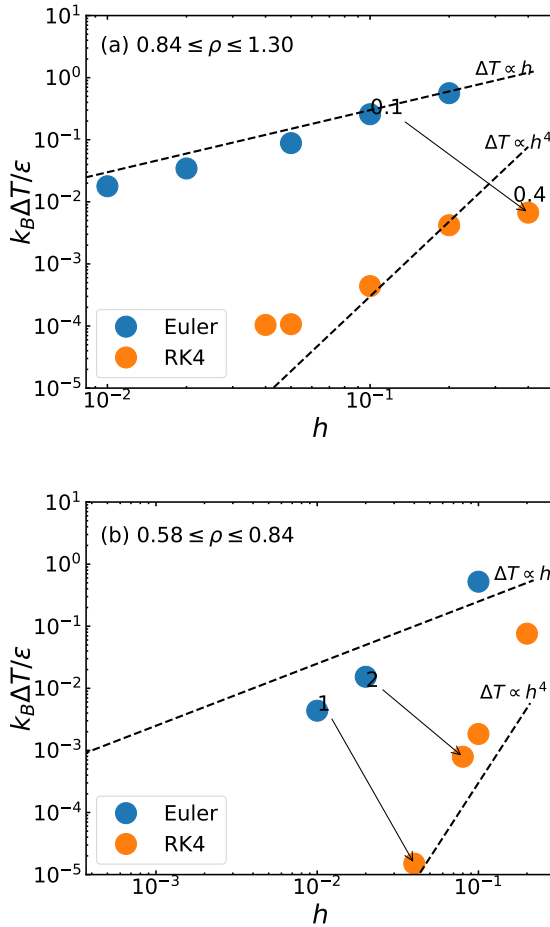


**Figure A.2.** (a) The temperature difference  $\Delta T$  of the forward-backward integration in Fig. A.1, for different steps sizes  $h$ . The blue dots show results for Euler integration and the orange dots show results for RK4 integration. The temperature difference measures the maximum error in the integration interval  $0.84 \leq \rho \leq 1.30$ . The RK4 is significantly more accurate than the Euler algorithm, which allows for larger  $h$  steps. The dashed lines indicate the expected scaling of the global error from truncation – deviations stem from statistical errors on the estimated slopes (slopes are evaluated using simulations lengths of  $\tau = 655$ ). The arrow connects Euler and RK4 calculations with approximately the same computational cost (see Fig. A1). (b) Same analysis for the integration interval  $0.58 \leq \rho \leq 0.84$ .

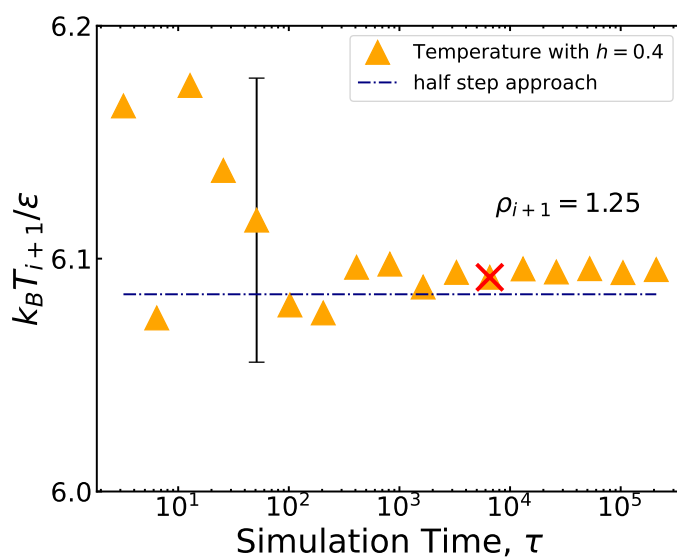


**Figure A.3.** The difference in temperature between using a full step of  $h = 0.4$  and two half steps of  $h = 0.2$  when integrating from  $\rho = 0.84$  up to  $\rho = 1.25$ , plotted against the simulation time per slope evaluation. The desired  $h$  can change and the simulation time changes accordingly. The red  $\times$  marks the simulation time used in the paper.

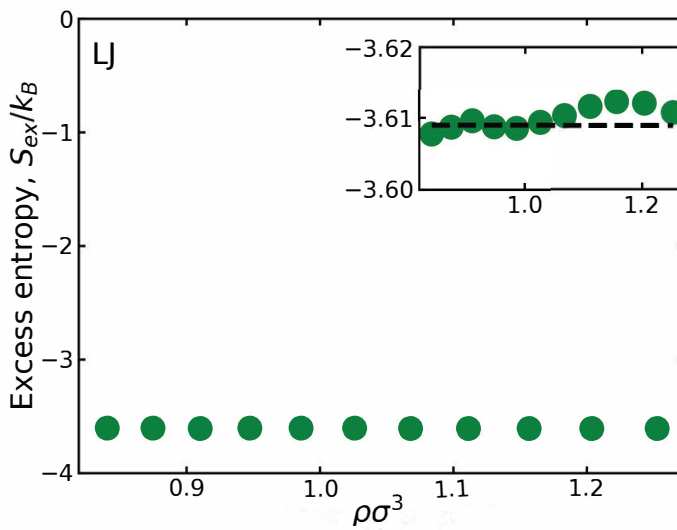


**Figure A.4.** The excess entropy values plotted against the densities of the state points on the configurational adiabat traced out for the single-component LJ system starting from the triple point ( $\rho = 0.84$ ,  $T = 0.694$ ) using RK4 with  $h = 0.04$ . The values are zoomed in to see the deviation from the average value, the black dotted line.



# APPENDIX B

## Data Analysis Tools for LAMMPS: Useful Home-made Scripts

---

```
1 #The first two functions are to extract data from the data
2 #files using LAMMPS package (Recall chapter 3 in simulated
3 #systems).
4 #If the user is using file format, the first two functions
5 #should be altered accordingly.
6
7 !/usr/bin/env python3
8
9 import numpy as np
10 import matplotlib.pyplot as plt
11 import numba
12 from math import floor
13 from numpy import sqrt, pi, histogram
14
15 #Function 1
16 def find_index_of_column(columns, name_of_column):
17     for i, name in enumerate(columns):
18         if name == name_of_column:
19             return i
20     return None
```

```
21 #Function 2
22 def read_data(filename):
23     number_of_atoms = 0
24     box_length = np.array([1.0, 1.0, 1.0], dtype=np.float32)
25     frames = []
26     with open(filename) as file:
27         l = file.readline()
28         while l:
29             spl = l.split(':')
30             sp = l.split()
31             if spl[0] == 'ITEM' and len(spl) > 1:
32                 if spl[1] == 'NUMBER OF ATOMS\n':
33                     l = file.readline()
34                     number_of_atoms = int(l)
35             if spl[1] == 'BOX BOUNDS pp pp pp\n':
36                 for i in range(3):
37                     l = file.readline().split()
38                     lbox = float(l[1]) - float(l[0])
39                     box_length[i] = lbox
40             if sp[1] == 'ATOMS':
41                 columns = sp[2:]
42                 data = np.zeros((number_of_atoms, len(columns)),
43                                 dtype=float)
44                 for n in range(number_of_atoms):
45                     l = file.readline().split()
46                     for c in range(len(columns)):
47                         data[n, c] = float(l[c])
48             id_index = find_index_of_column(columns, 'id')
49             data = data[np.argsort(data[:, id_index])]
50             frames.append(data)
51             l = file.readline()
52     return columns, np.array(frames), box_length,
        number_of_atoms
```

## B.1 Calculations of the Mean Square Displacement (MSD)

```
1 @numba.jit(parallel=True)
2 def get_msd(columns, frames,
3     number_of_atoms, box_length, rho, max_lag=np.inf, stride
4     =1):
5     id_xs = columns[0]
6     id_ys = columns[1]
7     id_zs = columns[2]
8     id_ix = columns[3]
9     id_iy = columns[4]
10    id_iz = columns[5]
11    lx = box_length[0]
12    ly = box_length[1]
13    lz = box_length[2]
14    msd = np.zeros(len(frames)-1, dtype=np.float32)
15    norm = np.zeros(len(frames)-1, dtype=np.int32)
16    max_lag = min(len(frames)-1, max_lag)
17    print(max_lag)
18    for lag in range(1, max_lag):
19        for f0 in range(0, len(frames)-lag, stride):
20            f1 = f0+lag
21            data_0 = frames[f0]
22            data_1 = frames[f1]
23            for n in range(len(data_0)):
24                xs_0 = data_0[n, id_xs]
25                ys_0 = data_0[n, id_ys]
26                zs_0 = data_0[n, id_zs]
27                #print (f' xs_0 is {xs_0}')
28                ix_0 = data_0[n, id_ix]
29                iy_0 = data_0[n, id_iy]
30                iz_0 = data_0[n, id_iz]
31                xs_1 = data_1[n, id_xs]
```

```
32     ys_1 = data_1[n, id_ys]
33     zs_1 = data_1[n, id_zs]
34
35     iy_1 = data_1[n, id_iy]
36     ix_1 = data_1[n, id_ix]
37     iz_1 = data_1[n, id_iz]
38
39     new_x_0 = lx*(xs_0 + ix_0)
40     #print (new_x_0, (xs_0 - ix_0) )
41     new_y_0 = ly*(ys_0 + iy_0)
42     new_z_0 = lz*(zs_0 + iz_0)
43
44     new_x_1 = lx*(xs_1 + ix_1)
45     new_y_1 = ly*(ys_1 + iy_1)
46     new_z_1 = lz*(zs_1 + iz_1)
47     dr_2 = (new_x_1-new_x_0)**2
48     +(new_y_1-new_y_0)**2 +
49     (new_z_1-new_z_0)**2
50     msd[lag] = msd[lag] + dr_2
51     norm[lag] = norm[lag] + 1
52     msd=msd/norm
53     return(msd)
54
55 #Getting the figure
56 columns, frames, box_length, number_of_atoms = read_data(
57     filename)
58 id_sx = find_index_of_column(columns, 'xs')
59 id_sy = find_index_of_column(columns, 'ys')
60 id_sz = find_index_of_column(columns, 'zs')
61 id_ix = find_index_of_column(columns, 'ix')
62 id_iy = find_index_of_column(columns, 'iy')
63 id_iz = find_index_of_column(columns, 'iz')
64 id_index = find_index_of_column(columns, 'id')
65 columns = id_sx, id_sy, id_sz, id_ix, id_iy, id_iz,
66     id_index
67 msd = get_msd(columns, frames, number_of_atoms, box_length,
68     rho=rho, stride=1)
```

```
67 t= np.arange(0, len(msd))*0.001 #time between frames
68 plt.loglog(t, msd, '-', label=keyword)
69 plt.ylabel(r'MSD')
70 plt.xlabel(r'$t$')
71 plt.legend(fontsize=15)
72 plt.savefig('msd.pdf')
73 plt.legend()
74 plt.show()
```

## B.2 Calculation of the Radial Distribution Function (RDF)

```
1
2 def rdf(datafile, d_r=0.05):
3     columns, frames, box_length,
4     number_of_atoms = read_data(datafile)
5     n=number_of_atoms
6     box=box_length[0]
7
8     for i in range(len(frames)-1):
9         r=frames[i]
10        r=r/box
11
12        dr= d_r
13        dr = dr / box_length[0]
14        nk = floor(0.5/dr)
15
16        r_max = nk*dr
17        h= np.zeros(nk, dtype=np.int_)
18        #nstep = 0
19        # Counts configurations (incase you are using RUMD)
20
```

```
21 # Simple approach calculating all pairs at once
22 rij      = r[:,np.newaxis,:] - r[np.newaxis,:,:]
23 rij      = rij - np rint(rij)
24
25 # Apply periodic boundaries
26 rij_mag  = np.sqrt(np.sum(rij**2,axis=-1))
27 rij_mag  = rij_mag[np.triu_indices_from(rij_mag,k=1)]
28 hist,edges = np.histogram(rij_mag,bins=nk,
29 range=(0.0,r_max))
30 h        = h + 2*hist
31
32 rho      = float(n)
33 h_id     = ( 4.0 * np.pi * rho / 3.0) * ( edges[1:nk+1]**3
34 - edges[0:nk]**3 ) # Ideal number
35 g        = h / h_id / (n)
36 if i ==0:
37     n_g=g
38 else:
39     n_g += g
40
41 edges    = edges*box # Convert bin edges back to sigma=1
         units
42 r_mid    = 0.5*(edges[0:nk]+edges[1:nk+1]) # Mid points of
         bins
43 print ('Writing the rdf file')
44 np.savetxt(f'rdf.dat',np.c_[r_mid,n_g/(len(frames)-1)]
45 ,fmt="%15.8f")
46
47 rdf('traj.atom') #this is the file name you get from
         LAMMPS
48
49 def plot_fig(file):
50     file= np.loadtxt(main_directory + file)
51     x=file[:,0]
52     y=file[:,1]
53     plt.plot(x, y, '-')
54
55 plot_fig('rdf.dat')
```

```
56 plt.xlabel(r'Pair Distance')
57 plt.ylabel(r'Radial Distribution Function')
58 plt.ylim(0,4)
59 plt.xlim(0, 6)
60 plt.savefig('rdf.pdf')
61 plt.show()
62
```

## B.3 Calculations of the Velocity Auto-correlation (VAC) Function

```
1 #Numba is optimizing the python script, yet it
2 #has some restrictions, it prefers arrays and
3 #knowing the type of data right away.
4 #You can use it when the script takes too long to compile
5 .
6 @numba.jit(parallel=True)
7 # Getting the Velocity autocorelation
8 def get_VACF(vel_columns, frames, number_of_atoms, rho, T,
9 max_lag=np.inf, stride=1):
10 id_vx = vel_columns[0]
11 id_vy = vel_columns[1]
12 id_vz = vel_columns[2]
13 cvv = np.zeros(len(frames)-1, dtype=np.float32)
14 norm = np.zeros(len(frames)-1, dtype=np.int32)
15 max_lag = min(len(frames)-1, max_lag)
16 print(max_lag)
17 for lag in range(0, max_lag):
18     for f0 in range(0, len(frames)-lag, stride):
19         f1 = f0+lag
20         data_0 = frames[f0]
```

```
21 data_1 = frames[f1]
22 for n in range(len(data_0)):
23     vx_0 = data_0[n, id_vx]
24     vy_0 = data_0[n, id_vy]
25     vz_0 = data_0[n, id_vz]
26     vx_1 = data_1[n, id_vx]
27     vy_1 = data_1[n, id_vy]
28     vz_1 = data_1[n, id_vz]
29     dot_product = vx_0*vx_1 +
30     vy_0*vy_1 + vz_0*vz_1
31     cvv[lag] = cvv[lag] + dot_product
32     norm[lag] = norm[lag] + 1
33 return cvv/norm
34
35 #Getting the Figure
36
37 columns, frames, box_length, number_of_atoms =
38 read_data(datafile)
39 id_vx = find_index_of_column(columns, 'vx')
40 id_vy = find_index_of_column(columns, 'vy')
41 id_vz = find_index_of_column(columns, 'vz')
42 vel_columns = id_vx, id_vy, id_vz
43 time_between_frames = 0.001
44 cvv= get_VACF(vel_columns, frames,
45 number_of_atoms, rho, T, stride=1)
46 t = np.arange(0, len(cvv))*time_between_frames
47 plt.plot(t, cvv/cvv[0], '-')
48
49 #Figure paramters
50 plt.ylim(0, 1.0)
51 plt.xlim(0, 1.0)
52 plt.ylabel('$c_{vv}(t)$')
53 plt.xlabel(r'Time, $t$')
54 plt.legend()
55 plt.savefig('cvv.png')
56 plt.show()
```

## B.4 Calculations of the Rotational Auto-correlation (RAC) Function

```

1
2 #Getting the RACF
3 @numba.jit(parallel=True)
4 def get_RACF(columns, frames, number_of_atoms,
5 box_length, max_lag=np.inf, stride=1):
6     id_xs = columns[0]
7     id_ys = columns[1]
8     id_zs = columns[2]
9     id_ix = columns[3]
10    id_iy = columns[4]
11    id_iz = columns[5]
12    #id_index= columns[6]
13    lx = box_length[0]
14    ly = box_length[1]
15    lz = box_length[2]
16    RACF = np.zeros(len(frames)-1, dtype=np.float32)
17    norm = np.zeros(len(frames)-1, dtype=np.int32)
18    max_lag = min(len(frames)-1, max_lag)
19    for lag in range(0, max_lag):
20        for f0 in range(0, len(frames)-lag, stride):
21            f1 = f0+lag
22            data_0 = frames[f0]
23            data_1 = frames[f1]
24            for n in range (0, len(data_0), 2):
25                xs_0= data_0[n, id_xs]
26                ys_0 = data_0[n, id_ys]
27                zs_0 = data_0[n, id_zs]
28                ix_0 = data_0[n, id_ix]
29                iy_0 = data_0[n, id_iy]
30                iz_0 = data_0[n, id_iz]
31                xs_1 = data_0[n+1, id_xs]
32                ix_1 = data_0[n+1, id_ix]

```

```
33     ys_1 = data_0[n+1, id_ys]
34     iy_1 = data_0[n+1, id_iy]
35     zs_1 = data_0[n+1, id_zs]
36     iz_1 = data_0[n+1, id_iz]
37     new_x_0 = lx*(xs_0 + ix_0)
38     new_y_0 = ly*(ys_0 + iy_0)
39     new_z_0 = lz*(zs_0 + iz_0)
40     new_x_1 = lx*(xs_1 + ix_1)
41     new_y_1 = ly*(ys_1 + iy_1)
42     new_z_1 = lz*(zs_1 + iz_1)
43     v1_x = (new_x_1 - new_x_0)
44     v1_y = (new_y_1 - new_y_0)
45     v1_z = (new_z_1 - new_z_0)
46     xs_2= data_1[n, id_xs]
47     ys_2 = data_1[n, id_ys]
48     zs_2 = data_1[n, id_zs]
49     ix_2 = data_1[n, id_ix]
50     iy_2 = data_1[n, id_iy]
51     iz_2 = data_1[n, id_iz]
52     new_x_2 = lx*(xs_2 + ix_2)
53     new_y_2 = ly*(ys_2 + iy_2)
54     new_z_2 = lz*(zs_2 + iz_2)
55     xs_3 = data_1[n+1, id_xs]
56     ys_3 = data_1[n+1, id_ys]
57     zs_3 = data_1[n+1, id_zs]
58     ix_3 = data_1[n+1, id_ix]
59     iy_3 = data_1[n+1, id_iy]
60     iz_3 = data_1[n+1, id_iz]
61     new_x_3 = lx*(xs_3 + ix_3)
62     new_y_3 = ly*(ys_3 + iy_3)
63     new_z_3 = lz*(zs_3 + iz_3)
64     v2_x = (new_x_3 - new_x_2)
65     v2_y = (new_y_3 - new_y_2)
66     v2_z = (new_z_3 - new_z_2)
67     dotproduct = v1_x* v2_x + v1_y*v2_y + v1_z*v2_z
68     RACF[lag] = RACF[lag] + dotproduct
69     norm[lag] = norm[lag] + 1
70     return (RACF/norm)
```

```
71 |
72 | columns, frames, box_length, number_of_atoms = read_data(
    |     datafile)
73 |
74 | #Getting the figure
75 | id_sx = find_index_of_column(columns, 'xs')
76 | id_sy = find_index_of_column(columns, 'ys')
77 | id_sz = find_index_of_column(columns, 'zs')
78 | id_ix = find_index_of_column(columns, 'ix')
79 | id_iy = find_index_of_column(columns, 'iy')
80 | id_iz = find_index_of_column(columns, 'iz')
81 | columns = id_sx, id_sy, id_sz, id_ix, id_iy, id_iz
82 | output = get_RACF(columns, frames, number_of_atoms,
    |     box_length)
83 | t= np.arange(0, len(output))*0.001 #time between frames
84 | plt.plot(t, output/output[0], '-')
85 | plt.ylabel(r'$\langle \vec{n}(0) \cdot \vec{n}(\tilde{t}) \rangle$')
86 | plt.xlabel(r'Time, $t$')
87 | plt.legend(fontsize=15)
88 | plt.savefig('rac.png')
89 | plt.show()
```



# Reprints of Articles and Posters

---

**Extreme case of density scaling: The Weeks-Chandler-Andersen system at low temperatures**Eman Attia<sup>\*,†</sup>, Jeppe C. Dyre<sup>\*,†</sup> and Ulf R. Pedersen<sup>\*,‡</sup>*Glass and Time, IMFUFA, Department of Science and Environment, Roskilde University,  
P.O. Box 260, 4000 Roskilde, Denmark*

(Received 27 January 2021; accepted 28 May 2021; published 24 June 2021)

This paper studies numerically the Weeks-Chandler-Andersen system, which is shown to obey hidden scale invariance with a density-scaling exponent that varies from below 5 to above 500. This unprecedented variation makes it advantageous to use the fourth-order Runge-Kutta algorithm for tracing out isomorphs. Good isomorph invariance of structure and dynamics is observed over more than three orders of magnitude temperature variation. For all state points studied, the virial potential-energy correlation coefficient and the density-scaling exponent are controlled mainly by the temperature. Based on the assumption of statistically independent pair interactions, a mean-field theory is developed that rationalizes this finding and provides an excellent fit to data at low temperatures.

DOI: [10.1103/PhysRevE.103.062140](https://doi.org/10.1103/PhysRevE.103.062140)**I. INTRODUCTION**

Density scaling is an important experimental discovery of the past 20 years' liquid-state research, which by now has been demonstrated for high-pressure data of hundreds of systems [1–4]. The crucial insight is that, in order to characterize a thermodynamic state point, the relevant variable supplementing the temperature  $T$  is not the pressure  $p$ , but the number density  $\rho \equiv N/V$  (considering  $N$  particles in volume  $V$ ) [1–6]. If  $\gamma$  is the so-called density-scaling exponent, plotting data for the dynamics as a function of  $\rho^\gamma/T$  results in a collapse [1–4]. In other words, the dynamics depends on the two variables of the thermodynamic phase diagram only via the single variable  $\rho^\gamma/T$ . This provides a significant rationalization of data, as well as an important hint for theory development. It should be noted, though, that density scaling does not apply universally; for instance, it usually works better for van der Waals liquids than for hydrogen-bonded liquids [2,4].

Some time after these developments were initiated, a framework for density scaling was provided in terms of the isomorph theory [7,8], which links density scaling to Rosenfeld's excess-entropy scaling method [9,10]. According to isomorph theory, any system with strong correlations between the fixed-volume virial and potential-energy equilibrium fluctuations has curves of invariant structure and dynamics in the thermodynamic phase diagram. These "isomorphs" [7,11] are defined as curves of constant excess entropy  $S_{\text{ex}}$ , which is the entropy minus that of an ideal gas at the same temperature and density ( $S_{\text{ex}} < 0$  because any system is more ordered than an ideal gas).

If the potential energy is denoted by  $U$  and the virial by  $W$ , their Pearson correlation coefficient  $R$  is defined by

$$R = \frac{\langle \Delta U \Delta W \rangle}{\sqrt{\langle (\Delta U)^2 \rangle \langle (\Delta W)^2 \rangle}}. \quad (1)$$

Here  $\Delta$  denotes the deviation from the thermal average and the angular brackets are canonical ( $NVT$ ) averages. The pragmatic criterion defining strong correlation is  $R > 0.9$  [12,13]. Systems with strong correlations have good isomorphs, i.e., approximate invariance of structure and dynamics along the configurational adiabats [7]. Such systems are termed  $R$ -simple, signaling the simplification of having an effectively one-dimensional thermodynamic phase diagram in regard to structure and dynamics when these are given in so-called reduced units (discussed below). Hydrogen-bonded systems usually have  $R < 0.9$  and are thus not  $R$ -simple [12]; this explains why density scaling does not apply universally.

Isomorph theory is only rigorously correct in the unrealistic case of an Euler-homogeneous potential-energy function that is realized, for instance, in systems with inverse-power-law (IPL) pair potentials [14]. Nevertheless, isomorph-theory predictions apply to a good approximation for many systems, e.g., Lennard-Jones-type liquids [7,15–17], the exponential pair-potential system at low temperatures [18,19], simple molecular models [20–22], polydisperse systems [23], crystals [24], nanoconfined liquids [25], polymerlike flexible molecules [26], metals [27,28], and Yukawa plasmas [29,30].

In some cases, isomorphs are well described by the equation  $\rho^\gamma/T = \text{const}$  with a constant  $\gamma$  [31], which as mentioned accounts for density scaling as discussed in most experimental contexts [2]. Isomorph theory, however, does not require  $\gamma$  to be constant throughout the thermodynamic phase diagram, and  $\gamma$  indeed does vary in most simulations [16,32–34]. The general isomorph-theory definition of the density-scaling exponent  $\gamma$  at a given state point [7,10] is

$$\gamma \equiv \left( \frac{\partial \ln T}{\partial \ln \rho} \right)_{S_{\text{ex}}} = \frac{\langle \Delta U \Delta W \rangle}{\langle (\Delta U)^2 \rangle}. \quad (2)$$

<sup>\*</sup>attia@ruc.dk<sup>†</sup>dyre@ruc.dk<sup>‡</sup>urp@ruc.dk

The second equality gives the statistical-mechanical expression of  $\gamma$  in terms of the constant-volume canonical-ensemble fluctuations of potential energy and virial.

The question whether experimental density-scaling exponents are strictly constant throughout the phase diagram has recently come into focus [35,36]. In simulations, isomorphs are in many cases described by the equation [1,8,32,37]

$$\frac{h(\rho)}{T} = \text{const}, \quad (3)$$

in which  $h(\rho)$  is a function of the density. For the Lennard-Jones (LJ) system, for instance, one has  $h(\rho) \propto (\gamma_0/2 - 1)(\rho/\rho_0)^4 - (\gamma_0/2 - 2)(\rho/\rho_0)^2$ , in which  $\gamma_0$  is the density-scaling exponent at a reference state point of density  $\rho_0$  [32,37]. For isomorphs given by Eq. (3), Eq. (2) implies

$$\gamma = \frac{d \ln h(\rho)}{d \ln \rho}. \quad (4)$$

We see that unless  $h(\rho)$  is a power-law function, the density-scaling exponent depends on the density. More generally,  $\gamma$  also depends on the temperature [33]. This is the case, for instance, for the LJ system approaching very high temperatures: For  $T \rightarrow \infty$  at a fixed density, the LJ system is dominated by the repulsive  $r^{-12}$  term of the pair potential, implying that  $\gamma$  approaches  $\frac{12}{3} = 4$  in this limit and that Eq. (3) cannot apply.

A likely reason that many experiments are well described by a constant  $\gamma$  is the fact that density often does not vary much. As shown by Casalini and co-workers [36,38], when extreme pressure is applied, the density-scaling exponent is no longer constant. Although it is now clear that  $\gamma$  is not a material constant [35,36], its variation is as mentioned often insignificant in experiments. This paper gives an example in which  $\gamma$  varies dramatically. We present a study of the noted Weeks-Chandler-Andersen (WCA) system [39,40] that 50 years ago introduced the idea of a cutoff at the potential-energy minimum of the LJ system [41–46]. This idea is still very popular and used in many different contexts [47–53].

We show below that the WCA system has strong virial potential-energy correlations and thus is  $R$ -simple. We find that  $\gamma$  varies by more than two decades in the investigated part of the phase diagram. In comparison, the LJ system has a density-scaling exponent that varies less than 50% throughout the phase diagram. To the best of our knowledge, the  $\gamma$  variation of the WCA system is much larger than has so far been reported for any system in simulations or experiments. For all state points studied, we find that  $\gamma$  depends primarily on the temperature. A mean-field theory is presented that explains this observation and accounts well for the low-temperature and low-density behavior of the system.

After providing a few technical details in Sec. II, we present the thermodynamic phase diagram with the state points studied numerically in Sec. III. The paper's focus is on three isomorphs, numbered 1–3. Each of these is associated with an isotherm and an isochore, the purpose of which is to put into perspective the isomorph variation of structure and dynamics by comparing it to what happens when a similar density or temperature variation is studied, keeping the other variable constant. In Sec. III we also give data for the virial potential-energy correlation coefficient  $R$  and the

density-scaling exponent  $\gamma$ , demonstrating that all state points studied have strong correlations ( $R > 0.9$ ) while  $\gamma$  varies from about 5 to above 500. A mean-field theory is developed in Sec. IV, predicting that  $R$  and  $\gamma$  both depend primarily on the temperature. Section V presents simulations of the structure and dynamics along the isotherms, isochores, and isomorphs. Despite the extreme  $\gamma$  variation, which implies that an approximate inverse-power-law description fails entirely, we find good isomorph invariance of the reduced-unit structure and excellent isomorph invariance of the reduced-unit dynamics. Section VI gives a brief discussion. The Appendix details the implementation of the fourth-order Runge-Kutta method for tracing out isomorphs and compares its predictions to those of the previously used simple Euler method.

## II. MODEL AND SIMULATION DETAILS

Liquid model systems are often defined in terms of a pair potential  $v(r)$ . If  $r_{ij} = |\mathbf{r}_i - \mathbf{r}_j|$  is the distance between particles  $i$  and  $j$ , the potential energy  $U$  as a function of all particle coordinates  $\mathbf{R} \equiv (\mathbf{r}_1, \mathbf{r}_2, \dots, \mathbf{r}_N)$  is given by

$$U(\mathbf{R}) = \sum_{i < j} v(\mathbf{r}_{ij}). \quad (5)$$

We study in this paper the single-component WCA system [39], which cuts the standard LJ pair potential at its minimum and subsequently shifts the potential by adding a constant such that the minimum is lifted to zero [39,54]. The result is the purely repulsive pair potential given by

$$v(r) = \begin{cases} 4\epsilon \left[ \left(\frac{r}{\sigma}\right)^{-12} - \left(\frac{r}{\sigma}\right)^{-6} \right] + \epsilon & (r < 2^{1/6}\sigma) \\ 0 & (r > 2^{1/6}\sigma). \end{cases} \quad (6)$$

Like the LJ pair potential,  $v(r)$  involves two parameters:  $\sigma$  that reflects the particle radius and  $\epsilon$  that is the numerical value of the energy of the LJ potential at its minimum at  $r = 2^{1/6}\sigma$ .

The WCA system was studied by molecular dynamics (MD) simulations in the canonical ( $NVT$ ) ensemble using the Nosé-Hoover thermostat [55]. The simulated system consisted of 4000 particles in a cubic box with periodic boundaries. The simulations were performed using the open-source Roskilde University molecular dynamics software (RUMD) that runs on GPUs (graphics processing units) [56,57]. For updating the system state, the leapfrog algorithm was employed with a reduced-unit time step of 0.0025. At each state point, a simulation first ran for  $25 \times 10^6$  time steps for equilibration. This was followed by  $50 \times 10^6$  time steps for the production run.

The simulations were conducted in the reduced-unit system of isomorph theory in which the energy unit is  $e_0 \equiv k_B T$ , the length unit is  $l_0 \equiv \rho^{-1/3}$ , and the time unit is  $t_0 \equiv \rho^{-1/3} \sqrt{m/k_B T}$ , where  $m$  is the particle mass [7]. A few simulations were also carried out in MD units to check for consistency. Using reduced units in a simulation implies that density and temperature are both equal to unity; the state point is changed by varying  $\sigma$  and  $\epsilon$ , i.e., by changing the pair potential. In contrast, performing simulations in MD units implies setting  $\sigma = \epsilon = 1$ , i.e., fixing the pair potential and varying  $\rho$  and  $T$  in order to change the state point. The two methods are mathematically equivalent, of course. Simulating

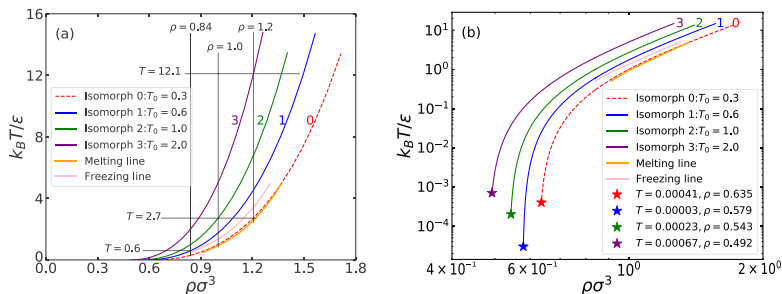


FIG. 1. (a) The three isomorphs in focus (denoted by 1–3) shown as full curves in the temperature-density thermodynamic phase diagram. Each isomorph was generated as described in the text and in the Appendix, starting from the reference state point  $(\rho_0, T_0)$  with  $\rho_0 = 0.84$  and  $T_0$  equal to 0.6, 1.0, and 2.0, respectively. A fourth isomorph (denoted by 0) marked by the red dashed line is in the supercooled liquid phase. The horizontal lines are three isotherms and the vertical lines are three isochores, which are studied in order to compare their structure and dynamics variation to those along the isomorphs. The freezing and melting lines are shown as yellow and orange lines, respectively [41,45]; note that these are parallel to the isomorphs. (b) The four isomorphs shown in a logarithmic temperature-density phase diagram. The slope  $\gamma$  [Eq. (2)] increases significantly as the temperature is lowered along an isomorph. The stars mark the lowest simulated temperature and density on each isomorph; these state points are used in Fig. 9 below.

in reduced units is convenient because the time step is then automatically adjusted to take into account the thermal velocity.

Reduced quantities are generally marked by a tilde, for instance,  $\tilde{r} \equiv r/l_0 = \rho^{1/3}r$ . These units are used below for all quantities except for the density and the temperature; thermodynamic state points are reported by giving density and temperature in standard MD units, i.e.,  $\rho$  is given in units of  $\sigma^{-3}$  and  $T$  in units of  $\varepsilon/k_B$ .

### III. SIMULATED STATE POINTS

Figure 1(a) shows the thermodynamic phase diagram of the WCA system. The yellow and orange lines are the freezing and melting lines [41,45]. The blue, green, and purple lines marked 1, 2, and 3, respectively, are the isomorphs of main focus below, while the red dashed line is a fourth isomorph marked 0, which is in the liquid-solid coexistence region. Note that the freezing and melting lines are both approximate isomorphs [7,58].

Each isomorph was traced out starting from a reference state point of density 0.84. Isomorphs are often identified by integrating Eq. (2) using the simple first-order Euler integration scheme for density changes of order 1% [7,16,20]. The extreme variation of  $\gamma$  found for the WCA system, however, means that Euler integration can only be used reliably for very small density changes and a more accurate integration scheme is called for. We used the fourth-order Runge-Kutta integration (RK4) as detailed in the Appendix, where it is demonstrated that RK4 is 10–100 times more computationally efficient than Euler integration for tracing out isomorphs with a given accuracy. Data for selected state points of the four isomorphs are listed in Table I.

In order to investigate the degree of isomorph invariance of the reduced-unit structure and dynamics (Sec. V), for each isomorph we also performed simulations along an isotherm and an isochore, limiting all simulations to state points in the

equilibrium liquid phase. Figure 1(b) shows the isomorphs and the melting and freezing lines in a diagram with logarithmic density and temperature axes. In this diagram the density-scaling exponent  $\gamma$  is the isomorph slopes [compare Eq. (2)], which increases significantly along each isomorph as the density is lowered.

A configurational adiabat is an isomorph only for state points with strong virial potential-energy correlations, i.e., when  $R \gtrsim 0.9$  at the relevant state points in which  $R$  is given by Eq. (1). This condition is validated in Fig. 2, which shows  $R$  for all state points simulated. Figure 2(a) shows  $R$  as a function of the density, while Fig. 2(b) shows  $R$  as a function of the temperature. We see that  $R$  increases with increasing density and temperature, approaching unity. This reflects the fact that the  $(r/\sigma)^{-12}$  term of the pair potential dominates the interactions in these limits and that an IPL pair potential has  $R = 1$ . An important observation from Fig. 2 is that strong correlations are maintained even at the lowest densities and temperatures studied. A comparison of Figs. 2(a) and 2(b) reveals that  $R$  is primarily controlled by the temperature. This may be understood from a mean-field theory, which assumes that the interactions at low temperatures and densities are dominated by single-pair interactions (Sec. IV).

Figure 3 gives data for the density-scaling exponent  $\gamma$  at the state points simulated, plotted in different ways using the same symbols as in Fig. 2. We see that  $\gamma$  increases monotonically as either density, pressure, or temperature is lowered, eventually reaching values above 500. Figure 3(a) shows  $\gamma$  as a function of the density  $\rho$ . Clearly, knowledge of  $\rho$  is not enough to determine  $\gamma$ , implying that Eq. (4) does not apply for the WCA system. It has been suggested that  $\gamma$  is controlled by the pressure [59]. This works better than the density for collapsing data, but there is still some scatter [Fig. 3(b)]. Figure 3(c) plots  $\gamma$  as a function of the temperature. We here observe a quite good collapse, concluding that

TABLE I. State-point data for (a) isomorph 0, (b) isomorph 1, (c) isomorph 2, and (d) isomorph 3 (see Fig. 1).

$\rho\sigma^3$	$k_B T/\epsilon$	$P\sigma^3/\epsilon$	$\gamma$	$R$	$U/N\epsilon$	$W/N\epsilon$
(a)						
1.714	13.41	464.2	4.288	0.9995	50.67	257.5
1.636	10.98	357.7	4.329	0.9993	39.92	207.7
1.493	7.360	211.9	4.435	0.9988	24.52	134.6
1.366	4.933	125.2	4.582	0.9978	14.84	86.70
1.254	3.307	73.86	4.787	0.9961	8.841	55.59
1.156	2.217	43.60	5.068	0.9936	5.190	35.49
1.071	1.486	25.81	5.445	0.9902	3.007	22.60
0.9985	0.9960	15.35	5.939	0.9860	1.721	14.38
0.9364	0.6677	9.200	6.571	0.9808	1.298	9.157
0.9091	0.5466	7.145	6.945	0.9782	0.7332	7.313
0.8610	0.3664	4.341	7.835	0.9726	0.4117	4.675
0.8400	0.3000	3.396	8.353	0.9698	0.3079	3.743
0.8207	0.2456	2.664	8.932	0.9671	0.2300	2.100
0.7592	0.1104	1.034	11.94	0.9566	0.0711	1.251
0.7168	0.04960	0.4159	16.42	0.9475	0.0218	0.5306
0.6877	0.02230	0.1725	23.09	0.9402	0.006653	0.2285
0.6680	0.009059	0.06587	33.06	0.9349	0.001742	0.08984
0.6546	0.004972	0.03509	47.83	0.9304	0.0007115	0.04379
0.6456	0.002021	0.01382	69.90	0.9277	0.0001853	0.01938
0.6353	0.0004081	0.002703	152.0	0.9243	0.00001690	0.003846
(b)						
1.565	14.72	340.4	4.337	0.9993	39.48	202.9
1.495	12.05	262.7	4.385	0.9991	31.11	163.7
1.366	8.078	156.1	4.506	0.9983	19.14	106.2
1.252	5.415	92.69	4.671	0.9971	11.61	68.63
1.151	3.630	55.03	4.893	0.9954	6.956	44.18
1.024	1.992	25.27	5.366	0.9913	3.149	22.70
0.9527	1.335	15.12	5.799	0.9875	1.830	14.53
0.8916	0.8951	9.101	6.351	0.9831	1.053	9.310
0.8400	0.6000	5.520	7.041	0.9782	0.6015	5.972
0.7961	0.4022	3.377	7.899	0.9730	0.3412	3.840
0.7590	0.2696	2.085	8.955	0.9677	0.1925	2.477
0.7280	0.1807	1.299	10.25	0.9624	0.1081	1.603
0.7019	0.1211	0.8161	11.84	0.9574	0.06048	1.041
0.6708	0.06648	0.4129	14.88	0.9504	0.02517	0.5491
0.6543	0.04456	0.2646	17.48	0.9465	0.01399	0.3598
0.6245	0.01639	0.08940	26.75	0.9380	0.003198	0.1268
0.6060	0.006031	0.03111	42.01	0.9319	0.0007245	0.04532
0.5945	0.002219	0.01105	67.19	0.9282	0.0001632	0.01637
0.5787	0.00002724	0.0001290	579.6	0.9222	0.0000002251	0.0001957
(c)						
1.403	13.46	219.9	4.415	0.9989	27.20	143.3
1.341	11.02	169.8	4.474	0.9985	21.39	115.6
1.228	7.389	101.2	4.620	0.9976	13.12	75.04
1.128	4.953	60.34	4.814	0.9961	7.946	48.53
1.040	3.320	36.01	5.070	0.9940	4.756	31.30
1.001	2.718	27.85	5.225	0.9926	3.664	25.11
0.9637	2.226	21.56	5.399	0.9919	2.814	20.14
0.8972	1.492	12.96	5.820	0.9876	1.648	12.95
0.8675	1.221	10.07	6.071	0.9856	1.256	10.39
0.8400	1.000	7.837	6.350	0.9834	0.9557	8.330
0.8146	0.8187	6.110	6.663	0.9811	0.7256	6.683
0.7494	0.4493	2.930	7.828	0.9737	0.3141	3.461
0.6987	0.2466	1.432	9.411	0.9659	0.1342	1.803
0.6295	0.07427	0.3613	14.45	0.9515	0.02378	0.4998
0.5945	0.02734	0.1204	21.64	0.9420	0.005505	0.1752

TABLE I. (Continued.)

$\rho\sigma^3$	$k_B T/\epsilon$	$P\sigma^3/\epsilon$	$\gamma$	$R$	$U/N\epsilon$	$W/N\epsilon$
0.5694	0.008230	0.03360	36.68	0.9337	0.0009355	0.05084
0.5591	0.003698	0.01464	53.01	0.9300	0.0002851	0.02248
0.5507	0.001360	0.005242	85.02	0.9268	0.00006423	0.008158
0.5436	0.0002747	0.001034	185.1	0.9238	0.000005878	0.001628
(d)						
1.261	14.79	160.7	4.468	0.9986	21.25	112.7
1.206	12.10	124.4	4.531	0.9982	91.04	16.73
1.106	8.110	74.47	4.687	0.9971	10.30	59.25
1.060	6.640	57.64	4.781	0.996	8.044	47.75
0.9766	4.451	34.57	5.011	0.9946	4.870	30.95
0.9389	3.644	26.80	5.148	0.9934	3.774	24.90
0.9036	2.984	20.79	5.304	0.9922	2.917	20.03
0.8400	2.000	12.55	5.675	0.9890	1.730	12.94
0.8114	1.638	9.771	5.892	0.9873	1.327	10.41
0.7603	1.098	5.947	6.410	0.9833	0.7760	6.725
0.6787	0.4932	2.248	7.836	0.9741	0.2592	2.820
0.6196	0.2216	0.8762	9.977	0.9641	0.08440	1.192
0.5776	0.0996	0.3520	13.15	0.9548	0.02690	0.5098
0.5481	0.04474	0.1453	17.89	0.9466	0.008466	0.2204
0.5276	0.02010	0.06135	24.92	0.9395	0.002630	0.09617
0.5135	0.009033	0.02636	35.42	0.9347	0.0008093	0.04231
0.5038	0.004059	0.01148	50.9571	0.9305	0.0002475	0.01873
0.4973	0.001824	0.005048	74.1566	0.9278	0.00007535	0.008328
0.4920	0.0006709	0.001824	119.9858	0.9254	0.00001656	0.003037

$\gamma$  is primarily controlled by the temperature. Figures 3(d)–3(f) show data for all the state points simulated in logarithmic plots as functions of density, pressure, and temperature, respectively.

#### IV. MEAN-FIELD THEORY FOR $R$ AND $\gamma$ AT LOW DENSITIES

This section presents a mean-field theory for estimating the virial potential-energy correlation coefficient  $R$  and the density-scaling exponent  $\gamma$ . Along the lines of

Refs. [18,33,60,61], we assume that the individual pair interactions are statistically independent; this is expected to be a good approximation at relatively low densities.

In MD units the truncated WCA pair potential (6) is

$$v(r) = 4r^{-12} - 4r^{-6} + 1 \quad \text{for } r < r_c \equiv 2^{1/6} = 1.122 \dots \quad (7)$$

and zero otherwise. The virial of the configuration  $\mathbf{R}$  is given by  $W(\mathbf{R}) = \sum_{i>j}^N w(r_{ij})$ , in which the pair virial is defined as  $w(r) \equiv -(r/3)v'(r)$  [55]. Although the WCA potential is

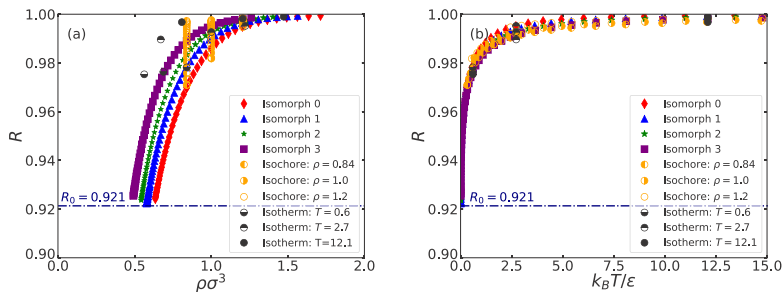


FIG. 2. Virial potential-energy correlation coefficient  $R$  [Eq. (1)] for all state points studied (Fig. 1): (a)  $R$  as a function of the density, (b)  $R$  as a function of the temperature. There are strong correlations everywhere ( $R > 0.9$ ). The horizontal dash-dotted lines mark the low-temperature low-density limit of the mean-field-theory prediction  $R_0 = \sqrt{8/3\pi} = 0.921$  [Eq. (20)]. The correlations are mainly controlled by the temperature.

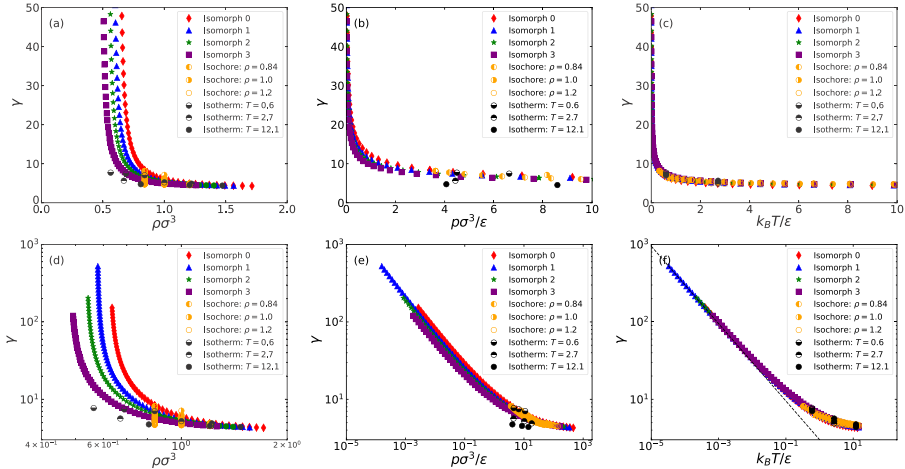


FIG. 3. Density-scaling exponent  $\gamma$  defined in Eq. (2) for the state points studied (Fig. 1). Closed symbols are isomorph state-point data and half open circles are isochore and isotherm data. Data are given for (a)–(c) state points with  $\gamma$  below 50 and (d)–(f) all state points: (a)  $\gamma$  as a function of the density, (b)  $\gamma$  as a function of the pressure, (c)  $\gamma$  as a function of the temperature, (d)  $\gamma$  as a function of the density in a log-log plot, (e)  $\gamma$  as a function of the pressure in a log-log plot, and (f)  $\gamma$  as a function of the temperature in a log-log plot.  $\gamma$  is clearly primarily a function of the temperature. The dashed line in (f) marks the low-temperature limit of the mean-field theory [Eq. (19)].

our primary focus, the arguments given below apply to any truncated purely repulsive potential.

In general, the partition function of the configurational degrees of freedom is given by  $Z \propto \int_{V^N} d\mathbf{r}_1 \cdots d\mathbf{r}_N \exp[-\sum_{i<j} v(r_{ij})/k_B T]$ . At low densities it is reasonable to regard the pair distances as uncorrelated, i.e., to treat the interactions in a mean-field way. This leads to the approximation  $Z \propto Z_s^N$ , in which  $Z_s = \int_V d\mathbf{r} \exp[-v_s(\mathbf{r})/k_B T]$  is the partition function of a single particle moving in the potential  $v_s(\mathbf{r})$  of all other particles frozen in space. In the low-density limit, none of the frozen particles overlap and  $Z_s$  has two contributions, one for the positions for which  $v(\mathbf{r}) = 0$  and one for the positions at which the particle interacts with one of the frozen particles. The former is the free volume that in the low-density limit approaches the entire volume  $V$ . The latter is  $N$  times the following integral (putting, for simplicity,  $k_B = 1$  in this section):

$$Z_1(T) = \int_0^{r_c} 4\pi r^2 \exp\left(-\frac{v(r)}{T}\right) dr. \quad (8)$$

In terms of  $Z_1(T)$  the single-particle partition function is thus in the thermodynamic limit given by

$$\frac{Z_s(\rho, T)}{N} = Z_1(T) + \frac{1}{\rho}. \quad (9)$$

Based on the above, any pair-defined quantity  $A(r)$  that is zero for  $r > r_c$  has an expectation value that is computed as (in which  $p(r) = 4\pi r^2 \exp[-v(r)/T]$  is the unnormalized

probability)

$$\langle A \rangle = \int_0^{r_c} \frac{A(r)p(r)dr}{Z_s(\rho, T)}. \quad (10)$$

Based on Eqs. (2) and (1), one gets

$$\gamma(\rho, T) = \frac{\langle wv \rangle - \langle w \rangle \langle v \rangle}{\langle v^2 \rangle - \langle v \rangle^2} \quad (11)$$

and

$$R(\rho, T) = \frac{\langle wv \rangle - \langle w \rangle \langle v \rangle}{\sqrt{(\langle w^2 \rangle - \langle w \rangle^2)(\langle v^2 \rangle - \langle v \rangle^2)}}. \quad (12)$$

Figure 4 compares the predictions of the mean-field theory (lines) to data along isomorphs and isochores. There is good overall agreement. Systematic deviations are visible in Figs. 4(b) and 4(d), however, which focus on densities that are not low enough to avoid frozen-particle overlap.

We proceed to discuss the low-density limit in which  $Z_s \rightarrow \infty$ . Terms that involve a single expectation value ( $\langle v^2 \rangle$ ,  $\langle w^2 \rangle$ , and  $\langle wv \rangle$ ) scale as  $1/Z_s$ , while terms that involve a multiplication of expectation values, i.e.,  $\langle v \rangle^2$ ,  $\langle w \rangle^2$ , and  $\langle v \rangle \langle w \rangle$ , scale as  $1/Z_s^2$ . Consequently, at low densities one can neglect terms that involve multiplications of expectation values [18,33,60,61], leading to

$$\gamma(T) = \langle wv \rangle / \langle v^2 \rangle \quad (13)$$

and

$$R(T) = \langle wv \rangle / \sqrt{\langle w^2 \rangle \langle v^2 \rangle}. \quad (14)$$

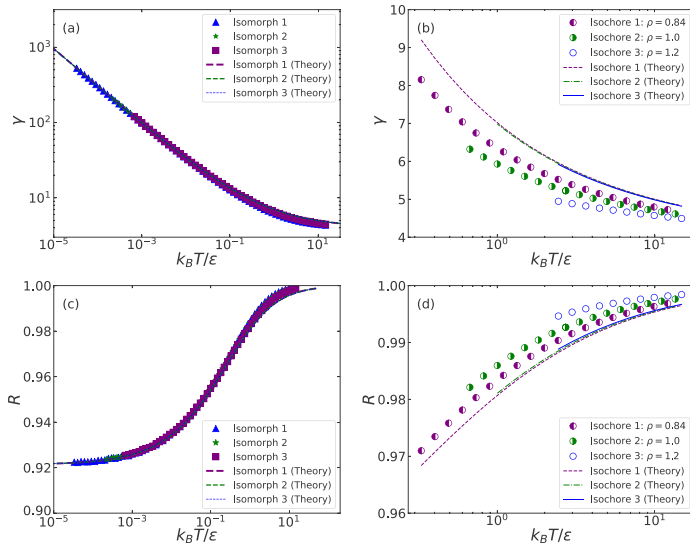


FIG. 4. Comparison of the predictions of the mean-field theory for  $\gamma$  and  $R$  as functions of the temperature (lines) to simulation results. (a) and (c) Results along the three isomorphs. (b) and (d) Results along the three isochores, focusing on higher densities where the mean-field theory is not expected to be accurate.

Note that these averages do not depend on  $Z_s$  since both numerators and denominators scale as  $1/Z_s$ . This implies that  $\gamma$  and  $R$  at low densities depend only of  $T$ , which explains the observation in Fig. 3.

Consider now the further assumption of a low temperature. In that case the probability distribution  $p(r)$  concentrates near  $r_c$  and one can expand around  $x \equiv r_c - r = 0$  by writing the pair potential as

$$v(x) = k_1 x + \frac{k_2 x^2}{2} + \frac{k_3 x^3}{6} + \dots \quad (15)$$

The pair virial then becomes [15]

$$w(x) = (r_c - x) \left( \frac{k_1}{3} + \frac{k_2 x}{3} \right) + \frac{k_3 r_c x^2}{6} + \mathcal{O}(x^3). \quad (16)$$

For the WCA potential  $k_1 = 0$  and  $k_2 = 36\sqrt[3]{4}$ . Since  $p(x)$  is concentrated near  $x = 0$ , the upper limit of the integral (17) may be extended to infinity, leading to

$$\langle A \rangle = \int_0^\infty \frac{A(x)p(x)dx}{Z} \quad (T \rightarrow 0), \quad (17)$$

in which

$$p(x) = 4\pi(r_c - x)^2 \exp\left(-\frac{k_2 x^2}{2T}\right). \quad (18)$$

The Gaussian integrals can be evaluated by hand or, e.g., using the SYMPY PYTHON library for symbolic mathematics. We find

that  $\gamma$  and  $R$  are given by

$$\gamma_0 = \frac{4r_c \sqrt{2k_2}}{9\sqrt{\pi T}} = \frac{16}{3\sqrt{\pi T}} \quad (T \rightarrow 0) \quad (19)$$

and

$$R_0 = \sqrt{\frac{8}{3\pi}} = 0.921\dots \quad (T \rightarrow 0). \quad (20)$$

Figure 5 shows the mean-field predictions for  $\gamma$  and  $R$  at  $T = 0.01$  plotted as a function of the density. As expected, the theory works well at low densities, even though one is here still not quite at the  $T \rightarrow 0$  limit marked by the horizontal lines.

## V. VARIATION OF STRUCTURE AND DYNAMICS ALONG ISOTHERMS, ISOCHORES, AND ISOMORPHS

The considerable  $\gamma$  variation of the WCA system means that it cannot be described approximately by an Euler-homogeneous potential-energy function. This section investigates to which degree the reduced-unit structure and dynamics are, nevertheless, invariant along isomorphs 1–3. Isomorph invariance is rarely exact, so in order to put the simulation results into perspective, we present also results for the variation of the reduced-unit structure and dynamics along isotherms and isochores. As a measure of the structure, we look at the radial distribution function (RDF) as a function of the radial distance. As a measure of the dynamics, we look at the mean-square displacement (MSD) as a function

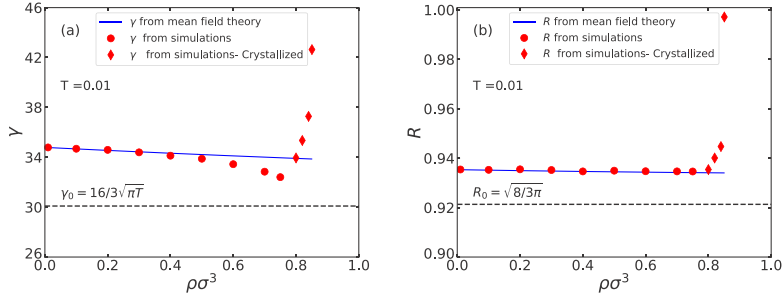


FIG. 5. Density dependence of (a)  $\gamma$  and (b)  $R$  at  $T = 0.01$ . The full blue lines are the mean-field theory predictions. The horizontal black dashed lines mark the low-temperature limits of the mean-field theory. Results are also shown for high-density samples that crystallized during the simulations.

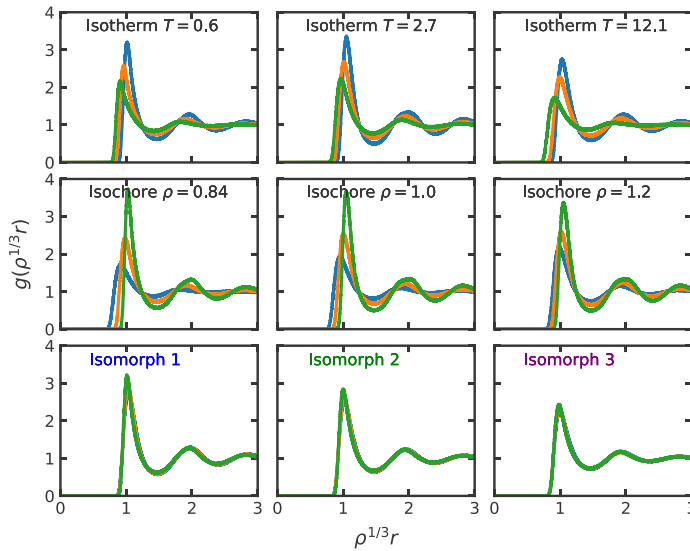


FIG. 6. Reduced-unit radial distribution functions for the three isotherms, isochores, and isomorphs (Fig. 1). The green curves give the lowest temperature and density, the orange curves give the intermediate temperature and density, and the blue curves give the highest temperature and density. Although the first-peak maximum is not entirely isomorph invariant, in comparison to isotherms and isochores we see an excellent RDF invariance along the isomorphs. This is the case even though the density variation of the isotherms and the temperature variation of the isochores are somewhat smaller than those of the isomorphs (compare Fig. 1). For the isotherms, the green curves give data for  $(\rho, T) = (0.56, 0.60)$ ,  $(0.82, 2.72)$ , and  $(0.81, 12.1)$ ; the orange curves for  $(\rho, T) = (0.69, 0.60)$ ,  $(1.0, 2.72)$ , and  $(1.21, 12.1)$ ; and the blue curves for  $(\rho, T) = (0.84, 0.60)$ ,  $(1.22, 2.72)$ , and  $(1.47, 12.1)$ . For the isochores, the green curves give data for  $(\rho, T) = (0.84, 0.33)$ ,  $(1.00, 0.82)$ , and  $(1.21, 2.44)$ ; the orange curves for  $(\rho, T) = (0.84, 1.99)$ ,  $(1.00, 3.32)$ , and  $(1.21, 6.64)$ ; and the blue curves for  $(\rho, T) = (0.84, 14.72)$ ,  $(1.00, 13.46)$ , and  $(1.21, 14.78)$ . For the isomorphs, the green curves give data for the reference state points  $(\rho, T) = (0.84, 0.60)$ ,  $(0.84, 1.00)$ , and  $(0.84, 2.00)$ ; the orange curves for  $(\rho, T) = (1.06, 2.43)$ ,  $(1.04, 3.32)$ , and  $(0.94, 3.64)$ ; and the blue curves for  $(\rho, T) = (1.57, 14.72)$ ,  $(1.40, 13.46)$ , and  $(1.26, 14.78)$ .

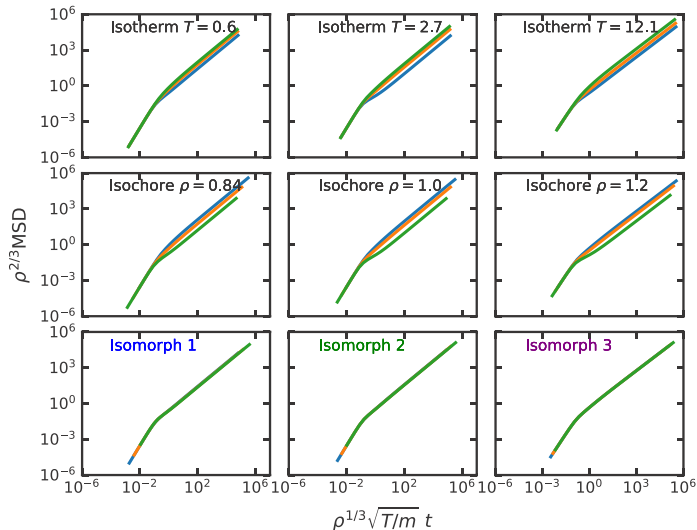


FIG. 7. Reduced-unit radial mean-square displacement plotted against time for the three isotherms, isochores, and isomorphs (Fig. 1). The state points and color codings are the same as in Fig. 6. The dynamics is isomorph invariant to a very good approximation.

of the time, as well as of the reduced diffusion coefficient  $\tilde{D}$  identified from the long-time MSD.

Starting with structure, Fig. 6 shows reduced-unit RDF data along the three isotherms, isochores, and isomorphs of Fig. 1. The isotherms span almost the same density range and the isochores span almost the same temperature range as the corresponding isomorphs (restricted to the equilibrium liquid phase, i.e., to data above the freezing line). Along the isomorphs the RDFs show some variation at the first peak maximum (bottom row), but in comparison to the isotherms and isochores, there is excellent overall isomorph invariance of the RDF.

For all three isomorphs we find that the peak height increases as the temperature decreases. This is an effect of larger  $\gamma$  resulting in a higher first peak, which may be understood as follows. Consider the IPL pair-potential system with  $v(r) \propto r^{-n}$ , which has  $\gamma = n/3$  and perfect isomorphs [62]. The larger  $n$  is, the more harshly repulsive the forces are. From the Boltzmann probability of finding two particles at the distance  $r$ , proportional to  $\exp[-v(r)/k_B T]$ , it follows that particle near encounters become less likely as  $n \rightarrow \infty$ , thus suppressing the RDF at distances below the first peak. If there is isomorph invariance of the number of particles within the first coordination shell, as  $n$  increases some of the RDF must therefore move from small  $r$  to larger  $r$  within the first coordination shell, resulting in a higher first peak. This argument has recently been confirmed by the observation that the bridge function, a fundamental quantity of liquid-state theory [54], is isomorph invariant to a very good approxima-

tion [63]. A similar increase of the height of the first RDF peak with increasing  $\gamma$  has been observed for the exponential system (Fig. 5 in Ref. [33]). In that case it was a much less dramatic effect, however, because the exponential system's  $\gamma$  variation at the investigated state points covered less than a factor of 3 compared to more than a factor of 100 for the WCA state points studied here. Interestingly, for both systems the data imply that  $\gamma \rightarrow \infty$  as  $T \rightarrow 0$  along an isomorph, i.e., both systems become more and more hard-sphere-like as the temperature is lowered.

Proceeding to investigate the dynamics, Fig. 7 shows data for the reduced-unit MSD as a function of the reduced time along the three isotherms, isochores, and isomorphs. There is only invariance along the isomorphs. Along the isotherms, the lowest density (green) gives rise to the largest reduced diffusion coefficient. This is because the mean collision length increases when the density is decreased. Along the isochores, the lowest temperature (green) has the smallest reduced diffusion coefficient. This is because the effective hard-sphere radius increases when temperature is decreased, leading to a smaller mean-collision length. In MD units, the MSDs are also not invariant along the isotherms or isochores (data not shown); thus the lack of invariance for the isotherms and isochores is not a consequence of the use of reduced units. In regard to the isomorph data, with Fig. 6 in mind we conclude that the noninvariant first-peak heights of the RDFs along the isomorphs have little influence on the dynamics. This is consistent with expectations from liquid-state quasiuniversality, according to which many systems have structure and

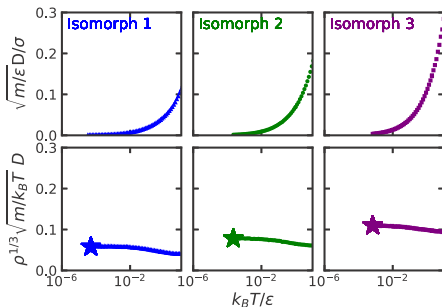


FIG. 8. Diffusion coefficients along isomorphs 1–3 in MD units (top row) and in reduced units (bottom row), plotted as functions of the logarithm of the temperature. When given in MD units, the diffusion coefficients vary significantly along the isomorphs, while they are fairly constant in reduced units. This illustrates the importance of using reduced units when checking for isomorph invariance. From end point to end point of the isomorphs, the variation in the reduced diffusion coefficient  $\tilde{D}$  is, respectively, 39%, 23%, and 14%. The corresponding numbers are 1000%, 880%, and 549% along the isochores and 214%, 893%, and 305% along the isotherms.

dynamics similar to those of the exponential generic liquid system, which as mentioned also exhibits varying first-peak heights along its isomorphs [33].

The reduced diffusion coefficient  $\tilde{D} \equiv \rho^{1/3} \sqrt{m/k_B T} D$  is extracted from the data in Fig. 7 by making use of the fact that the long-time reduced MSD is  $6\tilde{D}t$ . Figure 8 shows how both  $D$  and  $\tilde{D}$  vary along the three isomorphs. The top row demonstrates a large variation in  $D$  along each isomorph. The bottom row shows  $\tilde{D}$ , which is rigorously invariant for a system with perfect isomorphs ( $R = 1$ ). This is not the case for the WCA system, but the variation is below 40% for all three isomorphs in situations where the temperature varies by more than four orders of magnitude. Thus the reduced diffusion coefficient is isomorph invariant to a good approximation.

Figure 8 suggests that  $\tilde{D}$  stabilizes as  $T \rightarrow 0$ , and for each isomorph one can tentatively identify this low-temperature limit. Figure 9 plots estimates of these limiting values obtained at the lowest density simulated on each isomorph. An obvious question is which density corresponds to  $\tilde{D} = 0$ . At very low temperature, because  $\gamma$  becomes very large the WCA system behaves increasingly as a system of hard spheres (HSs). The disordered HS system has a maximum density corresponding to the random closed-packed structure at roughly 64% packing fraction. In Fig. 9, the black star at  $\tilde{D} = 0$  marks the corresponding density. Our data are consistent with a convergence to this point.

## VI. DISCUSSION

We have studied three isomorphs of the WCA system and showed that along them the density-scaling exponent varies by more than a factor of 100. This extreme variation means that the WCA system cannot be considered as an effective

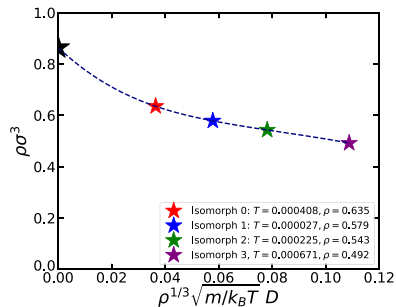


FIG. 9. Reduced diffusion coefficients at the lowest temperature and density for isomorphs 1–3 supplemented by data for isomorph 0, plotted versus the density of the lowest-temperature state point simulated on the isomorph in question. The points are fitted by a cubic spline function (dashed curve), which by construction goes through the random close packing (rcp) density ( $\rho = 0.864$ ) marked by the half black star on the y axis. As rcp is approached, one expects  $\tilde{D} \rightarrow 0$  because the system jams. This is consistent with our data. The rcp density is calculated as follows. With  $r_c = 2^{1/6}$  one finds  $V_{\text{sphere}} = \pi r_c^3/6 = 0.740$ . The rcp volume fraction is roughly 64%; setting this equal to  $\rho V_{\text{sphere}}$ , one arrives at  $\rho = 0.864$ .

IPL system [15]. In the LJ case, the pair potential may be approximated by the so-called extended IPL pair potential, which is a sum of an IPL term  $\sim r^{-18}$ , a constant, and a term proportional to  $r$  [15]. The latter two terms contribute little to the fluctuations of virial and potential energy [15], which explains the strong correlations of the LJ system as well as why  $\gamma$  is close to 6 (not to 4 as one might guess from the repulsive  $r^{-12}$  term of the potential). The WCA situation is very different. Because the WCA system is purely repulsive, it has no liquid-gas phase transition and no liquid-gas coexistence region. This means that isomorphs may be studied over several orders of magnitude of temperature and, in particular, followed to very low temperatures. Interestingly, even here the strong-correlation property is maintained. At the same time,  $\gamma$  increases dramatically. Despite this, the reduced-unit structure and dynamics are both invariant to a good approximation along the isomorphs. The significant difference between the LJ and WCA systems in regard to isomorph properties is also emphasized by the fact that the density-scaling exponent  $\gamma$  of the LJ system is primarily a function of the density and well described by Eq. (3). This is explained by the above-mentioned approximate extended IPL pair-potential argument [15].

The finding that  $R$  and  $\gamma$  of the WCA system are both primarily functions of the temperature is accounted for by a mean-field theory based on the assumption of statistically independent pair interactions. The same feature is observed for the exponential pair-potential system [33], and also here both  $R$  and  $\gamma$  at low densities primarily depend on the temperature. Another situation where this is expected to apply is for the repulsive Yukawa pair-potential system at low densities [29,30].

In summary, the WCA systems presents a striking case where the density-scaling exponent is very far from being constant throughout the thermodynamic phase diagram [35,36]. Nevertheless, the system is  $R$ -simple and has good isomorph invariance of the structure and dynamics.

#### ACKNOWLEDGMENT

This work was supported by the VILLUM Foundation's Matter grant (No. 16515).

#### APPENDIX: USING THE RUNGE-KUTTA METHOD FOR TRACING OUT ISOMORPHS EFFICIENTLY

The density-scaling exponent  $\gamma$  is the slope of the lines of constant  $S_{\text{ex}}$  in the  $(\ln T, \ln \rho)$  plane [Eq. (2)]. By numerical integration one can, from Eq. (2), compute the lines of constant  $S_{\text{ex}}$ , the configurational adiabats, which are isomorphs for any  $R$ -simple system. The density-scaling exponents required for the integration are determined from the thermal equilibrium virial potential-energy fluctuations in an  $NVT$  simulation [Eq. (2)]. In the following we denote the theoretical slope by  $f$ , i.e., the slope without the unavoidable statistical noise of any MD simulation. Let  $(x, y)$  be  $(\ln \rho, \ln T)$  [occasionally it is better to choose instead  $(x, y) = (\ln T, \ln \rho)$ ]. In this notation, let

$$\frac{dy}{dx} = f(x, y) \quad (\text{A1})$$

be the first-order differential equation to be integrated. Several methods have been developed to do this numerically [64]. The simplest one is Euler's method. Imagine that one has estimated the slope at some point  $(x_i, y_i)$  by computing  $\gamma = f(x_i, y_i)$  from the virial potential-energy fluctuations by means of Eq. (2). The point  $(x_{i+1}, y_{i+1})$  is then calculated from

$$\begin{aligned} x_{i+1} &= x_i + h, \\ y_{i+1} &= y_i + hf(x_i, y_i) + O(h^2). \end{aligned} \quad (\text{A2})$$

Here  $h$  is the size of the numerical integration step along  $x$ . The truncation error on the estimated  $y_{i+1}$  scales as  $h^2$ .

The statistical error on the numerical calculation of the slope  $f$  scales as  $1/\sqrt{\tau}$ , where  $\tau$  is the simulation time. Thus, the statistical error on  $y_{i+1}$  scales as  $h/\sqrt{\tau}$  (rounding errors from the finite machine precision are not relevant for the  $h$ 's investigated here). The scaling of the total error is thus proportional to  $h^2 + ch/\sqrt{\tau}$ , in which  $c$  is a constant. We are interested, however, in the global truncation error, i.e., the accumulated error for some integration length  $\Delta x$ . Let  $N = \Delta x/h$  be the number of steps needed to complete the integration. The total simulation time is  $t = N(\tau + \tau_{\text{eq}})$ , where  $\tau_{\text{eq}}$  is the time it takes for the system to come into equilibrium when temperature and density are changed. Thus  $\tau = t/N - \tau_{\text{eq}}$ , and with  $h = \Delta x/N$  the statistical error on  $y$  is  $ch/\sqrt{\tau} = c\Delta x/\sqrt{Nt - N^2\tau_{\text{eq}}}$ . The global error from truncation scales as  $N$  since it is systematic, while the statistical error scales as  $\sqrt{N}$  due to its randomness. Thus, the total global error is proportional to  $(\Delta x)^2/N + c\Delta x/\sqrt{t - N\tau_{\text{eq}}}$ . The first term is lowered by making  $N$  large, while the second term favors small  $N$ 's and diverges as  $N \rightarrow t/\tau_{\text{eq}}$ . Thus, since  $c$  is in general unknown, the optimal choice of  $N$  for a given  $t$  and  $\Delta x$  is not straightforward to determine. We give below a recipe for the optimal parameter choice. First, however, we show how to reduce the truncation error significantly by adopting a higher-order integration method, using the often favored fourth-order Runge-Kutta (RK4) method: For a given point  $(x_i, y_i)$ , if one defines

$$\begin{aligned} k_1 &= hf(x_i, y_i), \\ k_2 &= hf\left(x_i + \frac{h}{2}, y_i + \frac{k_1}{2}\right), \\ k_3 &= hf\left(x_i + \frac{h}{2}, y_i + \frac{k_2}{2}\right), \\ k_4 &= hf(x_i + h, y_i + k_3), \end{aligned} \quad (\text{A3})$$

the next point  $(x_{i+1}, y_{i+1})$  is computed as

$$\begin{aligned} x_{i+1} &= x_i + h, \\ y_{i+1} &= y_i + \frac{k_1}{6} + \frac{k_2}{3} + \frac{k_3}{3} + \frac{k_4}{6} + O(h^5). \end{aligned} \quad (\text{A4})$$

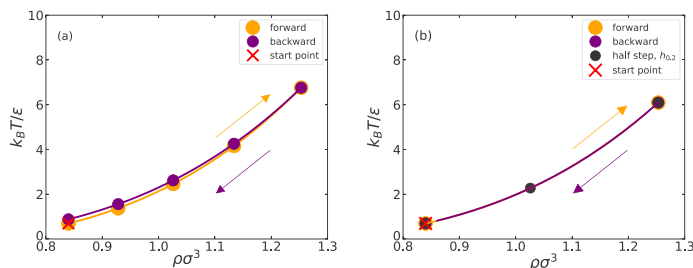


FIG. 10. Configurational adiabat of the WCA system traced out in the thermodynamic phase diagram for (a) the Euler method and (b) the RK4 method. The Euler integration uses a log-density step of size  $h = 0.1$  (steps in density of  $e^{0.1} - 1 \simeq 10\%$ ), while the RK4 uses  $h = 0.4$ , corresponding to a density variation of  $e^{0.4} - 1 \simeq 50\%$ . The temperature difference of the here presented combined forward-backward integration  $\Delta T$  provides a convenient measure of the maximum error of the predicted temperature. We find  $\Delta T \simeq 0.186$  for the Euler algorithm and  $\Delta T \simeq 0.002$  for the RK4 algorithm. The solid lines are interpolations using a cubic Hermite spline.

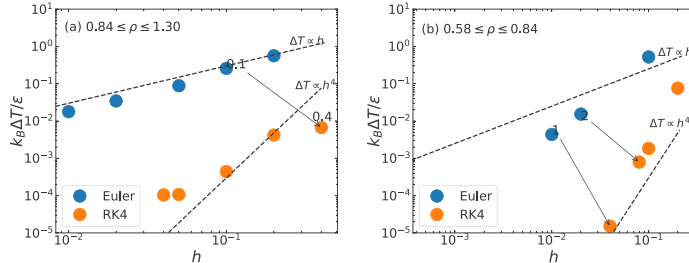


FIG. 11. (a) Temperature difference  $\Delta T$  of the forward-backward integration in Fig. 10, for different steps sizes  $h$ . The blue circles show results for Euler integration and the orange circles show results for RK4 integration. The temperature difference measures the maximum error in the integration interval  $0.84 \leq \rho \leq 1.30$ . The RK4 is significantly more accurate than the Euler algorithm, which allows for larger  $h$  steps. The dashed lines indicate the expected scaling of the global error from truncation; deviations stem from statistical errors on the estimated slopes (slopes are evaluated using simulations lengths of  $\tau = 655$ ). The arrow connects Euler and RK4 calculations with approximately the same computational cost (see Fig. 10). (b) Same analysis for the integration interval  $0.58 \leq \rho \leq 0.84$ .

While the simple Euler method has a truncation error scaling as  $O(h^2)$ , the truncation error of RK4 scales as  $O(h^5)$ . This allows for significantly larger steps along  $x$  and thus smaller  $N$ . From the same type of arguments as given above for the Euler method, the global error of the RK4 method scales approximately as  $(\Delta x)^5/N^4 + c\Delta x/\sqrt{t - N\tau_{\text{eq}}}$ , where  $c$  is a (new) unknown constant.

To compare the Euler and RK4 methods, we use each of them for integrating from the initial state point  $(\rho, T) = (0.84, 0.694)$  to density 1.25 and back again to the initial density of 0.84 (see Fig. 10). This involves a  $\gamma$  variation from 6.825 at the initial density to 4.539 at  $\rho = 1.25$ . The difference between the final temperature of the down integration and the initial temperature, denoted by  $\Delta T$ , provides a measure of the maximum temperature error. Ideally  $\Delta T = 0$ . Since the RK4 involves four simulations per step, we compare its accuracy where  $h$  is four times larger than for the Euler method, which corresponds to approximately the same wall-clock time for the computation. With this constraint, the RK4 is still about two orders of magnitude more accurate: We find  $\Delta T = 0.186$  for the Euler algorithm and  $\Delta T \cong 0.002$  for RK4. Figure 11 shows estimates of the maximum error  $\Delta T$  for several values of  $h$ . To focus on the truncation error, we performed long-time simulations with  $\tau \cong 650$ . Nonetheless, this analysis demonstrates that a significantly smaller  $N$  (larger  $h$ ) is allowed for with the RK4.

Since the RK4 algorithm allows for large  $h$ , it can be necessary to interpolate in order to identify additional state points on the isomorph. The solid lines in Fig. 10 show such interpolations using a cubic Hermite spline. Define  $x_\phi$  as a point between the two adjacent points  $x_i$  and  $x_{i+1}$ , i.e., let  $x_i \leq x_\phi < x_{i+1}$ , where  $x_\phi = x_i + \phi[x_{i+1} - x_i]$  and  $0 \leq \phi \leq 1$ . The interpolated  $y_\phi$  is given by the third-degree polynomial  $y_\phi = Ax_\phi^3 + Bx_\phi^2 + Cx_\phi + D$ , where  $y_\phi = y_i + [y_{i+1} - y_i][a\phi^3 + b\phi^2 + c\phi]$ . For simplicity, we introduce the notation  $y'_\phi = [y_\phi - y_i]/[y_{i+1} - y_i]$  and write the polynomial as  $y'_\phi = a\phi^3 + b\phi^2 + c\phi$ . The coefficients yielding smooth first derivative are  $a = f'_i + f'_{i+1} - 2$ ,  $b = 3 - 2f'_i - f'_{i+1}$ ,

and  $c = f'_i$ , in which  $f'_i = f_i(x_{i+1} - x_i)/(y_{i+1} - y_i)$  and  $f'_{i+1} = f_{i+1}(x_{i+1} - x_i)/(y_{i+1} - y_i)$  are reduced slopes at the start and end points, respectively. The  $f'$  slopes are given by known  $\gamma$ 's along the configurational adiabat; thus no extra simulations are needed to evaluate the interpolation.

We investigated the local error by comparing a full  $h$  step to two half steps of size  $h/2$ . The small black circle near the middle of Fig. 10(b) shows the results of two such half steps. The truncation error for the half-step approach is then raised to the sixth order [64], one order higher than RK4 (the consequence is that one must perform twice as many simulations for each integration step). The triangles in Fig. 12 show the resulting  $T_{i+1}$  starting from the reference state point  $(\rho, T) = (0.84, 0.694)$ , using a full step with  $h = 0.4$  and

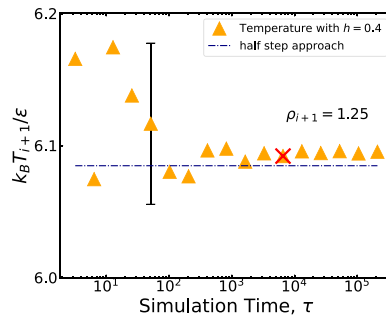


FIG. 12. Difference in temperature between using a full step of  $h = 0.4$  and two half steps of  $h = 0.2$  when integrating from  $\rho = 0.84$  up to  $\rho = 1.25$ , plotted against the simulation time per slope evaluation. The desired  $h$  can change and the simulation time changes accordingly. The error bar indicates the bad statistics with few blocks mentioned in the text, computed from Eq. (28) in Ref. [65]. The red  $\times$  marks the simulation time used in the paper.

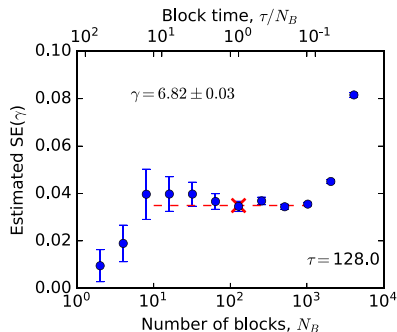


FIG. 13. Estimate of the statistical error on  $\gamma$  from the blocking method. The analysis indicates that  $N_B = 128$  is a good choice for the number of blocks. This gives  $SE(\gamma) = 0.03$  on the estimated  $\gamma = 6.82$ .

varying  $\tau$ 's. For comparison, the dashed line results from long-time simulations using the half-step algorithm. The distance from triangles to the dashed line provides an estimate of the total error. For short simulation times (small  $\tau$ 's) the statistical error dominates, as shown by the scatter. The truncation error dominates at long simulation times, as shown by the triangles' systematic deviation from the dashed line. For efficient calculation we suggest choosing  $h$  and  $\tau$  such that the statistical and truncation errors are of the same order of magnitude. The red cross in Fig. 12 indicates the simulation time  $\tau$  used for the figures in the paper.

The above analysis to arrive at the optimal computation time  $\tau$  is tedious and involves computationally expensive simulations. We proceed to suggest an efficient optimization recipe that utilizes the fact that the local statistical error of the slopes can be estimated by dividing a given simulation into blocks. If the simulation time for each block is sufficiently long, the blocks are statistically independent. The 67% confidence standard error is then given by  $SE(\gamma) = \sqrt{\text{Var}(\gamma)/(N_B - 1)}$ , where  $\text{Var}(\gamma)$  is the variance of the  $\gamma$ 's using  $N_B$  blocks [65]. If the blocks are independent,  $\text{Var}(\gamma)$  scales as  $N_B$  and  $SE(\gamma)$  will be independent of the number of blocks. If we divide the simulation into few blocks,  $\text{Var}(\gamma)$  may give a bad estimate of the underlying distribution's theoretical variance. On the other hand, if one divides the simulation into many blocks, the simulation time for each block ( $\tau/N_B$ ) may be brief and the blocks are not independent. In effect, the above formula for  $SE(\gamma)$  gives an overestimate. The optimal  $N_B$  is determined by tests of several different  $N_B$ , as shown in Fig. 13 (the red cross corresponds to a good choice of  $N_B = 128$ ). The statistical error on  $y_{i+1}$  can now be estimated as  $SE(y_{i+1}) = SE(\gamma)h/2$ . Here  $2 = \sqrt{4}$  enters since the RK4 algorithm includes four independent estimates

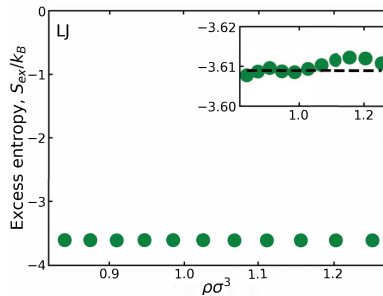


FIG. 14. Excess entropy values plotted against the densities of the state points on the configurational adiabat traced out by the single-component LJ system starting from the triple point ( $\rho = 0.84$ ,  $T = 0.694$ ) using RK4 with  $h = 0.04$ . The view is zoomed in on the values to see the deviation from the average value, the black dotted line.

of slopes (the factor is unity for the Euler algorithm and  $\sqrt{8}$  for the double-step RK4).

Based on the above analysis, we propose the following recipe for efficient and accurate computation of a configurational adiabat.

(i) Make an  $NVT$  simulation at a reference state point of temperature  $T_0$  and density  $\rho_0$ . The simulation time  $\tau$  should be sufficiently long that the equilibration time  $\tau_{\text{eq}}$  can be determined using any standard method (e.g., as the time when the mean-square displacement has reached the diffusive limit). Use the block method to determine  $SE(\gamma)$ , using only the equilibrated part of the trajectory.

(ii) Choose  $h$ . Make a full RK4 step and estimate the local statistical error using  $SE(y_{i+1}) = hSE(\gamma)/\sqrt{4}$ . Use the RK4 two-half-step approach to estimate the total local error. If the total local error is unacceptably large, then either (a) increase  $\tau$  if the statistical error is of the same magnitude as the total error or (b) decrease  $h$  if the total error is larger than the statistical error. Small errors suggest that the simulation time  $\tau$  could be decreased or that  $h$  can be increased to make the calculation more efficient;  $h$  may safely be increased or  $\tau$  decreased if the statistical and total errors are of similar magnitude.

(iii) Compute adiabatic state points using the RK4 algorithm with the parameters determined in the above steps. Based on these, a continuous curve can be produced by interpolation using a cubic spline.

(iv) Estimate the maximum error by integrating backward. This error estimate quantifies the accuracy of the computed adiabat.

As a consistency check of this recipe, Fig. 14 shows the excess entropy from the equation of state (EOS) of the single-component LJ system in Ref. [66]. The agreement with the configurational adiabat of this EOS is excellent.

- [1] C. Alba-Simionesco, A. Caillaux, A. Alegria, and G. Tarjus, Scaling out the density dependence of the alpha relaxation in glass-forming polymers, *Europhys. Lett.* **68**, 58 (2004).
- [2] C. M. Roland, S. Hensel-Bielowka, M. Paluch, and R. Casalini, Supercooled dynamics of glass-forming liquids and polymers under hydrostatic pressure, *Rep. Prog. Phys.* **68**, 1405 (2005).
- [3] E. R. Lopez, A. S. Pensado, J. Fernandez, and K. R. Harris, On the density scaling of  $pVT$  data and transport properties for molecular and ionic liquids, *J. Chem. Phys.* **136**, 214502 (2012).
- [4] K. Adrjanowicz, M. Paluch, and J. Pionteck, Isochronal superposition and density scaling of the intermolecular dynamics in glass-forming liquids with varying hydrogen bonding propensity, *RSC Adv.* **6**, 49370 (2016).
- [5] D. Gundermann, U. R. Pedersen, T. Hecksher, N. P. Bailey, B. Jakobsen, T. Christensen, N. B. Olsen, T. B. Schröder, D. Fragiadakis, R. Casalini, C. M. Roland, J. C. Dyre, and K. Niss, Predicting the density-scaling exponent of a glass-forming liquid from Prigogine-Defay ratio measurements, *Nat. Phys.* **7**, 816 (2011).
- [6] D. Kivelson, G. Tarjus, X. Zhao, and S. A. Kivelson, Fitting of viscosity: Distinguishing the temperature dependences predicted by various models of supercooled liquids, *Phys. Rev. E* **53**, 751 (1996).
- [7] N. Gnan, T. B. Schröder, U. R. Pedersen, N. P. Bailey, and J. C. Dyre, Pressure-energy correlations in liquids. IV. "Isomorphs" in liquid phase diagrams, *J. Chem. Phys.* **131**, 234504 (2009).
- [8] J. C. Dyre, Hidden scale invariance in condensed matter, *J. Phys. Chem. B* **118**, 10007 (2014).
- [9] Y. Rosenfeld, Relation between the transport coefficients and the internal entropy of simple systems, *Phys. Rev. A* **15**, 2545 (1977).
- [10] J. C. Dyre, Perspective: Excess-entropy scaling, *J. Chem. Phys.* **149**, 210901 (2018).
- [11] T. B. Schröder and J. C. Dyre, Simplicity of condensed matter at its core: Generic definition of a Roskilde-simple system, *J. Chem. Phys.* **141**, 204502 (2014).
- [12] U. R. Pedersen, N. P. Bailey, T. B. Schröder, and J. C. Dyre, Strong Pressure-Energy Correlations in van der Waals Liquids, *Phys. Rev. Lett.* **100**, 015701 (2008).
- [13] N. P. Bailey, U. R. Pedersen, N. Gnan, T. B. Schröder, and J. C. Dyre, Pressure-energy correlations in liquids. I. Results from computer simulations, *J. Chem. Phys.* **129**, 184507 (2008).
- [14] D. M. Heyes and A. C. Branka, Physical properties of soft repulsive particle fluids, *Phys. Chem. Chem. Phys.* **9**, 5570 (2007).
- [15] N. P. Bailey, U. R. Pedersen, N. Gnan, T. B. Schröder, and J. C. Dyre, Pressure-energy correlations in liquids. II. Analysis and consequences, *J. Chem. Phys.* **129**, 184508 (2008).
- [16] T. B. Schröder, N. Gnan, U. R. Pedersen, N. P. Bailey, and J. C. Dyre, Pressure-energy correlations in liquids. V. Isomorphs in generalized Lennard-Jones systems, *J. Chem. Phys.* **134**, 164505 (2011).
- [17] T.-J. Yoon, M. Y. Ha, E. A. Lazar, W. B. Lee, and Y.-W. Lee, Topological extension of the isomorph theory based on the Shannon entropy, *Phys. Rev. E* **100**, 012118 (2019).
- [18] A. K. Bacher, T. B. Schröder, and J. C. Dyre, The EXP pair-potential system. I. Fluid phase isotherms, isochores, and quasiuniversality, *J. Chem. Phys.* **149**, 114501 (2019).
- [19] A. K. Bacher, U. R. Pedersen, T. B. Schröder, and J. C. Dyre, The EXP pair-potential system. IV. Isotherms, isochores, and isomorphs in the two crystalline phases, *J. Chem. Phys.* **152**, 094505 (2020).
- [20] T. S. Ingebrigtsen, T. B. Schröder, and J. C. Dyre, Isomorphs in model molecular liquids, *J. Phys. Chem. B* **116**, 1018 (2012).
- [21] D. Fragiadakis and C. M. Roland, Intermolecular distance and density scaling of dynamics in molecular liquids, *J. Chem. Phys.* **150**, 204501 (2019).
- [22] K. Koperwas, A. Grzybowski, and M. Paluch, Virial-potential-energy correlation and its relation to density scaling for quasireal model systems, *Phys. Rev. E* **102**, 062140 (2020).
- [23] T. S. Ingebrigtsen and H. Tanaka, Effect of size polydispersity on the nature of Lennard-Jones liquids, *J. Phys. Chem. B* **119**, 11052 (2015).
- [24] D. E. Albrechtsen, A. E. Olsen, U. R. Pedersen, T. B. Schröder, and J. C. Dyre, Isomorph invariance of the structure and dynamics of classical crystals, *Phys. Rev. B* **90**, 094106 (2014).
- [25] T. S. Ingebrigtsen, J. R. Errington, T. M. Truskett, and J. C. Dyre, Predicting how Nanoconfinement Changes the Relaxation Time of a Supercooled Liquid, *Phys. Rev. Lett.* **111**, 235901 (2013).
- [26] A. A. Veldhorst, J. C. Dyre, and T. B. Schröder, Scaling of the dynamics of flexible Lennard-Jones chains, *J. Chem. Phys.* **141**, 054904 (2014).
- [27] F. Hummel, G. Kresse, J. C. Dyre, and U. R. Pedersen, Hidden scale invariance of metals, *Phys. Rev. B* **92**, 174116 (2015).
- [28] L. Friedeheim, J. C. Dyre, and N. P. Bailey, Hidden scale invariance at high pressures in gold and five other face-centered-cubic metal crystals, *Phys. Rev. E* **99**, 022142 (2019).
- [29] A. A. Veldhorst, T. B. Schröder, and J. C. Dyre, Invariants in the Yukawa system's thermodynamic phase diagram, *Phys. Plasmas* **22**, 073705 (2015).
- [30] P. Toliaas and F. L. Castello, Isomorph-based empirically modified hypernetted-chain approach for strongly coupled Yukawa one-component plasmas, *Phys. Plasmas* **26**, 043703 (2019).
- [31] T. B. Schröder, U. R. Pedersen, N. P. Bailey, S. Toxvaerd, and J. C. Dyre, Hidden scale invariance in molecular van der Waals liquids: A simulation study, *Phys. Rev. E* **80**, 041502 (2009).
- [32] T. S. Ingebrigtsen, L. Böhling, T. B. Schröder, and J. C. Dyre, Thermodynamics of condensed matter with strong pressure-energy correlations, *J. Chem. Phys.* **136**, 061102 (2012).
- [33] A. K. Bacher, T. B. Schröder, and J. C. Dyre, The EXP pair-potential system. II. Fluid phase isomorphs, *J. Chem. Phys.* **149**, 114502 (2018).
- [34] D. M. Heyes, D. Dini, L. Costigliola, and J. C. Dyre, Transport coefficients of the Lennard-Jones fluid close to the freezing line, *J. Chem. Phys.* **151**, 204502 (2019).
- [35] A. Sanz, T. Hecksher, H. W. Hansen, J. C. Dyre, K. Niss, and U. R. Pedersen, Experimental Evidence for a State-Point-Dependent Density-Scaling Exponent of Liquid Dynamics, *Phys. Rev. Lett.* **122**, 055501 (2019).
- [36] R. Casalini and T. C. Ransom, On the experimental determination of the repulsive component of the potential from high pressure measurements: What is special about twelve?" *J. Chem. Phys.* **151**, 194504 (2019).
- [37] L. Böhling, T. S. Ingebrigtsen, A. Grzybowski, M. Paluch, J. C. Dyre, and T. B. Schröder, Scaling of viscous dynamics in simple liquids: Theory, simulation and experiment, *New J. Phys.* **14**, 113035 (2012).
- [38] T. C. Ransom, R. Casalini, D. Fragiadakis, and C. M. Roland, The complex behavior of the "simplest" liquid: Breakdown of

- density scaling in tetramethyl tetraphenyl trisiloxane, *J. Chem. Phys.* **151**, 174501 (2019).
- [39] J. D. Weeks, D. Chandler, and H. C. Andersen, Role of repulsive forces in determining the equilibrium structure of simple liquids, *J. Chem. Phys.* **54**, 5237 (1971).
- [40] D. Chandler, J. D. Weeks, and H. C. Andersen, Van der Waals picture of liquids, solids, and phase transformations, *Science* **220**, 787 (1983).
- [41] A. de Kuijper, J. A. Schouten, and J. P. J. Michels, The melting line of the Weeks-Chandler-Anderson Lennard-Jones reference system, *J. Chem. Phys.* **93**, 3515 (1990).
- [42] M. Bishop, A. Masters, and J. H. R. Clarke, Equation of state of hard and Weeks-Chandler-Anderson hyperspheres in four and five dimensions, *J. Chem. Phys.* **110**, 11449 (1999).
- [43] D. Ben-Amotz and G. Stell, Reformulation of Weeks-Chandler-Anderson perturbation theory directly in terms of a hard-sphere reference system, *J. Phys. Chem. B* **108**, 6877 (2004).
- [44] A. E. Nasrabad, Thermodynamic and transport properties of the Weeks-Chandler-Anderson fluid: Theory and computer simulation, *J. Chem. Phys.* **129**, 244508 (2008).
- [45] A. Ahmed and R. J. Sadus, Phase diagram of the Weeks-Chandler-Anderson potential from very low to high temperatures and pressures, *Phys. Rev. E* **80**, 061101 (2009).
- [46] R. Benjamin and J. Horbach, Crystal growth kinetics in Lennard-Jones and Weeks-Chandler-Anderson systems along the solid-liquid coexistence line, *J. Chem. Phys.* **143**, 014702 (2015).
- [47] B. Atreyee and D. J. Wales, Fragility and correlated dynamics in supercooled liquids, *J. Chem. Phys.* **153**, 124501 (2020).
- [48] N. Dawass, P. Krüger, S. K. Schnell, O. A. Moulton, I. G. Economou, T. J. H. Vlugt, and J.-M. Simon, Kirkwood-Buff integrals using molecular simulation: Estimation of surface effects, *Nanomaterials* **10**, 771 (2020).
- [49] F. Gußmann, S. Dietrich, and R. Roth, Toward a density-functional theory for the Jagla fluid, *Phys. Rev. E* **102**, 062112 (2020).
- [50] A. Mirzaeinia and F. Feyzi, A perturbed-chain equation of state based on Wertheim TPT for the fully flexible LJ chains in the fluid and solid phases, *J. Chem. Phys.* **152**, 134502 (2020).
- [51] T. P. O. Nogueira, H. O. Frota, F. Piazza, and J. R. Bordin, Tracer diffusion in crowded solutions of sticky polymers, *Phys. Rev. E* **102**, 032618 (2020).
- [52] H. Tong and H. Tanaka, Role of Attractive Interactions in Structure Ordering and Dynamics of Glass-Forming Liquids, *Phys. Rev. Lett.* **124**, 225501 (2020).
- [53] S. Ueda and K. Morita, Theoretical calculation of the free energy of mixing of liquid transition-metal alloys using a bond-order potential and thermodynamic perturbation theory, *J. Non-Cryst. Solids* **528**, 119743 (2020).
- [54] J.-P. Hansen and I. R. McDonald, *Theory of Simple Liquids: With Applications to Soft Matter*, 4th ed. (Academic, New York, 2013).
- [55] M. P. Allen and D. J. Tildesley, *Computer Simulation of Liquids* (Oxford Science, Oxford, 1987).
- [56] N. P. Bailey, T. S. Ingebrigtsen, J. S. Hansen, A. A. Veldhorst, L. Böhling, C. A. Lemarchand, A. E. Olsen, A. K. Bacher, L. Costigliola, U. R. Pedersen, H. Larsen, J. C. Dyre, and T. B. Schröder, RUMD: A general purpose molecular dynamics package optimized to utilize GPU hardware down to a few thousand particles, *SciPost Phys.* **3**, 038 (2017).
- [57] <http://rumd.org>, version 3.5 (Glass and Time, Roskilde, 2020).
- [58] U. R. Pedersen, L. Costigliola, N. P. Bailey, T. B. Schröder, and J. C. Dyre, Thermodynamics of freezing and melting, *Nat. Commun.* **7**, 12386 (2016).
- [59] R. Casalini and T. C. Ransom, On the pressure dependence of the thermodynamical scaling exponent  $\gamma$ , *Soft Matter* **16**, 4625 (2020).
- [60] T. Maimbourg and J. Kurchan, Approximate scale invariance in particle systems: A large-dimensional justification, *Europhys. Lett.* **114**, 60002 (2016).
- [61] T. Maimbourg, J. C. Dyre, and L. Costigliola, Density scaling of generalized Lennard-Jones fluids in different dimensions, *SciPost Phys.* **9**, 90 (2020).
- [62] D. M. Heyes, D. Dini, and A. C. Branka, Scaling of Lennard-Jones liquid elastic moduli, viscoelasticity and other properties along fluid-solid coexistence, *Phys. Status Solidi B* **252**, 1514 (2015).
- [63] F. L. Castello, P. Toliás, and J. C. Dyre, Testing the isomorph invariance of the bridge functions of Yukawa one-component plasmas, *J. Chem. Phys.* **154**, 034501 (2021).
- [64] W. H. Press, S. A. Teukolsky, W. T. Vetterling, and B. P. Flannery, *Numerical Recipes: The Art of Scientific Computing*, 3rd ed. (Cambridge University Press, Cambridge, 2007).
- [65] H. Flyvbjerg and H. G. Petersen, Error estimates on averages of correlated data, *J. Chem. Phys.* **91**, 461 (1989).
- [66] J. Kolafa and I. Nezbeda, The Lennard-Jones fluid: An accurate analytic and theoretically-based equation of state, *Fluid Phase Equilib.* **100**, 1 (1994).

# Isomorph invariance in the liquid and plastic-crystal phases of asymmetric dumbbell models

Eman Attia,<sup>\*</sup> Jeppe C. Dyre,<sup>†</sup> and Ulf R. Pedersen<sup>‡</sup>  
*Glass and Time, IMFUFA, Department of Science and Environment,  
Roskilde University, P.O. Box 260, DK-4000 Roskilde, Denmark*  
(Dated: September 26, 2022)

This paper presents a numerical study of the asymmetric dumbbell model consisting of “molecules” constructed as two different Lennard-Jones spheres connected by a rigid bond. In terms of the largest (A) particle radius, we report data for the structure and dynamics of the liquid phase for the bond lengths 0.05, 0.1, 0.2, and 0.5, and analogous data for the plastic crystalline phase for the bond lengths 0.05, 0.1, 0.2, and 0.3. Structure is probed by means of the AA, AB, and BB radial distribution functions. Dynamics is probed via the A and B particle mean-square displacement as functions of time and via the rotational time-autocorrelation function. Consistent with the systems’ strong virial potential-energy correlations, the structure and dynamics are both found to be isomorph invariant to a good approximation in reduced units, while they generally vary considerably along isotherms of the same (20%) density variation. Our findings provide the first validation of isomorph-theory predictions for plastic crystals for which isomorph invariance, in fact, is found to apply even better than in the liquid phase of asymmetric dumbbells.

arXiv:2209.11498v1 [cond-mat.soft] 23 Sep 2022

---

<sup>\*</sup> attia@ruc.dk  
<sup>†</sup> dyre@ruc.dk  
<sup>‡</sup> urp@ruc.dk

## I. INTRODUCTION

This paper presents a systematic study of the asymmetric dumbbell model (ASD) consisting of two different-sized Lennard-Jones (LJ) spheres connected by a rigid bond. The ASD model is designed to be a simple molecular model [1–3]. Because of the asymmetry, the liquid phase of the model is easily supercooled, i.e., the model does not readily crystallize [2]. This makes it suitable for numerical studies as a simple, single-component glass-forming model of non-spherically symmetric constituents [2, 4–8].

The focus here is not on supercooling and glass formation, however, but on investigating what happens when the bond length is varied in the less viscous liquid and plastic-crystalline phases. It was previously shown that for the bond length 0.58 (in units of the largest (A) particle’s radius used henceforth for reporting bond lengths), the ASD model obeys the hidden-scale invariance symmetry; this manifests itself in strong virial potential-energy correlations in the thermal-equilibrium constant-volume fluctuations [2]. This implies the existence of so-called isomorphs, which are lines in the thermodynamic phase diagram along which structure and dynamics in proper reduced units are invariant to a good approximation [2, 9, 10]. We confirm this below and demonstrate that the existence of isomorphs is robust to bond-length changes. This is done by simulating the ASD model in the liquid phase with bond lengths 0.05, 0.1, 0.2, and 0.5. We also investigate the model’s plastic crystalline phase with a focus on the existence of isomorphs; here the largest bond length simulated is 0.3 because for larger bond lengths the system was liquid at the chosen reference state point.

Our investigation reports data illuminating the degree of isomorph invariance of structure and dynamics. This is done by comparing results along isomorphs with results along isotherms of the same density variation. Specifically, the structure is investigated by monitoring radial distribution functions (RDF), while the dynamics is investigated by the mean-square displacement (MSD) as functions of time as well as the rotational time-autocorrelation function (RAC). We find good isomorph invariance of both structure and dynamics.

The present paper presents the first investigation of the consequences of hidden scale invariance for a system of molecules forming plastic crystals. In the plastic crystalline phase the molecules are free to rotate at their lattice positions. We find excellent isomorph invariance here, in fact somewhat better than in the liquid phase.

## II. MODEL AND SIMULATION DETAILS

The asymmetrical dumbbell is a constrained molecular model. It consists of two different Lennard Jones (LJ) spheres, one big (A) and one smaller (B). If the two spheres are connected by a rigid bond of length = 0.584 in A particle LJ units, the model mimics toluene [2, 11]. The values of the parameters used below are as follow. For particle A the distance and energy parameters are  $\sigma_{AA} = \varepsilon_{AA} = 1$  and the particle mass is  $m_A = 1$ ; for particle B one has  $\sigma_{BB} = 0.788$ ,  $\varepsilon_{BB} = 0.117$  and  $m_B = 0.195$  (in A particle units); for the AB interaction one has  $\sigma_{AB} = 0.894$  and  $\varepsilon_{AB} = 0.342$  [11].

The system is studied by molecular dynamics simulations in the canonical  $NVT$  ensemble using the Nosé-Hoover thermostat [12]. The simulated system consists of 4000 molecules in a cubic box with periodic boundaries. Simulations are performed using the open-source Roskilde University molecular dynamics software (RUMD) that runs on GPUs (graphics processing units) [13]. The leapfrog algorithm is used with time step  $dt = 0.001$  (in LJ units). First,  $NVE$  simulations were carried out for  $10^6$  time steps for equilibration and  $10^6$  time steps for production runs with time step sizes 0.0005, 0.005, 0.001, 0.002, and 0.01 in order to investigate how constant the energy is at the reference state point defined by  $\rho = 1.5$  and  $T = 1.5$  ( $\rho$  is the density defined as the total number of atoms (8000) divided by the simulation box volume  $V$ ,  $T$  is the temperature). The bond lengths chosen for these  $NVE$  simulations were 0.05 and 0.5. We concluded that the time step 0.001 in both cases shows good energy conservation; in the limit of zero time step rigorous energy conservation is ensured, so the “best” time step is a compromise between efficiency and energy conservation. For the subsequent  $NVT$  simulations used for generating the data presented below, at each state point the simulations again ran for  $10^6$  time steps for equilibration and  $10^6$  time steps for production runs.

For the post analysis of the structure and dynamics, the units used are the isomorph-theory’s reduced units defined as follows: energy unit:  $e_0 \equiv k_B T$ , length unit:  $l_0 \equiv \rho^{-1/3}$ , time unit:  $t_0 \equiv \rho^{-1/3} \sqrt{m_A/k_B T}$ . Note that these units vary with state point. Exceptions to the use of reduced units apply for density and temperature that are by definition both unity in reduced units; these quantities are reported in the above LJ units.

## III. ESSENTIAL ISOMORPH THEORY

Hidden scale invariance is a symmetry of the potential energy function  $U(\mathbf{R})$  in which the configuration  $\mathbf{R}$  in terms of the particle coordinates is defined by  $\mathbf{R} \equiv (\mathbf{r}_1, \dots, \mathbf{r}_N)$ . If  $\mathbf{R}_a$  and  $\mathbf{R}_b$  are two same-density configurations, hidden

scale invariance is defined by the following scale-invariance mathematical implication (in which  $\lambda$  is a uniform-scaling parameter)

$$U(\mathbf{R}_a) < U(\mathbf{R}_b) \Rightarrow U(\lambda\mathbf{R}_a) < U(\lambda\mathbf{R}_b). \quad (1)$$

This symmetry is only rigorously obeyed if  $U(\mathbf{R})$  is an Euler-homogeneous function plus a constant, but it applies to a good approximation for many other systems, e.g., single- and multicomponent LJ systems, the Yukawa pair potential, and the Morse pair potential [2, 9, 10, 14]. Equation (1) may also apply for molecular models like the ASD model, in which case the centers of masses are scaled uniformly whereas intramolecular bond lengths and molecular orientations are kept unchanged.

Consider a system in equilibrium at the (number) density  $\rho \equiv N/V$  where  $N$  is the number of atoms (in our case 8000) and  $V$  is the volume. The excess entropy  $S_{\text{ex}}$  is defined as the entropy minus that of an ideal gas at the same density and temperature. Any state point of the thermodynamic phase diagram is fully characterized by the two thermodynamic variables  $\rho$  and  $T$ , but other variables may of course also be used to characterize a state point. We define the *microscopic excess-entropy* function  $S_{\text{ex}}(\mathbf{R})$  by [14]

$$S_{\text{ex}}(\mathbf{R}) \equiv S_{\text{ex}}(\rho, U(\mathbf{R})). \quad (2)$$

Here  $S_{\text{ex}}(\rho, U)$  is the excess entropy of the state point  $(\rho, U)$  in which  $U$  is the average potential energy. It follows from statistical mechanics that  $S_{\text{ex}}(\mathbf{R})$  is proportional to the logarithm of the number of configurations with the same density and potential energy as  $\mathbf{R}$  [15]. Inverting Eq. (2) leads to

$$U(\mathbf{R}) = U(\rho, S_{\text{ex}}(\mathbf{R})). \quad (3)$$

Here,  $U(\rho, S_{\text{ex}})$  is the average potential energy of the state point of density  $\rho$  and excess entropy  $S_{\text{ex}}$ .

It can be shown that Eq. (1) implies the function  $S_{\text{ex}}(\mathbf{R})$  is scale invariant, i.e.,  $S_{\text{ex}}(\lambda\mathbf{R}) = S_{\text{ex}}(\mathbf{R})$  [14]. In this case,  $S_{\text{ex}}(\mathbf{R})$  depends only on the configuration's so-called reduced coordinate vector  $\tilde{\mathbf{R}} \equiv \rho^{1/3}\mathbf{R}$  (which is invariant upon a uniform scaling):

$$S_{\text{ex}}(\mathbf{R}) = S_{\text{ex}}(\tilde{\mathbf{R}}). \quad (4)$$

Consequently, Eq. (3) becomes

$$U(\mathbf{R}) = U(\rho, S_{\text{ex}}(\tilde{\mathbf{R}})). \quad (5)$$

All identities of the isomorph theory may be derived from Eq. (5) [14]. In particular, Eq. (5) implies strong correlations between the constant-volume fluctuations of the virial  $W$  and the potential energy  $U$ . Thus the equilibrium deviations from the average of these two variables,  $\Delta W$  and  $\Delta U$ , obey [16–18]

$$\Delta W \cong \gamma \Delta U. \quad (6)$$

Here the so-called density-scaling exponent  $\gamma$  is defined and characterized by [9]

$$\gamma \equiv \left( \frac{\partial \ln T}{\partial \ln \rho} \right)_{S_{\text{ex}}} = \frac{\langle \Delta U \Delta W \rangle}{\langle (\Delta U)^2 \rangle}. \quad (7)$$

The second equality sign allows one to calculate  $\gamma$  from the constant-volume thermal-equilibrium canonical-ensemble fluctuations at the state point in question.

Using the identity  $T = (\partial U / \partial S_{\text{ex}})_{\rho}$ , a first-order Taylor expansion of Eq. (5) leads [14] to

$$U(\mathbf{R}) \cong U(\rho, S_{\text{ex}}) + T(\rho, S_{\text{ex}}) \left( S_{\text{ex}}(\tilde{\mathbf{R}}) - S_{\text{ex}} \right). \quad (8)$$

Consider two state points  $(\rho_1, T_1)$  and  $(\rho_2, T_2)$  with average potential energies  $U_1$  and  $U_2$  and same excess entropy  $S_{\text{ex}}$ , and suppose that  $\mathbf{R}_1$  and  $\mathbf{R}_2$  are equilibrium configurations of the two state points with the same reduced coordinates,

i.e.,  $\rho_1^{1/3}\mathbf{R}_1 = \rho_2^{1/3}\mathbf{R}_2 \equiv \tilde{\mathbf{R}}$ . In that case, by elimination of  $S_{\text{ex}}(\tilde{\mathbf{R}}) - S_{\text{ex}}$ , Eq. (8) implies that with  $T_1 \equiv T(\rho_1, S_{\text{ex}})$  and  $T_2 \equiv T(\rho_2, S_{\text{ex}})$  one has

$$\frac{U(\mathbf{R}_1) - U_1}{k_B T_1} \cong \frac{U(\mathbf{R}_2) - U_2}{k_B T_2}. \quad (9)$$

This implies that

$$e^{-U(\mathbf{R}_1)/k_B T_1} \cong C_{12} e^{-U(\mathbf{R}_2)/k_B T_2} \quad (10)$$

in which  $C_{12}$  is a constant. Equation (10) is the original 2009 definition of isomorphic state points [9], which stated that the canonical probabilities of configurations that scale uniformly into one another are identical along an isomorph (the value of the constant  $C_{12}$  is irrelevant because probabilities are normalized). This identity of the probabilities of scaled configurations implies that the  $S_{\text{ex}}$  is constant along an isomorph. In fact, the 2014 version of the isomorph theory, which introduced Eq. (1), *defined* isomorphs as lines of constant excess entropy in the thermodynamic phase diagram [14].

It can be shown, either from Eq. (10) [9] or from Eq. (5) [14], that the dynamics at two isomorphic state points are identical in the following “same movie” sense: Filming the molecules’ motion at one state point results in the same movie at a different, isomorphic state point – except for a uniform scaling of space and time. This implies several dynamic isomorph invariants and that the reduced-unit structure is isomorph invariant.

How does one decide whether a given system is expected to have good isomorphs? According to Eq. (6) this is the case when the virial and potential-energy fluctuations are highly correlated, which can be investigated by evaluating their Pearson correlation coefficient defined by

$$R = \frac{\langle \Delta U \Delta W \rangle}{\sqrt{\langle (\Delta U)^2 \rangle \langle (\Delta W)^2 \rangle}}. \quad (11)$$

A system is “R-simple”, i.e., simple in the sense of having good isomorphs and thus an essentially one-dimensional thermodynamic phase diagram, if  $R > 0.9$  at the state points of interest [14, 16, 17]. This is a somewhat arbitrary criterion, though, in the sense that the “good-isomorph” property depends on the quantity in question because in practice some reduced-unit quantities are more isomorph invariant than others. Note also that how invariant a given property appears to be, of course, depends on how large a density range is being explored.

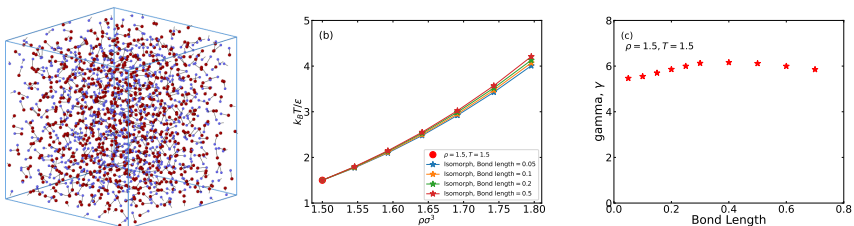


FIG. 1. (a) Snapshot of a liquid configuration at  $\rho = 0.8, T = 0.8$ . The bond length between particle A (red) and B (blue) in this configuration is 0.58 in A particle units [2]. (b) Four isomorphs traced out in the liquid regime of the ASD thermodynamic phase diagram using the fourth-order Runge-Kutta (RK4) method with density step size 0.01. Each isomorph is traced out with a different bond length, going from 0.05 till 0.5. The isomorphs are qualitatively similar, but we observe a slight increase in the temperatures of the traced state points with increasing bond length. (c) The variation of the density-scaling exponent  $\gamma$  (Eq. (7)) at the reference state point  $\rho = 1.5, T = 1.5$  of each isomorph for the different bond lengths. Data for a few extra bond lengths have been added in order to have a better view of the  $\gamma$  variation. We see that  $\gamma$  has a maximum around bond length 0.3-0.4, indicating a change of physics here.

TABLE I. Thermodynamic parameters of the liquid reference state point, giving temperature, density, and pressure (in A particle LJ units), as well as the density-scaling exponent  $\gamma$  and the virial potential-energy correlation coefficient  $R$ .

Bond length [ $1/\sigma_{AA}$ ]	$\rho$ [ $1/\sigma_{AA}^3$ ]	$T$ [ $\epsilon_{AA}/k$ ]	$p$ [ $\sigma_{AA}^3\epsilon_{AA}$ ]	$\gamma$	$R$
0.05	1.5	1.5	1.089	5.474	0.850
0.10	1.5	1.5	1.049	5.548	0.850
0.20	1.5	1.5	1.606	5.941	0.894
0.50	1.5	1.5	7.496	6.116	0.961

#### IV. RESULTS FOR THE LIQUID PHASE

In this section we investigate the liquid phase for the bond lengths 0.05, 0.1, 0.2, and 0.5. First, however, Figure 1(a) shows a snapshot of the ASD liquid at the bond length previously studied by Ingebrigtsen *et al.* [2] (0.58 in A particle LJ units) [2] at a liquid state point. The larger A particles are red, the smaller B particles are blue. We see the typical disorder of a liquid configuration. Reducing the bond length results in a system that is increasingly like the atomic LJ liquid, but even for the smallest bond length studied below (0.05) we still find typical molecular-liquid behavior (see below).

Isomorphs, i.e., curves of constant excess entropy  $S_{\text{ex}}$ , are traced out by numerically integrating Eq. (7). In this way one avoids the tedious thermodynamic integrations necessary to determine  $S_{\text{ex}}$  throughout the thermodynamic phase diagram. Specifically, the last term of Eq. (7) specifies how the density-scaling exponent  $\gamma$  may be calculated numerically from an  $NVT$  simulation at the state point in question. Integrating the first-order differential equation defined by the second equality sign in Eq. (7), in order to determine how temperature varies with density along an isomorph, is in principle straightforward. The highly accurate fourth-order Runge-Kutta (RK4) integration method was recently implemented for this [19]. We used that method here with a density change of 1%. For all four bond lengths we start the integration at the reference state point  $(\rho, T) = (1.5, 1.5)$ . Thus all four isomorphs pass through this state point in common. Table I gives the pressure, density-scaling exponent, and virial potential-energy correlation coefficient for the four bond lengths at the reference state point.

The isomorphs are not very different (Fig. 1(b)), but we note in that larger bond lengths result in somewhat larger temperatures at a given density. This reflects larger density-scaling exponents  $\gamma$  for the larger bond lengths, as is evident from Fig. 1(c) which shows  $\gamma$  at the reference state point for several bond lengths. A value of  $\gamma$  between 5 and 6 is typical for atomic LJ system [17, 18] so these results are not unexpected. We note a slight drop of  $\gamma$  at the largest bond length studied, but the overall  $\gamma$  variation is just 15% while, as we shall see, the physics varies considerably when the bond length is changed from 0.05 to 0.5.

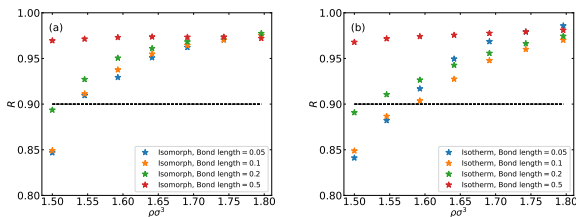


FIG. 2. (a) Variation of the virial potential-energy correlation coefficient  $R$  along each isomorph plotted for the four bond lengths. (b) The variation of  $R$  plotted as a function of density along along the  $T = 1.5$  isotherms for the four bond lengths.

As mentioned, the isomorph theory only applies for systems with strong virial potential-energy correlations. To ensure that this requirement is obeyed, we evaluated the correlation coefficient  $R$  (Eq. (11)) along the isomorphs and along the  $T = 1.5$  isotherms. The results are shown in Fig. 2 as functions of the density in which the  $R = 0.9$  pragmatic limit for isomorph theory to apply is marked by horizontal dashed lines. We see that the majority of state points are above this line, suggesting that isomorph invariance applies. The strongest correlations are found for the

largest bond length (0.5).

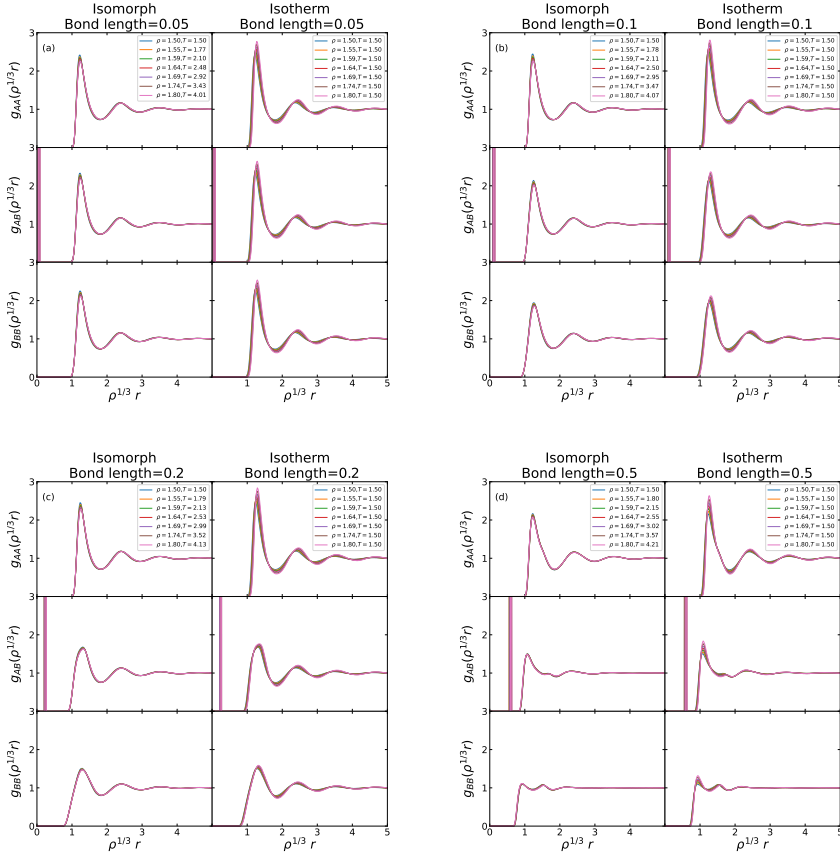


FIG. 3. (a) AA, AB and BB radial distribution functions (RDF) at the reduced pair distance  $\rho^{1/3}r$  where  $r$  is the pair distance in non-reduced units. The RDFs are shown along the isomorph for the bond length 0.05, and for comparison the same RDFs are shown along a reference-state-point temperature isotherm of the same (20%) density variation. We see good, but not perfect invariance along the isomorph, unlike along the isotherm. The thick vertical line in the AB RDF comes from the fixed bond length, which in reduced units varies with density. (b), (c), and (d) show similar plots for bond lengths 0.1, 0.2, and 0.5, respectively. There is good isomorph invariance of all three RDFs in comparison to their isotherm variation. We note that the first peak of the BB RDF gets lower as the bond length increases. This reflects an increased spread of the B particle positions relative to each other. At the same time the AB RDFs become lower and their second peak almost disappears.

To investigate to which degree isomorph invariance of the reduced-unit structure applies, we performed simulations of the three radial distribution function (RDF)  $g(r)$  defined by the AA, AB, and BB particle pairs along the isomorphs. The results are shown in Fig. 3, which for comparison also shows data for simulations carried out at reference-state

point isotherms of the same density variation, i.e., for densities between that of the reference state point (1.5) and 1.8. All three RDFs are nicely invariant along the isomorphs compared to their variation along the isotherms. Focusing henceforth on the isomorph RDFs, we note that the AA RDF does not change very much as the bond length is increased. In fact, this RDF looks much like that of the standard single-component LJ liquid, which is also very similar to that of, e.g., the hard-sphere, Yukawa, and inverse-power-law liquids' RDFs [20].

The observed variation of the AB and BB RDFs can be interpreted as a consequence of the near invariance of the AA particle RDF as the bond length is increased: The structure of the ASD liquid may be thought of as primarily determined by the large A particles, which behave like standard LJ particles that are not bothered much by existence of the B particles. This is because the B particles are smaller and, in particular, have significantly lower interaction energy parameters. In this picture, the B particles are to a significant degree “slaves” of the A particles, and one expects what is observed in Fig. 3: The BB RDF changes significantly with increasing bond length, and at bond length 0.5 it is almost constant. This is because the B particles place themselves in many possible positions around the A particles, which as mentioned for all bond lengths more or less have the RDF of a single-component LJ liquid. This effect is present at all bond lengths, but for the smaller bond lengths it does not give rise to any significant spread of the BB RDF because the B particles are constrained to be close to the A particle of the same molecule. Indeed, the BB particle RDF is very similar to the AA RDF for the small bond length 0.05. This “B slaving A” picture is confirmed by the AB RDF, which (except for the vertical line coming from the intramolecular AB bond correlation) gives data for the AB correlations between different ASD molecules. This RDF is also significantly smeared out as the bond length increases, but less so than the BB RDF because the relative order of the A particles is partly inherited by the AB RDF.

Figure 4 shows data for the (reduced) time dependence of the reduced-unit mean-square displacement of the A and B particles in a log-log plot. The data are isomorph invariant to a good approximation, but not invariant along the isotherm except in the short-time ballistic regime where the invariance is a rigorous consequence of the use of reduced units (which implies unity thermal velocities). Focusing on the behavior along the isomorphs, we note that the A particle motion is pretty similar for all bond lengths. This is consistent with the above picture according to which the A particles to a significant extent behave as if the B particles were not present, i.e., as in a single-component LJ liquid. In the ballistic regime, the B particles move faster than the A particles because of their lower mass. At long times, the A and B particles are constrained to follow each other, resulting in the same long-time MSD for all bond lengths (this, of course, also applies along the isotherms). An interesting feature appears at intermediate times for the B particle MSD, which for short bond lengths have a slight kink that at longer bond lengths develops into an indication of a plateau. We interpret this as an effect of the fact that the fast ballistic motion of the B particles in their motion around the A particles eventually “saturates”. This is confirmed in Fig. 5 discussed next, showing that the rotational time-autocorrelation function for short bond lengths has a (negative) minimum in this range of the reduced times (around 0.1).

Figure 5 shows data for the rotational time-autocorrelation function (RAC) defined as the autocorrelation of the unit vector from particle A to particle B,  $\mathbf{n}$ , plotted as a function of the reduced time. Because of the normalization, this quantity always starts in unity at time zero. The upper row shows data for the isotherms, the lower for the isomorphs. There is little difference and good collapse in both cases, except at the largest bond length 0.5 for which the data are significantly less invariant along the isotherm. At this bond length there is also a change of behavior in the sense that the RAC never becomes negative as it does at intermediate times for the lower bond lengths. This negative value of the RAC signals a more than 90 degree rotation of the molecule. This finding for bond length 0.5 is consistent with the above observation that a change of physics appears to set in around bond length 0.3-0.4. Note that, in contrast to the RDF and the MSD, the RAC is not predicted to be isomorph invariant because the moment of inertia is not isomorph invariant (the bond length is fixed and not scaled with the density by the factor  $\rho^{-1/3}$  required for a constant reduced-unit moment of inertia).

## V. RESULTS FOR THE PLASTIC CRYSTALLINE PHASE

We proceed to report results for the plastic crystalline phase for the bond lengths 0.05, 0.1, 0.2, and 0.3 (for bond lengths larger than 0.3 the systems were liquid at the reference state point). As reference state point we chose that of density 2.2 and temperature 0.5, which is in the solid phase for all four bond lengths. Table II gives the pressure, density-scaling exponent, and virial potential-energy correlation coefficient for the four bond-length models at the reference state point. A typical crystal configuration is shown in Fig. 6. We clearly see that the system is ordered (compare Fig. 1(a)). The order is not perfect, however, because the bond directions are disordered. This is the signal of a plastic crystal in which the center-of-masses order on a crystalline lattice (in this case a face-centered cubic lattice) while the molecular orientations vary more or less randomly because the molecules are free to rotate [21–25]. At a lower temperature, there is a phase transition to a perfectly ordered phase in which the bond orientations are

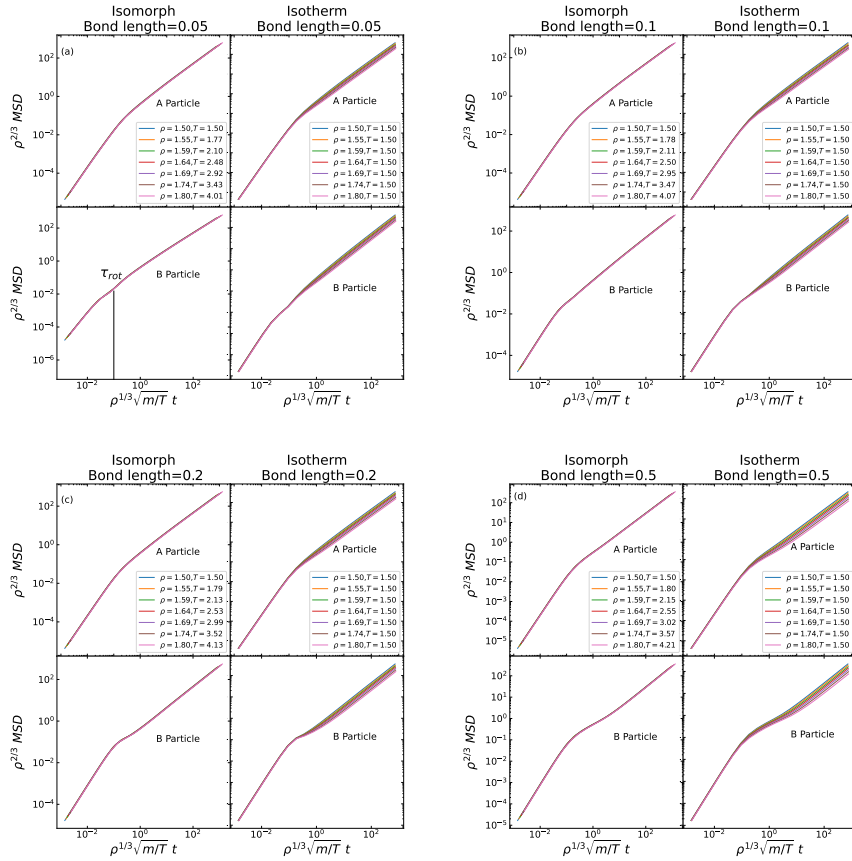


FIG. 4. (a) The A and B reduced-unit mean-square displacement (MSD) along the isomorph and the isotherm for bond length 0.05. There is invariance along the isomorph for both the A and B reduced MSD, but not along the corresponding isotherm. (b), (c), and (d) show similar plots for bond lengths 0.1, 0.2, and 0.5, respectively. Also here is there invariance along the isomorphs for both MSDs, but not along the corresponding isochores.

also ordered, but we did not investigate that transition.

Before proceeding to probe the extent of isomorph invariance, we first look at the properties of the reference state point. Figure 7(a) shows the AA particle RDFs for the four bond lengths. These show a well-defined order due to the (almost) crystalline ordering of the A particles; the AA particle RDFs are moreover very similar for all bond lengths. In contrast, the AB and BB RDFs vary significantly because of the rotation of the B particles around the A particles. In these cases, the most ordered RDFs are those of the shortest bonds, which reflects the slaving of the B particles to the A particles that are well ordered.

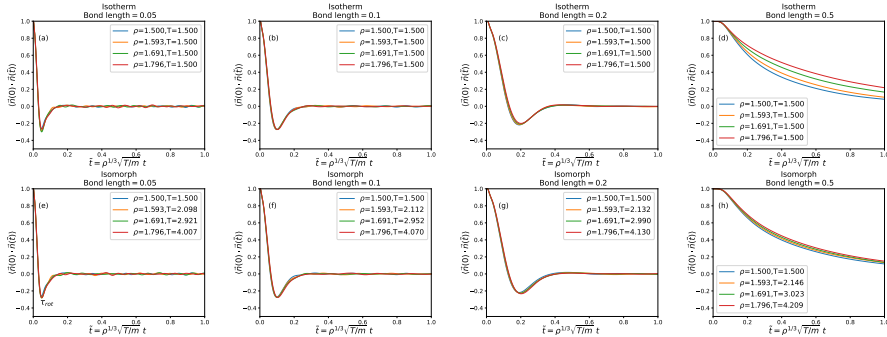


FIG. 5. The rotational time-autocorrelation function (RAC) along the isotherms (upper row) and the isomorphs (lower row) for the four different bond lengths. As the bond length increases, the decay to zero becomes significantly slower, reflecting the increased moment of inertia. The largest bond length (0.5) behaves differently from the others by never going below zero.

TABLE II. Thermodynamic parameters of the plastic-crystal reference state point, giving temperature, density, and pressure in LJ units, as well as the density-scaling exponent  $\gamma$  and the virial potential-energy correlation coefficient  $R$ .

Bond length [ $l/\sigma_{AA}$ ]	$\rho$ [ $l/\sigma_{AA}^3$ ]	$T$ [ $\varepsilon_{AA}/k$ ]	$p$ [ $\sigma_{AA}^3 \varepsilon_{AA}$ ]	$\gamma$	$R$
0.05	2.2	0.5	0.497	5.497	0.997
0.10	2.2	0.5	1.173	5.503	0.996
0.20	2.2	0.5	5.191	5.191	0.992
0.30	2.2	0.5	15.279	5.579	0.990

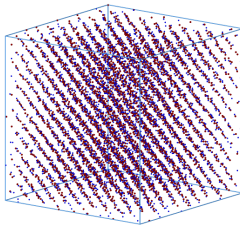


FIG. 6. Snapshot of a plastic crystal configuration at the reference state point  $(\rho, T) = (2.2, 0.5)$ . The bond length between particles A (red) and B (blue) is in this case 0.2.

Figure 8 shows the MSDs of the A and B particles as functions of (reduced) time. For the A particles the results are very similar for the different bond lengths, although bond length 0.3 deviates from the three smaller ones by having a somewhat larger long-time plateau. We have no good explanation for this, but deviations for the longest bond length from the three others are also noted in some of the later figures. The B particle plateaus vary considerably, with larger plateaus observed for larger bond lengths. This is because the B particles rotate around the A particles and a larger bond length gives them more freedom to do so, resulting in a larger long-time plateau.

Figure 9 shows  $\gamma$  and  $R$  at the reference state point as a function of the bond length (with data for a few more). We see that  $\gamma$  is almost independent of the bond length and has the typical LJ value between 5 and 6 [17]. The correlation coefficient drops somewhat with increasing bond length, but stays comfortably above 0.9.

As in the liquid phase, we generated isomorphs from the reference state point by integrating Eq. (7) using the RK4

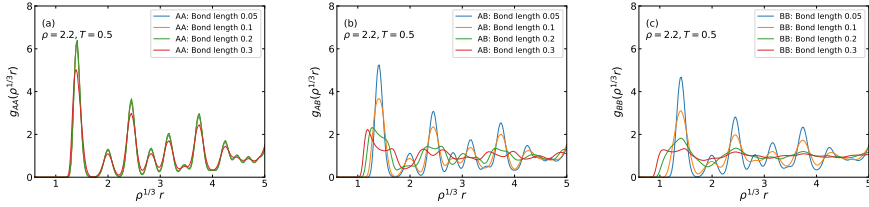


FIG. 7. (a) AA particle RDFs at the reference state point  $\rho = 2.2, T = 0.5$  for each of the bond lengths 0.05, 0.1, 0.2, 0.3. (b), (c) AB and BB particle RDFs, respectively, at the same state point.

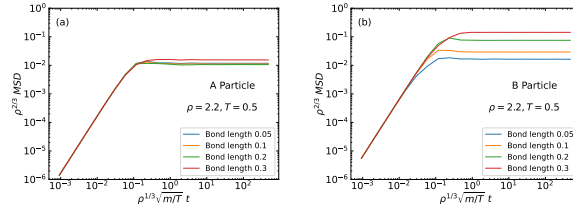


FIG. 8. (a) A particle MSDs as functions of time at the reference state point  $(\rho, T) = (2.2, 0.5)$  for each of the bond lengths 0.05, 0.1, 0.2, 0.3. The long-time stabilization to a plateau shows that the system is a solid. (b) B particle MSDs at the same state point.

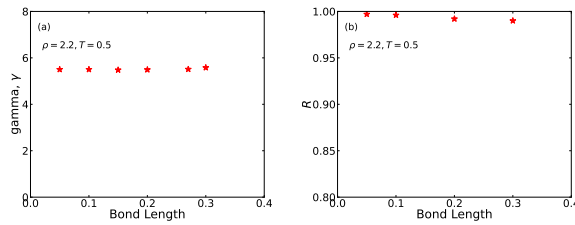


FIG. 9. Variation of the density-scaling exponent  $\gamma$  and of the virial potential-energy correlation coefficient  $R$  at the reference state point plotted as functions of the bond length. Data for a few extra bond lengths have been added. (We can add the dash line but we can't have more bond length after 0.3, I can try with 0.35 and 0.4, but I will first check that the system stays as plastic crystal. Update: At density 2.20, they don't stay as plastic crystals with 0.4 as a bond length as well.)

algorithm [19] for density steps of magnitude 0.01. Also as in the liquid case, we chose to increase the density by 20% from the reference state-point density (2.2). This corresponds roughly to realistic density changes of high-pressure experiments. The four isomorphs are shown in Fig. 10. We see that they are quite similar.

Figure 11 shows the reduced RDFs along the isomorphs and, for comparison, along reference-temperature isotherms of the same density variation. For the smallest bond length (0.05), we see a very good collapse of all three RDFs along the isomorph, but not along the isotherm. Moreover, the three RDFs are quite similar, which is a consequence of the fact that all B particles are constrained to be very close to an A particle. Moving to larger bond lengths, we see

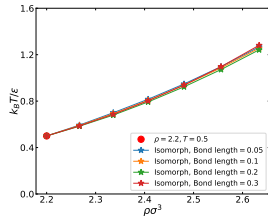


FIG. 10. Four isomorphs traced out in the plastic crystalline regime of ASD thermodynamic phase diagram using the RK4 method with density step size 0.01. The isomorphs are traced for bond lengths 0.05, 0.1, 0.2, and 0.3.

in all cases a very good isomorph collapse and note that, with increasing bond length, the AB and BB particle RDFs become increasingly smeared out compared to the AA particle RDF. The same was seen in the liquid phase (Fig. 3), and as in the liquid phase we interpret this as deriving from rotations of the molecules. In particular, it confirms that the crystals are plastic. Interestingly, the AA particle RDF becomes more invariant along the isotherm as the bond length is increased, but for all bond lengths this quantity is still less isotherm than isomorph invariant.

For the MSDs as functions of reduced time (Fig. 12), we note that these are all isomorph invariant to a good approximation. In contrast, there is a notable variation along the corresponding isotherms for both A and B particles. Only at short times (in the ballistic regime) do we observe invariance along the isotherms, but this is as mentioned a consequence of the definition of the reduced units.

Proceeding finally to the RACs, Fig. 13 shows these where the upper two presents the RACs along the isotherms for the four bond lengths and the lower row corresponding data for the RACs along the isomorphs. With the notable exception of bond length 0.3, we see a quite good isomorph invariance of the RACs. Despite the already-mentioned fact that the RAC is not expected to be isomorph invariant because the reduced moment of inertia is not, for all bond lengths we find that the invariance along isomorphs is better than along the isotherms (and much better in the bond-length 0.3 case).

## VI. SUMMARY

We have presented a numerical study of the liquid and plastic crystalline phases of asymmetric dumbbell models with different bond lengths with the purpose of testing the isomorph-theory predictions of invariant structure and dynamics. In the liquid case, the bond lengths 0.05, 0.1, 0.2, and 0.5 were studied, while in the crystalline case the largest bond length was 0.3. At all state points the virial potential-energy correlation coefficients were above 0.84; in the vast majority of cases it was above 0.9, and for the plastic crystals it was very close to unity. This implies that the isomorph theory is expected to apply [9, 10]. Indeed, we found good isomorph invariance of the reduced-unit RDFs, MSDs, and RACs in the liquid phase and excellent invariance in the plastic crystalline phase. In contrast, these quantities were generally not invariant along isotherms of the same (20%) density variation. The behavior of the B particles conform to a picture in which they are “slaves” of the A particles that behave almost like single-component LJ particles, i.e., are not much affected by the B particles.

The present paper is the first time the isomorph theory has been shown to apply for plastic crystals of simple two-atom dumbbell molecules. In conjunction with recent papers demonstrating the applicability of isomorph theory to liquid crystals [26, 27], this serves to emphasize the generality of this theoretical framework derived from the hidden-scale-invariance condition Eq. (1) and that the theory applies independent of which phase the system is in. It would be interesting to investigate the transition from the plastic crystal to the ordinary, orientationally ordered crystal phase and, in particular, whether the phase transition line is close to an isomorph as the liquid-solid transition line is [28].

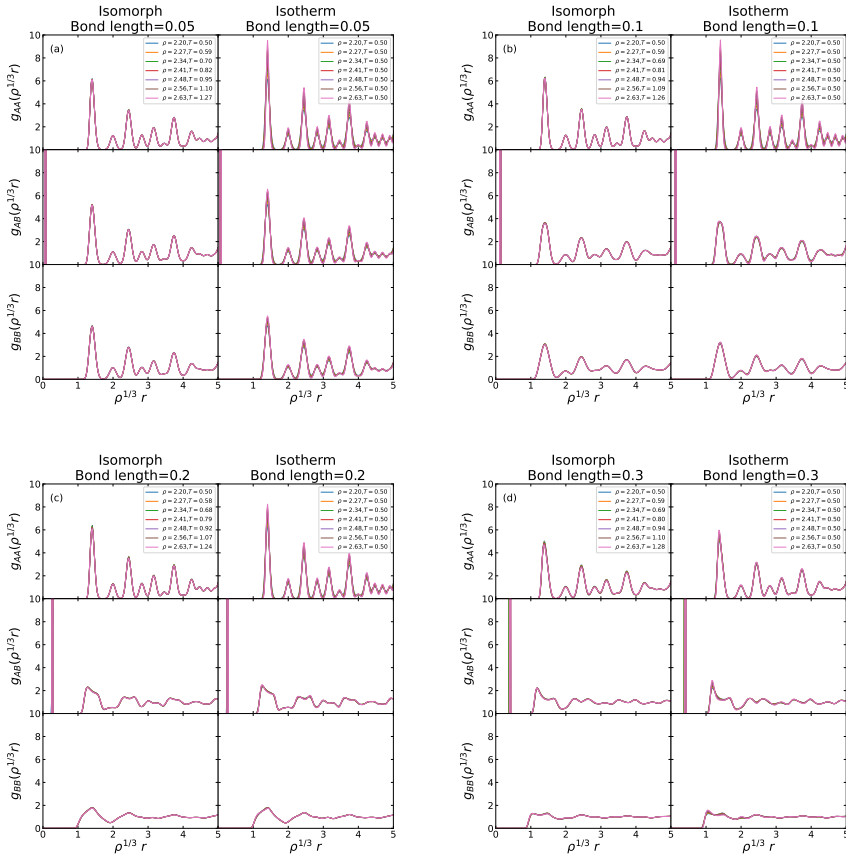


FIG. 11. (a) AA, AB and BB RDFs at the reduced pair distance  $\rho^{1/3}r$  where  $r$  is the pair distance in non-reduced units. The RDFs are shown along the isomorph for the bond length 0.05, and for comparison the same RDFs are shown along a reference-state-point isotherm of the same (20%) density variation. We almost perfect invariance along the isomorph, unlike along the isotherm. The vertical line in the AB RDF comes from the fixed bond length, which in reduced units varies with density. (b), (c), and (d) show similar plots for bond lengths 0.1, 0.2, and 0.3, respectively. There is a very good isomorph invariance of all three RDFs in comparison to their isotherm variation. The first peak of the BB RDF gets lower as the bond length increases, which reflects an increased spread of the B particle positions relative to each other. At the same time the AB RDFs become lower.

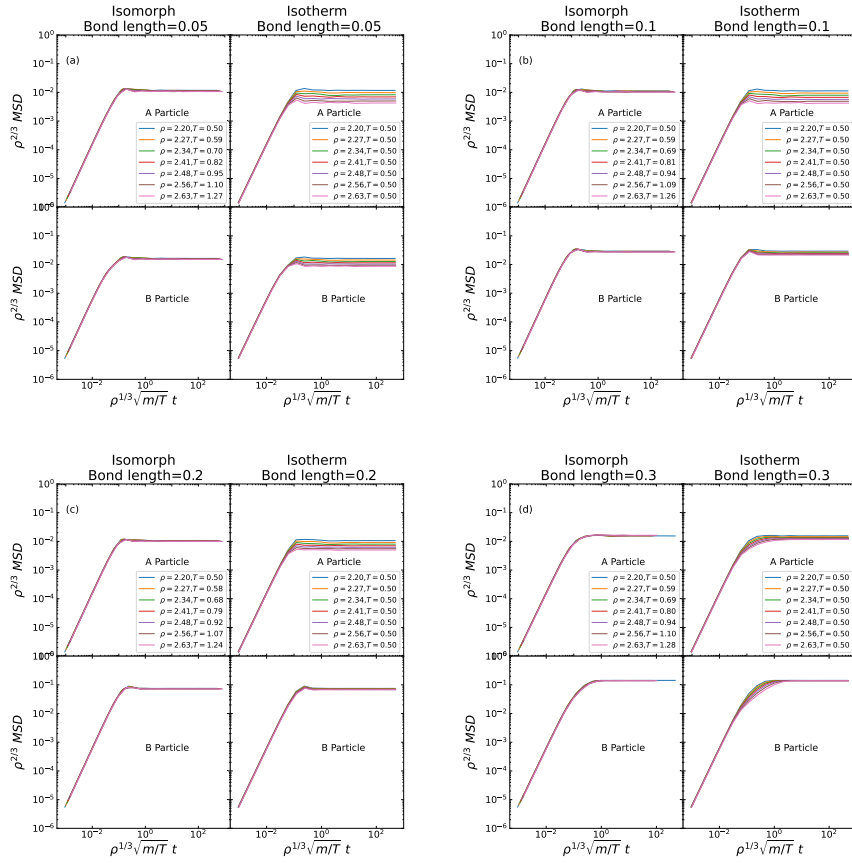


FIG. 12. (a) The A and B reduced-unit MSDs along the isomorph and the isotherm for bond length 0.05. There is good invariance along the isomorph for both the A and B reduced MSDs, but not along the corresponding isotherm. The short-time invariance in both cases derives simply from the definition of reduced units, but the long-time plateau is far from invariant along the isotherm. (b), (c), and (d) show similar plots for bond lengths 0.1, 0.2, and 0.3, respectively. Also here is there invariance along the isomorphs for both MSDs, but not along the corresponding isotherms.

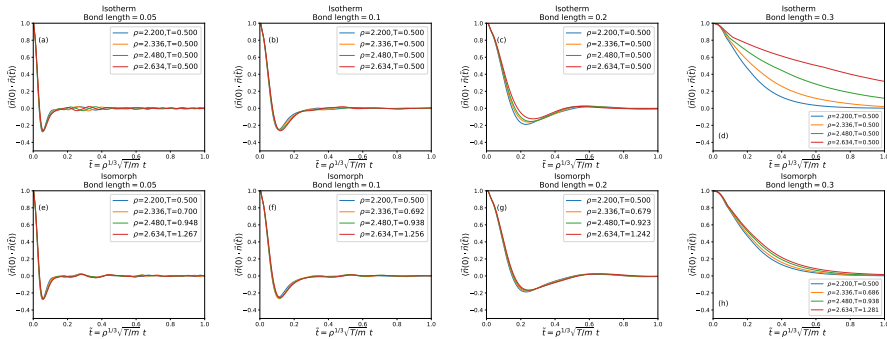


FIG. 13. (a) The RACs along the isotherms (upper row) and the isomorphs (lower row) for four bond lengths. As the bond length increases, the decay to zero becomes significantly slower, reflecting the increased moment of inertia. The largest bond length (0.3) behaves differently from the others by never going below zero.

#### ACKNOWLEDGMENTS

This work was supported by the VILLUM Foundation's *Matter* grant (16515).

- [1] M. B. Sweatman, A. Atamas, and J.-M. Leyssale, "The self-referential method for linear rigid bodies: Application to hard and Lennard-Jones dumbbells," *J. Chem. Phys.* **130**, 024101 (2009).
- [2] T. S. Ingebrigtsen, T. B. Schröder, and J. C. Dyre, "Isomorphs in model molecular liquids," *J. Phys. Chem. B* **116**, 1018–1034 (2012).
- [3] S. Lee, M. Kim, and J. Chang, "Chemical potential and solid-solid equilibrium of near-spherical Lennard-Jones dumbbell crystal," *Korean J. Chem. Eng.* **33**, 1047 (2016).
- [4] S. Kämmerer, W. Kob, and R. Schilling, "Dynamics of the rotational degrees of freedom in a supercooled liquid of diatomic molecules," *Phys. Rev. E* **56**, 5450–5461 (1997).
- [5] R. Chopra, T. M. Truskett, and J. R. Errington, "Excess entropy scaling of dynamic quantities for fluids of dumbbell-shaped particles," *J. Chem. Phys.* **133**, 104506 (2010).
- [6] D. Fragiadakis and C. M. Roland, "Characteristics of the Johari-Goldstein process in rigid asymmetric molecules," *Phys. Rev. E* **88**, 042307 (2013).
- [7] D. D. Daub, P.-O. Åstrand, and F. Bresme, "Thermo-molecular orientation effects in fluids of dipolar dumbbells," *Phys. Chem. Chem. Phys.* **16**, 22097 (2014).
- [8] D. Fragiadakis and C. M. Roland, "Intermolecular distance and density scaling of dynamics in molecular liquids," *J. Chem. Phys.* **150**, 204501 (2019).
- [9] N. Gnan, T. B. Schröder, U. R. Pedersen, N. P. Bailey, and J. C. Dyre, "Pressure-energy correlations in liquids. IV. "Isomorphs" in liquid phase diagrams," *J. Chem. Phys.* **131**, 234504 (2009).
- [10] J. C. Dyre, "Hidden scale invariance in condensed matter," *J. Phys. Chem. B* **118**, 10007–10024 (2014).
- [11] U. R. Pedersen, T. Christensen, T. B. Schröder, and J. C. Dyre, "Feasibility of a Single-Parameter Description of Equilibrium Viscous Liquid Dynamics," *Phys. Rev. E* **77**, 011201 (2008).
- [12] M. P. Allen and D. J. Tildesley, *Computer Simulation of Liquids* (Oxford Science Publications (Oxford), 1987).
- [13] N. P. Bailey, T. S. Ingebrigtsen, J. S. Hansen, A. A. Veldhorst, L. Böhling, C. A. Lemarchand, A. E. Olsen, A. K. Bacher, L. Costigliola, U. R. Pedersen, H. Larsen, J. C. Dyre, and T. B. Schröder, "RUMD: A general purpose molecular dynamics package optimized to utilize GPU hardware down to a few thousand particles," *SciPost Phys.* **3**, 038 (2017).
- [14] T. B. Schröder and J. C. Dyre, "Simplicity of condensed matter at its core: Generic definition of a Roskilde-simple system," *J. Chem. Phys.* **141**, 204502 (2014).
- [15] L. D. Landau and E. M. Lifshitz, *Statistical Physics* (Pergamon, Oxford, 1958).
- [16] U. R. Pedersen, N. P. Bailey, T. B. Schröder, and J. C. Dyre, "Strong pressure-energy correlations in van der Waals liquids," *Phys. Rev. Lett.* **100**, 015701 (2008).
- [17] N. P. Bailey, U. R. Pedersen, N. Gnan, T. B. Schröder, and J. C. Dyre, "Pressure-energy correlations in liquids. I. Results from computer simulations," *J. Chem. Phys.* **129**, 184507 (2008).

- [18] N. P. Bailey, U. R. Pedersen, N. Gnan, T. B. Schröder, and J. C. Dyre, "Pressure-energy correlations in liquids. II. Analysis and consequences," *J. Chem. Phys.* **129**, 184508 (2008).
- [19] E. Attia, J. C. Dyre, and U. R. Pedersen, "Extreme case of density scaling: The Weeks-Chandler-Andersen system at low temperatures," *Phys. Rev. E* **103**, 062140 (2021).
- [20] J. C. Dyre, "Simple liquids' quasuniversality and the hard-sphere paradigm," *J. Phys. Condens. Matter* **28**, 323001 (2016).
- [21] R. Brand, P. Lunkenheimer, and A. Loidl, "Relaxation dynamics in plastic crystals," *J. Chem. Phys.* **116**, 10386 (2002).
- [22] J. M. Pringle, P. C. Howlett, D. R. MacFarlane, and M. Forsyth, "Organic ionic plastic crystals: recent advances," *J. Mater. Chem.* **20**, 2056 (2010).
- [23] A. Vispa, M. Romanini, M. A. Ramos, L. C. Pardo, F. J. Bermejo, M. Hassaine, A. I. Krivchikov, J. W. Taylor, and J. Ll. Tamarit, "Thermodynamic and kinetic fragility of Freon 113: The most fragile plastic crystal," *Phys. Rev. Lett.* **118**, 105701 (2017).
- [24] A. Aznar, P. Lloveras, M. Barrio, P. Negrier, A. Planes, L. Mañosa, N. D. Mathur, X. Moya, and J.-L. Tamarit, "Reversible and irreversible colossal barocaloric effects in plastic crystals," *J. Mater. Chem. A* **8**, 639–647 (2020).
- [25] M. Das, C. F. Schmidt, and M. Murrell, "Introduction to active matter," *Soft Matter* **16**, 7185–7190 (2020).
- [26] S. Mehri, M. A. Kolmangadi, J. C. Dyre, and T. S. Ingebrigtsen, "Lines of invariant physics in the isotropic phase of the discotic Gay-Berne model," *J. Non-Cryst. Solids: X* **14**, 100085 (2022).
- [27] S. Mehri, J. C. Dyre, and T. S. Ingebrigtsen, "Hidden scale invariance in the Gay-Berne model," *Phys. Rev. E* **105**, 064703 (2022).
- [28] U. R. Pedersen, L. Costigliola, N. P. Bailey, T. B. Schröder, and J. C. Dyre, "Thermodynamics of freezing and melting," *Nat. Commun.* **7**, 12386 (2016).

# Comparing four hard-sphere approximations for the low-temperature WCA melting line

Cite as: J. Chem. Phys. 157, 034502 (2022); doi: 10.1063/5.0097593

Submitted: 29 April 2022 • Accepted: 27 June 2022 •

Published Online: 19 July 2022



Eman Attia, Jeppe C. Dyre, and Ulf R. Pedersen <sup>a1</sup>

## AFFILIATIONS

Glass and Time, IMFUFA, Department of Science and Environment, Roskilde University, P.O. Box 260, DK-4000 Roskilde, Denmark

**Note:** This paper is part of the JCP Special Topic on Fluids Meets Solids.

<sup>a1</sup>Author to whom correspondence should be addressed: [ulf@urp.dk](mailto:ulf@urp.dk)

## ABSTRACT

By combining interface-pinning simulations with numerical integration of the Clausius–Clapeyron equation, we accurately determine the melting-line coexistence pressure and fluid/crystal densities of the Weeks–Chandler–Andersen system, covering four decades of temperature. The data are used for comparing the melting-line predictions of the Boltzmann, Andersen–Weeks–Chandler, Barker–Henderson, and Stillinger hard-sphere approximations. The Andersen–Weeks–Chandler and Barker–Henderson theories give the most accurate predictions, and they both work excellently in the zero-temperature limit for which analytical expressions are derived here.

Published under an exclusive license by AIP Publishing. <https://doi.org/10.1063/5.0097593>

## I. INTRODUCTION

While systems of purely repulsive particles are rarely found in nature, they provide convenient models for both fluids and solids.<sup>1</sup> Examples are the inverse-power law (IPL) systems based on a homogeneous pair potential that varies with distance  $r$  as  $(r/\sigma)^{-n}$  (in which  $\sigma$  is a length)<sup>2–5</sup> and the exponential repulsive (EXP) pair potential that varies with distance as  $\exp(-r/\sigma)$ .<sup>3–8</sup> The oldest and most important purely repulsive system is that of hard spheres (HS),<sup>9–12</sup> which despite its simplicity provides a good zeroth-order model of realistic systems with both repulsive and attractive interactions.<sup>13–18</sup> A purely repulsive system has a single fluid phase and no gas–liquid phase transition. In contrast, the symmetry-breaking liquid–solid transition is present in all purely repulsive systems. Because of the absence of a gas phase, the liquid–solid phase boundary here extends to zero temperature.

This paper studies the noted Weeks, Chandler, and Andersen (WCA) purely repulsive system,<sup>17–44</sup> which is arrived at by cutting and shifting the Lennard-Jones (LJ) interaction at its minimum.<sup>17</sup> In contrast to the IPL and EXP systems, the WCA pair potential has a finite range beyond which pair forces are zero, such as those of the HS system. At the cutoff, the WCA pair potential and pair forces are smooth, and at low temperatures, one expects HS approximations to apply because only insignificant “overlaps” are possible.

Thus, studies of the low-temperature melting line of the WCA system provide an excellent testing ground for comparing different HS approximations, which motivates the present study. Section II introduces the WCA system and the four HS approximations considered and gives a few simulation details. Section III details how we determined the WCA melting line by interface pinning and Clausius–Clapeyron integration. The predictions of the different HS approximations with regard to pressure and fluid/solid densities at melting are compared in Sec. IV. Finally, Sec. V provides a brief outlook.

## II. THE WCA SYSTEM AND HARD-SPHERE APPROXIMATIONS

### A. The WCA system

We consider mono-disperse systems. Let  $\mathbf{R} = (\mathbf{r}_1, \mathbf{r}_2, \dots, \mathbf{r}_N)$  be the collective coordinate vector of  $N$  particles with mass  $m$  confined to the volume  $V$  (with periodic boundaries) and define the (number) density by  $\rho \equiv N/V$ . The potential energy  $U(\mathbf{R})$  is assumed to be a sum of pair contributions,

$$U(\mathbf{R}) = \sum_{n>m}^N v(|\mathbf{r}_m - \mathbf{r}_n|). \quad (1)$$

Recall that the LJ pair potential is defined<sup>45,46</sup> by

$$v(r) \equiv 4\epsilon[(r/\sigma)^{-12} - (r/\sigma)^{-6}] \quad (2)$$

in which  $\epsilon$  has units of energy and  $\sigma$  units of length. The WCA pair potential (Fig. 1) is defined by cutting and shifting the LJ potential at its minimum, which leads to<sup>7</sup>

$$v(r) = 4\epsilon[(r/\sigma)^{-12} - (r/\sigma)^{-6}] + 1/4 \quad \text{for } r \leq r_c \quad (3)$$

and zero otherwise, where

$$r_c = \sqrt[3]{2}\sigma \approx 1.1225\sigma. \quad (4)$$

The WCA pair potential is purely repulsive since the pair force  $-dv/dr$  is non-negative for all  $r$ 's, and it is smooth since both  $v(r)$  and its first derivative are continuous (the second derivative is discontinuous at  $r_c$ , though). All quantities obtained by simulations are below reported in units derived from  $m$ ,  $\sigma$ ,  $\epsilon$ , and the Boltzmann constant  $k_B$ .

Simulations of the WCA system were conducted using the RUMD software package version 3.5.<sup>47</sup> An initial configuration is first constructed by setting up  $8 \times 8 \times 20$  face-centered cubic (FCC) unit cells, resulting in a system of  $N = 5120$  particles. This initial configuration is then scaled uniformly to the desired density  $\rho$ . If a liquid configuration is needed, the crystal is melted in a high-temperature simulation. The Newtonian equations of motion are discretized using the leap-frog algorithm<sup>48</sup> with the temperature-dependent time step,

$$dt = 0.001 \frac{\sigma}{\sqrt{k_B T/m}}. \quad (5)$$

Simulations in the  $NVT$  ensemble<sup>47-51</sup> are realized using a Langevin thermostat with relaxation time given by

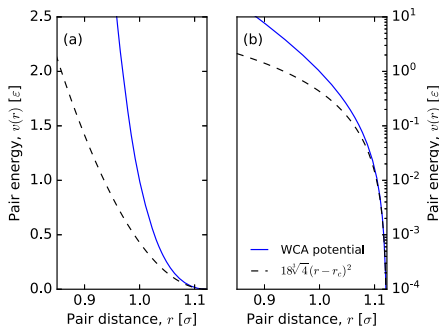


FIG. 1. (a) The solid line shows the WCA pair potential [Eq. (3)], and the dashed line shows the harmonic approximation of Eq. (38). (b) The same pair potential on a logarithmic energy scale, showing a steep slope at low pair energies.

$$t_r = 0.2 \frac{\sigma}{\sqrt{k_B T/m}}. \quad (6)$$

For  $Np_z T$  Langevin simulations,<sup>47,50,51</sup> we used the same thermostat relaxation time and the barostat relaxation time,

$$t_p = 100 \frac{\sigma}{\sqrt{k_B T/m}}. \quad (7)$$

We have found that introducing this  $1/\sqrt{T}$  scaling to the relaxation times<sup>25</sup> provides a simple way to ensure stability and efficiency of computations spanning four orders of magnitude in temperature (see Ref. 43 for a different approach). Note that in this way, the average number of steps needed to travel the distance  $\sigma$  for a thermal particle is the same at all temperatures. The model approaches hard spheres at low temperatures, and in effect, the interaction distance narrows. Thus, we expect that shorter time steps are needed for temperatures lower than those investigated here.

## B. Hard-sphere approximations to the WCA system

Perturbation theories have proven successful for describing many fluids near freezing.<sup>1,15-25,52-66</sup> The basic assumption is that the pair interaction can be written as

$$v(r) = v_0(r) + v_1(r) \quad (8)$$

in which  $v_0(r)$  is the pair potential of some well-known reference system and  $v_1(r)$  is a small perturbation. Often, the HS system is used as the reference. Several suggestions have been made for choosing the appropriate HS diameter,  $d$ . Below, we list the four HS criteria that in Sec. IV are evaluated with respect to their ability to locate the solid-liquid coexistence line.

In the zero-temperature limit ( $T \rightarrow 0$ ), the WCA pair potential approaches that of a HS<sup>9-12</sup> system with diameter  $d = r_c$ , i.e., the system described by

$$v_d(r) = \infty \quad \text{for } r < d \quad (9)$$

and zero otherwise. While this may not be intuitively obvious since the WCA pair potential goes smoothly to zero at the cutoff, it becomes clear when the WCA potential is shown in a log-plot [Fig. 1(b)]. The simplest way of assigning an effective HS diameter to a WCA particle is to use the truncation distance

$$d = r_c. \quad (10)$$

This criterion is exact for  $T \rightarrow 0$ . At finite temperatures, however, the effective HS diameter will be smaller, and here one needs to make some physical assumptions to improve Eq. (10) and arrive at better approximations. We next list four well-known HS approximations.

### 1. Boltzmann's hard-sphere criterion

In his 1890 *Lectures on Gas Theory*,<sup>67</sup> Boltzmann suggested that the effective HS diameter  $d$  should be identified with the distance of closest approach when the velocities of two head-on colliding particles are given by their average kinetic energy at far distances. This criterion results in

$$v(d) = k_B T, \quad (11)$$

which for the WCA system leads to

$$d = \frac{r_c}{\sqrt{1 + \sqrt{k_B T/\epsilon}}} \quad (12)$$

Boltzmann's idea, which provides the simplest HS approximation, has been used to estimate the effective HS diameter of the WCA system by a number of authors.<sup>19–22,24,25</sup>

## 2. The Andersen–Weeks–Chandler hard-sphere criterion

A more sophisticated HS criterion was suggested in 1971 by Andersen, Weeks, and Chandler (AWC).<sup>56</sup> Their motivation was to match as well as possible the Helmholtz free energy of the pair potential in question to the associated HS system. The AWC criterion may be summarized as follows: If

$$e(r) = \exp(-v(r)/k_B T) \quad (13)$$

is the pair-potential Boltzmann probability factor, the AWC effective HS diameter  $d$  is identified from

$$\int_0^\infty r^2 y_d(r) \Delta e(r) dr = 0 \quad (14)$$

in which  $\Delta e(r) = e(r) - e_d(r)$  is the so-called blip function and  $y_d(r)$  is the cavity function of the HS fluid. In the Percus–Yevick (PY) approximation, the cavity function is given analytically,<sup>1,59–62,68,69</sup> which is convenient for applications of Eq. (14). The appearance of the blip function in Eq. (14) effectively limits the AWC integral to values near  $d$ . Thus, it is sufficient to consider the zeroth and first shell of  $y_d(r)$  to evaluate the AWC integral of Eq. (14) with a high accuracy. We used the following implementation of the cavity function in the determination of the HS diameter  $d$  via Eq. (14).<sup>60</sup> If  $s \equiv r/d$ ,

$$y_d(s) = \begin{cases} c_0 - c_1 s + c_3 s^3 & \text{for } s < 1, \\ H_1(s)/s & \text{for } 1 < s < 2, \end{cases} \quad (15)$$

where

$$H_1(s) = a_1 \exp A(s-1)r + a_2 \exp B(s-1) \cos C(s-1) + a_3 \exp B(s-1) \sin C(s-1). \quad (16)$$

The parameters depend on the packing fraction  $\eta$  [see Eqs. (6) and (15)–(17) in Ref. 60], leading for the coexistence packing fraction  $\eta = 0.4909$  (corresponding to the density  $0.9375d^{-3}$ ) to  $c_0 = 58.4514$ ,  $c_1 = 67.9928$ ,  $c_3 = 14.3461$ ,  $A = 1.58498$ ,  $B = -3.68494$ ,  $C = 3.85160$ ,  $a_1 = 0.56770$ ,  $a_2 = 4.23705$  and  $a_3 = -1.41141$ . We evaluated the AWC integral numerically using the Python module SciPy's<sup>70</sup> implementation of QUADPACK.<sup>71</sup>

The pressure of a hard-sphere fluid is given by the value of  $y_d(s)$  at the hard-sphere contact distance,  $s = 0$ . The above theory underestimates the coexistence pressure by only 8%. The PY approximation works best at low densities. Other theoretical approaches<sup>61,72–78</sup> provide analytical and more accurate expression for the HS radial distribution functions and, in effect, give a better prediction of the pressure. We have not investigated whether the improved theories provide more accurate AWC predictions since they do not provide the needed cavity function as presented. In addition, we have not investigated Lado's refinement<sup>68</sup> of the AWC theory.

## 3. The Barker–Henderson hard-sphere criterion

The Barker and Henderson (BH) theory,<sup>55</sup> which predates the AWC theory, can be viewed as a simplification of the AWC theory.<sup>1</sup> Specifically, it is assumed that  $r$ -squared times the cavity-function is a constant,  $r^2 y_d = \text{const.}$ , implying that Eq. (14) can be written as

$$0 = \int_0^\infty ([1 - e(r)] - [1 - e_d(r)]) dr. \quad (17)$$

Since the integral of  $1 - e_d(r)$  is  $d$ , one arrives at the following HS criterion:

$$d = \int_0^\infty [1 - e(r)] dr. \quad (18)$$

The  $r^2 y_d = \text{const.}$  assumption is reasonable since the blip function limits the integral to values near  $d$  where  $y_d$  does not change much when the temperature is sufficiently low. As  $T$  is lowered, the blip function narrows; thus, the AWC diameter reduces to the BH criterion when  $T \rightarrow 0$ . Note that the BH criterion depends on temperature but not on density, while the AWC criterion depends on both temperature and density. The BH integral of Eq. (18) is easily evaluated numerically using, e.g., the Python module SciPy's<sup>70</sup> implementation of QUADPACK.<sup>71</sup>

## 4. Stillinger's hard-sphere criterion

At low temperatures, the integrand of the BH criterion Eq. (18) changes rapidly from nearly unity for  $r < d$  to nearly zero for  $r > d$ . This motivated the HS criterion proposed by Stillinger in 1976.<sup>40,79,80</sup> He pragmatically identified the HS diameter as the distance at which the pair-potential Boltzmann factor equals one half, i.e.,

$$e(d) = \frac{1}{2}. \quad (19)$$

This was introduced in connection with a study of the Gaussian-core model,<sup>79</sup> but the same idea can also be applied to the WCA potential leading<sup>40</sup> to

$$d = \frac{r_c}{\sqrt{1 + \sqrt{k_B T \ln(2)/\epsilon}}}. \quad (20)$$

Note that the functional form of this HS criterion is identical to that of Boltzmann if  $T$  is replaced by  $T \ln(2)$ : The factor 2 comes from Eq. (19); with  $e(d) = 1/\exp(1)$ , one arrives at Boltzmann's criterion.<sup>24</sup>

## III. NUMERICAL DETERMINATION OF THE PHASE TRANSITION LINE

The interface pinning method<sup>81–90</sup> is used to compute the solid–liquid chemical potential difference  $\Delta\mu$  for isothermal state points at temperatures  $0.002\epsilon/k_B$ ,  $0.02\epsilon/k_B$ ,  $0.2\epsilon/k_B$ ,  $2\epsilon/k_B$ , and  $20\epsilon/k_B$ . For a given temperature, we first set up a FCC crystal elongated in the  $z$ -direction with the given density and compute the equilibrium pressure in an NVT simulation. From this, a half-crystal/half-fluid configuration is constructed by a high-temperature simulation, where particle positions are only updated for half of the particles (resulting in melting for these particles). This produces a

configuration similar to the one shown in the inset of Fig. 2. We then perform an  $NpT$  simulation by adding a harmonic bias-field to the potential part of the Hamiltonian,

$$U_{\text{IP}}(\mathbf{R}) = U(\mathbf{R}) + \frac{\kappa}{2}(Q(\mathbf{R}) - a)^2, \quad (21)$$

which forces the system toward configurations with a fluid–crystal interface. Here,  $\kappa$  and  $a$  are parameters of the bias-field, and  $Q(\mathbf{R})$  is an order parameter that measures crystallinity through long-range order [see Eq. (15) in Ref. 81]. The chemical potential difference between the two phases,  $\Delta\mu$ , is computed from the average force,  $\kappa(Q(\mathbf{R}) - a)$ , which the bias field results in on the system [see Eq. (9) in Ref. 81]. This is then repeated for several FCC densities (and thus pressures) near coexistence. As an example, Fig. 2 shows the pressures vs the computed chemical potentials at  $2\varepsilon/k_B$ , considering 11 pressures slightly above  $31.7\varepsilon/\sigma^3$ . The coexistence state point at  $\Delta\mu = 0$  is determined by linear regression (compare the solid line in Fig. 2). From this, we find the coexistence pressure  $p = 31.8086(66)\varepsilon/\sigma^3$ , where the number in parentheses gives the statistical error on the last two digits using a 95% confidence interval. Table I reports the thermodynamic coexistence data obtained by the interface-pinning (IP) method and numerical integration of the Clausius–Clapeyron (CC) relation as detailed below.

While the interface-pinning method is accurate and provides specific error estimates, it can be computationally expensive because long simulations are needed to properly represent interface fluctuations, which are usually significantly slower than fluctuations of the bulk solid and fluid.<sup>81</sup> As an alternative, we determine most

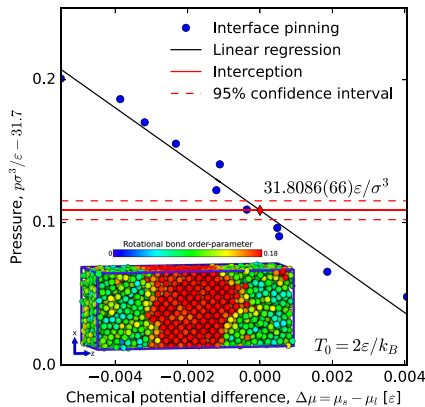


**FIG. 2.** Determination of the coexistence pressure at the temperature  $T_0 = 2\varepsilon/k_B$  (red diamond) by means of the interface-pinning method<sup>81–83</sup> [see Eq. (21)]. The inset shows an interface-pinned configuration where the colors indicate the rotational bond order parameter  $\hat{q}_4$  defined in Ref. 91. With this coloring, crystalline particles are reddish and fluid particles are greenish.

**TABLE I.** Selected state points on the coexistence line determined by the interface pinning (IP) method and by numerical integration of the Clausius–Clapeyron (CC) relation (all data are available in Zenodo at <http://doi.org/10.5281/zenodo.6505218>). The numbers in parentheses give the statistical uncertainty of the IP data (95% confidence interval).

$T$ [ $\varepsilon/k$ ]	$p$ [ $\varepsilon/\sigma^3$ ]	$\rho_l$ [ $1/\sigma^3$ ]	$\rho_s$ [ $1/\sigma^3$ ]	Method
20	634.33(14)	1.784 10(10)	1.859 34(10)	IP
20	633.309	1.783 28	1.858 50	CC
2	31.808 6(66)	1.084 41(5)	1.151 92(6)	IP
2	31.753 2	1.084 13	1.151 63	CC
0.2	2.051 69(33)	0.800 04(3)	0.873 56(4)	IP
0.2	2.051 18	0.799 92	0.873 58	CC
0.02	0.174 944(47)	0.706 38(5)	0.778 89(6)	IP
0.002	0.016 687(3)	0.677 17(3)	0.747 91(3)	IP
0.002	0.016 680	0.677 05	0.747 92	CC

points on the coexistence line by numerical integration of the Clausius–Clapeyron relation (below  $s$  and  $v$  are entropy and volume per particle)

$$\frac{dp}{dT} = \frac{\Delta s}{\Delta v}. \quad (22)$$

This is an example of the Gibbs–Duhem integration methods discussed by Kofke,<sup>92,93</sup> which do not involve slow fluctuations of an interface. The volume difference  $\Delta v = v_l - v_s$  and the entropy difference  $\Delta s = s_l - s_s = (\Delta u + p\Delta v - \Delta\mu)/T$  can both be evaluated from standard  $NpT$  simulations of the two bulk phases at coexistence ( $\Delta\mu = 0$ ).

We use a trapezoidal predictor-corrector method to compute coexistence pressures at the temperatures  $T_i = 0.02 \times 10^{(i/24)}$ , where  $i$  is an integer (compare the solid black line in Fig. 3). Substituting  $t = T$  and  $y = p$ , the first-order differential equation to be solved is rewritten in the standard form as

$$y' = f(t, y), \quad (23)$$

where  $f$  is the slope evaluated as  $\Delta s/\Delta v$  [Eq. (22)]. Suppose one knows the point  $(t_i, y_i)$  on the coexistence line, either from the interface-pinning method or from a previous step of the Clausius–Clapeyron integration, and wishes to compute the next point  $(t_{i+1}, y_{i+1})$ . If  $h = t_{i+1} - t_i$ , the prediction of the simple Euler algorithm is

$$y_{i+1}^{(0)} = y_i + hf(t_i, y_i). \quad (24)$$

A better estimate is provided by Heun’s method,

$$y_{i+1}^{(1)} = y_i + \frac{h}{2}[f(t_i, y_i) + f(t_i + h, y_{i+1}^{(0)})]. \quad (25)$$

The next estimate in an iterative predictor-corrector approach is

$$y_{i+1}^{(2)} = y_i + \frac{h}{2}[f(t_i, y_i) + f(t_i + h, y_{i+1}^{(1)})] \quad (26)$$

or, in general,

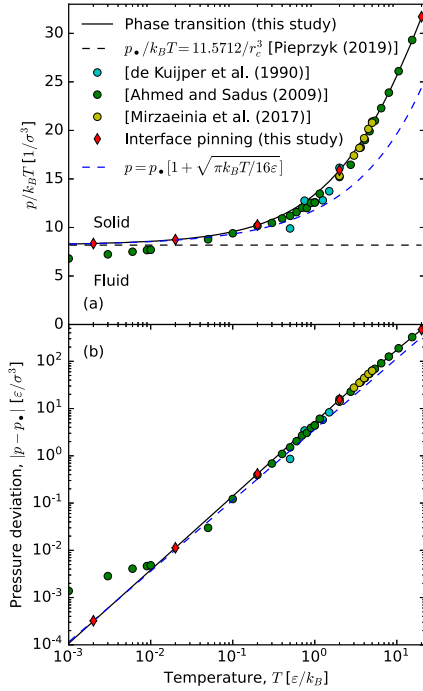


**FIG. 3.** Coexistence pressure as a function of the temperature. (a) The solid black line shows the reduced coexistence pressure  $p/k_B T$  as a function of the temperature (this study). The black dashed line is the  $T \rightarrow 0$  HS limit,  $p_*/k_B T$ , and the colored dots represent literature coexistence pressures.<sup>42–44</sup> The red diamonds were computed with the interface-pinning method (this study). The blue dashed line shows that at low temperatures, the pressure scales as  $T^{3/2}$ , as expected from HS theories [inset Eq. (30) into Eq. (46)]. (b) The absolute value of the coexistence pressure in excess of its  $T \rightarrow 0$  limit. The red diamonds were computed with the interface-pinning method (this study).

$$y_{i+1}^{k+1} = y_i + \frac{h}{2} [f(t_i, y_i) + f(t_i + h, y_{i+1}^k)]. \quad (27)$$

In the limit of large  $k$ 's, this converges to the trapezoidal rule of integration, where forward and backward integrations yield the same result.

Which criterion to use in order to determine when the iterations have converged? To answer this, we note that since the slopes are evaluated from finite  $NpT$  simulations, one expects a significant statistical error on the  $f$ 's used above. If  $\hat{f}(t, y)$  is the theoretical slope,  $f(t, y) = \hat{f}(t, y) + e_f$ , where  $e_f$  is drawn from a

normal distribution with standard deviation  $\sigma_f$ . This error is estimated by dividing  $NpT$  simulations into statistically independent blocks.<sup>34</sup> The error on  $y_{i+1}^{k+1}$  is  $e_y = h e_f$  and  $\sigma_y = |h| \sigma_f$ . We terminate the predictor-corrector iteration when

$$|y_{i+1}^{k+1} - y_{i+1}^k| < \sigma_y, \quad (28)$$

since this indicates that changes of  $y_{i+1}$ 's are mainly due to the statistical uncertainty on the slopes.

In summary, numerical integration of the Clausius–Clapeyron relation comes with errors from ignoring higher-order terms and

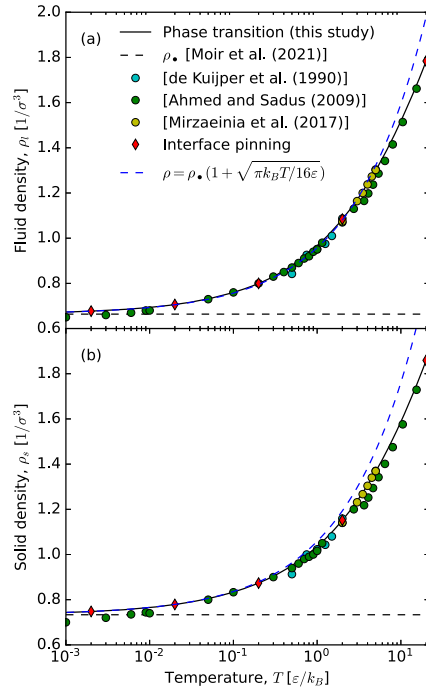


**FIG. 4.** Fluid density at freezing and solid density at melting as functions of the temperature. (a) The solid black line shows the density of the fluid at coexistence (this study). The dashed line is the  $T \rightarrow 0$  limit [see Eq. (47)], and the colored dots are literature data.<sup>42–44</sup> The red diamonds are densities computed with the interface-pinning method. (b) The solid black line shows the density of the solid at coexistence (this study), the dashed line is the  $T \rightarrow 0$  limit, and the colored dots represent literature data.<sup>42–44</sup> The red diamonds were computed with the interface-pinning method (this study).

from the statistical uncertainty of the slopes. To quantify the overall error of the integration, one can compare to accurate estimates from interface pinning at selected state points. As an example, for  $T_{48} = 2\epsilon/k_B$ , from the Clausius–Clapeyron integration we estimate the coexistence pressure to be  $31.7532\epsilon/\sigma^3$ , which should be compared to  $31.8086(66)\epsilon/\sigma^3$  for the interface-pinning method (see Table I). The error of the computed phase-transition line is not visible in most figures of this paper, with notable exceptions at low temperatures (error bars are shown in the figures whenever errors are significant).

Figures 3 and 4 show coexistence pressures and densities, respectively, from this study and from the literature.<sup>42–44</sup> We note that the low-temperature estimates of Ref. 43 are not accurate, whereas the high-temperature estimates of Refs. 42–44 are consistent with our results. As a consistency check, we note that the computed coexistence line reaches the HS limit<sup>95</sup> when  $T \rightarrow 0$  (the dashed lines in Figs. 3 and 4 show the HS limits).

#### IV. COMPARING THE PREDICTIONS OF DIFFERENT HARD-SPHERE THEORIES

Having accurately located the WCA phase transition, we use this to test the HS theories by comparing their predictions to the low-temperature WCA melting-line data.

##### A. Coexistence pressure and densities

Starting with the coexistence pressure, we first need coexistence information on the HS system. Fernandez *et al.*<sup>96</sup> estimated that the HS coexistence pressure is given by  $p_d = 11.5727(10)k_B T/d^3$ . This value is consistent with

$$p_d = 11.5712(10) k_B T/d^3, \quad (29)$$

computed more recently by Pieprzyk *et al.*<sup>95</sup> we use the latter value in this paper. In the zero-temperature limit, the HS diameter of the WCA interaction is  $d = r_c$ , which gives the coexistence pressure

$$p_* = 8.1821(7) k_B T/\sigma^3. \quad (30)$$

The bullet subscript “•” refers throughout this paper to the HS limit of the WCA model that is approached when  $T \rightarrow 0$ , i.e., setting  $d = r_c$ .

The solid black line in Fig. 5(a) shows the coexistence pressure divided by the thermal energy,  $p/k_B T$ , and the black dashed line shows the  $d = r_c$  prediction. The predicted pressure is too low since the effective HS diameter, as mentioned, is smaller than  $r_c$  at finite temperatures where particles may overlap. In Fig. 5(a), we also consider other criteria for  $d$ 's [by insertions into Eq. (29)]. At  $T = 0.02\epsilon/k_B$ , the  $d = r_c$  criterion underestimates the coexistence pressure by 7%, while the AWC and BH criteria give only a 1% error. Thus, the HS theories give a significant improvement of the predicted coexistence pressure. It is hard to decide from Fig. 5 which theory is best since this depends on the temperature. We return below to the low-temperature limit that provides a definite answer. First, we turn to the HS theories' predictions of the melting- and freezing densities.

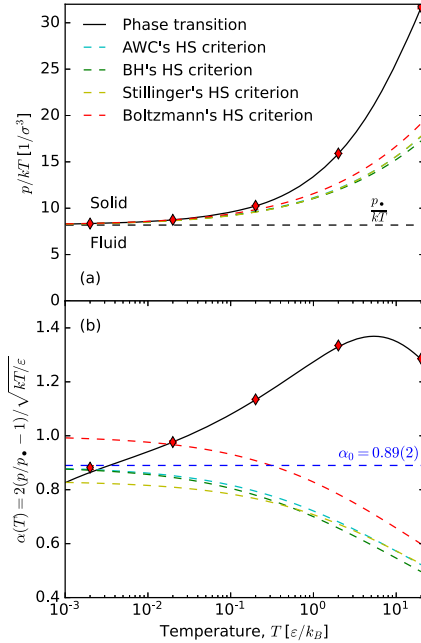


**FIG. 5.** Melting-line pressure compared to HS predictions. (a) The solid black line shows the reduced coexistence pressure,  $p/k_B T$ . The dashed lines show predictions of the HS theories [see Eqs. (12), (14), (18), and (20)]. The red diamonds show coexistence pressures computed with the interface-pinning method. (b)  $\alpha_p(T) = 2(p/p_* - 1)/\sqrt{k_B T/\epsilon}$  [Eq. (43)] along the computed phase transition line (black solid) and the theoretical predictions also shown in the upper panel (dashed lines). The blue dashed line [ $\alpha_0 = 0.89(1)$ ] is the  $T \rightarrow 0$  limit determined from coexistence densities [see Fig. 6(b)]. AWC and BH give accurate predictions in the low-temperature limit. The red diamonds are the results of the interface-pinning method where blue error bars indicate the statistical error. There is a systematic inaccuracy of the Clausius–Clapeyron integration (solid black) at the lowest temperatures.

The HS fluid freezing density was computed recently by Moir, Lue, and Bannerman to the value<sup>97</sup>

$$\rho_d^{(f)} = 0.93890(7)/d^3 \quad (31)$$

and the melting density of the solid to

$$\rho_d^{(s)} = 1.03715(9)/d^3. \quad (32)$$

In the zero-temperature limit of the WCA system ( $d = r_c$ ), we get

$$\rho_*^{(f)} = 0.66390(5)/\sigma^3 \quad (33)$$

and

$$\rho_{\bullet}^{(s)} = 0.73337(6)/\sigma^3. \quad (34)$$

When inserting the  $d$ 's of the above HS criteria, we get the temperature-dependent density predictions shown in Fig. 6(a) as colored dashed lines.

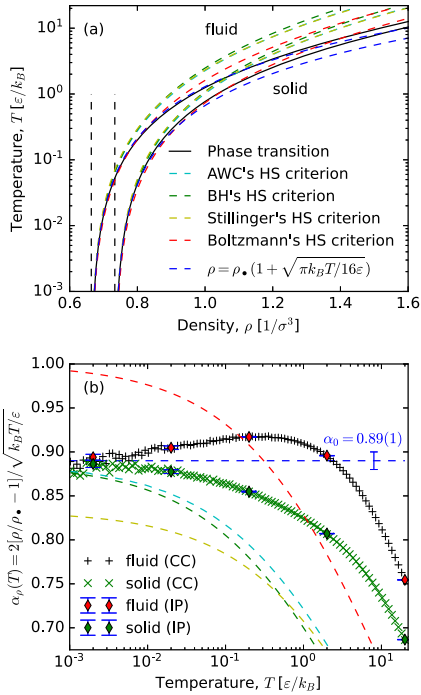


**FIG. 6.** Density-temperature phase diagram. (a) The solid black lines are the coexistence densities (compare Fig. 4). The vertical black dashed lines mark the  $T \rightarrow 0$  HS limits, i.e., the quantities  $\rho_{\bullet}^{(f)}$  and  $\rho_{\bullet}^{(s)}$ . The turquoise, green, yellow, and red dashed curves are predictions of the HS theories, see Eqs. (12), (14), (18), and (20). The two blue dashed lines are the low-temperature fits  $\rho_f = \rho_{\bullet}^{(f)} [1 + 0.445\sqrt{k_B T/\epsilon}]$  and  $\rho_s = \rho_{\bullet}^{(s)} [1 + 0.445\sqrt{k_B T/\epsilon}]$ . (b) The black '+'s show  $\alpha_0(T) = 2(\rho/\rho_{\bullet} - 1)/\sqrt{k_B T/\epsilon}$ , where the densities  $\rho$  and  $\rho_{\bullet}$  refer to the fluid. The green 'x's is  $\alpha_0(T)$  using the solid densities. Red and green diamonds are densities computed with the interface-pinning method. The blue error bars indicate the 95% confidence interval. We find that the zero-temperature limit gives  $\alpha_0 = \lim_{T \rightarrow 0} \alpha(T) = 0.89(1)$ . The turquoise, green, yellow, and red dashed curves are predictions of the HS theories. The AWC and BH give the correct low-temperature limit within the statistical accuracy.

## B. Analytical treatment of the low-temperature limit

Inspired by the functional form of Stillinger's and Boltzmann's HS criteria [Eqs. (12) and (20)], we write the low-temperature limit of the effective HS diameter as

$$d_{\alpha} = r_c \left( 1 - \frac{\alpha_0}{6} \sqrt{k_B T/\epsilon} \right) \quad \text{for } T \rightarrow 0, \quad (35)$$

which implies that

$$d_{\alpha}^{-3} = r_c^{-3} \left( 1 + \frac{\alpha_0}{2} \sqrt{k_B T/\epsilon} \right) \quad \text{for } T \rightarrow 0. \quad (36)$$

For the Boltzmann criterion, one has  $\alpha_0 = 1$  while Stillinger's criterion gives  $\alpha_0 = \sqrt{\ln(2)} \approx 0.83$ .

Since  $d$  is the same for the AWC and BH criteria in the  $T \rightarrow 0$  limit (see Sec. II B 3), the  $\alpha_0$ 's are also identical. To evaluate  $\alpha_0$ , we first note that the BH integral defining the HS diameter [Eq. (18)] can be written as

$$d = r_c - \int_0^{r_c} \exp(-v(r)/k_B T) dr. \quad (37)$$

Since the WCA pair potential is purely repulsive, it reaches its minimum at zero when  $r = r_c$ . Thus, at low temperatures, the above integral is centered near  $r_c$ , i.e., near  $x = 0$ , where  $x = r_c - r$ . Keeping the first non-vanishing term in a Taylor expansion, we get

$$v(x) = \frac{1}{2} k_2 x^2 \quad \text{for } T \rightarrow 0 \quad (38)$$

and  $x \geq 0$  (distances shorter than  $r_c$ ) with<sup>35</sup>

$$k_2 \equiv \left. \frac{d^2 v}{dr^2} \right|_{r_c} = 36\sqrt{4}\epsilon/\sigma^2. \quad (39)$$

(This approximation is shown as a black dashed line in Fig. 1.) Finding  $d$  from Eq. (37) involves solving a Gaussian integral in  $x$ . Expanding the upper limit of the integral to infinity (which is exact as  $T \rightarrow 0$ ), we find

$$d = r_c - \sqrt{\frac{\pi k_B T}{2k_2}}. \quad (40)$$

By equating  $d = d_{\alpha}$  [Eqs. (35) and (40)], we get

$$\alpha_0 = \frac{6}{r_c} \sqrt{\frac{\pi \epsilon}{2k_2}} \quad (41)$$

or  $\alpha_0 = \sqrt{\pi}/2 \approx 0.886227$ . The theoretical  $\alpha_0$  values are summarized in Table II.

**TABLE II.**  $\alpha_0$  values.

From simulations	$\alpha_0 = 0.89(1)$
Boltzmann	$\alpha_0 = 1$
AWC and BH	$\alpha_0 = \frac{1}{2} \sqrt{\pi} = 0.886 \dots$
Stillinger	$\alpha_0 = \sqrt{\ln(2)} = 0.833 \dots$

To estimate  $\alpha_0$  from the simulations, we insert  $d_{\alpha}^{-3}$  of Eq. (36) into Eq. (29) for the coexistence pressure, leading to

$$p = p_{\bullet} \left[ 1 + \frac{\alpha_0}{2} \sqrt{k_B T / \epsilon} \right] \quad \text{for } T \rightarrow 0. \quad (42)$$

Thus, a way to determine  $\alpha_0$  is to define the function [Fig. 5(b)]

$$\alpha_p(T) = \frac{2}{\sqrt{k_B T / \epsilon}} \left[ \frac{p(T)}{p_{\bullet}} - 1 \right], \quad (43)$$

for which we note that  $\alpha_0 = \alpha(T)$  for  $T \rightarrow 0$ . Similarly, for the densities  $\rho = \rho_f$  or  $\rho = \rho_s$ , we get

$$\rho = \rho_{\bullet} \left[ 1 + \frac{\alpha_0}{2} \sqrt{k_B T / \epsilon} \right] \quad \text{for } T \rightarrow 0 \quad (44)$$

and define

$$\alpha_p(T) = \frac{2}{\sqrt{k_B T / \epsilon}} \left[ \frac{\rho(T)}{\rho_{\bullet}} - 1 \right]. \quad (45)$$

Figure 6(a) shows the temperature dependence of the fluid and solid densities at coexistence (solid lines). These densities yield the  $\alpha_p(T)$ 's shown with black '+'s and green 'x's, respectively, in Fig. 6(b). From the low-temperature points, we estimate  $\alpha_0 = 0.89(1)$ . The colored dashed lines show the predictions of the HS theories (the  $T \rightarrow 0$  limits agree with the values of Table II). We conclude that the AWC and BH theories gives excellent agreement as  $T \rightarrow 0$ . Figure 5(b) shows  $\alpha_p(T)$  computed using the coexistence pressure. In agreement with the results for the  $\alpha_p(T)$ 's, we find that  $\alpha_0 = 0.89(1)$  (blue dashed line).

The success of the AWC and BH theories suggests writing the coexistence pressure and densities as follows [inserting  $\alpha_0 = \sqrt{\pi}/2$  into Eqs. (42) and (44)]:

$$p = p_{\bullet} \left[ 1 + \sqrt{\frac{\pi k_B T}{16\epsilon}} \right] \quad (46)$$

and

$$\rho = \rho_{\bullet} \left[ 1 + \sqrt{\frac{\pi k_B T}{16\epsilon}} \right], \quad (47)$$

respectively (see the blue dashed lines of Figs. 3–5). Interestingly, this low-temperature approximation gives better predictions than the *neat* HS theories—even at high temperatures (with the exception of Boltzmann's criterion near  $T \approx 0.5\epsilon/k_B$ ). We do not have an explanation for this.

Equations (46) and (47) summarize an important result of this paper, providing an analytical HS approximation for the low-temperature freezing of the WCA fluid. This can be generalized to any other purely repulsive pair-potential  $v(r)$  that is truncated smoothly at  $r = r_c$  by the following steps:

1. Compute  $k_2$  using Eq. (39).
2. Derive  $\alpha_0$  within the BH theory by inserting  $k_2$  into Eq. (41).
3. Low-temperature predictions for the coexistence pressure and densities are then provided by inserting  $\alpha_0$  into Eqs. (42) and (44), respectively.

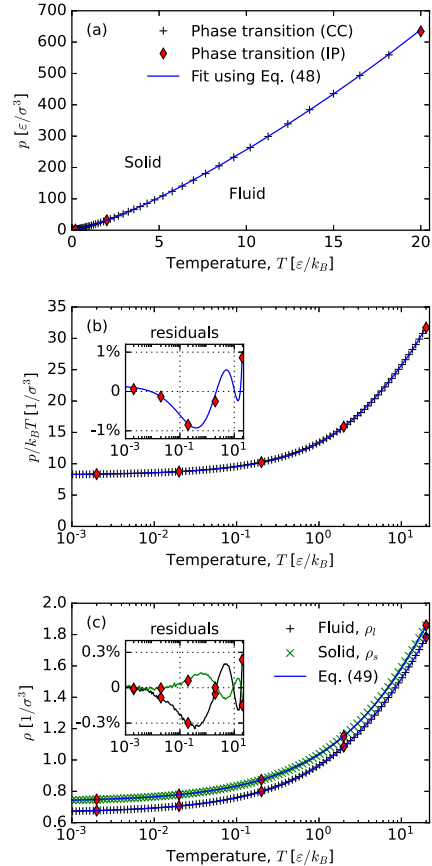


FIG. 7. (a) Empirical fit [Eq. (48)] (blue dashed line) to the phase transition pressure (+). The red diamonds show the phase transition pressure computed with the interface pinning method. (b) Empirical fit [Eq. (48)] to the reduced pressure,  $p/T$ . The inset shows the residuals in percent. (c) Empirical fit [Eq. (49)] to the freezing density of the fluid ( $\rho_f$ ) and the melting density of the solid ( $\rho_s$ ).

### C. Empirical fit to the coexistence line

We have provided a theory for low temperatures. To provide a practical description of the coexistence line that includes high temperatures, we continue the power series in  $\tau = \sqrt{k_B T / \epsilon}$  by writing the coexistence pressure as

$$p(T) = p_\bullet \left[ 1 + \sqrt{\frac{\pi}{16}} \tau + \tilde{a}_2 \tau^2 + \tilde{a}_3 \tau^3 + \tilde{a}_4 \tau^4 \right]. \quad (48)$$

The parameters  $\tilde{a}_2 = 0.2619$ ,  $\tilde{a}_3 = -0.0871$ , and  $\tilde{a}_4 = 0.0087$  are determined by non-linear least squares to fit to the reduced pressure,  $p/T$  [see Eq. (30) for  $p_\bullet$ ]. The accuracy of the fit is within 1% for the investigated temperatures [see Figs. 7(a) and 7(b)]. Similar for the coexistence densities, we define

$$\rho(T) = \rho_\bullet \left[ 1 + \sqrt{\frac{\pi}{16}} \tau + \tilde{a}_2 \tau^2 + \tilde{a}_3 \tau^3 + \tilde{a}_4 \tau^4 \right]. \quad (49)$$

A non-linear least squares fit to the freezing density of the liquid ( $\rho_l$ ) yields  $\tilde{a}_2 = 0.0240$ ,  $\tilde{a}_3 = -0.0178$ , and  $\tilde{a}_4 = 0.00206$ . A fit to the melting density of the solid ( $\rho_s$ ) yields  $\tilde{a}_2 = -0.03336$ ,  $\tilde{a}_3 = 0.00447$ , and  $\tilde{a}_4 = -0.000457$  [see Eqs. (33) and (34) for  $\rho_\bullet = \rho_\bullet^{(l)}$  and  $\rho_\bullet = \rho_\bullet^{(s)}$ , respectively]. The accuracy of the fits is within 0.3% and 0.15% for the liquid and solid densities, respectively. The fits to the densities are shown in Fig. 7(c).

## V. OUTLOOK

We have shown that HS theories give excellent predictions of the WCA melting line at low temperatures, in particular, for the AWC and BH approximations. At higher temperatures, the HS theories are less accurate. This is not surprising because the WCA model only resembles a HS system at low temperatures. How to predict the WCA melting-line pressures and coexistence densities at high temperatures? One possibility is to generalize the low-temperature HS approximation by considering the lines of constant excess entropy  $S_{\text{ex}}$  (the entropy in excess of the ideal gas entropy at the same density and temperature, a negative quantity that in some textbooks<sup>88</sup> is referred to as the residual entropy). For the HS system, these lines are determined entirely by the density, i.e., they are vertical in the density–temperature phase diagram. In Ref. 35, it was shown that the WCA system’s structure and dynamics are near-invariant along the lines of constant excess entropy, which are referred to as isomorphs.<sup>99,100</sup> An isomorph can be computed by

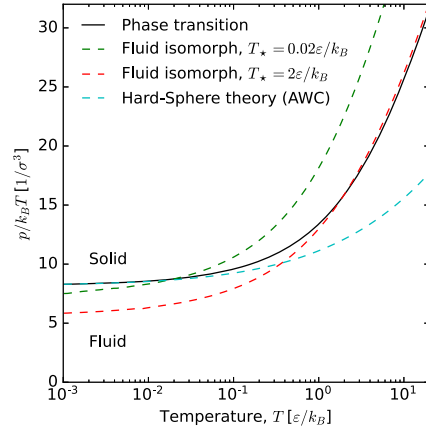


**FIG. 8.** The solid black line shows the reduced coexistence pressure  $p/k_B T$  as a function of the temperature. The red and green dashed lines are isomorphs of the fluid, i.e., lines along which the excess entropy is constant. By construction, the isomorphs touch the phase-transition line at  $T_* = 0.02\epsilon/k_B$  and  $T_* = 2\epsilon/k_B$ , respectively. The turquoise dashed line is the prediction of the AWC theory.

numerical integration in the  $\ln T - \ln \rho$  plane [e.g., using the fourth-order Runge–Kutta method (RK4)<sup>55</sup>] for which the required slope is  $f = 1/\gamma$ , where<sup>99,101,102</sup>

$$\gamma \equiv \left( \frac{\partial \ln T}{\partial \ln \rho} \right)_{S_{\text{ex}}}. \quad (50)$$

The “density-scaling exponent”  $\gamma$  may be computed from virial and potential-energy fluctuations in the NVT ensemble via the statistical-mechanical identity  $\gamma = \langle \Delta W \Delta U \rangle / \langle (\Delta U)^2 \rangle$ .<sup>99</sup> Figure 8 shows the reduced pressure  $p/k_B T$  of two fluid isomorphs that

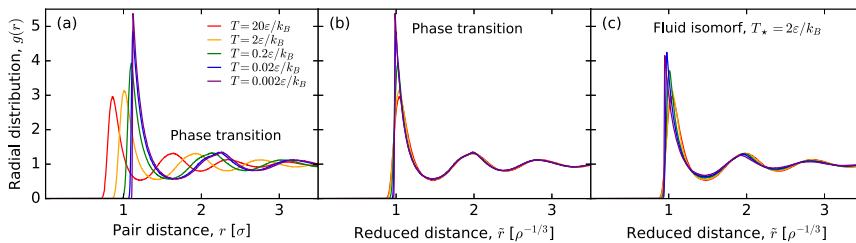


**FIG. 9.** (a) The radial distribution function  $g(r)$  of the fluid at coexistence. (b) The radial distribution function as a function of the reduced distance  $\tilde{r} = r\sqrt[3]{\rho}$  for the fluid at coexistence. (c) The radial distribution as a function of the reduced distance  $\tilde{r} = r\sqrt[3]{\rho}$  for a fluid isomorph that touches the coexistence line at  $T_* = 2\epsilon/k_B$ .

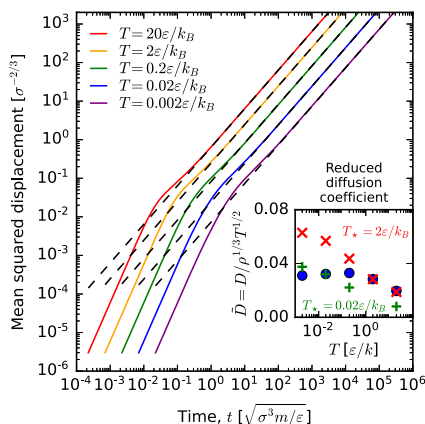


**FIG. 10.** The solid lines show the mean-square displacement  $\langle |r(t) - r(0)|^2 \rangle$  for selected state points along the coexistence line (see Table I). The dashed lines are long-time fits to  $\langle |r(t) - r(0)|^2 \rangle = 6Dt$ , where  $D$  is the diffusion coefficient. The dots in the inset show the reduced diffusion coefficient  $\bar{D} = D\rho^{1/3}T^{1/2}$ . The red 'x's and green '+'s are the reduced diffusion coefficient for state points along the isomorphs with  $T_* = 2\epsilon/k_B$  and  $T_* = 0.02\epsilon/k_B$ , respectively.

overlap with the coexistence line at  $T_* = 0.02\epsilon/k_B$  and  $T_* = 2\epsilon/k_B$ , respectively (dashed green and red lines). For comparison, the turquoise dashed line shows the prediction of the reduced coexistence pressure of the AWC theory. For the entire temperature span, the isomorphs give predictions with an overall accuracy comparable to that of the best HS approximation (AWC).

Figures 9 and 10 show the structure and dynamics along the melting line and the fluid isomorph in reduced units.<sup>99</sup> The physics is more invariant along the coexistence lines than along the isomorph, which is in contrast to previous findings for the LJ system where the opposite applies.<sup>103</sup> We note, however, that isomorphs only follow the coexistence lines to a first approximation. For the LJ system, accurate predictions for the thermodynamics of freezing and melting are arrived at within the isomorph-theoretical perturbation framework proposed in Ref. 103—we plan to apply the same method to the WCA system.

#### ACKNOWLEDGMENTS

This work was supported by the VILLUM Foundation's Matter Grant (No. 16515).

#### AUTHOR DECLARATIONS

##### Conflict of Interest

The authors have no conflicts to disclose.

#### Author Contributions

**Eman Attia:** Data curation (equal); Investigation (equal). **Jeppe C. Dyre:** Conceptualization (supporting); Formal analysis (supporting); Funding acquisition (lead); Supervision (equal); Writing – original draft (supporting); Writing – review & editing (supporting). **Ulf R. Pedersen:** Conceptualization (lead); Data curation (lead); Formal analysis (equal); Investigation (lead); Software (lead); Supervision (equal); Validation (lead); Visualization (lead); Writing – original draft (lead); Writing – review & editing (lead).

#### DATA AVAILABILITY

The data that support the findings of this study are openly available in Zenodo at <http://doi.org/10.5281/zenodo.6505217>, reference number 6505217.

#### REFERENCES

- <sup>1</sup>J.-P. Hansen and I. R. McDonald, *Theory of Simple Liquids: With Applications to Soft Matter*, 4th ed. (Academic, New York, 2013).
- <sup>2</sup>W. G. Hoover, S. G. Gray, and K. W. Johnson, "Thermodynamic properties of the fluid and solid phases for inverse power potentials," *J. Chem. Phys.* **55**, 1128–1136 (1971).
- <sup>3</sup>W. G. Hoover, D. A. Young, and R. Grover, "Statistical mechanics of phase diagrams. I. Inverse power potentials and the close-packed to body-packed cubic transition," *J. Chem. Phys.* **56**, 2207–2210 (1972).
- <sup>4</sup>D. M. Heyes and A. C. Brańka, "Physical properties of soft repulsive particle fluids," *Phys. Chem. Chem. Phys.* **9**, 5570–5575 (2007).
- <sup>5</sup>A. C. Brańka and D. M. Heyes, "Pair correlation function of soft-sphere fluids," *J. Chem. Phys.* **134**, 064115 (2011).
- <sup>6</sup>A. K. Bacher, T. B. Schroder, and J. C. Dyre, "The EXP pair-potential system. I. Fluid phase isotherms, isochores, and quasuniversality," *J. Chem. Phys.* **149**, 114501 (2019).
- <sup>7</sup>A. K. Bacher, T. B. Schroder, and J. C. Dyre, "The EXP pair-potential system. II. Fluid phase isomorphs," *J. Chem. Phys.* **149**, 114502 (2018).
- <sup>8</sup>U. R. Pedersen, A. K. Bacher, T. B. Schroder, and J. C. Dyre, "The EXP pair-potential system. III. Thermodynamic phase diagram," *J. Chem. Phys.* **150**, 174501 (2019).
- <sup>9</sup>B. J. Alder and T. E. Wainwright, "Phase transition for a hard sphere system," *J. Chem. Phys.* **27**, 1208–1209 (1957).
- <sup>10</sup>W. Wood and J. D. Jacobson, "Preliminary results from a recalculation of the Monte Carlo equation of state of hard spheres," *J. Chem. Phys.* **27**, 1207–1208 (1957).
- <sup>11</sup>B. J. Alder and T. E. Wainwright, "Studies in molecular dynamics. I. General method," *J. Chem. Phys.* **31**, 459–466 (1959).
- <sup>12</sup>B. J. Alder and T. E. Wainwright, "Studies in molecular dynamics. II. Behavior of a small number of elastic spheres," *J. Chem. Phys.* **33**, 1439–1451 (1960).
- <sup>13</sup>J. O. Hirschfelder, C. F. Curtiss, and R. B. Bird, *Molecular Theory of Gases and Liquids* (John Wiley & Sons, New York, 1954).
- <sup>14</sup>J. D. Bernal, "The Bakerian lecture, 1962. The structure of liquids," *Proc. R. Soc. London, Ser. A* **280**, 299–322 (1964).
- <sup>15</sup>B. Widom, "Intermolecular forces and the nature of the liquid state," *Science* **157**, 375–382 (1967).
- <sup>16</sup>J. A. Barker and D. Henderson, "What is 'liquid'? Understanding the states of matter," *Rev. Mod. Phys.* **48**, 587–671 (1976).
- <sup>17</sup>J. D. Weeks, D. Chandler, and H. C. Andersen, "Role of repulsive forces in determining the equilibrium structure of simple liquids," *J. Chem. Phys.* **54**, 5237–5247 (1971).
- <sup>18</sup>D. Chandler, J. D. Weeks, and H. C. Andersen, "Van der Waals picture of liquids, solids, and phase transformations," *Science* **220**, 787–794 (1983).
- <sup>19</sup>F. C. Andrews, "A simple approach to the equilibrium statistical mechanics of two-dimensional fluids," *J. Chem. Phys.* **64**, 1941–1947 (1976).

- <sup>20</sup>R. J. Speedy, F. X. Prielmeier, T. Vardag, E. W. Lang, and H.-D. Lüdemann, "Diffusion in simple fluids," *Mol. Phys.* **66**, 577–590 (1989).
- <sup>21</sup>D. Ben-Amotz and D. R. Herschbach, "Estimation of effective diameters for molecular fluids," *J. Phys. Chem.* **94**, 1038–1047 (1990).
- <sup>22</sup>S. Hess, M. Kröger, and H. Voigt, "Thermomechanical properties of the WCA–Lennard-Jones model system in its fluid and solid states," *Physica A* **250**, 58–82 (1998).
- <sup>23</sup>D. Ben-Amotz and G. Stell, "Hard sphere perturbation theory for fluids with soft-repulsive-core potentials," *J. Chem. Phys.* **120**, 4844–4851 (2004).
- <sup>24</sup>D. Ben-Amotz and G. Stell, "Reformulation of Weeks–Chandler–Andersen perturbation theory directly in terms of a hard-sphere reference system," *J. Phys. Chem. B* **108**, 6877–6882 (2004).
- <sup>25</sup>D. M. Heyes and H. Okumura, "Equation of state and structural properties of the Weeks–Chandler–Andersen fluid," *J. Chem. Phys.* **124**, 164507 (2006).
- <sup>26</sup>L. Berthier and G. Tarjus, "Nonperturbative effect of attractive forces in viscous liquids," *Phys. Rev. Lett.* **103**, 170601 (2009).
- <sup>27</sup>U. R. Pedersen, T. B. Schröder, and J. C. Dyre, "Repulsive reference potential reproducing the dynamics of a liquid with attractions," *Phys. Rev. Lett.* **105**, 157801 (2010).
- <sup>28</sup>L. Berthier and G. Tarjus, "The role of attractive forces in viscous liquids," *J. Chem. Phys.* **134**, 214503 (2011).
- <sup>29</sup>S. A. Khrapak, M. Chaudhuri, and G. E. Morfill, "Communication: Universality of the melting curves for a wide range of interaction potentials," *J. Chem. Phys.* **134**, 241101 (2011).
- <sup>30</sup>L. Böhling, A. A. Veldhorst, T. S. Ingebrigtsen, N. P. Bailey, J. S. Hansen, S. Toxvaerd, T. B. Schröder, and J. C. Dyre, "Do the repulsive and attractive pair forces play separate roles for the physics of liquids?," *J. Phys.: Condens. Matter* **25**, 032101 (2012).
- <sup>31</sup>Z. E. Dell and K. S. Schweizer, "Microscopic theory for the role of attractive forces in the dynamics of supercooled liquids," *Phys. Rev. Lett.* **115**, 205702 (2015).
- <sup>32</sup>L.-C. Valdés, J. Gerges, T. Mizuguchi, and F. Aifouard, "Crystallization tendencies of modelled Lennard-Jones liquids with different attractions," *J. Chem. Phys.* **148**, 014501 (2018).
- <sup>33</sup>J. Chatteraj and M. P. Ciamarra, "Role of attractive forces in the relaxation dynamics of supercooled liquids," *Phys. Rev. Lett.* **124**, 028001 (2020).
- <sup>34</sup>Y. Zhou, B. Mei, and K. S. Schweizer, "Integral equation theory of thermodynamics, pair structure, and growing static length scale in metastable hard sphere and Weeks–Chandler–Andersen fluids," *Phys. Rev. E* **101**, 042121 (2020).
- <sup>35</sup>E. Attia, J. C. Dyre, and U. R. Pedersen, "Extreme case of density scaling: The Weeks–Chandler–Andersen system at low temperatures," *Phys. Rev. E* **103**, 062140 (2021).
- <sup>36</sup>S. S. Khali, D. Chakraborty, and D. Chaudhuri, "Two-step melting of the Weeks–Chandler–Anderson system in two dimensions," *Soft Matter* **17**, 3473–3485 (2021).
- <sup>37</sup>A. Banerjee and D. J. Wales, "Energy landscapes for a modified repulsive Weeks–Chandler–Andersen potential," *J. Phys.: Condens. Matter* **34**, 034004 (2021).
- <sup>38</sup>S. Toxvaerd, "Role of the attractive forces in a supercooled liquid," *Phys. Rev. E* **103**, 022611 (2021).
- <sup>39</sup>A. Singh and Y. Singh, "How attractive and repulsive interactions affect structure ordering and dynamics of glass-forming liquids," *Phys. Rev. E* **103**, 052105 (2021).
- <sup>40</sup>D. M. Heyes, S. Pieprzyk, and A. C. Brańka, "Application of cell models to the melting and sublimation lines of the Lennard–Jones and related potential systems," *Phys. Rev. E* **104**, 044119 (2021).
- <sup>41</sup>Y. Zhou, B. Mei, and K. S. Schweizer, "Activated relaxation in supercooled monodisperse atomic and polymeric WCA fluids: Simulation and ECNLE theory," *J. Chem. Phys.* **156**, 114901 (2022).
- <sup>42</sup>A. de Kuijper, J. A. Schouten, and J. P. J. Michels, "The melting line of the Weeks–Chandler–Anderson Lennard–Jones reference system," *J. Chem. Phys.* **93**, 3515–3519 (1990).
- <sup>43</sup>A. Ahmed and R. J. Sadus, "Phase diagram of the Weeks–Chandler–Anderson potential from very low to high temperatures and pressures," *Phys. Rev. E* **80**, 061101 (2009).
- <sup>44</sup>A. Mirzaeinia, F. Feyzi, and S. M. Hashemianzadeh, "Equation of state and Helmholtz free energy for the atomic system of the repulsive Lennard–Jones particles," *J. Chem. Phys.* **147**, 214503 (2017).
- <sup>45</sup>J. E. Lennard-Jones, "On the determination of molecular fields.—I. From the variation of the viscosity of a gas with temperature," *Proc. R. Soc. London, Ser. A* **106**, 441–462 (1924).
- <sup>46</sup>J. E. Lennard-Jones, "On the determination of molecular fields.—II. From the equation of state of a gas," *Proc. R. Soc. London, Ser. A* **106**, 463–477 (1924).
- <sup>47</sup>N. Bailey, T. Ingebrigtsen, J. S. Hansen, A. Veldhorst, L. Böhling, C. Lemarchand, A. Olsen, A. Bacher, L. Costigliola, U. R. Pedersen, H. Larsen, J. C. Dyre, and T. Schröder, "RUMD: A general purpose molecular dynamics package optimized to utilize GPU hardware down to a few thousand particles," *SciPost Phys.* **3**, 038 (2017).
- <sup>48</sup>D. Frenkel and B. Smit, *Understanding Molecular Simulation: From Algorithms to Applications*, 2nd ed. (Academic Press, San Diego, 2002).
- <sup>49</sup>N. Gronbech-Jensen, "Complete set of stochastic Verlet-type thermostats for correct Langevin simulations," *Mol. Phys.* **118**, e1662506 (2019).
- <sup>50</sup>N. Gronbech-Jensen and O. Farago, "Constant pressure and temperature discrete-time Langevin molecular dynamics," *J. Chem. Phys.* **141**, 194108 (2014).
- <sup>51</sup>N. Gronbech-Jensen, N. R. Hayre, and O. Farago, "Application of the G-JF discrete-time thermostat for fast and accurate molecular simulations," *Comput. Phys. Commun.* **185**, 524–527 (2014).
- <sup>52</sup>R. W. Zwanzig, "High-temperature equation of state by a perturbation method. I. Nonpolar gases," *J. Chem. Phys.* **22**, 1420–1426 (1954).
- <sup>53</sup>S. Rowlinson, "An equation of state of gases at high temperatures and densities," *Mol. Phys.* **7**, 349–361 (1964).
- <sup>54</sup>H. L. Frisch, J. L. Katz, E. Praestgaard, and J. L. Lebowitz, "High-temperature equation of state—Argon," *J. Phys. Chem.* **70**, 2016–2020 (1966).
- <sup>55</sup>J. A. Barker and D. Henderson, "Perturbation theory and equation of state for fluids. II. A successful theory of liquids," *J. Chem. Phys.* **47**, 4714–4721 (1967).
- <sup>56</sup>H. C. Andersen, J. D. Weeks, and D. Chandler, "Relationship between the hard-sphere fluid and fluids with realistic repulsive forces," *Phys. Rev. A* **4**, 1597–1607 (1971).
- <sup>57</sup>L. Verlet and J.-J. Weis, "Perturbation theory for the thermodynamic properties of simple liquids," *Mol. Phys.* **24**, 1013–1024 (1972).
- <sup>58</sup>F. Lado, "Choosing the reference system for liquid state perturbation theory," *Mol. Phys.* **52**, 871–876 (1984).
- <sup>59</sup>G. Kahl, "Analytic representation for the pair-correlation function of a hard-sphere Yukawa system," *Mol. Phys.* **67**, 879–889 (1989).
- <sup>60</sup>J. Chang and S. I. Sandler, "A real function representation for the structure of the hard-sphere fluid," *Mol. Phys.* **81**, 735–744 (1994).
- <sup>61</sup>A. Trokhymchuk, I. Nezbeda, J. Jirsák, and D. Henderson, "Hard-sphere radial distribution function again," *J. Chem. Phys.* **123**, 024501 (2005).
- <sup>62</sup>D. Henderson, "Analytic methods for the Percus–Yevick hard sphere correlation functions," *Condens. Matter Phys.* **12**, 127–135 (2009).
- <sup>63</sup>J. C. Dyre, "Simple liquids' quasiuniversality and the hard-sphere paradigm," *J. Phys.: Condens. Matter* **28**, 323001 (2016).
- <sup>64</sup>J. R. Solana, *Perturbation Theories for the Thermodynamic Properties of Fluids and Solids* (CRC Press, London, England, 2019).
- <sup>65</sup>B. P. Akhouri and J. R. Solana, "On the choice of the effective diameter in the high-temperature expansion for the Lennard–Jones fluid," *Mol. Phys.* **120**, e2028918 (2022).
- <sup>66</sup>T. van Westen, M. Hammer, B. Hafskjold, A. Aasen, J. Gross, and O. Wilhelmson, "Perturbation theories for fluids with short-ranged attractive forces: A case study of the Lennard–Jones spline fluid," *J. Chem. Phys.* **156**, 104504 (2022).
- <sup>67</sup>L. Boltzmann, *Lectures on Gas Theory* (Dover Publications, 1864).
- <sup>68</sup>M. S. Wertheim, "Exact solution of the Percus–Yevick integral equation for hard spheres," *Phys. Rev. Lett.* **10**, 321–323 (1963).
- <sup>69</sup>W. R. Smith, D. J. Henderson, P. J. Leonard, J. A. Barker, and E. W. Grundke, "Fortran codes for the correlation functions of hard sphere fluids," *Mol. Phys.* **106**, 3–7 (2008).
- <sup>70</sup>P. Virtanen *et al.*, "SciPy 1.0: Fundamental algorithms for scientific computing in Python," *Nat. Methods* **17**, 261–272 (2020).

- <sup>71</sup>R. Piessens, E. De Doncker-Kapenga, C. Uberhuber, and D. K. Kahaner, *Quadpack*, Springer Series in Computational Mathematics (Springer, Berlin, Germany, 1983).
- <sup>72</sup>L. Verlet, "Integral equations for classical fluids. I. The hard sphere case," *Mol. Phys.* **41**, 183–190 (1980).
- <sup>73</sup>L. Verlet, "Integral equations for classical fluids. II. Hard spheres again," *Mol. Phys.* **42**, 1291–1302 (1981).
- <sup>74</sup>G. A. Martynov and G. N. Sarkisov, "Exact equations and the theory of liquids. V," *Mol. Phys.* **49**, 1495–1504 (1983).
- <sup>75</sup>S. B. Yuste and A. Santos, "Radial distribution function for hard spheres," *Phys. Rev. A* **43**, 5418–5423 (1991).
- <sup>76</sup>Y. Tang and B. C. Y. Lu, "Improved expressions for the radial distribution function of hard spheres," *J. Chem. Phys.* **103**, 7463–7470 (1995).
- <sup>77</sup>*Theory and Simulation of Hard-Sphere Fluids and Related Systems*, edited by A. Mulero (Springer, Berlin, Heidelberg, 2008).
- <sup>78</sup>A. Santos, S. B. Yuste, and M. López de Haro, "Structural and thermodynamic properties of hard-sphere fluids," *J. Chem. Phys.* **153**, 120901 (2020).
- <sup>79</sup>F. H. Stillinger, "Phase transitions in the Gaussian core system," *J. Chem. Phys.* **65**, 3968–3974 (1976).
- <sup>80</sup>C. N. Likos, "Effective interactions in soft condensed matter physics," *Phys. Rep.* **348**, 267–439 (2001).
- <sup>81</sup>U. R. Pedersen, "Direct calculation of the solid-liquid Gibbs free energy difference in a single equilibrium simulation," *J. Chem. Phys.* **139**, 104102 (2013).
- <sup>82</sup>U. R. Pedersen, F. Hummel, G. Kresse, G. Kahl, and C. Dellago, "Computing Gibbs free energy differences by interface pinning," *Phys. Rev. B* **88**, 094101 (2013).
- <sup>83</sup>V. Thapar and F. A. Escobedo, "Extensions of the interfacial pinning method and application to hard core systems," *J. Chem. Phys.* **141**, 124117 (2014).
- <sup>84</sup>U. R. Pedersen, F. Hummel, and C. Dellago, "Computing the crystal growth rate by the interface pinning method," *J. Chem. Phys.* **142**, 044104 (2015).
- <sup>85</sup>B. Cheng, E. A. Engel, J. Behler, C. Dellago, and M. Ceriotti, "Ab initio thermodynamics of liquid and solid water," *Proc. Natl. Acad. Sci. U. S. A.* **116**, 1110–1115 (2019).
- <sup>86</sup>R. S. Newman, S. Nola, J. Dshemuchadse, and S. C. Glotzer, "Shape-controlled crystallisation pathways in dense fluids of *ccp*-forming hard polyhedra," *Mol. Phys.* **117**, 3819–3826 (2019).
- <sup>87</sup>K. G. Steenbergen, E. Pahl, and P. Schwerdtfeger, "Accurate, large-scale density functional melting of Hg: Relativistic effects decrease melting temperature by 160 K," *J. Phys. Chem. Lett.* **8**, 1407–1412 (2017).
- <sup>88</sup>A. K. Sharma and F. A. Escobedo, "Nucleus-size pinning for determination of nucleation free-energy barriers and nucleus geometry," *J. Chem. Phys.* **148**, 184104 (2018).
- <sup>89</sup>Y. Zou, S. Xiang, and C. Dai, "Investigation on the efficiency and accuracy of methods for calculating melting temperature by molecular dynamics simulation," *Comput. Mater. Sci.* **171**, 109156 (2020).
- <sup>90</sup>L.-F. Zhu, J. Janssen, S. Ishibashi, F. Körmann, B. Grabowski, and J. Neugebauer, "A fully automated approach to calculate the melting temperature of elemental crystals," *Comput. Mater. Sci.* **187**, 110065 (2021).
- <sup>91</sup>W. Lechner and C. Dellago, "Accurate determination of crystal structures based on averaged local bond order parameters," *J. Chem. Phys.* **129**, 114707 (2008).
- <sup>92</sup>D. A. Kofke, "Gibbs-Duhem integration: A new method for direct evaluation of phase coexistence by molecular simulation," *Mol. Phys.* **78**, 1331–1336 (1993).
- <sup>93</sup>D. A. Kofke, "Direct evaluation of phase coexistence by molecular simulation via integration along the saturation line," *J. Chem. Phys.* **98**, 4149–4162 (1993).
- <sup>94</sup>H. Flyvbjerg and H. G. Petersen, "Error estimates on averages of correlated data," *J. Chem. Phys.* **91**, 461–466 (1989).
- <sup>95</sup>S. Pieprzyk, M. N. Bannerman, A. C. Brańka, M. Chudak, and D. M. Heyes, "Thermodynamic and dynamical properties of the hard sphere system revisited by molecular dynamics simulation," *Phys. Chem. Chem. Phys.* **21**, 6886–6899 (2019).
- <sup>96</sup>L. A. Fernández, V. Martín-Mayor, B. Seoane, and P. Verrocchio, "Equilibrium fluid-solid coexistence of hard spheres," *Phys. Rev. Lett.* **108**, 165701 (2012).
- <sup>97</sup>C. Moir, L. Lue, and M. N. Bannerman, "Tethered-particle model: The calculation of free energies for hard-sphere systems," *J. Chem. Phys.* **155**, 064504 (2021).
- <sup>98</sup>I. Prigogine and R. Defay, *Chemical Thermodynamics* (Prentice Hall Press, 1954).
- <sup>99</sup>N. Gnan, T. B. Schroder, U. R. Pedersen, N. P. Bailey, and J. C. Dyre, "Pressure-energy correlations in liquids. IV. 'Isomorphs' in liquid phase diagrams," *J. Chem. Phys.* **131**, 234504 (2009).
- <sup>100</sup>T. B. Schroder and J. C. Dyre, "Simplicity of condensed matter at its core: Generic definition of a Roskilde-simple system," *J. Chem. Phys.* **141**, 204502 (2014).
- <sup>101</sup>J. C. Dyre, "Hidden scale invariance in condensed matter," *J. Phys. Chem. B* **118**, 10007–10024 (2014).
- <sup>102</sup>J. C. Dyre, "Perspective: Excess-entropy scaling," *J. Chem. Phys.* **149**, 210901 (2018).
- <sup>103</sup>U. R. Pedersen, L. Costigliola, N. P. Bailey, T. B. Schroder, and J. C. Dyre, "Thermodynamics of freezing and melting," *Nat. Commun.* **7**, 12386 (2016).

## 1. SUMMARY

1. Tracing out configurational adiabats numerically using two integration methods: Euler and fourth order Runge Kutta (RK4).
2. Check for isomorphism through checking the structure and dynamics along the adiabats in the light of Rosenfeld excess entropy scaling.

## 2. MODELS OF LIQUIDS

Liquid models are often defined via pair potentials  $v(r)$ . If  $r_{ij} = |\mathbf{r}_i - \mathbf{r}_j|$  is the distance between particles  $i$  and  $j$ , the potential energy  $U$  as a function of all particles coordinates is given by  $U = \sum_{i<j} v(r_{ij})$ . Three model systems are simulated by Molecular Dynamics in the canonical ( $NVT$ ).

1. The Lennard-Jones potential (LJ):

$$v(r) = 4\epsilon[(r/\sigma)^{-12} - (r/\sigma)^{-6}]$$

2. The Weeks Chandler-Andersen potential (WCA) is same as LJ potential but shifted upwards by  $\epsilon$  and truncated at the LJ pair potential minimum  $r = 2^{1/6}\sigma$ , which makes it a purely repulsive potential.

3. The Extended Simple Point Charge System (SPC/E):

$$U(\mathbf{R}) = U_q(\mathbf{R}) + U_{Bond}(\mathbf{R}) + U_{LJ}(\mathbf{R})$$

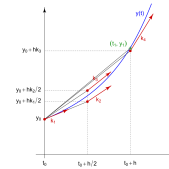
It is a standard water model.

## 6. REFERENCES

- [1] Y. Rosenfeld, "Relation between the transport coefficients and the internal entropy of simple systems," Phys. Rev. A 15, 2545–2549 (1977).
- [2] N. P. Bailey, U. R. Pedersen, N. Gnan, T. B. Schröder, and J. C. Dyre. Pressure-energy correlations in liquids. II. Analysis and consequences. J.Chem. Phys., 129(18):184508, 2008.
- [3] J. C. Dyre. Isomorphs, hidden scale invariance, and quasiuniversality. Phys. Rev. E, 88:042139, Oct 2013.
- [4] J. D. Weeks, D. Chandler, and H. C. Andersen. "Role of repulsive forces in determining the equilibrium structure of simple liquids," J.Chem. Phys. 54, 5237–5247 (1971).

## 3. CONFIGURATIONAL ADIABATS

1. Configurational adiabats are lines in the phase diagrams with the same excess entropy defined by  $S_{ex}(\rho, T) \equiv S(\rho, T) - S_{id}(\rho, T)$ .
2. Euler integration,  $t_1 = t_0 + h$ ,  $y_1 = y_0 + hf(t_0, y_0) + O(h^2)$ . The RK4 integration,  $t_1 = t_0 + h$ ,  $y_1 = y_0 + k_1/6 + k_2/3 + k_3/3 + k_4/6 + O(h^5)$ .



3. Configurational adiabats are considered "isomorphs" when there is invariance in the structure and dynamics along the state points of the configurational adiabat.

## 4. TESTING INTEGRATION METHODS

### Consistency check for the two integration methods.

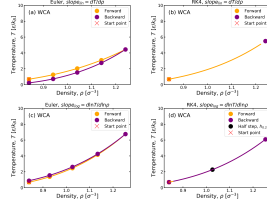


Figure 1: Configurational adiabat traced out in WCA phase diagram with  $h_{RK} = 0.4$  and  $h_{Euler} = 0.1$  (a) Euler, lin:  $\Delta T = 0.214$  (b) RK4, lin:  $\Delta T = 0.120$  (c) Euler, log:  $\Delta T = 0.186$  (d) RK4, log:  $\Delta T = 0.002$ .

**Conclusion 1:** This shows that RK4 with logarithmic expression for the slope gives best accuracy compared to Euler (lin and log) and RK4 (lin). The half step midpoint is plotted (black dot) to show the accuracy of the interpolation as well.

### Choosing the suitable step size and simulation time to optimize accuracy.

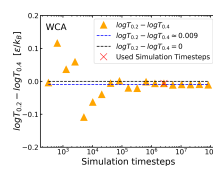


Figure 2: The difference in temperature from using full step  $h = 0.4$  and the two half steps  $h = 0.2$  from  $\rho = 0.84$  till  $\rho = 1.25$  plotted against simulation time per slope evaluation.

**Conclusion 2:** RK4 can be as accurate as the adaptive double step-size RK method within the corresponding simulation time. The desired  $h$  can change and the simulation time changes accordingly.

## 5. ISOMORPHISM CHECK (STRUCTURE & DYNAMICS)

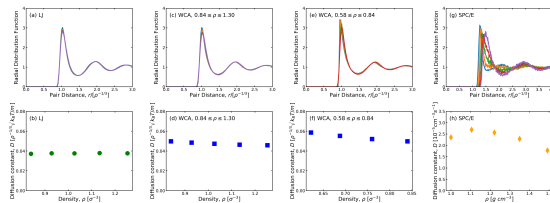


Figure 3: The Radial distribution functions and the diffusion constants of the configurational adiabats traced in the three systems.

**Conclusion 3:** Invariance in the structure and dynamics of LJ system is clearly visible in which configurational adiabats are considered isomorphic. In the lower density region for WCA model, configurational adiabats become less invariant reaching the hard sphere limit as  $\gamma$  changes rapidly. The SPC/E model shows variance in the structure and dynamics compared to the rest of the systems. The configurational adiabats deviate from being isomorphic.

# Declaration of Co-authorship

---

## Declaration of co-authorship

Co-authors should fulfill the requirements of the Vancouver rules<sup>1</sup>

1. Title of article *Extreme Case of density Scaling: The Weeks-Chandler Andersen System at low temperatures*
2. Declaration of the individual elements

The extent of the candidate's contribution to the article is assessed on the following scale.

- A. has contributed to the work (0-33%)  
B. has made a substantial contribution (34-66%)  
C. did the majority of the work (67-100%)

*physical Review E 103,062140 (2021)*

	Author 1	Author 2	Author 3	Author 4	Author 5
1. Formulation in the concept phase of the basic scientific problem on the basis of theoretical questions which require clarification, including a summary of the general questions which it is assumed will be answered via analyses or actual experiments/investigations.	A	A	C		
2. Planning of experiments/analyses and formulation of investigative methodology in such a way that the questions asked under (1) can be expected to be answered, including choice of method and independent methodological development.	A	A	C		
3. Involvement in the analysis or the actual experiments/investigation.	C	A	A		
4. Presentation, interpretation and discussion of the results obtained in the form of an article or manuscript.	B	C	A		

### 3. Signatures

Date	Name	Author #	Signature
26-09-2022	Eman Attia	1	<i>Eman Attia</i>
26/9-22	JEPPE DYRE	2	<i>Jeppe Dyre</i>
26/9-2022	ULF R PEDERSEN	3	<i>Ulf R Pedersen</i>

## Declaration of co-authorship

Co-authors should fulfill the requirements of the Vancouver rules<sup>1</sup>

1. Title of article *ISomorph invariance in the liquid and plastic-crystal phase of asymmetric dumbbell models*
2. Declaration of the individual elements

The extent of the candidate's contribution to the article is assessed on the following scale.

- A. has contributed to the work (0-33%)  
B. has made a substantial contribution (34-66%)  
C. did the majority of the work (67-100%)

*arXiv:2209.11498, 23 Sep. 2022*

	Author 1	Author 2	Author 3	Author 4	Author 5
1. Formulation in the concept phase of the basic scientific problem on the basis of theoretical questions which require clarification, including a summary of the general questions which it is assumed will be answered via analyses or actual experiments/investigations.	A,B or C <i>B</i>	A,B or C <i>B</i>	A,B or C <i>A</i>	A,B or C	A,B or C
2. Planning of experiments/analyses and formulation of investigative methodology in such a way that the questions asked under (1) can be expected to be answered, including choice of method and independent methodological development.	A,B or C <i>B</i>	A,B or C <i>B</i>	A,B or C <i>A</i>	A,B or C	A,B or C
3. Involvement in the analysis or the actual experiments/investigation.	A,B or C <i>C</i>	A,B or C <i>B</i>	A,B or C <i>A</i>	A,B or C	A,B or C
4. Presentation, interpretation and discussion of the results obtained in the form of an article or manuscript.	A,B or C <i>B</i>	A,B or C <i>C</i>	A,B or C <i>A</i>	A,B or C	A,B or C

### 3. Signatures

Date	Name	Author #	Signature
<i>26-09-2022</i>	<i>Eman Alkai</i>	<i>1</i>	<i>Eman Alkai</i>
<i>26/9-22</i>	<i>JEPPE DYRE</i>	<i>2</i>	<i>Jeppe Dyr</i>
<i>26/9-2022</i>	<i>ULF R PEDERSEN</i>	<i>3</i>	<i>Ulf R Pedersen</i>

## Declaration of co-authorship

Co-authors should fulfill the requirements of the Vancouver rules<sup>i</sup>

1. Title of article *Comparing four hard-sphere approximations for the low temperature WCA melting line*
2. Declaration of the individual elements *temperature WCA melting line*

The extent of the candidate's contribution to the article is assessed on the following scale.

- A. has contributed to the work (0-33%)
- B. has made a substantial contribution (34-66%)
- C. did the majority of the work (67-100%)

*J.chem.Phys. 157, 034502 (2022)*

	Author 1	Author 2	Author 3	Author 4	Author 5
1. Formulation in the concept phase of the basic scientific problem on the basis of theoretical questions which require clarification, including a summary of the general questions which it is assumed will be answered via analyses or actual experiments/investigations.	A,B or C <i>A</i>	A,B or C <i>A</i>	A,B or C <i>C</i>	A,B or C	A,B or C
2. Planning of experiments/analyses and formulation of investigative methodology in such a way that the questions asked under (1) can be expected to be answered, including choice of method and independent methodological development.	A,B or C <i>A</i>	A,B or C <i>A</i>	A,B or C <i>C</i>	A,B or C	A,B or C
3. Involvement in the analysis or the actual experiments/investigation.	A,B or C <i>A</i>	A,B or C <i>A</i>	A,B or C <i>C</i>	A,B or C	A,B or C
4. Presentation, interpretation and discussion of the results obtained in the form of an article or manuscript.	A,B or C <i>A</i>	A,B or C <i>B</i>	A,B or C <i>C</i>	A,B or C	A,B or C

### 3. Signatures

Date	Name	Author #	Signature
<i>25-09-2022</i>	<i>Eman Attia</i>	<i>1</i>	<i>Eman Attia</i>
<i>26/9-2022</i>	<i>JEPPE DYRE</i>	<i>2</i>	<i>Jeppe Dyre</i>
<i>26/9-2022</i>	<i>ULF R. PEDERSEN</i>	<i>3</i>	<i>Ulf R. Pedersen</i>